
Matteo Solazzo, B.Sc., M.Sc.

# Electroconductive Biomaterial Platforms: From Piezoresistive Sensors To Cardiac Tissue Engineering

---

Trinity College Dublin, June 2022

A thesis submitted to the University of Dublin in partial fulfilment of the requirements for the degree of

**Doctor of Philosophy**

**Supervisor**: Professor Michael G. Monaghan

**Internal examiner**: Professor Conor T. Buckley

**External examiner**: Professor Jonny Blaker

# Declaration

I declare that this thesis has not been submitted as an exercise for a degree at this or any other university and is entirely my own work.

I agree to deposit this thesis in the University's open access institutional repository or allow the library to do so on my behalf, subject to Irish Copyright Legislation and Trinity College Library conditions of use and acknowledgement.

Matteo Solazzo

Dublin 2022

# Summary

New classes of functional materials and the rapid advances being made in manufacturing technologies are key requirements to drive the next step forward in healthcare. In recent decades, conjugated polymers have gained interest due to their electroconductive properties and ease of processability. Amongst such materials, poly(*3,4*-ethylene dioxythiophene):poly(styrene sulfonate) (PEDOT:PSS) emerges as one promising candidate for long-term biomedical applications for which electrical and electronic features are key. PEDOT:PSS is dispersible in water-based solutions, benefiting of a tremendous advantage if considering the material processability. PEDOT:PSS can be directly applied as coating to pre-existing substrates via straight forward methods such as casting or dip coating, without the need of extra solvents. Furthermore, in its water-based form, PEDOT:PSS can be directly processed via ice-templating (also known as lyophilisation or freeze-drying) to obtain three-dimensional (3D) porous sponge-like constructs. To date, most studies have focussed on two-dimensional membranes or coatings, and much optimisation is required to fully translate PEDOT:PSS to 3D applications. In this thesis, I investigate strategies for the modification of 3D architectures achieved via ice-templating, determining how these impact on the electro-mechanical properties. Together, I explore new crosslinking molecules and post-treatment protocols to improve the electrical conductivity of these constructs, aiming to address the typical drop of electrical conductivity often associated with standard crosslinking methods. I then demonstrate the potential of 3D porous PEDOT:PSS from two perspectives.

First, I investigate wearable sensors. Such devices are applied within medicine, fitness, robotics and are a potential tool for implementing improved personalised healthcare. Amongst these assets, piezoresistive sensors are frequently used due to their high sensitivity, simple device structure, and easy to interpret readout. Relying on the intrinsic piezoresistivity of PEDOT:PSS and on the versatility of ice-templating as manufacturing

technique, I fabricated a family of sensors with diverse stiffness and microarchitecture. Studying their piezoresistivity, I explored how such features affected the performance of the sensor. Finally, the optimal combination of microarchitecture and stiffness was chosen as a candidate for the fabrication of a piezoresistive sensor prototype and the detection of simple body movements.

This research then focusses on another field benefiting from the optimisation of 3D electroconductive porous scaffolds, namely tissue engineering - specifically in vitro cardiac models. Although there have been multiple improvements in pharmacological therapies, cardiovascular disease remains a leading cause of mortality and morbidity worldwide. Tissue engineering has potential to provide improved repair to the damaged myocardium, and it can enable the development of more physiologically relevant platforms for the identification and testing of new drugs. The most modern of these constructs - also known as engineered heart tissues (EHT) - have been successful in replicating specific cellular mechanisms of the contractile unit of the heart.

In this context, I changed the chemistry of 3D porous PEDOT:PSS constructs, aiming to obtain scaffolds with more cardio-inductive stiffness as well as an electrical conductivity closer to that of the native myocardium. Using poly(ethylene glycol) diglycidyl ether (PEGDE) as crosslinker or alternatively a crystallisation post-treatment on glycidoxypropyl-trimethoxysilane (GOPS) crosslinked scaffolds, biocompatible constructs with enhanced softness and conductivity were obtained, resulting in more suitable candidates for the development of a scaffold-based EHT. Finally, I conceptualised, designed, and fabricated both a pacing bioreactor and a rig for the generation of electrically stimulated in vitro models combining the previously developed 3D scaffolds.

This body of work is clear demonstration of PEDOT:PSS having the potential and versatility required to unlock new frontiers for biomedical engineering. I have demonstrated that it is possible to tailor the morphological and physical features of PEDOT:PSS constructs to meet their target application, and that 3D PEDOT:PSS-based scaffolds can facilitate functional guidance platforms for tissue engineering.

# Acknowledgements

I never considered a career in research, let alone a PhD. Until six or seven years ago I did not even know what a PhD was. Therefore, first and foremost, I want to start my acknowledgements with the two people who, more than anyone else, were responsible for the brainwashing that led me to this PhD journey.

To Dr. Gabriele Nasello, who - back in September 2015 - inexplicably saw something in me and became a true friend since then. Thank you. Being in your proximity made me become a different person and make unprecedented choices. You talked me into following you to Pittsburgh and without that magical year I would not be here writing these lines. I meticulously keep memory of all our conversations as your wisdom is always profoundly appreciated.

To Prof. Antonio D'Amore, who introduced me to research and became my first academic mentor, thank you. Antonio, you are one of the most brilliant minds that I have ever met and one of the bravest and most relentless souls. Your passion and your work ethic have deeply influenced my vision of what a person can and should do. Your support helped me obtain the PhD scholarship in Dublin, and I will never stop being grateful to you.

I would like to sincerely thank my supervisor Prof. Michael Monaghan. The idea of being the first PhD student of a very young professor was a frightening one. I remember thinking "this can either end up incredibly bad or surprisingly well". Almost 5 years later, I can confidently say that we did pretty well. You were able to teach me invaluable lessons, and I like to believe that on many aspects we grew together. I am sincerely grateful for your constant support, trust, and positivity. Since the very beginning, you entrusted me with a number of extra tasks such as teaching assistantships, student supervision, conference organisation, peer-review, job interviews, research proposals… you name it. The list might sound overwhelming, but without that trust and responsibility I would have missed out on many important lessons about academia and life in general.

I would like to thank my examiners, Prof. Conor Buckley and Prof. Jonny Blaker for their comments and suggestions, and for offering me a very engaging discussion. I would also like to thank my chairperson, Prof. Richard Reilly for letting my defence be an enjoyable experience.

I was lucky enough to be surrounded by people who helped me with proofreading parts of this manuscript. Thanks Brooke, Morgan, Grace, Gabriele, Marcos, Sinead, and Olwyn.

Working on an independent project, I did not have many occasions to share experiments with others. But I want to sincerely thank all the students I had the pleasure of supervising and working with. A special mention to Grace, Alejandro, Gaetan, Elisa, and Linette. PEDOT:PSS will be our shared nightmare, but I hope that the overall research experience in Trinity was as positive for you as it has been for me.

TCBE revealed itself to be a surreal place, and that is mainly because of the people who work (or should I say “live”) there. Julia, Stefan, Pierluca, Mathieu, Olwyn, Cristina, Pedro, Ian, Grace, Brooke, Meena, Sinead, Rossana, Sophia, Dinorath, Morgan, Carolina, Stéphane, and Nadia. So many brilliant minds with the ability to be the cleverest of scientists and simultaneously the most implacable of party people. We shared countless good memories and experiences, and I cannot help but be nostalgic when I look back on them.

Thanks to my family: Mum, Dad, and Marco. You have always been supportive of me, trusting my judgement and decisions, not caring whether they were different from yours. I cannot put in words how much it meant to me to see you here in Dublin, amongst the crowd, attending my pre-viva talk and sharing those unforgettable days with me. There is no physical distance that love cannot bridge, and you persistently showed this to me. Of course, thanks also to Leila, Loki and Thor, who always welcome me with open hearts every time I come back home.

Thanks to Giovanni, Giorgio, and Marzio. With even more certainty than 5 years ago, I am so glad that our paths crossed and that since then you are family to me.

Thanks to my lifelong friends from San Donato, my hometown. Riccio, Vice, Cava, Canto, Monny, Pippo, Papi, Effe, Bubo, King, Mutto, and Sabba. In one way or another, you guys

eased the toughest of days with laughter and fun.

Thanks to Marco, who visited me in Dublin more than anyone else, probably becoming more of a Dubliner than me. Thanks Gabriella, Vincenzo, Francesco, Valentina, and all the “Teppisti”. Despite the distance, you guys have always been there for a chat and a drink every chance we got.

Thanks to the Dublin Italian crew: Gianluca, Bruno, Peppe, Marta, Paolo, Mario, Delva, Ema, and Zen. Our beloved Italy was never too far away when we shared meals, parties, drinks, and chats together.

Thanks to Rachele. Every time I came back to Italy our long walks and catch-up chats made me still feel connected to my previous life.

Thanks to Alessia. Life is odd - we learned it the hard way. Despite all the circumstances and changes, you were (and still are) there for me. Thanks for continuously believing in me.

Thanks to Chiara and Xavi. I know I am not the easiest person to handle, and that it must have been complicated to deal with me all these years. Thanks for your patience and thanks for making me always feel at home.

And last, but definitely not least, thanks to Angelica. You know why, when, where, and how. Thanks for bringing me to the finish line.

# Table of Contents

# List of Figures

# List of Schemes

# List of Tables

# Nomenclature

| | |
|---|---|
| 2D | two-dimensional |
| 3D | three-dimensional |
| α-act | sarcomeric α-actinin |
| Ag | silver |
| ANOVA | analysis of variance |
| Au | gold |
| AV | atrioventricular |
| BMSC | bone marrow stem cell |
| BSA | bovine serum albumin |
| CM | cardiomyocytes |
| CNTs | carbon nanotubes |
| CP | conjugated polymers |
| cTnT | cardiac troponin T |
| CV | cyclic voltammetry |
| Cx43 | connexin 43 |
| DAPI | *4',6*-Diamidine-*2'*-phenylindoledihydrochloride |
| EAS | electroactive sponge |
| ECM | extracellular matrix |
| EDC | *N*-(*3*-Dimethylaminoproypl)-*N*-ethylcarbodiimide hydrochloride |
| EHT | engineered heart tissue |
| EIS | electrochemical Impedance Spectroscopy |
| ESC | embryonic stem cells |
| FTIR | Fourier Transform Infrared Spectroscopy |
| GelMA | methacrylated gelatin |
| GO | graphene oxide |
| GOPS | glycidoxypropyltrimethoxysilane |
| HAc | acetic acid |
| hIPSC | human induced pluripotent stem cells |
| hIPS-CM | human induced pluripotent derived cardiomyocytes |

| | |
|---|---|
| ICP | Intrinsically conductive polymers |
| MI | myocardial infarction |
| microCT | X-ray microtomography |
| $M_n$ | molecular weight |
| MSC | mesenchymal stem cells |
| $Na_2HPO_4$ | sodium phosphate dibasic |
| NaCl | sodium chloride |
| NaOH | sodium hydroxide |
| NHS | *N*-Hydroxysuccinimide |
| NP | nanoparticles |
| nrCM | neonatal rat cardiomyocyte |
| PANI | polyaniline |
| PBS | phosphate buffered saline |
| PCL | polycaprolactone |
| PDMS | polydimethylsiloxane |
| PEDOT | poly(*3,4*-ethylene dioxythiophene) |
| PEG | poly(ethylene glycol) |
| PEGDE | poly(ethylene glycol) diglycidyl ether |
| PLA | polylactic acid |
| POMaC | poly(octamethylene maleate (anhydride) citrate) |
| PPy | polypyrrole |
| PSS | polystyrene sulfonate |
| PVDF | polyvinylidene difluoride |
| rGO | reduced graphene oxide |
| SEM | scanning electron microscopy |
| TCP | tissue culture plastic |
| $T_f$ | freezing temperature |
| XPS | X-ray photoelectron spectroscopy |

# Publications

### *Journal Articles*

1. **Solazzo, M**., Krukiewicz K., Zhussupbekova A., Fleisher K., Biggs M. J., Monaghan, M. G. PEDOT:PSS interfaces stabilised using a PEGylated crosslinker yield improved conductivity and biocompatibility. *Journal of Materials Chemistry B*. 7, 4811—4820 (2019).

   The candidate led the development of the concepts, designed and performed the experiments, and interpreted results. K.K. and M.B. performed the experiments and interpreted results concerning the electrical characterisation (i.e. Figure 5.2). A.Z. and K.F. performed the experiments and interpreted results related to the X-ray photoelectron spectroscopy (i.e. Figure 5.1 A-D). M.G.M. supervised the entire project. The candidate and M.G.M. wrote the paper.

2. **Solazzo, M**., O'Brien F., Nicolosi V., Monaghan, M. G. The rationale and emergence of electroconductive biomaterial scaffolds in cardiac tissue engineering. *APL Bioengineering*. 3, 041501 (2019).

   The candidate led the literature review process and prepared all graphics. V.N. provided the section "MXenes" (i.e. section 2.3.1.4). V.N. and F.O. provided consultation in the writing of the paper. M.G.M. supervised the entire project. The candidate and M.G.M. wrote the paper.

3. **Solazzo, M.,** Monaghan, M. G. Structural crystallization of crosslinked 3D PEDOT:PSS anisotropic porous biomaterials to generate highly conductive platforms for tissue engineering applications. *Biomaterials Science*. 9, 4317-4328 (2021).

   The candidate led the development of the concepts, designed and performed the

experiments, and interpreted results. M.G.M. supervised the entire project. The candidate and M.G.M. wrote the paper.

4. **Solazzo, M.,** Hartzell L., O'Farrell C., Monaghan, M. G. Beyond chemistry: Tailoring Stiffness and Microarchitecture to engineer highly sensitive biphasic elastomeric piezoresistive sensors. *ACS Applied Materials & Interfaces*, 14, 17, 19265–19277 (2022).

   The candidate led the development of the concepts, designed and performed the experiments, and interpreted results. L.H. and C.O. provided consultation in the experimental process. M.G.M. supervised the entire project. The candidate and M.G.M. wrote the paper.

5. **Solazzo, M**., Monaghan, M. G. Hydrophilic, conductive and flexible piezoresistive PEDOT:PSS 3D sensors with tunable microarchitecture and crosslinked using a PEGylated crosslinker. Submitted and under revision at *Synthetic Metals*.

   The candidate led the development of the concepts, designed and performed the experiments, and interpreted results. M.G.M. supervised the entire project. The candidate and M.G.M. wrote the paper.

6. Asaro, G. A., Suku, M., **Solazzo, M.**, Spurling, D., Genoud, K., O'Brien, F., Nicolosi, V., Monaghan, M. G. Development of MXene infused- collagen based materials as electroconductive in cardiac tissue engineering. In preparation.

***Patents:***

1. EU provisional patent application filed on 18/12/2020. Title: "A porous sponge material for use as active sensor in a piezoresistive sensor and one-step method for the manufacture thereof". Inventor contribution 50%.

# Conferences and symposia

***Podium presentations (*presenting author):***

1. **Solazzo, M.*,** Monaghan, M. G. Piezoresistive sensors and platforms in tissue engineering. 27th Bioengineering in Ireland 2022, Dublin. 20th and 21st of May 2022.
2. **Solazzo, M.*,** Monaghan, M. G. Development of electroconductive biohybrid scaffolds for in vitro cardiac models. 6th TERMIS World Congress, Maastricht, Netherlands, 15th to 19th of November 2021.
3. **Solazzo, M**.*. Monaghan, M. G. Engineered electroconductive biomaterial platforms for cardiac tissue engineering applications. TBSI Research Symposium 2019, Dublin, 4th of September 2019.
4. **Solazzo, M**.*, Zhussupbekova A., Krukiewicz K., Fleisher K., Biggs M. J. P., Monaghan, M. G. Minimally invasive 3D electroconductive biomaterial platforms for cardiac tissue engineering applications. TERMIS EU 2019, Rhodes, Greece, 27th to 31st of May 2019.
5. **Solazzo, M**.*, Wong S., Zhussupbekova A., Krukiewicz K., Fleisher K., Biggs M. J. P., Monaghan, M. G. Engineered electroconductive biomaterial platforms for cardiac tissue engineering applications. Sir Bernard Crossland Symposium 2019. Belfast, 17th and 18th of April 2019.
6. **Solazzo, M**.*, Monaghan, M. G. How to regenerate a broken heart. Trinity Research in Social Sciences. Dublin, 14th of February 2019.
7. **Solazzo, M**.*, Zhussupbekova A., Fleisher K., Monaghan, M. G. Minimally invasive 3D electroconductive biomaterial platforms for cardiac tissue engineering applications. 25th Bioengineering in Ireland 2019, Limerick. 18th and 19th of January 2019.
8. **Solazzo, M**.*, Monaghan, M. G. An electroconductive 3D porous PEDOT:PSS scaffold for cardiac tissue engineering applications. 24th Bioengineering in Ireland

2018, Dublin. 26-27 January 2018.

***Poster presentations (*presenting author):***

1. **Solazzo, M.***, Monaghan, M. G. Structural crystallization of crosslinked 3D PEDOT:PSS anisotropic porous biomaterials to generate highly conductive platforms for tissue engineering applications. TERMIS workshop: Cell-Matrix Interaction and Mechanobiology in Regenerative Medicine, Online event (Brno, Czech Republic), 10th and 11th of June 2021.
2. **Solazzo, M.*,** Monaghan, M. G. Structural crystallization of crosslinked 3D PEDOT:PSS anisotropic porous biomaterials to generate highly conductive platforms for tissue engineering applications. ESAO/TERMIS ONLINE Winter School, Online event (Jaca, Spain), 24th to 26th of February 2021.
3. **Solazzo, M.*,** Monaghan, M. G. Structural crystallization of crosslinked 3D PEDOT:PSS anisotropic porous biomaterials to generate highly conductive platforms for tissue engineering applications. 15th Annual International Electromaterials Science Symposium 2021, Online event (Wollogong, Australia), 3rd to 5th of February 2021.
4. **Solazzo, M**.*, Zhussupbekova A., Krukiewicz K., Fleisher K., Biggs M. J. P., Monaghan, M. G. Engineered electroconductive biomaterial platforms for cardiac tissue engineering applications. Gordon Research Seminar and Conference on Biomaterials and Tissue Engineering 2019, Barcelona, 28th July to 2nd of August 2019.
5. **Solazzo, M**.*, Zhussupbekova A., Fleisher K., Monaghan, M. G. An electroconductive 3D porous PEDOT:PSS scaffold for cardiac tissue engineering applications. AMBER Scientific Conference 2019, Kilkenny, Ireland. 10th January 2019.
6. **Solazzo, M**., Roudier G., Yelek C., Brogan C. G., Zhussupbekova A., Fleisher K., Monaghan, M. G.* An electroconductive 3D porous PEDOT:PSS scaffold for cardiac

tissue engineering applications. Signal Transduction by Engineered Extracellular Matrices, Gordon Research Conference. Andover, NH, US. 22nd to 27th of July 2018.

7. **Solazzo, M**.*, Roudier G., Yelek C., Brogan C. G., Zhussupbekova A., Fleisher K., Monaghan, M. G. An electroconductive 3D porous PEDOT:PSS scaffold for cardiac tissue engineering applications. 8th World Congress of Biomechanics, Dublin. 8th to 12th of July 2018.
8. Brogan, C. G.*, **Solazzo, M**., Monaghan, M. G. Evaluation of a 3D electro-conductive scaffold functionalized with Extracellular Matrix proteins. 24th Bioengineering in Ireland 2018, Dublin. 26th and 27th of January 2018.

# Awards

1. Winner of the Engineers Ireland Biomedical Research Medal at the 2022 Annual Conference of the Section of Bioengineering of the Royal Academy of Medicine in Ireland. Galway, 20th and 21st of May 2022
2. Best Poster Chair Awards. 6th TERMIS World Congress, Maastricht, Netherlands, 14th to 19th of November 2021.
3. 1st prize Poster Presentation. 15th Annual International Electromaterials Science Symposium 2021. Online event (Wollogong, Australia), 3rd to 5th of February 2021
4. Irish Research Council. Government of Ireland Postgraduate Scholarship. 2019/20 - 2020/21
5. 2nd prize Paper Presentation. Sir Bernard Crossland Symposium 2019. Belfast, 17th and 18th of April 2019.
6. Trinity Trust Travel Grant. Trinity College Dublin. 2019
7. 2nd prize. “Thesis in Three” competition at Trinity Centre for Biomedical Engineering Winter Symposium 2018. Dublin, 19th of December 2018.

# 1. Introduction

## *1.1. Electroconductive polymers: frontier in biomedical engineering*

Breakthroughs in biomedical engineering are key factors impacting the extension of human life expectancy.[1] Its growth is closely dependent on the discovery and development of new materials, one landmark example being nitinol which revolutionised the field of intravascular stents [2], or pyrolytic carbon that since its first use has consistently been adopted as the gold standard substrate for blood-contacting surfaces of heart valves.[3] Several biomedical applications - such as sensors [4] actuators [5], and tissue engineering [6] - rely on electrical and electronic components that demand a biomaterial with appropriate properties.

Electroconductive materials, and more precisely intrinsically electroconductive polymers (also known as conjugated polymers, CP), are one family of materials paving the way for new and more efficient products.[7] Polymers such as polyaniline (PANI), polypyrrole (PPy) and poly(*3,4*-ethylene dioxythiophene) (PEDOT) combine an ease of processing with notable electrical features.[7] CP are commonly coated onto devices, whereby delamination induced by cyclic deformation can limit performance and lifetime.[8] Researchers have also been investigating approaches to obtain three-dimensional (3D) structures partially or fully constituted by such polymers.[9] The inclusion of CP directly with standard non-conductive materials is one situation which can be attained during synthesis via addition of CP at concentrations higher than their percolation threshold - a material-specific concentration above which the final compound is electrically conductive.[10] In most cases, this strategy yields compounds with appropriate processability and with mechanical properties mainly dependent on the insulant material; however, the final conductivity is lower compared to the optimal magnitude of the pristine CP.[11] An alternative method to produce 3D conductive structures is lyophilisation of water-based polymers dispersions, such as poly(*3,4*-ethylene dioxythiophene):polystyrene sulfonate (PEDOT:PSS).[12] Several works have reported the

fabrication of highly porous sponge-like constructs where chemistry and microarchitecture can be modified to best match specific features.[9,13]

Given these approaches, there is room for better understanding of how to optimise 3D porous sponge-like scaffolds in terms of their physical properties. By tailoring the material composition and the fabrication protocols, more performant scaffolds can be generated. Such constructs can then find application in biomedical sciences ranging from wearable smart devices to biomaterials for improving the functionality of cells and tissues.

### *1.2. Engineered Heart Tissues: in vitro models for quicker and economic drug screening*

Despite therapeutic advances, cardiovascular disease remains a leading cause of mortality and morbidity worldwide.[14] The most common cause of acute damage to the heart is myocardial infarction (MI) [14,15], where oxygen depletion during MI leads to a rapid loss of cardiomyocytes (CMs) at the site of injury. The limited regeneration potential of the heart impedes appropriate functional tissue repair and therefore impairs the contractile force and aggravates patient quality of life.[15] The ongoing adverse compensatory mechanisms generates a fibrotic scar tissue that impairs the ability of electrical signals to travel across the heart wall and compromises the overall beating activity of the heart.[16]

Although advances in pharmacological therapies can partially address the main symptoms associated with MI, there is still a great need for new approaches to treat patients. Tissue engineering - a discipline that combines cells, materials and biochemical cues towards regenerative goals - can provide an appealing approach to repair the damaged myocardium [17], and develop more physiologically relevant platforms for the identification and testing of new drugs.[18] Engineered heart tissues (EHT) are in vitro models of myocardium that have been developed and ameliorated for over 20 years, with the goal to replicate the main features of the contractile unit of the heart.[19] Since their introduction [20], EHTs have evolved from collagen scaffolds populated with primary rat CMs [21], to systems combining complex gels and various types of cells derived from human induced pluripotent

stem cells (hiPSC).[17] Drastic improvements have also been made in terms of scale, starting from sub-millimetre scale tubules [22] to beating patches suitable for human heart geometry.[17] EHTs can replicate specific cellular mechanisms of the heart and they are expected to provide systematic drug screening by hospitals and pharmaceutical companies in the near future.[23]

Different types of stimulations - such as shear rate, mechanical deformation and electric field - can assist cell growth and maturation, resembling physiological tissue properties and response to drugs.[18] These cues are mostly delivered through custom-made bioreactors, although some commercial products - such as the C-dish™ line from IonOptix - are becoming available. On the biomaterial side, CP can provide therapeutic benefit for the regeneration of the heart wall after MI.[24-26] Thanks to their topographical, mechanical and electrical feature, CP are ideal candidates to enhance tissue biomimetics in EHT. However, CP inclusion in EHT has been limited only to 2D substrates of heart model [27,28], while 3D heart models still require further optimisation.

### *1.3. Contribution to current state of the art*

In this doctoral thesis, I describe the application of the electroconductive polymer PEDOT:PSS as 3D porous sponge-like scaffold in two biomedical engineering applications. Starting with a standard blend of glycidoxypropyltrimethoxysilane (GOPS)-crosslinked PEDOT:PSS (PEDOT:PSS-GOPS), I processed constructs with both isotropic and aligned morphology. I then explored the impact of stiffness and microarchitecture of such constructs towards a potential benefit for the development of next generation piezoresistive sensors for wearable applications.

Despite previous studies reporting the fabrication of biomaterials matching the conductivity properties of native heart tissue [29], to date an optimal substrate capable of combining electroconductivity, suitable microarchitecture, pro-cardiomyogenic stiffness and high biocompatibility has not yet been achieved.

## 1.4. Research objectives and hypotheses

**Main objective of the thesis**

Develop electroconductive 3D porous scaffolds
for applications in piezoresistive sensors and cardiac tissue engineering.

Specifically, the goal of this PhD thesis was to develop a 3D porous scaffold that was biocompatible, electroconductive and cardio-inductive, for the culture of cardiac in vitro models.

The specific aims of this study were:

1. To fabricate 3D porous PEDOT:PSS scaffolds and assess electromechanical properties.
2. To optimise the composition and electroconductivity of a PEDOT:PSS biomaterial for cardiac tissue engineering.
3. To apply lyophilisation, to create a 3D porous biomaterial scaffold with adequate electroconductivity, stiffness, morphology, and biocompatibility using the material developed in aim (2).
4. To incorporate the 3D porous PEDOT:PSS scaffolds into a bioreactor capable of inducing electrical pacing.

## 1.5. Thesis Structure

This thesis comprises the research carried out for the duration of the candidate's doctoral studies (**Figure 1-1**).

*Chapter 2* presents a review of the literature on electroconductive materials and their applications for cardiac tissue engineering. After an introduction on heart electrophysiology, a classification of extrinsically conductive materials and intrinsically conductive polymers is presented. It follows an analysis of the necessity and the rationale of electroconductive

biomaterials for assisting cardiac regeneration. *Chapter 3* reports the general methods adopted throughout the manuscripts, while descriptions of materials and techniques specific to a particular study are provided in the related experimental section. In *Chapter 4*, the CP PEDOT:PSS was processed into 3D porous scaffolds that were subsequently infused with elastomeric fillers at different stiffnesses. The obtained structures exhibited a combination of diverse inner architectures and stiffnesses and were then studied for their piezoresistivity and applicability as motion sensors.

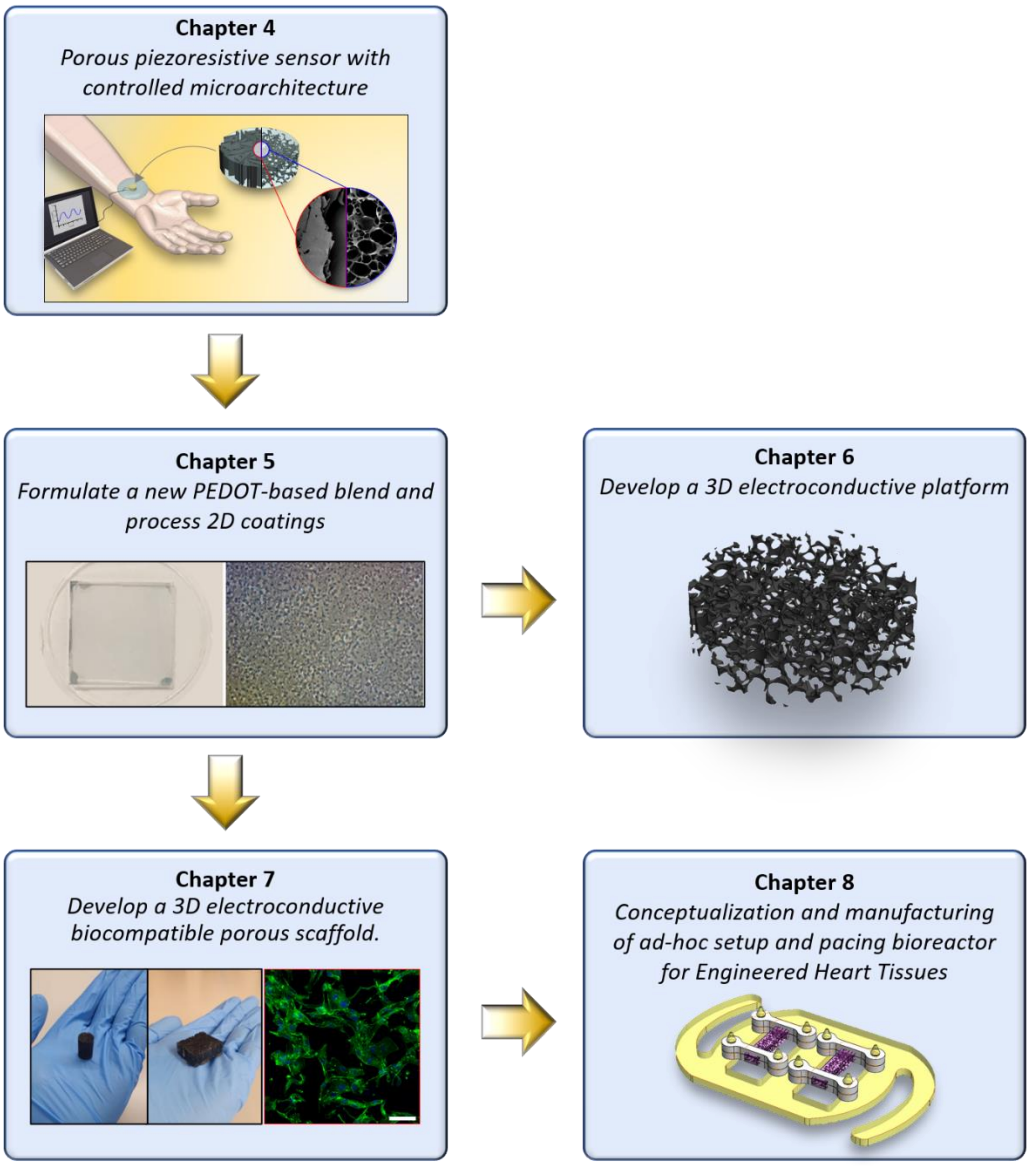


***Figure 1-1.*** *Structure of the doctoral thesis.* ***Chapter 4****: manufacturing and analysis of porous piezoresistive sensors.* ***Chapter 5****: implementation of a new crosslinking formulation for PEDOT:PSS coatings.* ***Chapter 6****: development of 3D scaffolds from the material of Chapter 5.* ***Chapter 7****: processing of biocompatible 3D scaffolds.* ***Chapter 8****: Conceptualisation and manufacturing of a rig for EHT model and of a bioreactor.*

In order to achieve structures with biomimetic conductivity, one should consider that the standard method of crosslinking PEDOT:PSS with GOPS is source for significant reduction in electrical conductivity.[30] Hence, there is a need for alternative crosslinkers with PEDOT:PSS that will not hinder ions and electron transport. *Chapter 5* demonstrates the use of poly(ethylene glycol) diglycidyl ether (PEGDE) as effective stabiliser of PEDOT:PSS in coating and drop casted films. This new formulation of PEDOT:PSS led to increased hydrophilicity and conductivity compared to standard GOPS crosslinking. In *Chapter 6*, 3D porous scaffolds were manufactured combining the fabrication method of *Chapter 4* - with and without the inclusion of elastomeric fillers - introducing PEGDE as replacement of GOPS, seeking enhanced conductivity of the material up to typical of native cardiac tissue. Although this crosslinked porous scaffold showed improved conductivity when crosslinked with PEGDE - this family of scaffolds did not satisfy stability and biocompatibility requirements.

Attention was moved to alternative strategies for conductivity enhancement, and in *Chapter 7* I developed a crystallisation post-treatment with sulphuric acid on PEDOT:PSS-GOPS scaffolds. Here I proved that such a post-treatment, which previously had only been adopted for 2D coatings [31], could be translated to 3D sponges-like scaffolds. Crystallisation induced important changes in mechanical and electrical properties without compromising the stability of the structures. The platforms exhibited suitable properties for use as biomimetic and cardio-inductive scaffolds for cardiac tissue engineering. Finally, in *Chapter 8*, I conceptualised, designed and fabricated a pacing bioreactor and a rig for the generation of electrically stimulated in vitro models consisting of 3D sponge-like scaffolds. Specific assembly and seeding sequences were established so to maximise repeatability and consistency of experiments. The system demonstrated both scaffold topography and the adoption of electrical stimulation to regulate cell orientation.

Taken together, it was proven that by tailoring the material composition and the processing parameters, PEDOT:PSS-based 3D constructs could be optimised both as piezoresistive sensors and electroconductive scaffolds for tissue engineering.

# 2. Literature review:

# The rationale and emergence of electroconductive biomaterial scaffolds in cardiac tissue engineering.

A significant amount of this *Chapter* has been published previously in:

**Solazzo, M**., O'Brien F., Nicolosi V., Monaghan, M. G. The rationale and emergence of electroconductive biomaterial scaffolds in cardiac tissue engineering. APL Bioengineering. 3, 041501 (2019).

## *2.1. Abstract*

The human heart possesses minimal regenerative potential which can often lead to chronic and inevitable failure following myocardial infarction. Despite the successes of assistive support devices and pharmacological therapies, only a whole heart transplantation can sufficiently address heart failure. Engineered scaffolds, implantable patches and injectable hydrogels are among the most promising solutions to restore cardiac function and coax regeneration, however; current biomaterials have yet to achieve ideal tissue regeneration and adequate integration due a mismatch of material physicochemical properties. Conductive fillers such as graphene, carbon nanotubes, metallic nanoparticles and MXenes, and conjugated polymers such as polyaniline, polypyrrole and poly(3,4-ethylendioxythiophene), can possibly achieve optimal electrical conductivities for cardiac applications with appropriate suitability for tissue engineering approaches. Many studies have focused on the use of these materials in multiple fields, exhibiting exciting effects on the regeneration of electrically active biological tissues such as orthopaedic, neural, and cardiac tissue. In this review, I critically discuss the role of heart electrophysiology and the rationale towards use of electroconductive biomaterials for tissue engineering. I present the emerging applications of these smart materials to create supportive platforms for cardiac

tissue engineering, and on the crucial role that electrical stimulation has been shown to exert in the recovery of heart function and maturation of cardiac progenitor cells.

## *2.2. Introduction*

Cardiac muscle relies on an intricate coordination of action potentials and calcium signal propagation in order to exert sufficient synchronous beating to pump blood around our bodies. This coordination is facilitated by membrane potential depolarisation, a pacemaker conduction system and specific intracellular communication networks.[32] Dysregulation of these processes can occur due to cardiac arrhythmic conditions, such as sinus node dysfunction or atrioventricular block, and depending on the severity of the pathology, a pacemaker device may be implemented to resynchronise cardiac synchronicity.[33]

Quite commonly, such coordination also becomes interrupted due to ischemic death of myocardial muscle stemming from the advent of atherosclerosis and myocardial infarction (MI), more commonly known as “heart attack”.[34-37] This ischemic insult to myocardial muscle often results in the formation of a fibrotic scar which, although lends some compensatory role to replace the necrotic myocardial core, is relatively inert to the electronical signalling of the heart and acts as an insulating tissue that isolates remote cardiomyocytes and impedes communication of healthy tissues. Additionally, to act as a compensatory mechanism in presence of conditions such as arterial hypertension or aortic stenosis [38], the heart develops hypertrophy that has been shown to have effects on the transmission of action potentials within the heart with possible development of arrhythmogenesis.[39]

The myocardial milieu has insufficient regenerative potential with an estimated cardiomyocyte turnover of 1% per year at the age of 25 and 0.45% at the age of 75.[40,41] Because of this, MI can lead to cardiac hypertrophy, myocyte slippage, arrythmia, tachycardia, and even complete heart failure. Current pharmaceutical treatments strive to alleviate further deterioration of cardiac function by administration of β-blockers, aspirin, thrombolytics, antiplatelet agents, and ACE inhibitors, yet do not stimulate regeneration.[41,42]

With an expanding and aging population, tissue engineering strategies are being

increasingly focused upon to deliver the next generation of treatments for ischemic myocardium. Efforts have been multifactorial and attempt to address this using a number of different avenues, which can consist of biomaterial scaffolds, cell therapies, localised drug delivery or a combination of any three. Local application of biomaterials has been postulated as a beneficial treatment with collateral support and mechanical strengthening being one of the mechanisms hypothesised to stem from this treatment.[43] Other approaches have included cell therapy in the form of somatic cell or stem cell delivery [44,45], and also a wide range of gene therapy approaches which are elegantly reviewed elsewhere.[46]

Regarding biomaterial approaches, typical biomaterials can be relatively inert in nature, composed of either synthetic or natural polymers or a combination of both, and existing in forms of injectable hydrogels [47], geometrically defined scaffolds [48], particulates [49] or as substrate coatings.[50] Such materials can possess predefined mechanical properties with adequate biocompatibility and often have been reported to improve [51] or maintain myocardial function.[52] However, these materials essentially exist as inert depots and at the most adding some mechanical support to the compromised myocardium. Such materials have evolved though to possess additional complexity with the incorporation of cells [53], drugs [54], and gene therapy.[55]

From a design point of view, one must appreciate that the myocardium exists as a contractile, active tissue with continuous cycles of ionic polarisation and depolarisation which can adapt to demands in corporeal oxygen demand, and therefore a tissue engineering approach must meet these design requirements. Such criteria include high porosity and adequate pore size to allow cell infiltration [56], aligned topography to promote intracellular communication [57,58], biocompatibility, flexibility, and matching/engagement with the host physicochemical properties.[59] One such property gathering significant momentum in recent years is that of the conductivity of biomaterials matching the bioconductance of the native myocardium.[60] Meeting such a criterion could restore myocardial/chamber signalling to re-establish efficient synchronous beating to hinder further myocardial aggravations as deterioration, slipping or hypertrophy. Despite electrical activity being a key

feature of several functions and organs in the human body [61], to date, most of materials adopted for tissue engineering have not been designed with this feature in mind.

Electrically conductive biomaterials investigated in the field can be categorised as either extrinsically conductive materials - predominantly fashioned by the incorporation of conductive fillers in an insulating material matrix - or intrinsically conductive polymers. Despite their different origin and mechanisms of conductivity, both these families can be applied in tissue engineering and specifically cardiac tissue engineering, due to their ease of manipulation and processing in combination with other materials, metal-like conductivity, and biocompatibility [6] (**Figure 2-1**). Their application in tissue engineering is rapidly expanding, still; much has to be discovered with regards to their long-term impact and potency in regenerating tissue in vivo. The complex electrical pathways of the myocardium must be fully appreciated and understood with a goal to achieving biomaterial chemistries, morphologies, and optimal tissue/material interfaces to exert a maximum benefit. This review is a discussion of this burgeoning field in adopting electroconductive materials to treat MI by their application and also in achieving cardiac organoids to study cardiac disease.

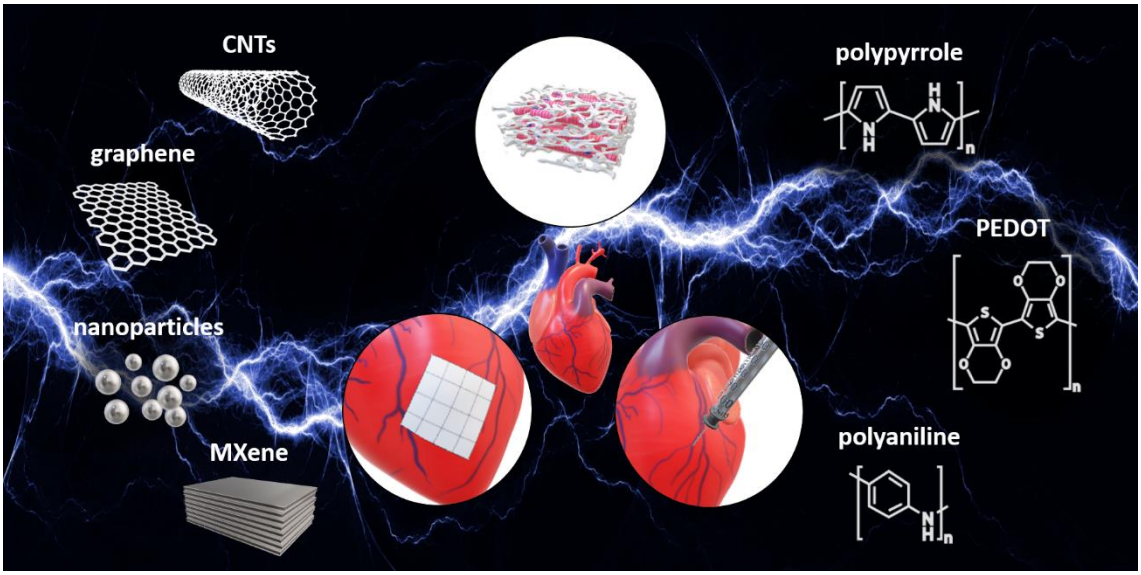


***Figure 2-1**. Illustration of the most common extrinsically conductive materials, intrinsically conductive polymers, and their possible uses for cardiac tissue engineering, namely scaffolds for in vitro models, patches, and injectable hydrogels.*

### *2.2.1. Cardiac electrophysiology*

To begin such understanding, let's consider first the myocardium, the involuntary striated muscular tissue occupying the inner portion of the heart wall and the major proponent of contractility, present as a framework of parallel myofibres. These fibres are precisely oriented across the myocardium, conferring the organ's characteristic twist during the contraction cycle [62,63] and are composed of a group of contractile muscle cells known as cardiomyocytes (CMs) together with supporting cells, and held together by strands of connective tissue. CMs constitute approximately 30% of all the myocardium cell population by number [64], 90% of its dry weight and 75% of its volume.[62,63] In their adult state, CMs are reported to have a diameter and a length in the order of 20 µm and 125 µm, respectively, and possessing a long tetrahedral shape.[65] Contraction is not the only function CMs have, as they have a crucial role in the synthesis of proteins and signalling molecules. Indeed it is estimated that CMs can replace the whole myocardium ECM in 1 week.[40,63,66] Amongst other resident cells - such as endothelial cells, smooth muscle cells and macrophages - cardiac fibroblasts are another main cell population in this region and the most abundant in number.[66] Although primarily associated with the task of synthesising new structural proteins, they also have a role in electromechanical coupling with CMs and fulfill a role in propagation of action potentials.[66] Cardiac fibroblasts play a key role in the remodeling of the heart during development and pathological conditions.[64]

Surrounding these cells and making up 5% of myocardial dry weight, the cardiac extracellular matrix (ECM) is specific with cells associated with it with a high concentration of collagen type I and III deposited by the cardiac fibroblasts, and collagen type IV and V in the basement membrane of the CMs.[63] The ECM not only executes a function of architectural support to the myofibres, but it also has a crucial role in the mechanotransduction of surrounding cells, causing changes in morphology and in deposition of proteins such as collagen, laminins, and fibronectin.[66] Finally, other populations as the pacemaker cells, atrial, atrioventricular, and Purkinje cells are present in the heart and they are specifically associated with initiating and conducting cardiac impulses

to the ventricular contractile cells.[62]

### *2.2.2. Homeostatic cardiac electroconductivity*

Three determinants drive the heart's electrical system: cardiomyocyte electrophysiology, intercellular connectivity, and its tissue structure that encompasses myofibers orientations and the structure of connective tissue. These three factors must be balanced to ensure an efficient and stable conduction of electrical impulses throughout the heart.[67]

For the heart to contract rhythmically with an average heart rate of 72 beats per minute, each sarcomere - the functional and structural unit of the cardiac muscle - within a particular muscle fibre must shorten coincidently. Cardiac electrical activity is initiated in the sinoatrial (SA) node, a discrete mass of specialised cells located in the right atrium. This electrical stimulus is generated at about 60 to 100 times per minute at regular intervals.[68] When the action potential is at -65 millivolts diastolic depolarisation begins and at -45 millivolts, the nodal action potential is triggered. As the electrical signal propagates along the atria towards the atrioventricular (AV) node, it stimulates the atria to contract. This signal pauses briefly at the AV node before continuing to the Bundle of *His* and the Purkinje fibres of the ventricles. These Purkinje fibres extend and propagate throughout the ventricular myocardium which allows for each cell within the myocardium to experience this action potential. A cascade proceeds as the signal permeates within cells which occurs in less than a third of a second allowing for simultaneous contraction.[69]

To understand how this permeating action potential elicits CMs contraction, one must first consider that myocardial activators of contraction (i.e. actin and myosin) become activated in the presence of calcium ions. This contractile function is primarily orchestrated by the interface at the sarcolemma, the cellular membrane on CMs; which serves to regulate the ionic concentrations in the intracellular and extracellular fluids.[62] CMs interact amongst themselves with approximately 5.3 connections laterally and 6.0 on their distal regions via intercalated disks, which are specific sites of the cell membrane where three types of cell to cell connections assist in the formation of a global contractile network.[63] The first of these

cell-to-cell connections are the the gap junctions, which are microchannels in the longitudinal portion of the intercalated disk that allow communication within the cytosol of one cell to the next. These gap junctions ensure that the action potential generated from pacemaker cells in the sinoatrial node, which then propagate in the heart conduction system, can rapidly spread throughout the muscle fibre network to allow the myocardium to function as a single unit. In the normal heart, the fibre-like disposition of cardiomyocytes and the presence of gap-junctions between adjacent cells are responsible for the characteristic electrical anisotropy of the ventricles, with a reported conduction speed ratio of 4:2:1 for the longitudinal, circumferential, and radial directions respectively.[67] The two other cell junction types are adherens and desmosomes, which contribute more to the mechanical functions by ensuring that the mechanical forces are transmitted throughout the entire myocardium.[70,71] It has been experimentally estimated that this efficient conduction system possesses conductivity values of approximately 0.48 S/m in the atria [61,72], and 0.3-0.6 S/m within the ventricles.[73,74]

Within CMs of the mature heart, the propagating action potential spreads via T-tubules. These specific invaginations of the cell-membrane at the Z-line are present in adult CMs [63,75], and rapidly release calcium ions ($Ca^{2+}$) in the cytosol via sarcoplasmatic and endoplasmic reticulum. Many factors influence the regulation of intracellular $Ca^{2+}$ transients. L-type calcium channels, that have been shown to play a role in the initiation of action potential at the SA node, are a major avenue for $Ca^{2+}$ exchange, exhibiting slower activation but faster deactivation compared to the embryonic T-type $Ca^{2+}$ channels. SERCA, a transmembrane protein, shifts $Ca^{2+}$ from the cytosol to the lumen of the sarcoplasmatic reticulum, while ion shuttling directly via the sarcolemma is orchestrated by the $Na^{+}Ca^{2+}$ exchanger. Positioned at the interface between the sarcoplasmatic reticulum and the cell membrane, RyR2 ryanodine receptors are primarily responsible for calcium-induced-calcium-release (CICR). Finally, an important role in the transmission of $Ca^{2+}$ is ensured by calcequestrin located at the junctional and corbular sites of the sarcoplasmatic reticulum. [65]

### *2.2.3. The pathological heart*

The myocardium is deemed ischemic when coronary blood flow is insufficient to meet metabolic needs. MI exerts profound alterations in cardiac structure as it can lead to a 50% reduction of healthy adjacent cardiomyocytes and therefore to a decrease in cellular connectivity and altered ion-channels activity.[67] With this deficiency in oxygen supply, CMs employ anaerobic glycolysis to generate energy, a process traditionally associated with a reduced ATP generation efficiency (2 ATP molecules produced for 1 molecule of glucose instead of 36 ATP molecules yielded by the oxidative phosphorylation). After degradation ATP becomes ADP, then AMP and adenosine. This purine nucleoside migrates from cells to interstitial fluid, but the loss of this adenosine from the myocytes leads to permanent injury and catastrophic consequences for the myocardium. The heart actuates compensatory mechanisms as hypertrophy that can lead to an adaptation in metabolism, with a decrease in fatty acid oxidative rates that will lead to a final decrease in ATP production. These functional modifications extend to mitochondria that undergo to abnormal morphology and reduced volume density. These events will eventually cause contractile disfunctions.[76]

Following MI, necrosed CMs are replaced by the laying down of a non-contractile collagen rich scar through a fibrotic phase distinguished by collagen production, and a remodelling phase that witnesses collagen stabilisation and crosslinking.[67] Myofibroblasts, fibroblastic cells that recapitulate features of smooth muscle cells, participate intensely to this process. They secret abundant amounts of collagen (up to 10-fold increase the content of the healthy myocardium) and are also responsible for the secretion of growth factors, cytokines, ECM, and proteases.[64]

Electrophysiological characterisations of the heart has focussed on the noncontractile infarcted region and has identified two interesting phenomena: the generation of tortuous propagation pathways responsible for reduced but not entirely absent conductivity, and the induction of ventricular tachyarrhythmia due to strands of viable tissue that penetrate the scar volume.[67] Heterotypic coupling between fibroblasts and myocytes plays a significant

role in the development of this condition.[64] Fibroblasts can also transmit action potentials between isolated CMs, propagate electrical waves through the scar, and can, at high densities; prevent arrhythmias.[67] Research in the field has shown that conduction velocity in hypertrophied ventricle is increased because of the bigger cell size and increasing number of intercalated disks, while it decreases in failed hearts that are characterised by faulty intercellular connections.[77]

### *2.2.4. Cell therapies and differentiation of stem cells towards cardiac phenotypes*

Despite the rapidly rising field of biomedical instrumentation and life assisting devices for heart support such as ventricle assisting device and intra-aortic balloon pumps [78], such solutions can only be considered as bridge therapies to the 'perfect' yet unrealistic treatment for heart failure: whole heart transplantation. It is estimated that only 10% of the patients requiring whole heart transplantation will benefit from such in their lifetime.[79]

At the turn of the millennium, promising results in terms of heart regeneration were reported via the implantation in situ of bone marrow stem cells (BMSCs) in a series of publications by the group of Anversa.[80-83] It was only more than one decade later, after the continued inability of other groups in the world to replicate these findings, that most of these studies have been retracted. Since then, it has become accepted that BMSCs cannot differentiated in situ to improve heart functionality, despite their anti-inflammatory paracrine effects being widely recognised.[84]

To date, three main approaches are currently being investigated: reprogramming of somatic cells, differentiation of adult stem cells, and differentiation of pluripotent stem cells.[85] Compared to multipotent stem cell sources, the use of transdifferentiation of somatic autologous cells is an approach that brings up less ethical issues and can be derived from a patient's own biological material.[47,86,87] However, the strategies so far applied such as, transcription factors, microRNAs, and more recently small molecule delivery to enhance epigenetic modifications, have only exhibited low to modest efficiencies.[88-90] Mesenchymal

stem cells (MSC) are broadly available in the adult human body in different sites, as the bone marrow and the adipose tissues, and have been investigated in several applications for decades.[91,92] However, although MSCs cannot independently differentiate into CMs in vitro, coculture of MSCs and primary CMs in vitro has been one successful approach to achieve an MSC derived cardiac phenotype.[93,94] The use of embryonic stem cells (ESCs), although providing a multipotent phenotype, creates ethical concerns that hinder its applicability.[95-97] Human induced pluripotent stem cells (hiPSCs) are conversely an easily available solution without moral dilemma, but an incomplete differentiation may generate a teratoma in situ.[98] hiPSCs have obtained the attention of the scientific community [99] and they have led to remarkable progress in the field of cardiac regeneration, having repopulated a decellularised mouse heart [100], and later regenerated an infarcted primate heart.[53] Recently, it has been also shown how hiPSC-CMs can also be adopted to exploit their paracrine effect and yield cardiac restoration via the administration of extracellular vesicles secreted in vitro.[101]

Yielding CMs from any of these cellular sources is often achieved through controlled manipulation using growth factors, small molecule modifies of epigenetics, and tissue engineering approaches. Specifically, tissue engineering approaches aim to recapitulate the cardiac microenvironment through mechanical, topographical, and ECM-mediated cues, with a substantial interest in the use of electrical stimulation using electrical pacing bioreactors, and more recently the use of electroconductive biomaterials to mimic the bioconductance of the myocardium.

### *2.3. Electroconductive biomaterials*

Recognising the important and intricate role of electrical signalling in the native myocardium, its dysregulation during disease, and recent bounds in research appreciating bioelectrical signalling, electroconductive biomaterials have emerged as a new class of building blocks in tissue engineering in a wide range of applications extending from neural [102] to musculoskeletal [9] to cardiac.[60] Scaffolds and conduits for regenerative medicine have

yet to fulfil several requirements to successfully support and drive cell behaviour, and to achieve mature and functional tissue formation. Biomaterials used to fabricate such structures not only need to mimic physiological electroconductivity values, but also possess other desired criteria such as biocompatibility and adequate degradation kinetics. These factors - together with the intrinsic chemical and physical properties of the chosen compound - are all important to determine the cytotoxic effect and, therefore, the overall application outcome. Broadly speaking, these materials can be classified as extrinsically conductive materials, which are traditionally known as universal conducting materials, and an emerging class of intrinsically conducting polymers. A large portion of studies with these materials has involved some limited in vitro work with some direct investigation in neural and orthopaedic applications. However, cardiac tissue engineering applications have garnered increased focus with much success.

### *2.3.1. Extrinsically conductive materials*

Researchers consider extrinsically conductive the compounds resulting from the combination of an insulating material and a conductive filler becoming electrically conductive, and defining as a percolation threshold the minimum content of filler necessary to achieve the transition to the conductive state.[103]

Despite concerns on their long-term effects as implants in the body, these materials are increasingly pursued due to the ease at which they can be processed and manipulated, incorporated with therapeutic natural polymers (i.e. ECM) [104], and their capability to be manufactured in large scale processes.

#### *2.3.1.1. Carbon nanotubes (CNTs)*

The hallmark synthesis of carbon nanotubes (CNTs) in 1991 paved the way for a captivating advancement in nanotechnology development.[105] CNTs are sheets of graphite rolled into cylindrical tubes consisting of diameters in the range of 0.4-2 nm with much longer lengths ranging from hundreds of nanometres to micrometres.[106,107] This leads to varying aspect ratios that can be used as an advantage or disadvantage in tissue engineering. They

can further be divided into single-walled CNTs (SWCNTs) and multi-walled CNTs (MWCNTs) depending on their geometry. Their superior properties, such as a 11-200 GPa tensile strength [108], Young's modulus of 0.27-1.34 TPa [105,109], electrical conductivities from $1x10^4$ S/cm and thermal conductivities at 5000 W/m×K [110,111], are known to improve the mechanical and chemical properties of biomaterials and polymers. The benefits of the introduction of these particles have been evident in tissue engineering since the early 2000s, notably in the fields of neural, bone, and cardiac regeneration with enhancement of tissue maturation.[112]

Several studies have reported their use in promoting neuronal maturation and increasing neurite outgrowth speed when processed into a rope-like shaped construct and subjected to electrical stimulation.[113] Applying CNTs as conductive fillers in polyvinyl alcohol-based tube-guide scaffolds has yielded increased conductivity and, once implanted for sciatic nerve repair in a mouse model, promoted better animal recovery to normal gait pattern compared to a nonconductive group.[102] It has been observed via transmission electron microscopy that CNTs can form intimate physical contacts with neuronal membranes, and these interfaces can result in electrical shortcuts between the proximal and distal regions of neurons.[114] CNTs have also proven effective in bone tissue engineering and, when integrated within a chitosan/hydroxyapatite scaffold, they increased osteoblast proliferation at 7 days in vitro compared to nonconductive control, having a role in calcium deposition.[115] Recently, to reach the desired - yet difficult to attain - fracture toughness target value for load bearing bone applications, the incorporation of acid-treated MWCNTs via a "slurry - compounding method" has been established.[116] Assessment via histological sections and microCT demonstrated that CNTs-loaded poly(propylene fumarate) scaffolds possessed higher scoring for tissue response, without affecting the degradation of the implant in a 12 week in vivo study in a rabbit femoral condyle defect model.[117] Porous scaffolds rendered electrically conductive via loading of CNTs have been realised with several techniques such as: solvent casting in PCL-based constructs [118]; in electrospun poly(glycerol sebacate):gelatin nanofibers; with 3D printing via screw-assisted extrusion of both SWCNTs

in alginate-based hydrogel [119] and MWCNTs blended in PCL, which resulted to be aligned with the printing direction in higher ordered structures.[120] Several studies have sought to address the toxicity concerns of CNTs at the cellular and systemic level. CNTs have been shown to have improved dispersion in cell culture media if functionalised with COOH-SWNT and demonstrated improved biocompatibility with human MSCs. Tracking these COOH-SWNTs confirmed that they can penetrate inside the cells and reach nuclei in 24h, without interfering with cellular ultrastructure, which is demonstrative of a potential for delivery of therapeutic and detective reagents into cells.[121] In vivo subcutaneous injection of MWCNTs, found that after an initial inflammatory reaction, the immune-response restored to stable values without tissue damage; with particles remaining in the injection sites or migrating to the closer lymph nodes but not to the other organs.[122] Moreover, the presence of CNTs has been suggested to elicit an antioxidant response with a free radical scavenger mechanism, that has been tested via infusion of doxorubicin, and attributed to adduct formation and neutralisation through electron transfer.[60]

#### *2.3.1.2. Graphene*

Pristine graphene is collectively defined as one-atom-thick flat sheet of carbon initially obtained via a simple “Scotch-tape” method to peel atomically thin layers [123] and later by epitaxial chemical vapor deposition (CVD).[124] Because of its unique structure, pristine graphene has been considered the thinnest and strongest material ever reported, manifesting superior electrical and optical conductive properties.[125] Graphene can be configured as graphene oxide (GO), a less pure version but more suitable for large-scale manufacturing.[126] The hydrophilic structure of GO is usually achieved via graphene liquid-phase exfoliation of a flaked graphite precursor, that yields an impure structure where epoxides, alcohols, ketone carbonyls, and carboxylic groups can contaminate the contiguous aromatic lattice.[127] GO possesses a nonconductive state and a chemical reduction process is necessary to achieve reduced GO (rGO), via, for example, exposure of hydrazine vapour merged with low-temperature annealing treatment.[128,129] Overall,

graphene and its derivatives possess exceptional thermal, electrical, and mechanical properties, gaining an increasing amount of attention in the past decade.[130] Since the first use of GO as a nanocarrier for drug delivery [131], several applications have been proposed in the biomedical field; specifically, in tissue engineering for bone [132], nerve [133] and cardiac regeneration.[134]

In vitro, adopting a graphene planar coating has improved the maturation of neural cells with increased neurite numbers and average neurite length when compared to cells grown on tissue culture plastic.[133] Many reports described the use of graphene as a conductive complement to polymeric matrices to realise conductive 3D scaffolds. A biohybrid, consisting in a thick flat substrate, could be achieved by blending pristine graphene directly to collagen type I.[134] rGO has been incorporated with collagen as a covalent coating upon 3D constructs of freeze-dried bovine collagen type I.[135] In this context, the flakes homogeneously distributed on porous collagen scaffolds, and the presence of rGO promoted an overall high cell viability in vitro and cell infiltration in vivo. Using a similar construct, an in vitro investigation on MSCs differentiation towards an osteogenic phenotype yielded increased cell proliferation, higher alkaline phosphatase and osteopontin expression - an early and a late osteogenic markers respectively - when compared to pure collagen scaffolds.[136]

Graphene-loaded hydrogels have been obtained using multiple approaches such as polymerisation of polyacrylamide directly within a suspension of graphene sheets [137], while a similar approach with rGO proved a promising candidate for muscle application, with a Young's modulus of 50 kPa and enhanced myogenic differentiation from a mouse myoblast cell line C2C12.[138] rGO has been widely used with methacrylated gelatin (GelMA) and, when tested at concentrations of 0, 1, 3, and 5 mg/mL, rGO particles increased the Young's modulus and stiffness of constructs. However, the presence of graphene compromised UV crosslinking of GelMA due to the intrinsic free-radical scavenger activity of carbon-based materials.[139] Polydopamine has been shown to possess a dual action of crosslinker and ability to convert GO into a conductive state within a chitosan-based hydrogel.[140] In addition

to good biocompatibility, this compound manifested a series of interesting features: high conductivity within the range of native myocardium and the ability to recover its original storage and the loss moduli after a deformation of up to 900%, or even a physical separation of the construct into multiple parts.[140]

Graphene exhibits lower cytotoxicity compared to CNTs, while the duration of the reduction process has revealed to be pivotal for cell survival, with the best results in cell response with 90 minute of reduction treatment.[141]

*2.3.1.3. Metallic nanoparticles*

Silver (Ag), gold (Au) and their combined alloy (AgAu) have been amongst the first materials ever used for medicine in the history of the humankind. Gold has been used in medicine since 2500 B.C. and in its metallic form it is unreactive and insoluble.[142] Silver inhibits enzymatic systems of the respiratory chain and alter the synthesis of DNA of bacteria via superficial contact, showing an outstanding antimicrobial activity also as nanoparticles (NPs) [143], and thanks to the ability to address the multidrug resistance of bacteria it is considered a valuable alternative to antibiotics.[144]

NPs are defined as elements of size ranging between 1 and 100nm [145].They can be manufactured either via a “top-down” approach from a macroscale material to a nanometric scale adopting mechanical techniques such as milling [146], or via a “bottom-up” strategy starting from an atomic/molecular level and scaling up with chemical and physical processes like aerosol or precipitation processes.[147] Although also palladium [148] and magnetic iron oxide [149] are used to manufacture NPs, to date AgNPs, AuNPs and AgAuNPs are the most common choices in biomedical applications, with potential use as nanoscale drug carriers and anticancer treatments.[150,151] The geometry of NPs is crucial for cells uptake, as it is reported that AuNPs with a diameter of 50 nm and an aspect ratio of 1:1 are absorbed most into mammalian cells.[152]

In the field of tissue engineering, incorporation of AgNPs and AuNPs into hydrogels has been the most common approach to generate a functionalised conductive biomaterial with

NPs.[153,154] The presence of AgNPs and AuNPs is generally well tolerated by a variety of cells in vitro. They have demonstrated applicability in dermal tissue with good biocompatibility observed on dermal fibroblasts and epidermal keratinocytes [155]; while osteoblast attachment and spreading is not compromised when NPs are loaded on methacrylate-based [156] and silk fibroin/nanohydroxyapatite hydrogels.[157] Amongst the many potential applications in scaffold fabrications, NPs can be used to modulate the inflammatory response to the presence of scaffold-degradation by-products as in the case of the incorporation of nanophase titanium dioxide ($TiO_2$) into 3D printed poly(lactic-co-glycolic acid) scaffolds during an in vitro assessment.[158] Differentiation of MSCs into neural cells without differentiation factors has been achieved via an electrospun fibrous scaffold consisting of magnetic NPs combined with GO nanosheets and both incorporated to a blend of piezoelectric polyvinylidene difluoride (PVDF) with the entire mixture subsequently electrospun.[159]

In vivo studies, investigating the regeneration soft tissue and bones, confirmed the anti-inflammatory action of these materials. Injected soft-fillers composed AuNPs loaded collagen- and hyaluronic acid-hydrogels, had extended longevity (up to six months) compared to nonconductive groups, and maintained low irritation levels in a swine ear model.[160] Implantation of AuNPs loaded GelMA hydrogels in a rabbit model at 8 weeks promoted bone formation in the same range of the group treated with osteoinductive BMP-2.

Several factors may have contributed to all the beneficial effects of NPs on cells and tissues reported by their applications in vitro and in vivo, such as their absorption into cell cytoplasm and nuclei [161], the increase in stiffness and electrical conductivity they infer[162], and also the modifications in nanometric topography and roughness.[163] However, it is important to consider the potential toxic effect of introducing NPs into the body [164], a size dependent toxicity has been demonstrated when delivering AgNPs to the lungs.[165] Comparing the effects of both AgNPs and AuNPs, Ag possesses a stronger antimicrobial activity but its dose must be tightly controlled as it can show much higher cytotoxicity

especially for high concentrations.[157]

#### *2.3.1.4. MXenes*

As the rising star in the 2D family, transition metal carbide and nitrides, known as MXenes, have emerged and rapidly drawn intensive research attention.[166,167] MXenes were developed by Barsoum and co-workers. Mn+1Xn layer (named as MXene) was fabricated by the selective extraction of A-element from layered ternary carbides of Mn+1AXn phases (n = 1–3), where M is an early transition metal, A is an A group element, and X is C or N.[166-169] MXenes typically have three different formulas: M2X, M3X2, and M4X3. Being the most widely investigated MXene type, titanium carbide (Ti3C2Tx, Tx stands for various surface functionalities such as –OH, –O, and/or –F, and n = 1, 2, or 3 [170,171] exhibits a metallic conductivity and excellent capacitive charge storage behaviour.[172-174]

Since the discovery of Ti3C2 in 2011, the family of transition metal carbides, carbonitrides and nitrides, collectively referred to as MXenes, has quickly expanded in many areas. By selectively etching of A-element layers from MAX precursor in aqueous fluoride-containing acidic solutions, such as hydrofluoric acid, HF, or in-situ formed HF from lithium fluoride and hydrochloric acid, LiF +HCl, or ammonium hydrogen bifluoride, multi-layered (m-)MXene is thus obtained. The abundant surface functional groups impart hydrophilicity to MXenes. When m-MXene is delaminated into monolayered or few-layered nanosheets (d-MXene), a stable aqueous solution can be thus obtained, due to the electrostatic force on the negatively charged MXene nanosheets. This allows a facile and environmentally friendly processing of the MXene solution into any items, such as composites, coatings and devices. Despite the presence of terminal surface groups, MXenes, especially the most intensively studied titanium carbide MXene (Ti3C2Tx), showcase a metallic conductivity as high as 9880 S/cm.[175] Compared to other metallic mesh and carbon nanomaterials, Ti3C2Tx MXene nanosheets have a series of advantages including high flexibility, ease of dispersing in water and biocompatibility.

To date, these 2D multifunctional MXenes and their composites have for example been

developed for theranostic applications including typical phototherapy of photothermal therapy, photothermal/photodynamic/chemo synergistic therapy, diagnostic imaging, antimicrobial, and biosensing.[173,176-181] Vast promise is envisaged in using MXenes as electrically conductive fillers in biocomposites.

### *2.3.2. Intrinsically conductive polymers*

Intrinsically conductive polymers (ICP) have been widely studied in the last 40 years in several engineering fields, since their discovering and development by Alan J. Heeger, Alan G. MacDiarmid, and Hideki Shirakawa, for which they were awarded the Nobel Prize in Chemistry "*for their discovery and development of conducting polymers*" in 2000. In 1977, these authors successfully doped polyacetylene and began the era of conductive polymers [182], and to understand the importance of this discovery I here report two citations of Alan J. Heeger's Nobel lecture, where he described his disclosure as "*the fourth generation of polymers*" that offers *"a unique combination of properties not available from any other known materials*".[183] The basis of intrinsically conductive polymers is their configuration as conjugated polymers in that, differently from common saturated polymers; presents the formation of a $\pi$ system created by the electrons of unoccupied *p* orbitals.[183] In their pristine state, conjugated polymers characteristically possess low conductivity and to compensate this lacking, external charges are introduced via doping processes such as electrochemical treatments or chemical reactions of oxidation or reduction (chemical doping). ICP have since then widely used in many fields of engineering and technology. Specifically in the field of biomedical engineering, polyaniline (PANI), polypyrrole (PPy) and polythiophene have been shown to possess adequate biocompatibility, as well as achieve electrical conductivity values to match those of biological tissues (**Figure 2-2**); therefore becoming a promising material for biomedical applications.[184]

#### *2.3.2.1. Polyaniline*

The first reports on the use of conductive polymers were carried more than 150 years ago with the work of Letheby [185] who electropolymerised aniline upon platinum electrodes;

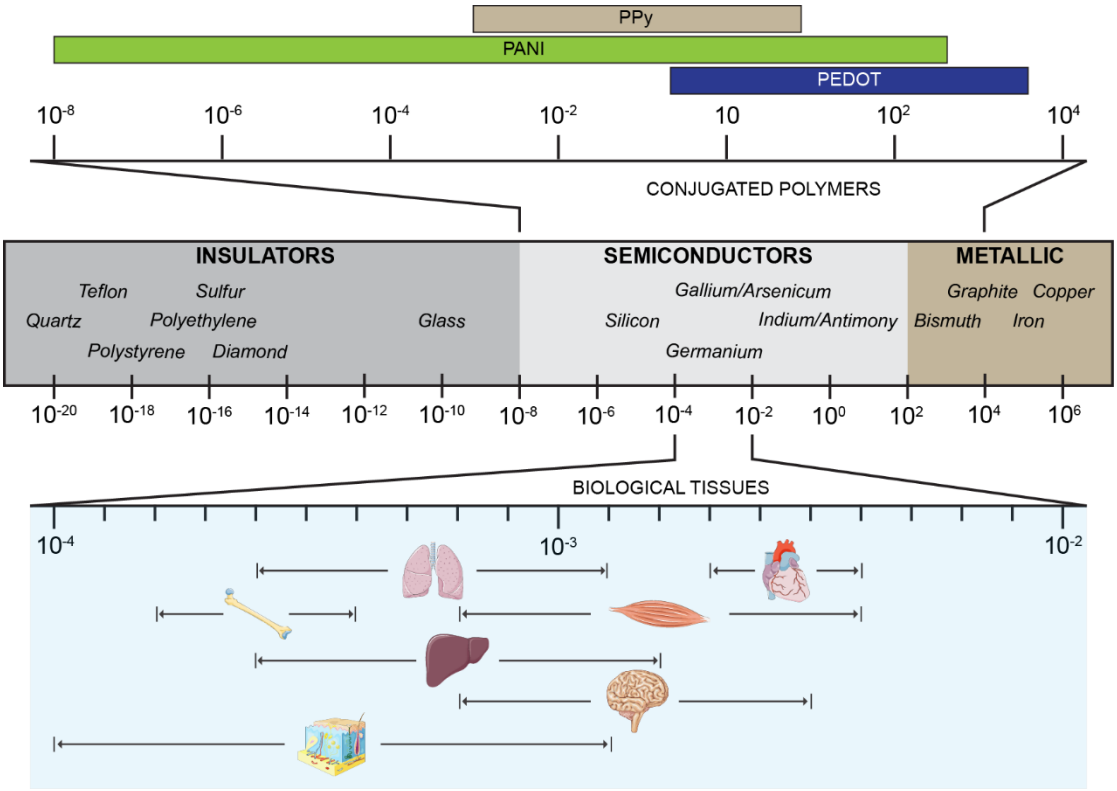


***Figure 2-2**. Schematic of typical electrical conductivity values of common materials categorised as insulators, semiconductors and metallic.[212] At the top: characteristic conductivities of conjugated polymers. At the bottom: average conductivities for biological organs.[72-74] Values are expressed in S/cm.*

although the material did not show the conductivity properties for which it is known nowadays. However, in 1967 stable electronic conductivity in completely dried samples of emeraldine [186] was established, and since then interest in PANI has dramatically risen due to the low cost of its monomer and a high yield polymerisation reaction.[187,188] Aniline can be found in three main oxidation states that can be converted from one to the other: leucoemeraldine (pale and reduced), emeraldine either insulator base or conductive salt (green and half-oxidised), and pernigraline (black and oxidised).[188,189] The nonconductive emeraldine base can be easily doped via electrochemical or chemical oxidation that alters the number of electrons in *p* orbitals, or via protonation - a unique mechanism typical of PANI, whereby the introduction of $H^+$ in the molecular chain results in spin-unpairing and a new charge state without changing the total number of electrons.[187,189] Because of its ease of processing and stability, PANI is often processed in its emeraldine base state and rendered conductive afterwards [187] via the use of various oxidative agents to switch between reduced/oxidised state.[189]

With its ease of processing and the biological applicability of its reduction/oxidation transitions, PANI has been widely investigated in the biomedical field and in tissue engineering as an electroconductive 2D surface and 3D electroactive scaffold.[190] PANI blended with poly(glycerol-sebacate) up to a concentration of 30 v/v% has been processed via solvent casting to generate conductive films. The conductivity and stiffness of such films correlate with the content of conductive polymer, while no detrimental effects have been reported in terms of biocompatibility response using C2C12 cells.[191] The realisation of 3D PANI-based constructs has been achieved via several techniques. Within a GelMA hydrogel, the incorporation of emeraldine salt PANI did not influence any biological or mechanical property of the hydrogel but did yield a two-fold increase in conductivity.[192] Drop-cast films of emeraldine salt PANI have been doped with a solution of HCl of increasing molarity, seeded with hMSCs, and subjected to electric fields of variable intensities between 10 mV/cm and 2 V/cm. After 7 days in culture, cells possessed morphologies indicative of neural differentiation, with a significative dependency on the doping level of HCl. Despite a decrease in cell count, a more conductive substrate was responsible for cytoskeleton reorganisation, promoted cell elongation and upregulation of hallmark neural gene expression with increases in both nestin and βIII tubulin mRNA.[193] More recently, a conductive conduit of a blend of poly-dl-lactic-acid/tetra-aniline for peripherical nerve regeneration had an increased stiffness, conductivity, and hydrophobicity, while no aggravation in the in vivo inflammatory response compared to a nonconductive control scaffold was observed after 4 weeks.[194] In the realm of wound healing, a PANI-based electroactive injectable hydrogel reporting a series of features such as self-healing, antimicrobial properties, haemostasis, adhesiveness, and radical scavenging attributes. The in vivo expression of healing characteristic growth factors as EGF, TGF-b and VEGF testified promotion of the wound healing process.[195]

Concerns on the use of PANI in biological application are related to the lack of biodegradability that can induce chronic inflammation in long-term implants.[196] A second limitation consists in the potential toxicity caused by the use of solvents for the processing

and of chemicals as strong acids for doping.[197] Despite these drawbacks, PANI has been widely investigated and huge potential has been shown across the decades, with efforts to increase its biocompatibility via blending with biodegradable polymers and reducing the presence of harmful substances.[196]

#### *2.3.2.2. Polypyrrole*

Polypyrrole (PPy) was the first polymer to manifest conductive properties [198], with the characteristic conductivity of 7.54 S/cm for "pyrrole black", the first conductive form of pyrrole achieved via chemical oxidation.[199] Its conductivity is dependent on many reaction factors and on the choice of the preparation technique, with variable conductivities reported ranging from 0.07 S/cm [200] up to 90 S/cm [201] with the addition of poly(ethylene glycol) during polymerisation.[201] Although widely accepted to be hydrophobic [202], unfunctionalised PPy also exhibits hygroscopic characteristic; therefore, it is important to maintain in dry conditions, which limits its biological application, especially in physiological environment.[201]

PPy is probably the most investigated conjugated polymer for tissue engineering applications. Being the first polymer to show electrical properties applicable to the technological industry, and exhibiting improved conductivity than PANI, this material has been shown to partially replicate the electrical features of metals but possesses a more optimal mechanical match with native biological tissues [203]; its first application in tissue engineering being 25 years ago.[204]

PPy has often been applied as a coating on substrates, with an in-situ polymerisation process.[205] Recently PPy has been applied to silk fibroin micropatterned films, with the objective to enhance both electrical and topographic stimuli to a population of human ESCs derived CMs (hES-CMs). In the absence of electrical stimulation, the PPy substrates increased the alignment of cells and tissue maturation towards adult phenotype.[205] In an engineered nerve guidance conduit, PPy was coated on a layer of electrospun chitosan-polyurethane that was also functionalised with MWCNTs. With a two-fold increase in conductivity and a reduction of hydrophilicity. The presence of PPy was hypothesised to

function as a protein depot and stimulate the secretion of proteins from Schwann cells to support neurite growth in PC12 cells.[206] PPy has also demonstrated potential as an actuator in fibrous PLGA electrospun scaffolds, with the actuation mechanism of this construct based on volumetric change. This phenomenon is based on the exchange of ions from the surrounding electrolyte in and out of the polymer to counteract the charge imbalance of the PPy backbone when induced by an applied potential.[207] PPy scaffolds were also fabricated adopting a similar combination of materials and used as substrates for the investigation of neural cell adaptation on oriented fibrous mat. The application of electrical stimulation yielded an increase in the size and the formation of neurites in the order of 50%, with an even higher promotion on aligned meshes with respect to randomly oriented ones.[208] 3D fibrous porous scaffolds fabricated using a blend of poly(caprolactone) and PPy modified and with poly(ethylene glycol) (PEG) via a multistep synthesis. Investigating two different molecular weights of PEG molecule; a higher molecular weight PEG produced scaffolds with higher mechanical properties but lower conductivity.[209]

Researchers have also managed to apply a lyophilisation process on a PPy-doped chitosan-based [210] and on a chitosan-gelatin cryogel [211], obtaining porous scaffolds with interconnected architectures. In vitro studies on MG-63, a human osteosarcoma cell line, showed no hindering on biocompatibility and mineralisation potential with prospects for bone regeneration [210]. In addition, experiments on the cell lines neuro2a and C2C12 confirmed the biocompatibility of the material and the crucial role of electrical stimulation on cell morphology and proliferation.[211]

At high concentrations (30 w/w% PPy mixed with PCL and gelatin) PPy has exhibited a toxic effect and reduction of cell proliferation.[202] PPy does not degrade in physiological conditions and many attempts to produce a biodegradable mixture via blending with natural polymers have been attempted; however, it has been recommended to maintain the lowest amount possible for in vivo application.[211]

#### *2.3.2.3. Polythiophene*

At the time of poly(3,4-ethylendioxythiophene) (PEDOT) discovery - the most investigated compound of the poly(thiophene) family - conductive polymers such as PANI and PPy possessed inadequate conductive stability when placed in contact with oxygen or water, which posed a key limitation for many technological fields.[212] PEDOT exhibits very unique and specific features, such as being stable both at very high temperatures and at humidity, and being soluble in water when combined with a proper counter-ion and primary dopant, such as poly(styrene sulfonate) (PSS).[212] PEDOT:PSS possesses both ionic and electronic conductive properties and because of its chemical stability and processability.[213] It has been the subject of extensive research in the fields of microelectronics [214], sensor technology [215], actuation [216], and it has been explored extensively in biological scaffold development, neural implant [217] and optoelectronic applications.[218]

Despite PSS being the most utilised counter-ion and primary dopant with PEDOT, the presence of PSS in excess has its drawbacks both from a conductive and a biocompatibility perspective. Moreover, one must take into consideration the crucial importance of the crosslinking treatment to adopt with PEDOT:PSS as this factor is responsible for drastic changes in conductivity. Indeed, conductivity values for PEDOT:PSS films have been reported in a broad range spanning from 0.2 S/cm up to 4380 S/cm achieved via acetone treatment [219] or crystallisation with sulphuric acid [31], respectively. Many effects of the material composition and its processing have been observed on cellular responses.[220] The so called “sponge-like” capacity of PEDOT:PSS to change the surrounding environment depending on its redox-oxidised state, has been shown to significantly affect the adhesion and proliferation of T98G, a glioblastoma multiforme cell line.[221] The combination of 2D PEDOT:PSS-GOPS substrate, and of a pulsatile ES (100 Hz, 1 V, 10 ms pulses) has promoted neurite elongation in a neuron population (Tuj1).[222] Scaling up to 3D, a hyaluronic acid PEDOT-doped complex was directly incorporated into a matrix of chitosan/gelatin, whereby particles were added to the solution, then the composite was freeze-dried, and finally crosslinked with EDC/NHS.[223] The presence of PEDOT caused an expected increase

in conductivity from $1.76\times10^{-7}$ to $2.91\times10^{-3}$ S/cm and a three-fold increase in stiffness up to 61.5 ± 0.5 kPa. Investigations on PC12, a rat pheochromocytoma cell line, has highlighted that the concentration of 8 wt.% PEDOT-HA provided optimal biocompatibility, and enhanced the expression of growth-associated protein and synaptophysin compared to nonfunctionalised chitosan/gelatin.

While the researchers focussed for decades on 2D substrates and superficial treatments [224,225], in the last few years, some progress has been made in processing of PEDOT to a 3D scale. The realisation of a coating of PEDOT via in situ polymerisation of EDOT monomer on a substrates has been explored, such as for core-shell microfibers with a lumen of drug-loaded bacterial cellulose single fibre obtained via a wet-spinning process [226], and as in a carboxymethyl chitosan hydrogel, that showed no toxic effects of PEDOT presence compared to a nonconductive control group.[227] PEDOT:PSS can be purchased as a ready to use water dispersed solution and, exploiting this, has been subjected to freeze-drying to achieve homogeneous highly porous 3D scaffold. Such a construct has been stabilised with 3-glycidoxypropyltrimethoxysilane (GOPS) seeded with MC3T3-E1, a mouse osteoblast precursor, and resulted in increased osteogenic markers; alkaline phosphatase RUNX2 and COL1A1.[9] The insolubility of PEDOT:PSS to the most common solvents, has hindered its processability with solvent-assisted techniques, however it has been recently processed via electrospinning in a blend with poly(ethylene oxide) and dimethylformamide in a humidity-controlled environment. While the authors achieved electroconductive nanofibers at a relative humidity of 7%, higher values provoked bead formation.[228] A functionalised PEDOT-COOH with pendant carboxylic groups was synthesised to overcome the classic insolubility of PEDOT:PSS in standard solvents. This compound could be reduced and oxidised, confirming its nature of conjugated polymer, and - after a second functionalisation step with *N*-(*3*-aminopropyl) methacrylamide hydrochloride - could be processed in a hydrogel form where poly(acrylic acid) and PEDOT sites were covalently linked via the addition of poly(ethylene glycol) diacrylate. In a preliminary evaluation in vitro on C2C12, the expression of the proliferation marker Ki67

and the increase in MHCIIb from day 3 to day 7 confirmed the biocompatibility of such a conductive hydrogel.[229] Recently, a photo-crosslinkable hydrogel based on PEDOT-poly(ethylene glycol) diacrylate has been successfully 3D printed. In this study, a neuronal cell line (50B11) was encapsulated in GelMA then incorporated within the conductive mesh and monitored for 2 days. The introduction of electrical stimulation effectively enhanced the expression of neural differentiation markers BDNF, NT-3 and erbB2 only in presence of the conductive mesh.[230] Another reported composition has seen the oxidative polymerisation of EDOT in water with a polysaccharide, xanthan gum; that could be later processed via freeze-drying. The final porous scaffolds obtained exhibited pore sizes in the range 10 to 150 μm and Young's moduli between 10 and 45 kPa. This conductive platform supported cell attachment and viability of both MDCK II epithelial cells, achieving good cell attachment.[231]

As it is clear, PEDOT is a very versatile material, and it has been investigated by many research groups using multiple processing approaches. However, to date, little or nothing is known on the potential immune reaction when implanted in vivo. Data regarding the use of PEDOT:PSS has observed a certain level of toxicity when at a high content, with C2C12 incorporated to a GelMA-based photo-crosslinkable hydrogel with 0.3 w/v% PEDOT:PSS exhibiting such. Researchers have speculated that this toxic effect may be due the excess of PSS and to the subsequent increase of anionic presence in the environment.[232] The complete removal of this excess of PSS or the use of a different type of PEDOT would be mandatory for future in vivo applications.

## *2.4. The application of electroconductive biomaterials and electrical stimulation towards cardiac regeneration*

### *2.4.1. The Impact of electrical signalling during in vitro cardiomyogenesis*

Recent decades have seen the development of smart biocompatible materials, disruptive advanced manufacturing techniques such as 3D printing, cell reprogramming and genome

editing [233], which has fostered a field of research to engineer organoids and organs on a dish.[234] Platforms produced using electroconductive biomaterials could recapitulate the physiological cardiac microenvironment and therefore progress the field of organoid cultures and become a potent asset. Such an asset could allow one to model the physiological and pathological myocardium towards the study of new drugs and for the study of cellular biology. Despite bounding efforts and advances, current models can often be considered lacking, in that they possess shortcomings in fully differentiated and mature cardiac phenotypes, arrythmias and lower strength compared to native tissue.[19,235] One possible approach which needs further consideration is development of a supporting framework that can truly recapitulate the cardiac microenvironment in terms of mechanical anisotropy, structure, geometry and also bioconductance.

#### *2.4.1.1. Delivery of external electrical stimulation*

In modelling physiological stimuli in vitro to drive tissue maturation, the application of electrical stimulation had proven to exert a potent influence. Early attempts in the development of three-dimensional in vitro heart models and demonstrations of the potential of electrical stimulation to achieve myocardium maturation are dated to the end of the last century.[20,236,237] Since then, great progresses in the field have been achieved. In one such instance, neonatal rat ventricular myocytes in ultrafoam collagen sponges had significant improvements in the cell morphology when exposed to 5 days of electrical pacing consisting in 2 ms rectangular pulses at 1 Hz and an intensity of 5 V/cm.[238] Cells also presented decreased nucleic volume, increased mitochondrial number, and more mature sarcomere structure when compared with non-stimulated controls.

Pharmacological inhibition of influxing $Ca^{2+}$ exerted only temporary effects which were reversible when constructs were stimulated during cultivation. Since this work, the application of electrical stimulation has become an attractive and effective method to increase CMs maturation by others. To date it is established that electrically paced cells tend to align in clusters along the direction of the applied electric field lines, an alignment

that can be enhanced when combined with the use of a substrate with oriented topography.[57,239] Such alignment has been hypothesised to stem from myoblast mechano-transduction, in such that alignment is dictated by a $Ca^{2+}$-independent mediator downstream of the PI3K pathway, a known key regulation factor both for cell-cell fusion during myogenic differentiation and cytoskeleton remodelling. Moreover, myofibrils achieved using this process have developed higher contraction force when they are conditioned with electrical stimulation [240] (**Figure 2-3.B**).

The numerous reports of cardiomyocyte pacing has been achieved with bioreactors of differing variations some of which are illustrated in **Figure 2-3** such as the conceptually direct model of Tandon et al.[241] (**Figure 2-3.A**) and the more recent designed by Visone et al.[242] (**Figure 2-3.C**) which can both perfuse and deliver electrical stimulation up to 18 independent constructs, while direct observation and monitoring of the tissue function can be done during contractility tests.

#### *2.4.1.2. Electroconductive biomaterials as scaffolds*

Aiming to mimic the electroactivity of native connective tissues, such as the Purkinje fibre network, researchers have investigated the influence of electroconductive biomaterial scaffolds on tissue development in vitro. Electroconductive substrates may present as smarter platforms to direct current flow, synchronise cell beating, and enhance myocardial-like tissue maturation with an increased expression of cardiac markers.[60]

Initial attempts have utilised the addition of metallic components or carbon-based particles to develop electrically conductive scaffolds in cardiac applications. Gold nanoparticles have been adopted in combination with hydrogels of hydroxyethyl methacrylate [243] and with thermosensitive chitosan-based hydrogels.[244] Both these formulations have yielded improved biomaterial conductivity and upregulated Cx43 expression in CMs [243] and the expression of cardiac markers in MSCs.[244] In recent years, graphene has garnered the attention of research groups and has been used in various formulations in combination with both synthetic and biologic polymers. The group of O'Brien

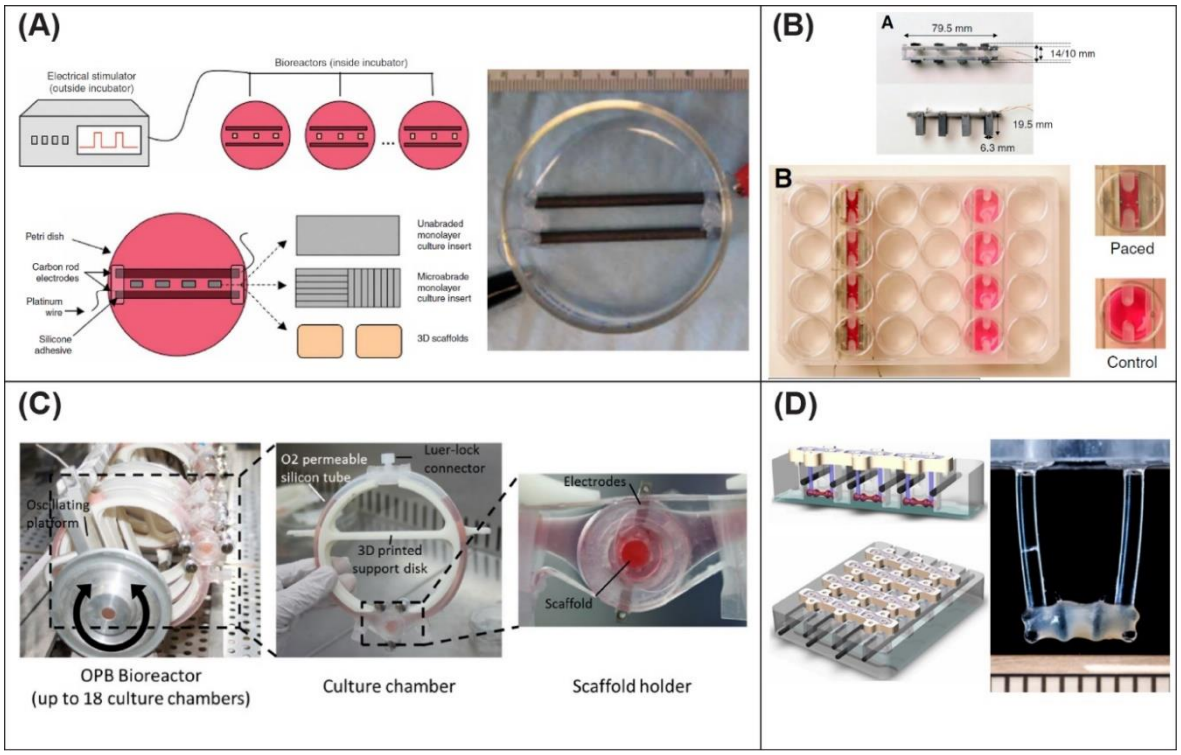


***Figure 2-3.*** *Representative examples of different designs for electrical stimulation bioreactors.* ***(A)*** *Bioreactor consisting of two parallel carbon rods, activated by a Grass stimulator and with the possibility to deliver excitation to both cell monolayers and 3D scaffolds. (Reprinted with permission from Ref.[241])* ***(B)*** *Bioreactor that can be combined to a standard tissue culture well plate and that can allocate both paced and not paced samples. (Reprinted with permission from Ref.[240])* ***(C)*** *A dual perfusion-electrical stimulation system, that can operate up to 18 systems in parallel and enables monitoring during contraction tests. (Reprinted with permission from Ref.[242])* ***(D)*** *Evolution of the systems in A and B, where the tissue is held between two flexible pillars. (Reprinted with permission from Ref.[19])*

[134] cultured murine ESC-CMs on a combined pristine graphene and collagen type I substrate, reporting an increase in cell alignment and CM maturation after the electrical stimulation (**Figure 2-4.B**). 3D porous foam-like scaffolds achieved via lyophilisation and based both on collagen type I [135] and GelMA [139] have been functionalised with rGO and were proved to yield increased CMs maturation in vitro and vasculogenesis when implanted subcutaneously.[139] Applying a thin layer of chemical vapor deposited graphene on a PEG substrate via a multistep processing that involved two intermediate steps with copper foil and poly(methyl methacrylate), Smith et al [245] achieved oriented micropatterning to mimic the anisotropic conductivity of the native myocardium. The hydrophilicity of the resultant graphene substrate led to significant improvements in the cell attachment, sarcomere length and expression of adult cardiac markers. Additionally, it was extrapolated that the presentation of graphene was promoting the recycling of $Ca^{2+}$ to the lumen of the

sarcoplasmic reticulum in cultured cardiac cells due to an increased intensity of $Ca^{2+}$ transient and upregulation of SERCA2 expression. Other carbon-based materials such as CNTs have imbibed increased strength and conductivity to blended materials and, owing to their morphology, these particles also present nanotopographic cues to cells. When dispersed in cell culture medium, CNTs exhibit biocompatibility at a concentration of 0.032 mg/ml [246] and enhance the differentiation of MSCs towards a cardiac lineage when combined with electrical stimulation.[121] CNTs have been combined with various materials and methods such as hydrogels within GelMA [60], as porous scaffolds with an elastic polyester polymer [247], with chitosan-based blend porous scaffolds [29], and as a core for coaxially fibers in poly(ethylene glycol)-poly(D,L-lactide) copolymers.[248]

Application of intrinsically conductive polymers mentioned previously is a more recent development in this field. In this instance, PANI has been blended with PLGA and processed via electrospinning to achieve aligned conductive fibrous meshes, with CMs seeded on this substrate grouping in isolated clusters with Cx43 expression and synchronous beating; and synchronous beating when a pacing regime is applied.[249] Similar beneficial effects have been observed using H9C2, a rat cardiac myoblast cell line; which when seeded on a thin film of conductive PLA-aniline pentamer and paced, had increased cell attachment, spreading and proliferation as well as increased levels of intracellular calcium with developed “pseudopodia”, deemed to be precursors of myocardial intercalated disks.[27] PPy has been combined with PCL both in 2D films [28] and 3D electrospun fibrous scaffolds [250], and the effects of its presence investigated on mouse atrial myocytes cell line HL-1 and primary rabbit CMs respectively. The presence of PPy promoted increased $Ca^{2+}$ propagation velocity and decreased calcium transient durations in 2D, enhanced cellular alignment in 3D, while Cx43 expression was significantly upregulated in both studies.

Electroconductive biomaterials have also improved CMs maturation in the absence of electrical stimulation. In the study of Wu et al [251], CNT-based biomaterials have been shown to increase the expression of cardiac features and markers. A conductive blend termed “Yarns” - composed of PCL, silk fibroin and CNTs - was processed using a wet−dry

electrospinning process which was then combined with GelMA. To model the multi-oriented architecture of native myocardium, two orthogonal layers of aligned CMs co-cultured with a third layer of endothelial cells was developed.[251] This continuing hypothesis that the presence of electroconductive scaffold can enhance cellular function even in absence of ES has been shown using an aniline-derivative polyurethane. Indeed, it was reported an increase in Troponin T Type 2 and Actinin alpha 4 gene expression of neonatal rat CMs compared to a nonconductive PCL control after 3 days.[252]

#### *2.4.1.3. Maturation of human induced pluripotent stem cells*

hESCs [253] and hiPSCs are an expandable and pluripotent source of cardiomyocyte progenitor cells [89]; however, despite efforts of many research groups, complete differentiation to adult cardiac phenotypes remains inadequate and is varies according to the batch of cells being used.[254]

The development of Biowire™ has been a milestone in the field of hiPSCs-CMs organs on a chip.[22] This setup is composed of a surgical suture in a type I collagen gel and seeded with a mixed population of hIPSC-CMs, fibroblast, smooth muscle cells and endothelial cells. After 1 week the cells and the gel clustered and created an organoid on the suture. Studies on this system have demonstrated that high frequency pacing at 6 Hz leads to improved tissue maturation with aligned Z discs, abundant mitochondria and desmosomes, and an increase in cell volume overtime similar to physiological hypertrophy. This organoid has been recently upgraded to a new configuration: Biowire™ II [18] (**Figure 2-4.A**), which consists of a hiPS-CM loaded hydrogel positioned between two poly(octamethylene maleate (anhydride) citrate) (POMaC) bars that enables real-time observation of tissue mechanical performance due to an inherent elasticity and autofluorescence of this material. The authors persisted organoid culture for up to 8 months in vitro, successfully achieving atrial and ventricular cardiac tissue in the two ends of the same tissue stripe; furthermore, the response of these two regions to drugs as Serotonin and Razolazine was achieved.

The ability of the cells to cluster together has been exploited by many groups to achieve

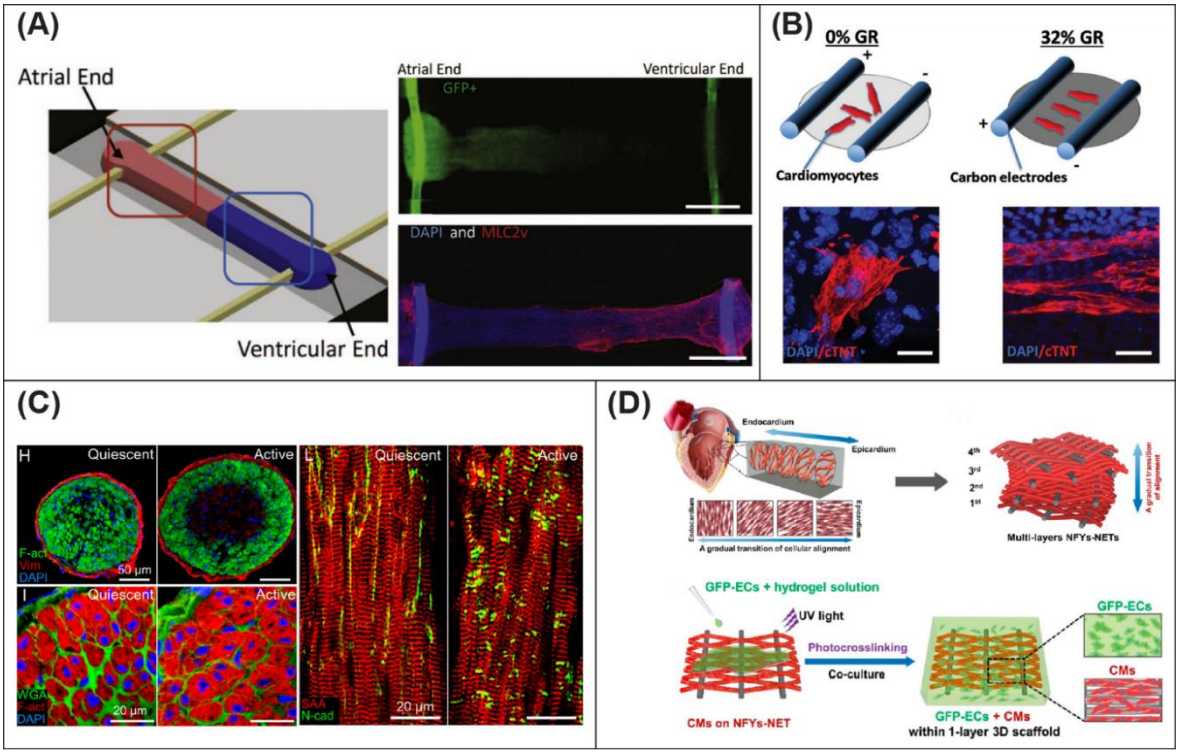


***Figure 2-4.*** *Development of in vitro cardiac models.* ***(A)*** *The system Biowire™ II invented by Radisic group. This organoid allows the simultaneous maturation of both atrial and ventricular population starting form hiPSCs. (Reprinted with permission from Ref.[18])* ***(B)*** *hESCs seeded on a substrate of collagen type I and pristine graphene and stimulated by two carbon rods. (Reprinted with permission from Ref.[134])* ***(C)*** *Studying the effect of thyroid hormone T3 on both quiescent and mechanically active via electrical stimulation "Cardiobundles". (Reprinted with permission from Ref.[235])* ***(D)*** *Heart model with multi-oriented architecture: two orthogonal layers of aligned CMs co-cultured with a third layer of endothelial cells was developed. (Reprinted with permission from Ref.[251])*

oriented tissue with hIPSCs-CMs in collagen-based [18,255] and fibrin-based hydrogels [19,256], providing a convenient platform to perform drug screening and biological investigations. Tests on these types of setup have demonstrated that "intensity training" stimulation - consisting of an increasing stimulation frequency from 2 Hz to 6 Hz by 0.33 Hz per day - yielded optimal tissue maturation when compared to unstimulated or constantly stimulated groups (**Figure 2-3.D**).[19] However, despite exhibiting morphological and genetic features typical of adult cardiac tissues, these "intensity trained" constructs generated inadequate contractile force.

The combined application of tissue straining (125% static strain) and pacing enhanced CM density and size, and alignment of both myofibril and collagen fibers when compared to an unstressed tissue; despite no structural improvements were observed compared to the group without electrical pacing. Contractile function, extrapolated from the calcium handling capacity of the cells, reached a 10-fold increase when static stress was applied,

and this reached a further 20-fold increase with the combined application of static stress and electrical stimulation. Electrical stimulation also led to an increase in cell volume fraction leading to double passive stiffness compared to the static stress group, despite it is still far from the native tissue perhaps because of the reduced cell alignment compared to the native one.[257]

Already, electroconductive polymers have been applied to enhance the maturation of hiPS-CMs in vitro. One of the earliest studies developed electromechanically active fibrous electrospun PLGA scaffolds functionalised by electro-polymerisation deposition of PPy.[207] These scaffolds had the capability to contract due to influx of ions from the surrounding media into the PPy coating when an electrical pacing was applied, therefore working as actuators. Differentiating hiPSCs seeded on these actuated platforms had increased Actinin, NKX2.5, GATA4, Myh6 expression when compared to a non-coated PLGA and to unstimulated PPy/PLGA scaffolds. Another fibrous platform was realised via electrospinning of a blend of PANI and polyetersulfone was shown to yield the differentiation of cardiovascular disease specific iPSCs towards cardiac phenotype proved by the upregulation of NKX2.5, GATA4, NPPA, and TNNT2.[258] Finally, despite reported toxicity when used at high concentration, PEDOT:PSS at concentration of 0.26 w/w% has been incorporated within biohybrid hydrogels of both collagen type I and alginate.[259] The presence of PEDOT:PSS in these hydrogels enhanced the maturation of rat primary CMs and hiPSC-CMs in vitro with faster and wider contraction, as well as increased sarcomere length comparable with CM adult values after 11 days of culture and electrical stimulation.

Conditioning via electrical stimulation showed to accelerate the differentiation process of hiPS-CMs in vitro with a differentiation efficacy of 80% compared to 60% of unstimulated cells; moreover, once implanted in vivo the stimulated group and conditioned with electrical pacing caused a reduced infarcted region.[260] In vitro electrical stimulation conditioning proved critical in inducing enhanced cardiac differentiation, maturation and functionality of the cell population, to yield an increased ejection fraction and left ventricle fractional shortening when applied to an in vivo MI model. However, the risk of arrhythmia and the

presence of a heterogenous CMs population was highlighted as a limiting challenge of the study.

### *2.4.2. Cardiac patches*

Mechanical support of the infarcted myocardium is an approach to restrict adverse ventricular dilatation and has been attempted by many through the application of cardiac patches applied on the external surface of the myocardium.[261] Research in the field has been focused on the development of biocompatible mesh-patches with suitable ranges of elasticity to provide optimal mechanical support, often incorporating cell therapies or regulatory signal release [262], and with suitable design to allow a minimally invasive in situ delivery.[54] Although mechanically sufficient, these attempts do not address a restriction of electromechanical coupling due to the presence of scar tissue. In the last few years electroconductive materials have been adopted to manufacture patches that can not only mechanically support the ventricle but that can bridge the electrical stimulation into and towards the infarcted area.[60]

Almost one decade ago, initial attempts to develop conductive cardiac patches were performed by electrospinning blends of PCL:PANI nanofibers [263] and fabricating alginate scaffolds doped with gold nanowires.[264] Both these studies established an advantage of using conductive substrates to improve cell response. The first manuscript reported a significant role in driving human MSCs differentiated into CMs, while the second one showed how an electroactive platform could bridge the electrical coupling between adjacent primary rat CMs and fibroblasts with higher cardiac markers expression and more synchronous beating then pure alginate.[264] Since then, a series of investigations have occurred with the application of varying electroconductive biomaterials and manufacturing techniques in vitro. GelMA patches doped with CNTs have demonstrated a significant enhancement of in vitro electrical functionality when compared with nonconductive control patches, namely the rhythmic contractility of cell seeded patches could assume a tubular shape when floating in the medium and that could contract when electrically stimulated.[60]

Advantageously, subsets of conductive particles and polymers can be processed via several techniques to achieve cardiac patches, such as via incorporation of CNTs in electrospun PCL [265], 3D bioprinting of alginate or methacrylated collagen hydrogel meshes crosslinked and reinforced with CNTs [266], and laser ablation to micropattern chitosan films which can be subsequently functionalised with PANI via in situ polymerisation (**Figure 2-5.D**).[267] Despite their relevance in the field, the available reports of these works are currently limited to in vitro evaluation.

More recently the application of conductive cardiac patches in vivo has been reported, for example with many solutions that described the versatile use of chitosan as a primary biomaterial for the incorporation of different electroconductive fillers. The implantation of these smart reinforcements improved the conduction propagation in MI heart in a series of studies where PANI [268,269], PPy [52], graphene oxide and gold nanosheets [270] were adopted as conductive auxiliary compounds. Such patches when preseeded with of CMs [271] (**Figure 2-5.C**) and hiPSC-CMs [270] prior to implantation have demonstrated a significant overall improvement in cardiac function after 4 and 5 weeks respectively. A novel approach aimed at recapitulating the mechanical and electrical anisotropy of the native human myocardium has utilised excimer laser microablation on a chitosan film to achieve an auxetic design, that was later made conductive via deposition of a coating in PANI (**Figure 2-5.B**). Although promising in vitro; modest effects were observed in vivo with no increase in conduction velocity of the electrical beating impulse compared to a mesh with standard design that was previously fabricated by the same research group.[268,269] Another study has looked at paintable adhesive hydrogel-patch based on a dopamine-PPy blend. This new type of material could be directly applied directly on the heart without sutures, and it showed to promote the recovery of cardiac function and revascularisation of the infarcted myocardium (**Figure 2-5.A**).[272] A final mention is the development of a two-layer hybrid construct based on a flexible collagen type I hydrogel that conferred mechanical support and consisted of a matrix of fibrous collagen doped with gold nanoparticles providing electrical properties. This platform induced upregulation of Cx43 expression in vitro after electrical stimulation, while

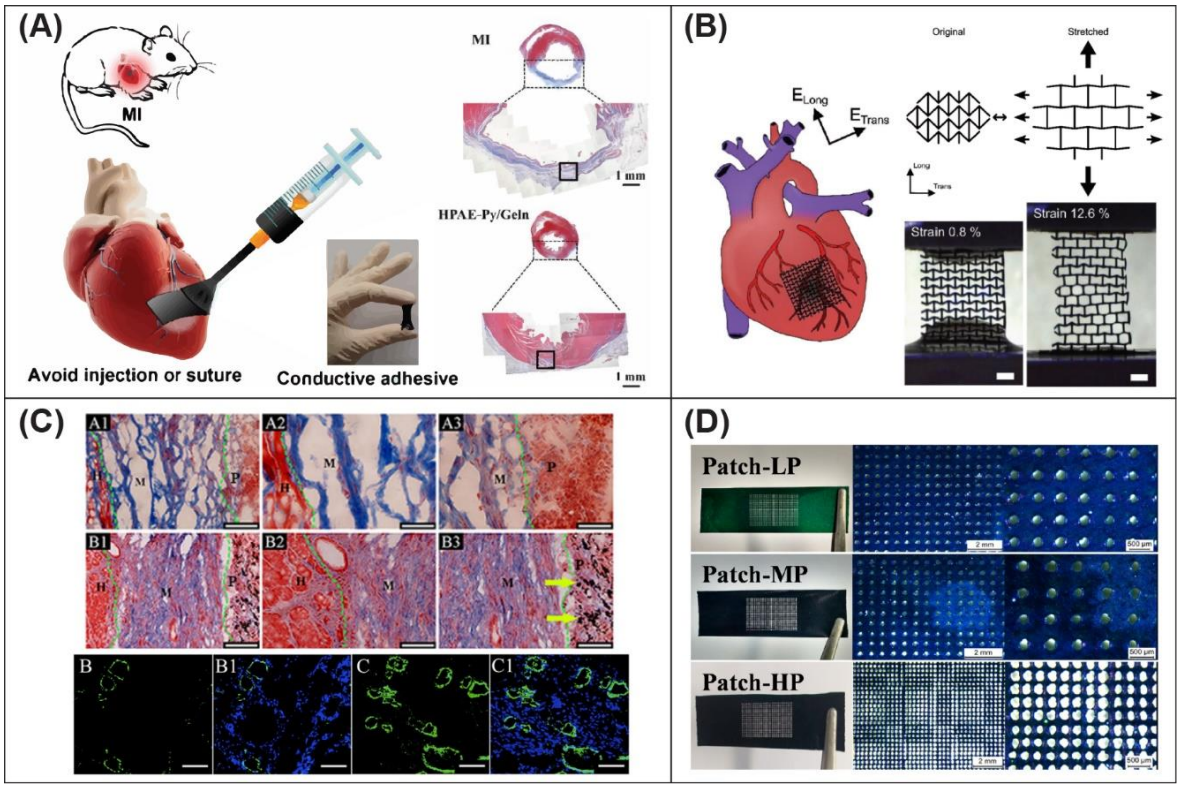


***Figure 2-5.*** *Smart electroactive cardiac patches designs.* ***(A)*** *A paintable hydrogel-patch that can be directly applied to the myocardium and drives tissue recovery. (Reprinted with permission from Ref.[272])* ***(B)*** *A conductive patch with auxetic design that can recapitulate the anisotropy characteristic of the myocardium(Reprinted with permission from Ref.[269])* ***(C)*** *Preseeding of CMs on a chitosan-PPy patch, promoted engraftment and cardiac function improvement. (Reprinted with permission from Ref.[271])* ***(D)*** *Chitosan-PANI film with porosity controlled via laser ablation and processed with three different pore sizes. (Reprinted with permission from Ref.[267])*

it improved cardiac function and vasculogenesis at 5 weeks in vivo, without provoking pro-inflammatory differentiation of macrophages.[273]

### *2.4.3. Injectable hydrogels*

In order to alleviate the loss of myocardial volume, and reaching a minimally invasive approach, injectable hydrogels have been widely adopted as a strategy to not only restore healthy heart geometry, but more importantly to locally deliver cell-based treatments [235] with or without other functional therapeutics [274] In the context of the subject matter of this review, groups have managed to synthesise electrically conductive hydrogels to recover cardiac function even further which is an exciting step forward in the field.

Maintaining its popularity, chitosan has also been adopted also to produce hydrogels in addition to be a substrate in vitro applications and cardiac patches discussed previously. Combining chitosan with PPy to achieve such a hydrogel has facilitated electrical coupling

in skeletal muscle tissue ex vivo [275] and between physically isolated CM populations in vitro [276] (**Figure 2-6.A**). In vivo implantation of chitosan/PPy hydrogels in an infarcted rat model has improved electrical impulse propagation across scarred tissue, decreased time of depolarisation of the right and left ventricles (i.e. QRS interval) with an increase in conduction velocity, and enhanced the cardiac function when compared to a non-conductive hydrogel of a similar nature.[275,276] An oxidised dextran crosslinked chitosan-graft-polyaniline hydrogel has also been used to develop electro-responsive smart drug carriers loaded with amoxicillin and ibuprofen and for antibacterial treatments. This hydrogel was pH-responsive and exhibited good biocompatibility both in vitro on L929, a mouse fibroblasts cell line, and in vivo via subcutaneous implantation in a rat model with almost total resorption at 28 days.[274]

Amongst the first to prove the efficacy of conductive nanomaterials in heart regeneration, a gelatin-based hydrogel doped with SWNTs has demonstrated an enhanced expression of cTnT and Cx43 in neonatal rat CMs in vitro, with synchronous beating after 8 days of culture. Application of this material with a cargo of primary rat CMs to a rat model of MI; host vasculature invaded into the hydrogel after 1 week, while at 4 weeks evidence that cells and scaffolds partially migrated into the host myocardium was revealed. However, the conductive hydrogel had the highest amount of M1 macrophages at the interface between the host tissue and hydrogel compared to the nonconductive control. The implantation of the conductive hydrogel led to limitation of further deterioration and to a series of improvements in heart function such as an increased fractional shortening and ejection fraction, and reduced progression of left ventricle enlargement. Molecular mechanisms triggered by the presence of SWNTs were investigated with speculation that the beneficial effects on cardiac repair can be related to the integrin-mediated mechano-transduction pathway, specifically of integrin-linked kinase, protein kinase B and β-catenin.[24]

Important results have been achieved with strategies involving the encapsulation of plasmid DNA (pDNA) into a biomaterial as a novel promising approach to enhance stem cell differentiation in situ. A first attempt consisted in the delivery into the myocardium of an

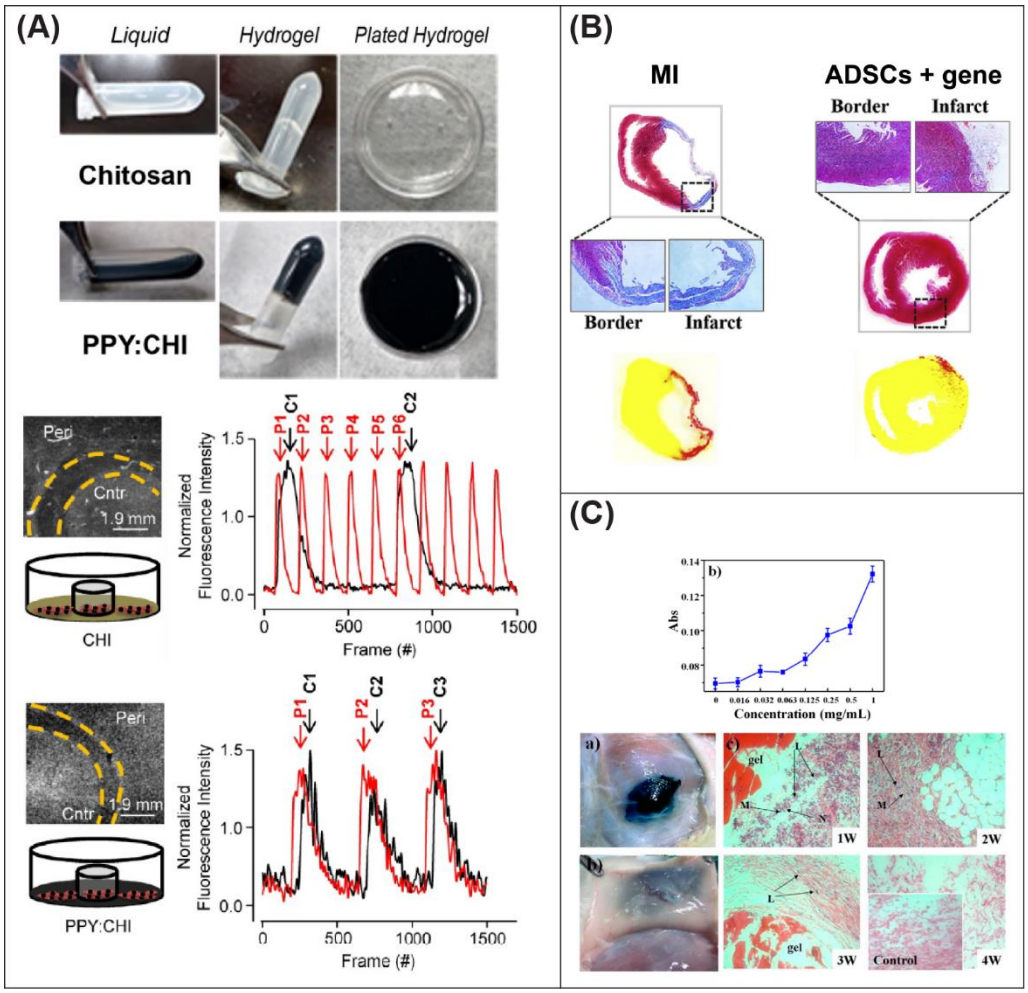


***Figure 2-6.*** *Promising injectable conductive hydrogels for in situ myocardium regeneration.* ***(A)*** *A chitosan-PPY hydrogel can electrically couple two separated CMs populations. (Reprinted with permission from Ref.[276]).* ***(B)*** *Adipose derived stem cells and pDNA incorporated in a conductive hydrogel, showed to improve the functionality of the heart in vivo. (Reprinted with permission from Ref.[51])* ***(C)*** *A PANI-doped hydrogel showed antioxidant effects after subcutaneous implantation. (Reprinted with permission from Ref.[278]).*

injectable conductive hydrogel composed of graphene oxide, GelMA and pDNA encoding $VEGF_{165}$.[55] The hydrogel was injected through a 22-gauge needle, and it was able to induce neoangiogenesis in a paracrine manner, not causing any cytotoxic effects. Similar positive outcomes in terms of tissue healing and angiogenesis have been achieved also via the implantation of a tetraaniline/hyaluronic acid conductive hydrogel delivering pDNA encoding endothelial nitric oxide synthase (eNOS) and adipose derived stem cells (**Figure 2-6.B**).[51] Improvement in heart function α-Smooth Muscle Actin (α-SMA) and Cx43 at 4 weeks have been achieved by the administration of adipose tissue-derived stromal cells encapsulated in a PEG diacrylate Melamine crosslinked with thiol-modified hyaluronic acid and doped with graphene oxide; in a rat model of MI.[277]

CNTs [60] and PANI [278] have revealed intrinsic radical scavenging activity that could be a key factor to modulate regeneration of the heart as reactive oxygen species are typical of an ischemic myocardium environment.[279] In vitro evaluation at 7 days on H9C2 cells proved that a tetraaniline copolymer poly(*N*-isopropylacrylamide-methoxy(polyethylene glycol)methacrylate-*2*-methylene-*1,3*-dioxepane-methacrylic-tetraaniline) (P(NIPAM-mPEGMA-MDO-MATA; PN-TA), may reduce the free radical-mediated oxidative cardiac damage, moreover the application of electrical stimulation enhanced the cellular response material biocompatibility (**Figure 2-6.C**). To evaluate the antioxidant effect in vitro, the authors used 2,2-diphenyl-1-picrylhydrazyl (DPPH) as a model, showing how the introduction of the antioxidant material improved significantly cell viability.[278] The authors repeated similar experiments adopting a different material [280] mixing tetraaniline copolymers and cyclodextrin. Again, histological staining of subcutaneous implantation demonstrated biocompatible response with almost no inflammatory response and sensible reduction of fibroblastic capsule at 3 weeks.

| Electro-conductive Biomaterial | Heart models in vitro | | Smart cardiac patches in vivo | | Injection of hydrogels in vivo | |
|---|---|---|---|---|---|---|
| | *Fabrication* | *Findings* | *Fabrication* | *Findings* | *Fabrication* | *Findings* |
| CNTs | GelMA hydrogels [60]<br>elastic polyester [247]<br>chitosan-based [29]<br>PEG-poly(D,L-lactide) [248] | nanotopographic cues to cells<br>↑ cardiac markers in MSCs | - | - | gelatin-based [24] | ↑ cTnT and Cx43 in vitro, angiogenesis in vivo |
| | Wet-dry electrospinning YARNS + GelMA [251] | ↑ cardiac feature and markers w/out electrical stimulation | | | | |
| Graphene | Film: pristine graphene + collagen [134] | ↑ cell alignment, hES-CMs maturation | GO + AuNPs + chitosan [270] | ↑ conduction velocity and contraction | GO with GelMA and pDNA ($VEGF_{165}$) [55] | ↑ angiogenesis |
| | Lyophilisation: rGO + collagen [135] | ↑ CMs maturation | | | | |
| | Lyophilisation: GelMA [139] | ↑ CMs maturation | | | GO with PEG diacrylate and ADSCs [277] | ↑ α-SMA and Cx43 in vivo |
| | coating PEG via CVD [245] | ↑ cell attachment<br>↑ sarcomere length | | | | |
| Metallic NPs | HEMA hydrogels [243] | ↑ Cx43 in CMs | Collagen hydrogel + collagen fibers [273] | ↑ heart function, vascularisation, absence of pro-inflammatory response | - | - |
| | chitosan hydrogels [244] | ↑ cardiac markers in MSCs | | | | |
| PANI | Electrospinning in blend with PLGA [249] | ↑ Cx43 expression, synchronous beating | Chitosan [268] | ↑ heart function, no induction of arrythmias | Chitosan as smart drug carriers [274] | Controlled inflammatory response in vivo |
| | Film in PLA [27] | ↑ cell proliferation, development of pseudopodia | | | hyaluronic acid, pDNA (eNOS) and ADSCs [51] | ↑ angiogenesis and tissue healing |
| | Polyurethane [252] | ↑ TNNT2 and Actinin alpha 4 gene w/out electrical stimulation | Microablation of chitosan film [269] | Auxetic design, mechanical and electrical anisotropy | Cyclodextrin [280] | ↓ inflammatory response, fibroblastic capsule in vivo |
| | Electospinning in blend with polyetersulfone [258] | ↑ NKX2.5, GATA4, NPPA, and TNNT2 | | | | |
| PPy | Film in PCL [28] | ↑ $Ca^{2+}$ propagation velocity<br>↑ Cx43 | paintable adhesive dopamine blend [272] | ↑ heart function and vascularisation | Chitosan [275] | electrical coupling in vitro and ex vivo |
| | Electrospinning in blend with PCL [250] | ↑ cellular alignment<br>↑ Cx43 | Chitosan gelfoam [52] | ↑ conduction velocity absence of arrhythmias | | |
| | Coating on PLGA electrospun scaffold [207] | ↑ Actinin, NKX2.5, GATA4, Myh6; actuation ability | | | | |
| PEDOT | Collagen/alginate hydrogel [259] | ↑ increased sarcomere length; faster and wider contraction | - | - | - | - |

***Table 2-1.*** *Overview of electroconductive biomaterial systems employed in the field of cardiac tissue engineering and cardiac biomaterials.*

.

## *2.5. Conclusions*

It is becoming increasingly evident that electroconductive biomaterials pose a significant factor in tissue engineering in the coming years to achieve smart solutions not only in the field of cardiac tissue engineering but other aetiologies of disease.

Based on the abundant evidence discussed in this review; electroconductive biomaterials and electrical stimulation are critical factors to be considered in achieving success in the maturation of cardiac organoids and to provide auxiliary paths for the conduction of action potentials within the impaired myocardium. In terms of CM differentiation, improvements have been reported with electroconductive biomaterials alone without the presence of electrical stimulation, and vice versa when electrical stimulation was applied in the absence of electroconductive biomaterial. As discussed above however, when these two features are combined; the best results are yielded highlighting the importance of applying these two factors together (**Table 2.1**).

Despite the advances and hype for electroconductive biomaterials in this field, none of the materials investigated in this review satisfy all the requirements for stable and successful in vivo applications.

To be a suitable candidate for any of the three categories mentioned in this review: scaffolds for in vitro models, cardiac patches or, injectable hydrogels – the biomaterial needs to address many factors. Mimicking physiological bioconductance of different organs is attainable with these materials, however one must keep in mind that the conductive properties of many of these compounds may diminish in physiological environments. Engrafted material should integrate appropriately with host networks to avoid risk of arrhythmia or worse still; add a pathway that adds detrimental to electrophysiological signalling in vivo. The compound needs to be processable into useful morphologies, such as defined macroscopic porous architectures and mechanical properties suitable for the in vitro or in vivo applications, which is especially important considering the anisotropic nature of the myocardium.

An ideal candidate material should not induce any toxic response at cellular or systemic level, do not induce immune reaction or chronic inflammatory response; however, the performance and translation of the here presented materials to the clinic has yet to be seen . Indeed, in vivo experimentations has been limited to subcutaneous or short-term studies, leaving unsolved many open queries regarding the long-term toxicity of these materials in vivo and their interplay with our innate and adaptive immune system.

A tenet of tissue engineering often focussed upon is the concept of biodegradable scaffolds providing initial structural support that gradually degrades as the host tissue regenerates. None of the electroconductive materials we have described are known to be metabolised in vivo. Aiming to generate conductive degradable biomaterials, some groups have explored the combination of a conductive polymer with a degradable matrix or hydrogel.[275,55] However, even succeeding in this method, the fate of electroconductive by-products released in the body is not clear as there is not univocal proof of their clearance through standard metabolic pathways.[281,282] One main concern is the penetration capability of these by-products into surrounding tissues and cells, as it is well established that nanoparticles with diameters less than 40 nm can penetrate both the cell membrane and the nucleus with the risk to generate a broad range of reactions, such as change in nucleus architecture and size or also affecting affect DNA methylation.[282] In vivo studies have shown contradictory results regarding the toxicity of extrinsically conductive materials, and negative effects have already been described for CNTs [283], Graphene [284] and NPs [164] which describe the infiltration of byproducts to internal organs and systemic circulation, However, a lack of univocal standard protocols for toxicity evaluation in vivo has led to ambiguity in these findings.[285] Given their recent development, the in vivo evaluation of MXene and of ICP is at an early stage. Their use in the field of implantable electronics suggests an acceptable tolerance of these substances when used as coatings [286] and an overall concentration-dependent toxicity.[287]

The regulatory track to get a new material to the clinical phase that requires a new substance to be accepted - and not only cleared - is a long and expensive process that may

discourage their introduction to the market. Indeed, despite metallic NPs being historically the most tested conductive materials, few iron-based nanoparticles have been approved for their use as contrast enhancement reagents for medical imaging and no AuNPs have been approved to date yet by the Food and Drug Administration.[288]

Potentially, an inert graft constituted of a fully nondegradable material, able to interact with the host without chronic inflammatory reaction or immune response, may be a more suitable solution. In recent years, growing expectations have been raised on the use of PEDOT and its derivatives. Because of its higher stability and conductivity compared to the other intrinsic conductive polymers, this compound may be the most suitable candidate for electroconductive grafts or scaffolds; and it has been shown to be manufactured into three-dimensional structures without the use of a complementary supporting material.[9] However, as we have been pointed out; long-term toxicity both in vitro and in vivo is yet to be evaluated. Notably, the presence of PSS as counterion has shown to lead to toxic effect, therefore, a full cleavage of the unreacted leftovers of this molecule must be guaranteed. One strategy to overcome this and increase the biocompatibility and biofunctionality of PEDOT is to incorporate biodopants such as dextran sulphate or alginate which have been shown to increase the absorption of fibronectin and collagen respectively.[289]

The growth and application of electroconductive biomaterials is testament to their potential for tissue engineering applications and especially for cardiac regeneration. As in vitro models do not require a strict characterisation of their degradability and long-term effects of their by-products at a systemic scale, it is most likely that this application will see impact sooner in where there is less risk and more control over electrical stimulation. However, with increasing advances in polymer chemistry, greater understanding of degradation kinetics, and the discovery of biological moieties that be used to improve material performance; electroconductive implants in cardiac settings could one day become a routine therapeutic option.

# 3. General Methods

## 3.1. Modelling and 3D printing

Throughout the project, several 3D models were designed and then fabricated via rapid prototyping. All software design was performed with Solidworks while 3D printing was achieved with either Original Prusa i3 MK3S (Prusa Research), Ultimaker 3 (Ultimaker BV) or stereolithography printer Form 3 (Formlabs).

## 3.2. Preparation of PEDOT:PSS solutions

PEDOT:PSS 1.3 wt.% dispersion in water (Sigma-Aldrich, Ireland) was mixed either with glycidoxypropyltrimethoxysilane (GOPS, average $M_n$ 236.34) or with poly(ethylene glycol) diglycidyl ether (PEGDE, average $M_n$ 500) (Sigma-Aldrich, Ireland) at variable concentrations. Blends were vortexed for 30 seconds, sonicated for 30 minutes and filtered with a 0.45 µm PVDF syringe filter to remove aggregates.

## 3.3. Isolation of Collagen Type I from porcine tendons

Collagen type I was isolated from porcine tendons following previously developed protocols.

First, tendons were isolated from 3-month-old porcine legs obtained from an abattoir. After having been separated from the muscle and hoof, tendons were cleaned of any additional fibrous tissue, submerged in 70 v/v% ethanol and then in PBS. Once liquid excess was removed, samples were stored at -80 °C until further use. Tendons were cut into pieces roughly 2-3 mm in length and pulverised using a SPEX sample prep Freezer/Mill® 6770 (SPEX sample prep, United Kingdom).

The isolation continued with removal of the proteoglycan content through solubilisation by adding 0.2 M sodium hydroxide (NaOH) (Sigma-Aldrich, Ireland) to the tendon powder, then intramolecular crosslinks within the collagen were cleaved by pepsin digestion. Briefly,

50 mg of tissue were added to 10 ml of 0.5 M acetic acid (HAc) (Sigma-Aldrich, Ireland) solution containing 150 units/ml pepsin (Sigma-Aldrich, Ireland) and incubated at a temperature less than 20 °C with a rotation of 4 rpm for 48 hours. Salt precipitation enabled the isolation of proteins via the addition of 0.5 M sodium chloride (NaCl) (Sigma-Aldrich, Ireland). For complete inactivation of any remaining pepsin and the elimination of residual proteoglycans, solutions were dialysed against 0.02 M sodium phosphate dibasic ($Na_2HPO_4$) (Sigma-Aldrich, Ireland) using pre-soaked dialysis membranes with molecular weight cut off between 12 and 14 kDa (Sigma-Aldrich, Ireland). Obtained materials were lyophilised using a freeze-dryer (FreeZone, Labconco Corporation, Kansas City, MO). applying a protocol with ramp to -40 °C, hold for 60 minutes, ramp to 10 °C at a rate of 1 °C per minute, hold for 18 hours with a vacuum of 0.2 mbar, ramp to 20 °C at a rate of 1 °C per minute, and hold for 2 hours. The obtained collagen type I was then solubilised in 0.1 M acetic acid to obtain the target final concentration of 15 mg/ml.

### *3.4. Fabrication of 3D sponges-like scaffolds.*

For *Chapters 4, 6, 7* and *8*, 3D sponge-like highly porous scaffolds were achieved through lyophilisation using a freeze-dryer (FreeZone, Labconco Corporation, Kansas City, MO). Collagen solutions or PEDOT:PSS blends - containing either 3 v/v% GOPS or 3 w/v% PEGDE were adopted.

Isotropic sponges were produced into standard cell culture multi-well plates, while a custom-made mould containing a bottom stainless-steel layer and a top polydimethylsiloxane (PDMS, SYLGARD® 184) was fabricated to induce ice crystal alignment by virtue of the different thermal conductivities of the two materials (**Figure S1**).

Except for *Chapters 4* and *6* - in which different freezing temperature were investigated - freeze-drying was performed with the same protocol described in section 3.3. Specimens containing GOPS required an additional annealing treatment in vacuum oven at 140 °C for 1 hour, afterwards samples for all groups were subjected to multiple washings using deionised water and finally, a second lyophilisation process was carried out to fully dry the

materials.

Collagen scaffolds were crosslinked with *N*-(*3*-Dimethylaminoproypl)-*N*-ethylcarbodiimide hydrochloride (EDC) (E1769, Sigma-Aldrich) and *N*-Hydroxysuccinimide (NHS) (130672, Sigma-Aldrich). A 5:5:1 molar ratio of EDC:NHS:carboxyl groups within the collagen sponges was added to pure ethanol and the pH adjusted to between 5.3 and 5.5.[290] Crosslinking took place under dynamic condition for 18 hours; samples were then rehydrated and lyophilised one more time.

### *3.5. Morphology assessment of 3D PEDOT:PSS sponges.*

For *Chapters 4, 6* and *7*, morphological study of the 3D scaffolds was performed.

Porosity was evaluated with ethanol intrusion technique. Briefly, samples were immerged in 70 v/v% ethanol solution and the volume of ethanol was derived from the global mass of the specimens and considered as the empty component of the structure as in equation 2, with $P_e$ = porosity by ethanol intrusion, $V_s$ = volume of the scaffold, $d_s$ = density of scaffold, $M_s$ = mass of the scaffold, $V_e$ = volume of ethanol solution, $d_e$ = density of ethanol solution, $M_e$ = mass of ethanol solution.

$$P_e = \frac{V_e}{V_s+V_e} = \frac{{M_e}/{d_e}}{{M_s}/{d_s}+{M_e}/{d_e}} \quad \textit{equation 1}$$

For qualitative high-magnification observation, samples were imaged via Scanning Electron Microscopy (SEM). Briefly, scaffolds were mounted on aluminium stubs with a conductive carbon tape (Ted Pella, USA), and a gold–palladium layer of approximately 5 nm was sputter coated on the sample surface. Specimens were observed using a Zeiss SUPRA 40 field emission SEM (Zeiss, Germany) with a 5 kV electron beam.

Quantitative analysis on pore size was performed similarly to how it has been reported by O'Brien group.[291] Samples were agarose-embedded and dehydrated using an automatic tissue processor (Leica ASP300), then wax embedded and finally sliced. A total of n=3 10 µm thick slices were sectioned using a rotary microtome (Leica Microtome RM2235) and sampled for imaging with a distance of 100 µm between samples, and n=3 replicates both

on the transversal and longitudinal directions per condition. Sections of the scaffolds were imaged with a ScanScope® (Aperio Technologies Inc., USA) after a multistep process of agarose and wax embedding as previously reported.[16] Quantification of parameters such as pore size, pore circularity and pore eccentricity were then performed with a custom-made Matlab® script able to threshold the image, skeletonise the structure and finally derive the average diameter pore size from the pore area approximated to a circle.

### *3.6. Water sorption of 3D scaffolds*

Samples with known and regular dimensions were weighed in their dry state and 1 hour after being soaked in distilled water. Water intake was estimated as ratio between wet and dry mass.

### *3.7. Stress-relaxation of 3D scaffolds in hydrated conditions*

For *Chapters 6* and *7*, a uniaxial unconfined compression tests were performed on n = 4 samples per group using a Zwick Roell® single column universal testing machine (Zwick Roell. UK) and a 10 N load cell. Tests were performed in hydrated conditions using PBS at room temperature. For isotropic samples, scaffolds with cylindrical shape and approximately 6 mm diameter and 3 mm thickness were prepared, while aligned scaffolds were prepared into rectangular cuboids.

In a similar manner to previous reports [292], the first test consisted of a stress-relaxation phase followed by a dynamic cyclic compression at physiological frequency. Initially, specimens were preloaded at 0.005 N, then a compression rate of 0.02 %/second was applied up to 15% strain, in this range, the slope of the curve was used to determine the Ramp Modulus of the material. Deformation was then kept constant for 45 minutes in order to understand the stress-relaxation response of the constructs and derive the Equilibrium Moduli. Finally, Dynamic Modulus was obtained from the averaged slope of n=5 cycles at 1 Hz between 15% and 16% strain.

## 3.8. Electroconductivity characterisation

For *Chapters 6* and *7*, electrical conductivity was determined using a custom made two-point probe testing setup. Samples were compressed to approximately 5% strain between two parallel brass plates and a sourcemeter Keithley 2400 (Tektronix, USA) was used to apply a sweep potential between -1 and +1 V and to measure the current with increment of 5 mV per second, to derive the characteristic I-V curve. Resistance R was measured as the slope of the linear regression in the linear region, and afterward the conductivity $\sigma$ was calculated as in equation 3, with $\rho$ = resistivity, $d$ = thickness of the sample, $A$ = area of the cross section (derived by the diameter of the sample).

$$\sigma = \frac{1}{\rho} = \frac{d}{R \times A} \qquad \textit{equation 2}$$

## 3.9. Cell culture and evaluation of biocompatibility

Despite experiments throughout the different *Chapters* had different nature and goals, here I reported some general cell culture techniques and methodologies that have been kept consistent in the project.

### 3.9.1. Expansion and handling of C3H10

C3H10 mouse embryonic fibroblasts (ATCC® CCL-226TM) were cultured in growth media prepared with Dulbecco's Modified Eagle's Medium (DMEM) low glucose (Sigma-Aldrich) containing 10 v/v% foetal bovine serum (FBS) (Gibco® by Life Technologies) and 2 v/v% Penicillin Streptomycin (Pen-Strep) (Sigma Aldrich) at 37 ºC with 5 v/v% $CO_2$. Cells between passages 12 and 15 were used.

### 3.9.2. Sterilisation of substrates

Films described in *Chapter 5* and 3D scaffolds of *Chapters 6-8* were sterilised straight before use undergoing multiple cycles of incubation in 70 v/v% ethanol under UV light, followed by sterile deionised water, and finally incubated overnight in growth media for 24 hours.

### *3.9.3. Live/dead assay*

Cell viability was assessed using a live/dead assay implementing a solution of 2 µl/ml Ethidium Homodimer and 0.5 µl/ml Calcein (Cambridge Bioscience) in PBS. Solution was incubated at 37°C for 1 hour and three washings with PBS followed. Samples were kept at 37°C until imaged.

Imaging was performed with a Leica SP8 scanning confocal microscope (Leica Microsystems, Germany) using different objectives between 10x and 40x. For quantification a minimum of 3 pictures per experimental replicate were taken and subsequently analysed with ImageJ (freely available from www.nih.gov). Cell viability was defined as the ratio of live cells over the total cell number (%), while the alive cell density was obtained as ratio between live and total cells normalised by the ROI area (cells/mm$^2$).

In the case of imaging of 3D scaffolds (i.e. *Chapters 6-8*), pictures were obtained as resultant z-projection of z-stack with different z-step and depth of penetration from the surface. Specifically, z-step size of 10 µm or 25 µm and depths of 100 µm or 125 µm were used, respectively for *Chapters 7* and *8*.

### *3.9.4. DAPI/Phalloidin fluorescent staining*

Cell spreading was evaluated using cytofluorescent staining. After three washing in PBS, samples were fixed in 4 w/v% paraformaldehyde for 60 minutes at room temperature. Following three more washings in PBS, samples were incubated with in a working dye solution prepared with 1 µl/ml phalloidin (Santa Cruz Technology, USA) and 4',6-Diamidine-2'-phenylindoledihydrochloride (DAPI, 1 mg/ml, Sigma-Aldrich, Ireland), to highlight filamentous actin (f-actin) of the cell cytoskeleton and cell nuclei respectively. Micrographs were obtained using either Leica SP8 scanning confocal microscope (Leica Microsystems, Germany) or an Olympus IX83 epifluorescent microscope (Olympus, Germany).

### *3.9.5. AlamarBlue™ metabolic assay*

To evaluate cell condition, I performed a standard AlamarBlue™ metabolic assay. After removal of cell culture media and one washing with PBS, AlamarBlue™ working solution

was added to the culture, with different incubation time and working solutions were adopted for monolayer and 3D cultures as the higher cell number typical of 3D culture could led to saturation of AlamarBlue™ reduction. Specifically, incubation of 3 hours and a working solution constituted by fresh media and 10 v/v% were used for monolayer cultures, while incubation time was reduced to 1 hour and the concentration of AlamarBlue™ reagent in the working solution was increased to 20 v/v% for 3D cultures. Media was gently mixed with pipette and incubated for 1 hour; afterwards the media was mixed again and moved to 96-well plate for analysis.

#### *3.9.6. Picogreen™ assay*

Biochemical assay was used to identify DNA content using a Picogreen™ assay. At specific timepoints, samples were washed in PBS and frozen at -80°C until the moment of the assay when a 18 hours digestion in papain enzymatic solution took place. Analysis was then performed accordingly to the provided standard protocol.

### *3.10. Statistical analysis*

Statistical analysis was performed using GraphPad Prism 9 (GraphPad Software, USA). Where appropriate a one-way or two-way analysis of variance (ANOVA) followed by Tukey's multiple comparison. If not otherwise specified, results are presented as mean ± standard deviation and differences are considered as statistically significant for $p < 0.05$.

# 4. Beyond chemistry: Tailoring Stiffness and Microarchitecture to engineer highly sensitive biphasic elastomeric piezoresistive sensors

A significant amount of this *Chapter* has been published previously in:

**Solazzo, M.,** Hartzell L., O'Farrell C., Monaghan, M. G. Beyond chemistry: Tailoring Stiffness and Microarchitecture to engineer highly sensitive biphasic elastomeric piezoresistive sensors. *ACS Applied Materials & Interfaces*, 14, 17, 19265–19277 (2022).

## *4.1. Abstract*

Carbon-based nanoparticles and conductive polymers are two classes of materials widely used in the production of three-dimensional (3D) piezoresistive sensors. One conductive polymer - poly(*3,4*-ethylenedioxythiophene):polystyrene sulfonate (PEDOT:PSS) has excellent stability and conductivity yet is limited in its application as a sensor, often existing upon a base, limiting its performance and potential. Despite much progress in the field of materials chemistry and polymer synthesis, one aspect I consider to be unexplored is the impact that microstructure and stiffnesses may have on the sensitivity of 3D sensors. In this study, I report a strategy for fabricating biphasic electroactive sponges (EAS) that combine 3D porous PEDOT:PSS scaffolds possessing either an isotropic or anisotropic microarchitecture, infused with insulating elastomeric fillers of varying stiffness. When characterising the electromechanical behaviour of these EAS, a higher stiffness yields a higher strain gauge factor, with values as high as 387 for an isotropic microarchitecture infused with a stiff elastomer. The approach I describe is cost-effective and extremely versatile, by which one can fabricate piezoresistive sensors with adaptable sensitivity ranges and excellent high strain gauge factor with the underlying microarchitecture and insulant stiffness dictating this performance.

## *4.2. Introduction*

Wearable sensor technology has seen dramatic growth in demand in recent years, with a range of applications as affordable and personalised diagnostic and continuous monitoring tools within medicine,[293,294] fitness, as well as within robotics for electronic skin [295] and tactile sensing.[296] Such sensors can aid in early detection of acute health deterioration in a hospital setting [297] or provide long-term monitoring in a patient's home.[298] A wide range of technologies have been developed and implemented, among which piezoresistive sensors are frequently used due to their high sensitivity, simple device structure and easy to interpret readout.[299]

Mechanical deformation of a piezoresistive material, emanating from applied stress or strain, causes transduction of the mechanical force into a change in piezoresistivity and material conductivity, known as the piezoresistive effect.[300] The performance of a piezoresistive material as a wearable strain sensor is based on certain criteria, including low hysteresis, high sensitivity, compressibility and electromechanical stability under repeated dynamic loading conditions.[301,302] Piezoresistive materials can also be used within pressure sensors, which have applications in detection of subtle pressures such as blood flow or "touch" in the context of, for example - brain machine interfaces.[303]

Conductive polymers have emerged as a candidate sensor material [4] with chemical, mechanical and electrical properties that can be tailored towards specific applications by virtue of the method by which they are manufactured as well as through various treatments.[6,304] Poly(*3,4*-ethylenedioxythiophene):polystyrene sulfonate (PEDOT:PSS) is a conjugated polymer with high chemical and environmental stability,[305,306] which has already seen many applications within the field of wearable sensors.[307-312] It consists of the highly conductive PEDOT combined with insulating PSS, which acts as a counterion to PEDOT to stabilise its chemical properties. When combined they exist as a semiconductive compound with piezoresistive properties which could be utilised for the purpose of a strain or pressure piezoresistive sensor. A drawback to PEDOT:PSS lies in its relatively brittle nature as it can

only be stretched to about 10% without plastic deformation,[313] and its proneness for delamination and redispersion in aqueous or humid environments. Crosslinking is a common method used in the context of enhancing stability of PEDOT:PSS in aqueous environments, with glycidoxipropyl-trimethoxysilane (GOPS) being an extensively used option.[30,306]

A balance between stretchability, sensitivity and linearity is a common challenge in piezoresistive sensors, with stretchability limiting sensitivity in both low strain or pressure ranges as well as causing increased mechanical and electrical hysteresis through the viscoelastic properties of polymers, which limits the use of piezoresistive sensors in the realm of dynamic high-frequency measurements. A porous or foam 3D structure can have improved stretchability and linearity of both the mechanical and electrical behaviour [314] which increases their applicability for dynamic loading conditions. Porous piezoresistive sensors to optimise sensor behaviour across a wide range of stresses and strains have therefore frequently been explored in recent years.[308,315-318] The use of optimised microstructures such as pyramids or biomimetic textures have been shown to enhance sensor performance further.[295,296,316] Three-dimensional porous PEDOT:PSS scaffolds can be produced through lyophilisation, during which pore size and alignment can be controlled through predefined parameters.[306] Although lyophilised PEDOT:PSS scaffolds are previously reported,[306] their electromechanical response and the applicability for piezoresistive sensor applications have never been explored.

One common approach for the fabrication of piezoresistive sensors consists in the introduction of conductive particles in an insulating polymer matrix and attaining conductive composites. Among such insulating matrices, polydimethylsiloxane (PDMS) is a silicone rubber elastomer unique in its high flexibility, along with high compressibility, wide operational temperature range and non-toxicity.[319] It can easily be fabricated in a laboratory and is one of the most frequently incorporated materials in flexible sensors, where its elastic behaviour offers the benefit of low mechanical drift and low hysteresis under cyclic loading.[320] When combined with conductive infills such as graphene,[321,322] carbon

nanotubes (CNTs),[315,323] carbon black,[324] or silver nanoparticles,[325] they form highly conductive nanocomposites with applications as piezoresistive sensors. Moreover, PDMS can be found in different chemical forms and this makes it possible to achieve final compounds with diverse mechanical properties by simple combination of these forms at specific ratios.[326]

While many reports describe piezoelectric materials with remarkably high sensitivity due to their chemistry, the impact of microarchitecture and the material stiffness on the performance of piezoresistive materials has not been investigated until recently- mostly limited to analysis of the size of the pores in foam-like structures [327] and rarely to the orientation of the pores.[328]

Here, I describe the electromechanical behaviour of porous, microstructured PEDOT:PSS-based electroactive sponges (EAS) and demonstrate their application as piezoresistive sensors for health monitoring. After predesigning EAS to possess either isotropic or aligned architectures I embedded them within PDMS insulant elastomeric matrices characterised of varying stiffnesses (**Figure 4-1.A**). This strategy facilitates biphasic EAS of different mechanical properties while maintaining the original morphology of the PEDOT:PSS-based scaffolds. These structures were introduced as sensor modules within a prototype sensor (**Figure 4-1.B**), where I demonstrate that the material has the capability to measure a variety of physiological signals, including swallowing, muscle tensing and limb movements including finger and knee bending (**Figure 4-1.C**).

## *4.1. Experimental methods*

### *4.1.1. Fabrication of 3D PEDOT:PSS sponges.*

Three different freezing temperature were adopted to influence the shape and size of the porous architecture, namely -20/-40/- 80 °C.

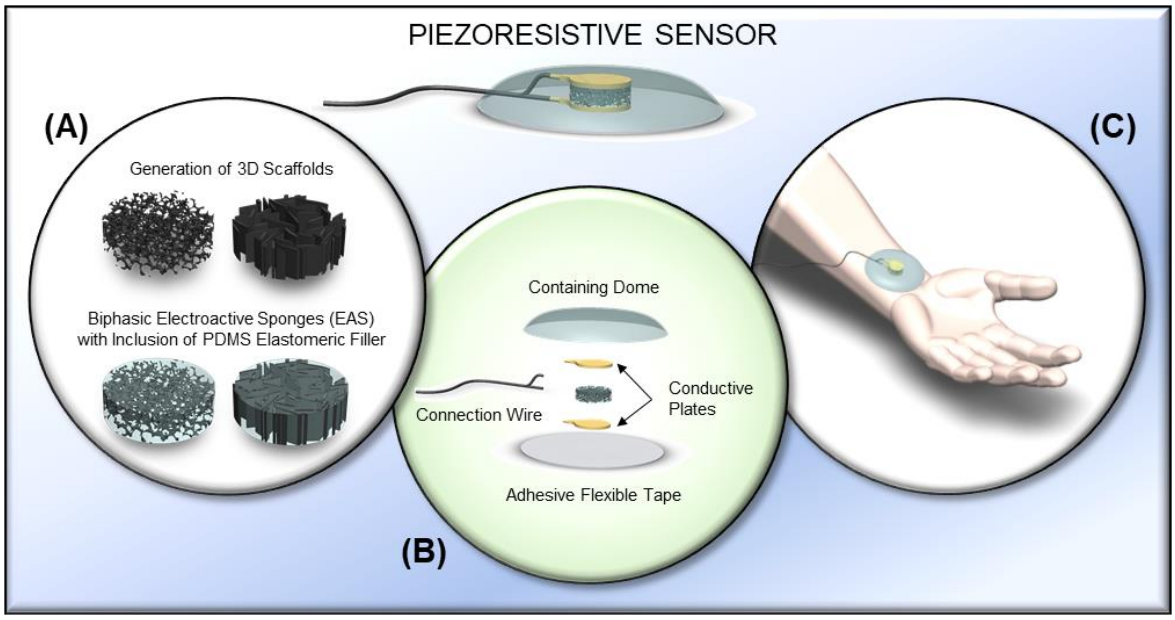


***Figure 4-1**. Conceptualisation of the PDMS-embedded PEDOT:PSS-based piezoresistive sensor. **(A)** Illustrations of the generation of 3D PEDOT:PSS-GOPS scaffolds with both isotropic and aligned microarchitecture; followed by the inclusion of a PDMS elastomeric filler to generate a biphasic EAS. **(B)** Schematic of the assembly of the piezoresistive sensor showing the components: a containing dome, two conductive plates, one EAS, an adhesive flexible tape and a connection wire. **(C)** Simulation of the application of the piezoresistive sensor to a body part for recording of physiological signals.*

### *4.1.2. Morphology of 3D PEDOT:PSS sponges.*

X-ray microtomography (µCT, Scanco, Switzerland) was employed to allow for a macroscopic 3D reconstruction of scaffold morphology.

### *4.1.3. Infusion of elastomeric fillers.*

Two formulations of polydimethylsiloxane (PDMS, Sylgard® 184 and Sylgard® 527) were combined to achieve different stiffness. Both products were individually prepared according to manufacturer instruction, whereby a “stiff” elastomer was obtained by pure Sylgard® 184, while a “soft” one was achieved by mixing the two products with a 1:5 ratio (184:527). PEDOT:PSS-GOPS sponges were then placed into standard plastic mould and PDMS was added up to fully cover the scaffolds and multiple cycles of vacuum were performed to allow for the elastomers to infiltrate throughout the whole scaffold. Constructs were cured at 60 °C for two hours to allow for PDMS polymerisation and afterwards they were embedded into an agarose solution to allow easier cutting into thin slices of desired thickness ranging from 0.5 to 3 mm via a vibratome (VT 1200S, Leica, Germany). Slices

were finally cut with standard cylindrical biopsy punches to obtain thin circular samples with fixed diameters of 5, 6 or 8 mm.

#### *4.1.4. Investigation into the electromechanical response.*

To perform the electromechanical analysis, I developed a custom-made setup similar to what has been reported elsewhere.[322] A Zwick Roell® twin column universal testing machine (ZO50, Zwick/Roell) with a 10 N load cell was used to apply static or cyclic strain to the EAS while a sourcemeter Keithley 2400 (Tektronix, USA), controlled via python software was used to measure the electrical resistance of the EAS as a function of time (**Figure 4-3.C**).

The EAS was placed on the bottom electrode, while the top platen was gradually lowered closer to the sample in increments of 10 μm using the machine's automatic adjustment feature until full surface contact was established. EAS with 2 mm thickness were used for the analysis.

A uniaxial cyclic and a ramp compression test were performed in a consecutive sequence, with a break of 60 seconds in between them. The testing sequence is represented by strain variation over time during the test and can be seen in **Figure S2**. The cyclic test consisted of 100 cycles applied to the sample between 1% and 2% strain, at a compression rate of 1% $s^{-1}$, or 0.5 Hz. The ramp test consisted of a single cycle where compressive strain was applied up to 30% of the sample height, at a compression rate of 0.1% $s^{-1}$. During the 60-second hold period between tests, strain returned to the pre-load value.

Subsequently, recordings from both the Zwick and Keithley were transferred to the control centre and the two datasets were merged at corresponding time intervals by using specialised python code to align the starting timestamp of both systems. Finally, any remaining electrical noise was filtered in Matlab® using a built-in *hampel* filter followed by a 3$^{rd}$ order *Savizky-Golay* smoothing filter and a 2$^{nd}$ order low-pass *Butterworth* filter.

A series of custom-made Matlab® scripts were written so to extrapolate multiple

measurements from this single cyclic-ramp combined test.

From the analysis of the cyclic phase, the dynamic strain-dependent and stress-dependent gauge factor, the mechanical hysteresis, the variances of the stiffness and of the sensitivity throughout the cycles were extrapolated.

From the ramp phase it was possible to define mechanical parameters such as TOE region range, TOE region stiffness, Young's Modulus and, where present, Yield Strain. The scripts allowed to identify three regions in the electro-mechanical signals and to derive measurements of the ranges of these regions in terms of strain [%] and stress [kPa] and the corresponding strain- and stress-dependent gauge factors.

#### *4.1.5. Sensor fabrication and testing.*

To investigate the sensor capability to detect and monitor physiological signals a proof-of-concept sensor was built and tested on a range of physiological motions such as finger and knee bending, swallowing, speech recognition, and muscle tensing. The sensor was fabricated taking inspiration from previously described methods.[318,329] A schematic of the components is reported in **Figure 4-1.B**, while the assembly sequence can be observed in **Figure S5** with two adhesive copper tapes having been connected to two wires while working as electrodes and being connected to the two sides of an *isotropic soft* piezoresistive insert in a sandwich-like structure. **Figure 4-6** shows a representation of this prototype. Once the sensor was applied to the skin through the use of a flexible adhesive tape, the electrical response was continuously monitored using the Keithley 2400 sourcemeter.

### *4.2. Results and discussion*

#### *4.2.1. Fabrication of biphasic electroactive sponges (EAS)*

Lyophilisation was employed to generate highly porous structures of PEDOT:PSS crosslinked using GOPS as reported previously.[306] This lyophilisation approach is a scalable process and facilitates constructs of different sizes and shape.

#### *4.2.1.1. Processing of PEDOT:PSS-GOPS scaffolds and morphological analysis*

Various microstructures have been proposed to enhance sensor performance, such as pinnate-veined pores created through solvent crystas due to freezing. [330] or biomimetically textured materials.[329] One previous study has looked to improve mechanical recovery of the foam under dynamic compression by fabricating an aligned CNT-thermoplastic PU material through directional freeze-drying, which exhibited excellent linear recovery in comparison to a disordered foam.[328]

In this study, I aimed to investigate to what extent the microarchitecture of an electroconductive sensor can influence the overall piezoresistive response. In this respect, I compared PEDOT:PSS-GOPS sponges that were designed to possess an isotropic or anisotropic structure. In our previous work [306], the adoption of standard plastic cell culture well plate and of custom-made moulds (**Figure S1**) yielded the fabrication of both isotropic and anisotropic architectures (**Figure 4-2**).

We first investigated the generation of isotropic sponges with the most homogeneous porosity and circularity of the pores, for a relevant comparison with the highly aligned microarchitecture typical of the anisotropic scaffolds. It is well established that freezing temperature ($T_f$) affects the pore microarchitecture; in particular, the wider the difference between the temperature of the material and the $T_f$ the faster the nucleation rate of the ice crystals and the slower the heat transfer from the nucleation site, ultimately causing smaller crystals and a reduction in pore size.[331] In addition, general cooling condition - such as cooling rate - determine the shape of the ice crystals, that can be described by their circularity and eccentricity.[332]

Here, I applied three different $T_f$ to produce PEDOT:PSS-GOPS scaffolds, namely -20/-40/-80 ºC. From an initial macroscale observation using microCT (**Figure 4-2.A**), no major pore differences were appreciable between the three processing conditions; however, SEM micrographs detected a more irregular porous architecture in the -80 ºC group (**Figure 4-2.B**). This was confirmed by a quantitative analysis on sectioned samples, through which a series of parameters were determined (**Figure 4-2.C**). Specifically, a statistically significant

increase in pore size was present at a $T_f$ of -20 ºC; average pore diameter of 153 ± 6 µm when compared with the 137 ± 7 µm and 135 ± 13 µm of the -40 ºC and -80 ºC, respectively (**Figure 4-2.D**). Scaffolds processed at -80 ºC showed significantly higher variance of pore diameter, lower circularity and higher eccentricity compared to the samples prepared with the other two conditions (**Figure 4-2.E-G**). Taken together, this data highlights that the microarchitecture was less homogeneous in pore diameter across the structures when prepared with a $T_f$ -80°C, with pores characterised by a more elongated and as well more irregular profile. In agreement with previous works [333], both findings are characteristic of quenching (i.e. rapid-freezing) and it could be concluded that at $T_f$ -80 ºC the freezing process occurred at dramatically higher cooling rate causing a preferential direction in the heat transfer and the subsequent generation of a more heterogeneous pore size distribution as well as in a preferential direction, despite the use of a standard mould.

From this I can conclude that both -20 and -40 ºC generated more isotropic samples, with -40 ºC also yielding a smaller pore size. Because of the high regularity of the pore geometry and the smaller pore size, the $T_f$ -40 ºC was identified as the most suitable candidate for a comparison with the aligned scaffolds and it was adopted for all subsequent experiments.

#### *4.2.1.2. Incorporation of PDMS elastomeric matrices generates biphasic EAS*

Three-dimensional scaffolds generated with PEDOT:PSS-GOPS have already been shown to be stable, insomuch that they have been used in wet applications such as tissue engineering.[9,306] However, because this material is non elastomeric and fragile,[313] repetitive mechanical deformation - typical of physiological applications - can eventually alter and deteriorate their stuctures. Such a change in morphology drives a modification of the piezoresistivity over time and therefore it is not compatibile with the development of long-lasting piezoresistive sensors.

Others have reported the incorporation of an elastomeric component at the moment of material processing as its presence can allow for more suitable mechanical properties.[323]

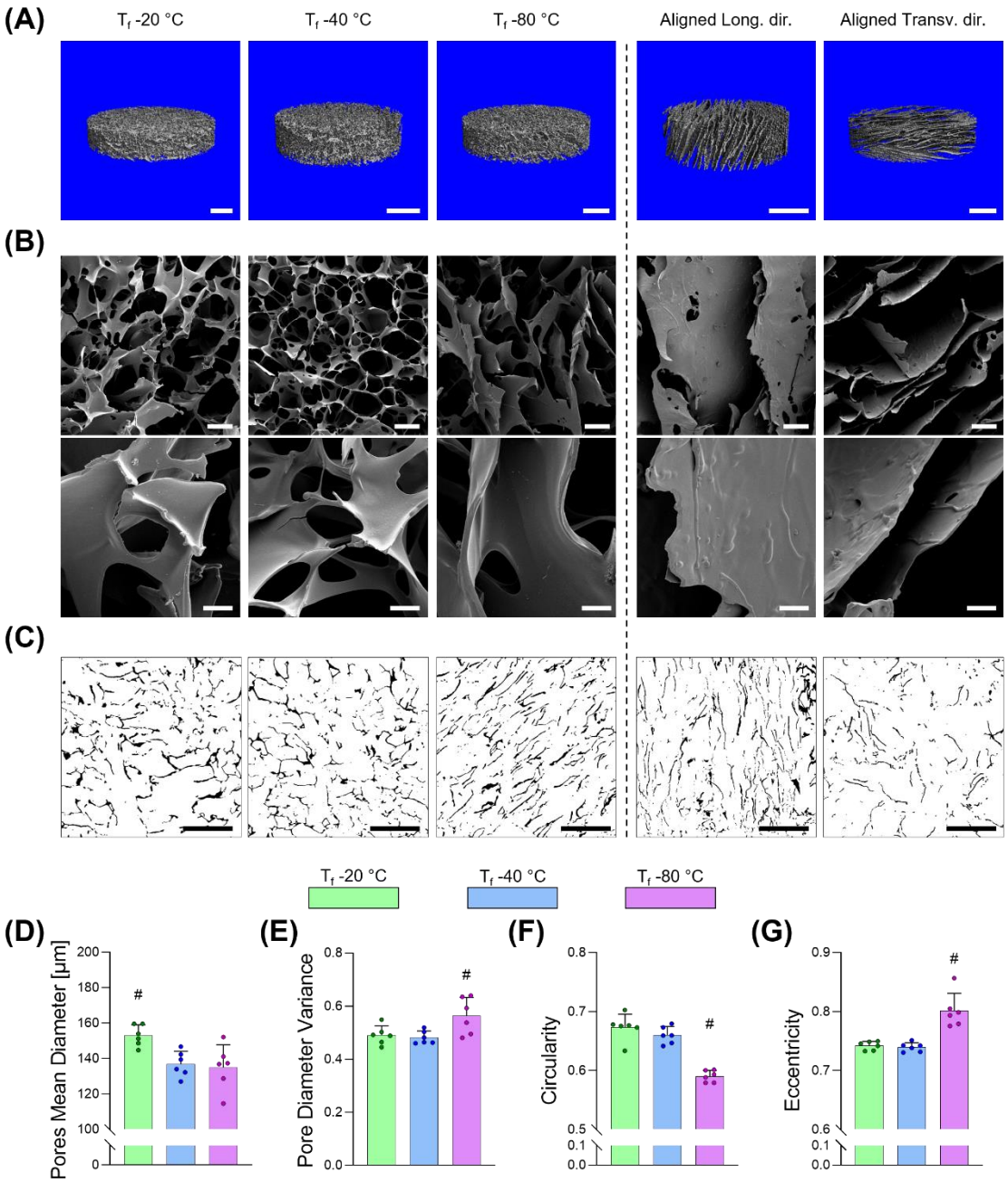


***Figure 4-2**. Morphological characterisation of EAS. **(A-C)** Image analysis of isotropic samples processed at different Freezing Temperatures ($T_f$), namely -20 / -40 /-80 ºC, and aligned samples observed along the longitudinal and the transversal directions with different techniques: **(A)** microCT, **(B)** SEM micrographs at different magnifications, **(C)** sliced agarose embedded scaffolds. **(D-G)** Quantitative analysis of the effect of $T_f$ on the size and shape of isotropic samples (n=3 per direction per sample): **(D)** Pores Mean Diameter, **(E)** Pores Mean Variance, **(F)** Circularity and **(G)** Eccentricity. Scale bars: A = 1 mm; B i = 100 µm; B ii = 20 µm; C = 500 µm. Bar graphs demonstrate the mean with error bars representing standard deviation. Data values are presented as associated points. # represents statistical significance ($p<0.05$) between the indicated group and all other groups using one-way ANOVA with Tukey's post-hoc test.*

However, such approaches can impact the electrical properties of the conductive polymers and they do not allow for the processing of different microarchitectures with the same simplicity as freeze-drying does. One common approach to incorporate a conductive

material and an elastomer is the functionalisation of a porous matrix with a thin coating of a conductive polymer or nanoparticles; an example being a sensor described by Yang et al. [295] who designed a porous PDMS containing a micro-pyramid structure adhered to and spaced upon a soft EcoFlex matrix and coated with AgNW.

Here I describe an alternative strategy, whereby I investigated the combination of an elastomeric matrix with conductive PEDOT:PSS scaffolds (**Figure 4-3.A**). I chose standard PDMS and engineered two contrasting stiffnesses by combining Sylgard 184 and Sylgard 527 at different ratios.[326] Pure Sylgard 184 to generate a *stiff* elastormeric matrix and a mix of 184 and 527 at ratio 1:5 for the *soft* one. This process can be expanded by adjusting the ratio between the two compounds in order to obtain stiffnesses between 50 kPa and 1.5 MPa.[326] Once the PEDOT:PSS-GOPS scaffold and the PDMS matrix were combined, they were fashioned into a cylindrical morphology using standard 5 mm biopsy punches and cut in slices ranging from the hundreds of µm up to 3 mm so as to suit diverse sensor designs (**Figure 4-3.B).**

We have previously reported this range of PEDOT:PSS-GOPS scaffolds with values of porosity as high as 95%.[306] With the addition of the PDMS infusion step, I ensured that all empty space within the scaffold porous structure were perfused by this insulant elastomer. The final product is a construct primarily composed of the PDMS insulant material that maintains the original electroconductive characteristic of the PEDOT:PSS-GOPS scaffold within.

### *4.2.2. Piezoresistivity analysis in ramp condition*

Electromechanical analysis of the EAS under a single compression cycle is reported in **Figure 4-3.C** and **S2**. From the stress-strain curves one can immediately observe the diverse mechanical responses of these constructs (**Figure 4-3.D** and **S3**).

Analysis of the strain extension of the toe region reveals a significant increase for the *isotropic-soft* group compared to all others (**Figure 4-3.E**). However, the more intriguing properties are those evidenced by the Young's moduli in both the toe and the linear regions

(**Figure 4-3.F,G**). As expected, the PEDOT:PSS-GOPS scaffolds with *noPDMS* exhibited significantly softer structures, with the aligned geometry showing less rigidity than the isotropic one, in accordance with our previous findings.[306] For the Young's moduli of both toe and elastic regions, a synergistic behaviour of the scaffold and the elastomeric matrix was evident, showing stiffer responses for the biphasic EAS groups than for the PDMS alone. In addition, no significant differences were found between isotropic or aligned samples when *stiff* or *soft* PDMS was used.

As shown in **Figure 4-3.H**, paying attention to the yield strain highlights that the introduction of a PDMS matrix increases the range of elastic deformation that can be applied to the EAS, shifting from approximately 9.6% up to beyond 30% for the isotropic group and from 14% up to 23.8% for the anisotropic one. This is an important finding, demonstrating that the mechanical behaviour of the elastomeric materials constituting the matrix phase dominates the mechanical behaviour.

Results of the piezoresistive characterisation when subjected to a ramp phase are reported in **Figure 4-4**. Undeformed biphasic EAS exhibit conductivity values that do not differ within the *isotropic* groups, while a decrease was observed for the *aligned stiff* compared to the *aligned noPDMS* (**Figure S4**). **Figure 4-4.A** and **4-4.B** illustrate the profiles of the average relative change in resistance over strain, whereby it is evident that in both isotropic and aligned conformations, the *stiff* matrices provide a more sudden response rather than the *soft* ones that are more similar to the *noPDMS* groups. As reported in other studies,[327] I identified three strain regions in which the gauge factor could be assumed to be constant, namely a "high" region with the biggest resistance variation, a "medium" region where a variation could still be perceived and finally a "low" region in which the variation is almost negligible (**Figure 4-4.C**).

**Figure 4-4.D-G** illustrates a series of key parameters that were quantified from the analysis of the curves, where the high sensitivity region was characterised by its extension range as maximum strain and maximum stress, as well as by the relative strain-dependent and stress-dependent gauge factors. *Soft* and *noPDMS* groups highlighted a wider range

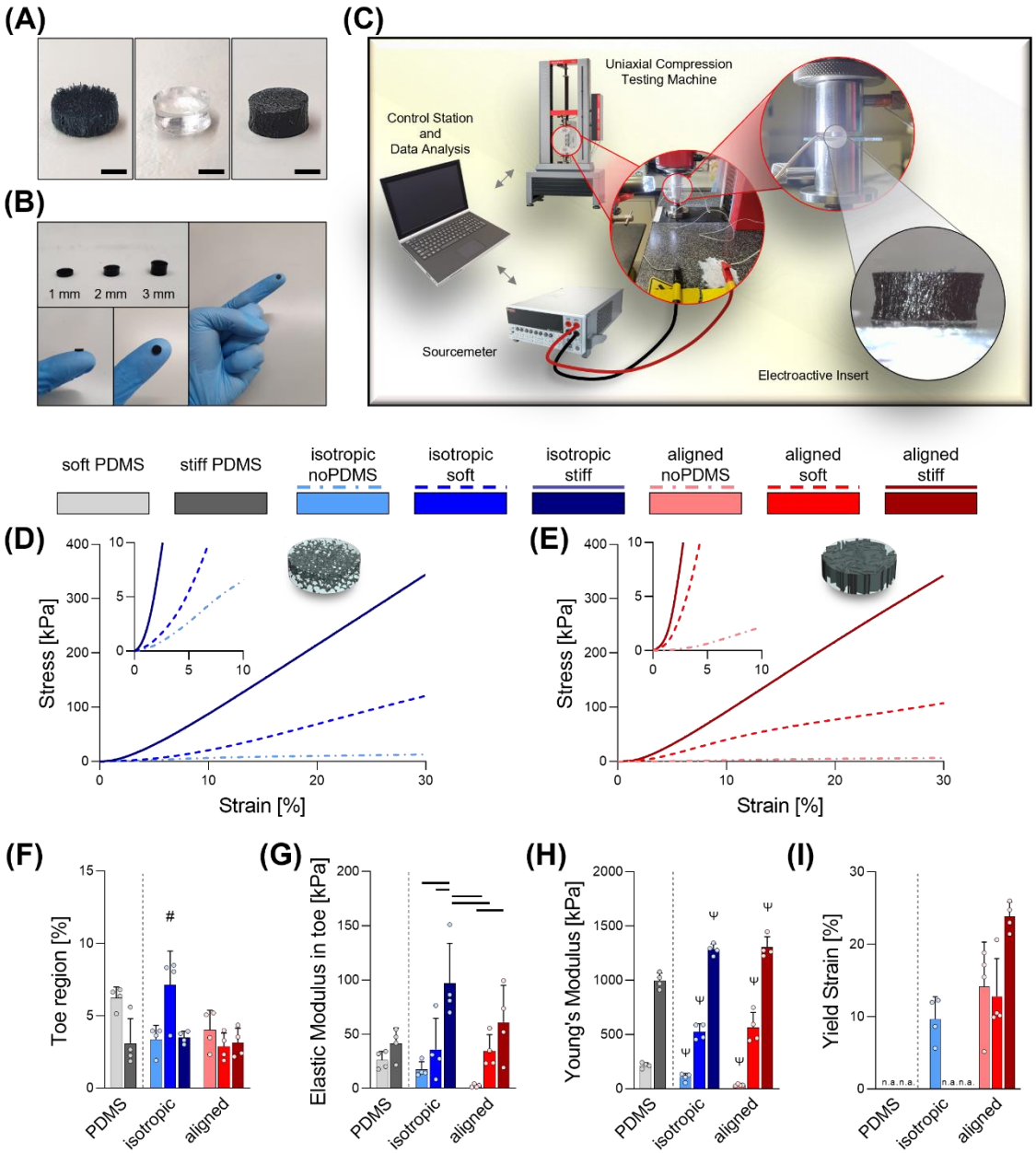


***Figure 4-3**. Manufacturing and testing of biphasic EAS. **(A)** Pictures of a PEDOT:PSS-GOPS scaffold (i), a pure PDMS sample (ii) and a biphasic EAS (iii). **(B)** Picture of three biphasic EAS cut at different thicknesses (i.e. 1 / 2 / 3 mm) and pictures of a 1 mm thick sample handled by the user. **(C)** Schematic of the piezoresistivity testing setup . **(D-E)** Mean stress-strain curves for scaffolds and EAS embedded with both soft and stiff elastomers, with isotropic **(D)** and aligned morphology **(E)**. Insets show details of the regions between 0-10 kPa stress and 0-10% strain. **(F-I)** Quantification of different mechanical parameters (n=4): **(F)** extension of the toe region , **(G)** Elastic Modulus of the toe region, **(H)** Young's Modulus and **(I)** Yield Strain, where "n.a.„ indicates that the yield strain was not reached in the range of deformation applied in the test. Scale bars: A = 1 mm. Bar graphs demonstrate the mean with error bars representing standard deviation. Data values are presented as associated points. PDMS-only groups were not included in the statistical analysis. Line represents statistical significance ($p<0.05$) between indicated groups, # represents statistical significance ($p<0.05$) between the indicated group and all other groups, ψ represents statistical significance ($p<0.05$) between the indicated group and all other groups excluded the one with same stiffness. Statistical analysis was performed using two-way ANOVA with Tukey's post-hoc test*

of deformation, while a significant increase between *aligned* or *isotropic* geometries was reported within the *soft* groups. The strain-dependent gauge factor followed an opposite

response and the highest gauge factors were reported for the *isotropic stiff* and the *aligned stiff* groups (387.8 ± 53.2 and 257 ± 30.4 respectively). The maximum stress range detected in this region were consistent among most of the groups tested, with the *aligned no-PMDS* condition showing a significant increase compared to the *aligned soft* group. As for the analysis of the strain, the stress-dependent gauge factor decreased when the stress limit increased. The *aligned noPDMS* reached values as high as 37 ± 16.4 $kPa^{-1}$, significantly higher than all other groups which reported sensitivities between 3.3 and 10.6 $kPa^{-1}$.

In **Figure 4-4.H-M**, the same parameters were quantified for the medium sensitivity regions where trends similar to the high sensitivity region were observed. The strain-dependent gauge factor showed an increasing trend with the augmented stiffness of the EAS, reaching values of 10.3 ± 4 and 15 ± 6.3 for the *isotropic stiff* and *aligned stiff* groups respectively. As for the high sensitivity region, the highest stress-dependent gauge factor was obtained for the *aligned noPDMS* group with 0.85 ± 0.59 $kPa^{-1}$.

Most works on compressive sensors report a significantly inferior strain-related gauge factor such as 26.07 for a polyurethane-based cracked cellulose silver nanowire (strain range 0-0.6%) [334] and 2.1 for a graphene oxide/polypyrrole polyurethane sponge (strain range 0-40%) [318]. Few reports describe strain-dependent sensitivities in this magnitude range,[327] with the only exception being that of a graphene-putty sensor.[335] However, it is important to consider that the biphasic EAS I am presenting here has a reduced range of deformation in the high sensitivity region, with potential limitations on its applications. Our work represents a significant development for the consideration of PEDOT:PSS within a compressive sensor. To date, PEDOT:PSS based materials have been successfully employed for their piezoresistive properties, but primarily as a coating, with the examples of the PDMS-based pressure sensor with micro-pyramid array structure and a PEDOT:PSS/polyurethane coating produced by Chong et al. [336]; and the PEDOT:PSS/Melamine sponge produced via dip-coating and freeze-drying procedure by Ding et al. [308]

The presence of an insulant elastomeric filler does not hinder the electrical conductivity

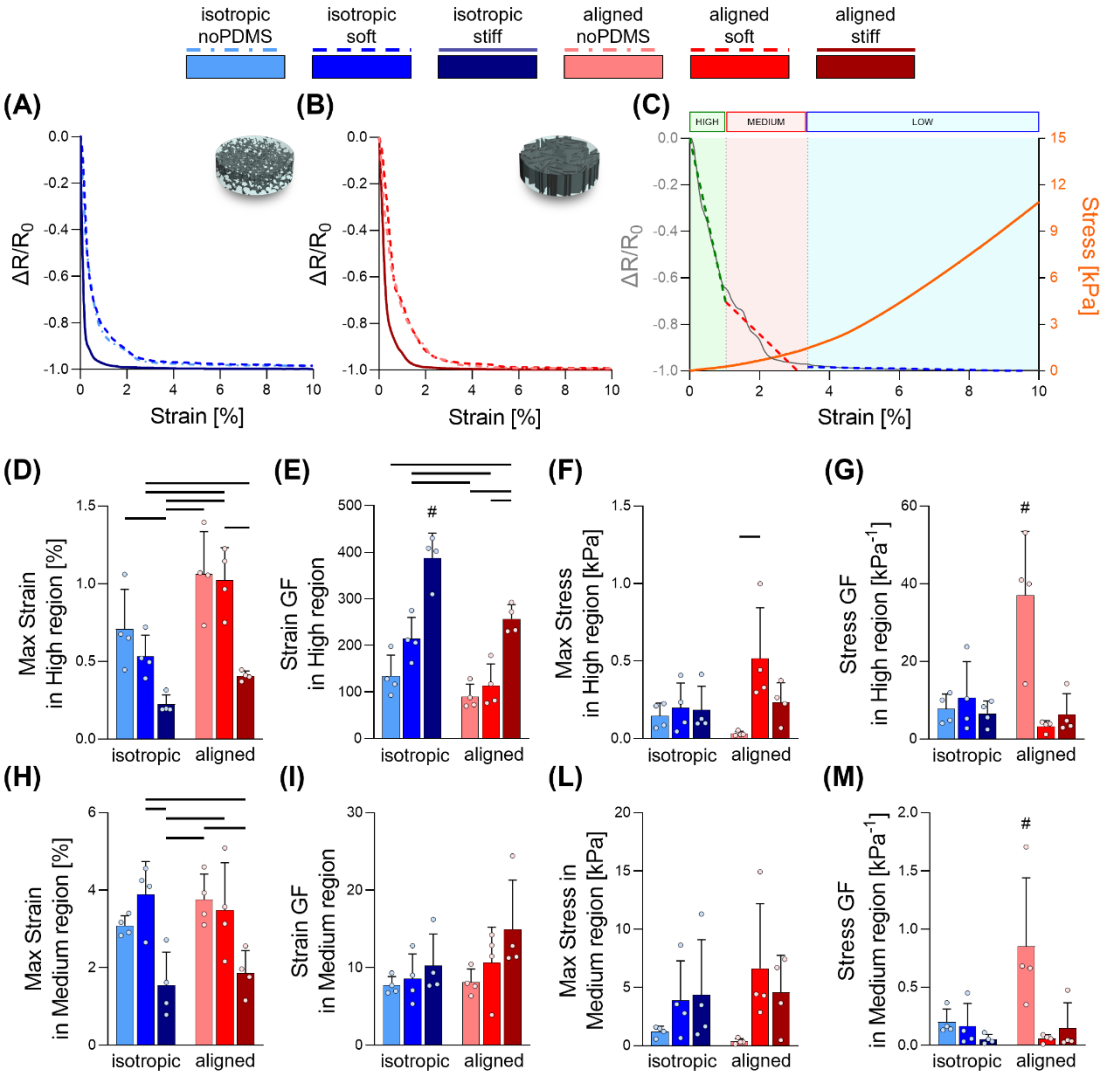


***Figure 4-4****. Analysis of the piezoresistive response of the biphasic EAS in the ramp phase.* ***(A-B)*** *Mean curves of the variation of resistivity over strain for scaffolds and biphasic EAS embedded with both soft and stiff elastomers with isotropic* ***(A)*** *and aligned morphology* ***(B)****.* ***(C)*** *Representative graph of the identification of High, Medium and Low output regions in the curves of the variation of resistivity over strain.* ***(D-M)*** *Quantification of different piezoresistivity parameters for the High region* ***(D-G)*** *and the Medium region* ***(H-M)*** *(n=4):* ***(D, H)*** *maximum strain in the region,* ***(E, I)*** *Strain gauge factor in the region,* ***(F,L)*** *maximum strain in the region and* ***(G, M)*** *Stress gauge factor in the region. Bar graphs demonstrate the mean with error bars representing standard deviation. Data values are presented as associated points. Line represents statistical significance (p<0.05) between indicated groups, # represents statistical significance (p<0.05) between the indicated group and all other groups. Statistical analysis was performed using two-way ANOVA with Tukey's post-hoc test.*

of the PEDOT:PSS-GOPS scaffold per se. On the contrary, the presence and stiffness of *PDMS* matrix profoundly impacts the mechanical properties of the materials and subsequently their piezoresistive response. Our analysis rationalises the effects that microarchitecture and stiffness can have on the overall performance of a piezoresistive sensor. Because of its lower stiffness together with a comparable extension of the high and medium sensitivity regions, the *aligned noPDMS* group underwent a significant smaller

increase in stress ultimately yielding the highest stress-dependent gauge factor. It is reasonable to declare that for a compressive porous sensor - considering a constant strain range - the lower the stiffness of the material the higher the output in terms of resistance variance will be. However, such a signal will be saturated for very low stress values. Further information can be gathered from the comparison between the *isotropic* and the *aligned* microstructure of the electroconductive scaffolds. In particular, *aligned* scaffolds allowed for a wider range of high sensitivity compared to *isotropic* ones, but also showing reduced strain-dependent gauge factor.

### *4.2.3. Piezoresistivity in dynamic condition*

Viscoelasticity is a common feature of polymeric materials, where the material exhibits a combination of elastic and viscous properties of mechanical recovery without energy dissipation and the capacity to dissipate energy respectively.[337] Under uniaxial strain, the combination of these two behaviours often results in hysteresis, where a difference in stress response occurs between the load and unload stage. Materials with viscoelastic properties respond to dynamic loading in a time-dependent manner, where both strain rate and amount of strain applied will have an impact on the mechanical behaviour.

Hysteresis error is a primary source of uncertainty in strain measurements [214] and a common challenge of stretchable polymer-based sensors as it also affects electrical properties which are closely correlated [299], producing a non-linear resistance output. Stress dissipation over dynamic cyclic loading is another property commonly seen in viscoelastic materials such as polymers, where a constant applied strain results in the materials gradually absorbing deformation and reducing stress to a final steady value.[300]

To understand the performance of the EAS under dynamic movements typical of muscoloskeletal movement, I examined the piezoresistive response during a cyclic regime and constant frequency. Mechanical and electrical variations were quantified in the range of deformation 1-2% and their variation over time was quantified (**Figure 4-5.A-C**).

Measurements in terms of the average data acquired in the last ten cycles of the tests

are reported in **Figure 4-5.D-G**. The applied deformation corresponded to very diverse average stress ranges: 0.07-0.44 kPa for *isotropic noPDMS*, 0.14-0.43 kPa for *isotropic soft,* 1.14-6.32 kPa for *isotropic stiff*, 0.006-0.11 kPa for *aligned noPDMS*, 0.38-2.31 kPa for *aligned soft*, 0.76-5.39 kPa for *aligned stiff*.

Compared to the results obtained in the ramp test, some differences can be observed in the quantification of the mechanical and piezoresistive properties, because of the adoption of a more limited strain range. In particular, it is evident that the *isotropic soft* group exhibited less rigid mechanics and how this lead to higher strain-dependent and stress-dependent gauge factors compared to the *isotropic stiff*. Significantly higher values for both these parameters were also reported for the *aligned noPDMS* group.

A significantly lower elastic hysteresis was present in the *aligned noPDMS* group, suggesting that a range of deformation as small as 2% already caused a less elastic response of the material.

I quantified the variation of stiffness and hysteresis over the cycles and similar trend for both *isotropic* and *aligned* geometries, with the two *noPDMS* groups showing significant higher reduction of mechanical properties over time. This confirmed how the presence of elastomeric matrices, either *soft* or *stiff*, paves the way for the use of biphasic EAS for long term applications. Indeed, this family of biphasic EAS can prevent the loss of mechanical stability and the consequent deteriation of piezoresistivity that would reduce of the sensor performance by structural failure. As it can be observed in **Figure 4-5.A**, the resistance variation is subjected to a quasi-linear drift over time. Such phenomenon is a common feature to several porous 3D sensors, and it has to be considered during the signal processing phase.[330,338] Finally, one has to take into account that in long-term cyclic applications, energy dissipation can be responsible for a variation in internal temperature of the sensor and consequently affect its piezoresistivity performance.[339,340] While the frequency, strain extension, and duration of the test here implemented do not provide a justification for this event to occurr, more challanging investigation will be required to define operational limits of this device, determine the conditions at which such event may incur,

and engineer a system for temperature compensation.

### *4.2.4. Validation of a piezoresistive sensor prototype*

A prototype piezoresistive sensor was manufactured following the sequence illustrated in **Figure S5**. This sensor could be applied directly to the skin or embedded within a

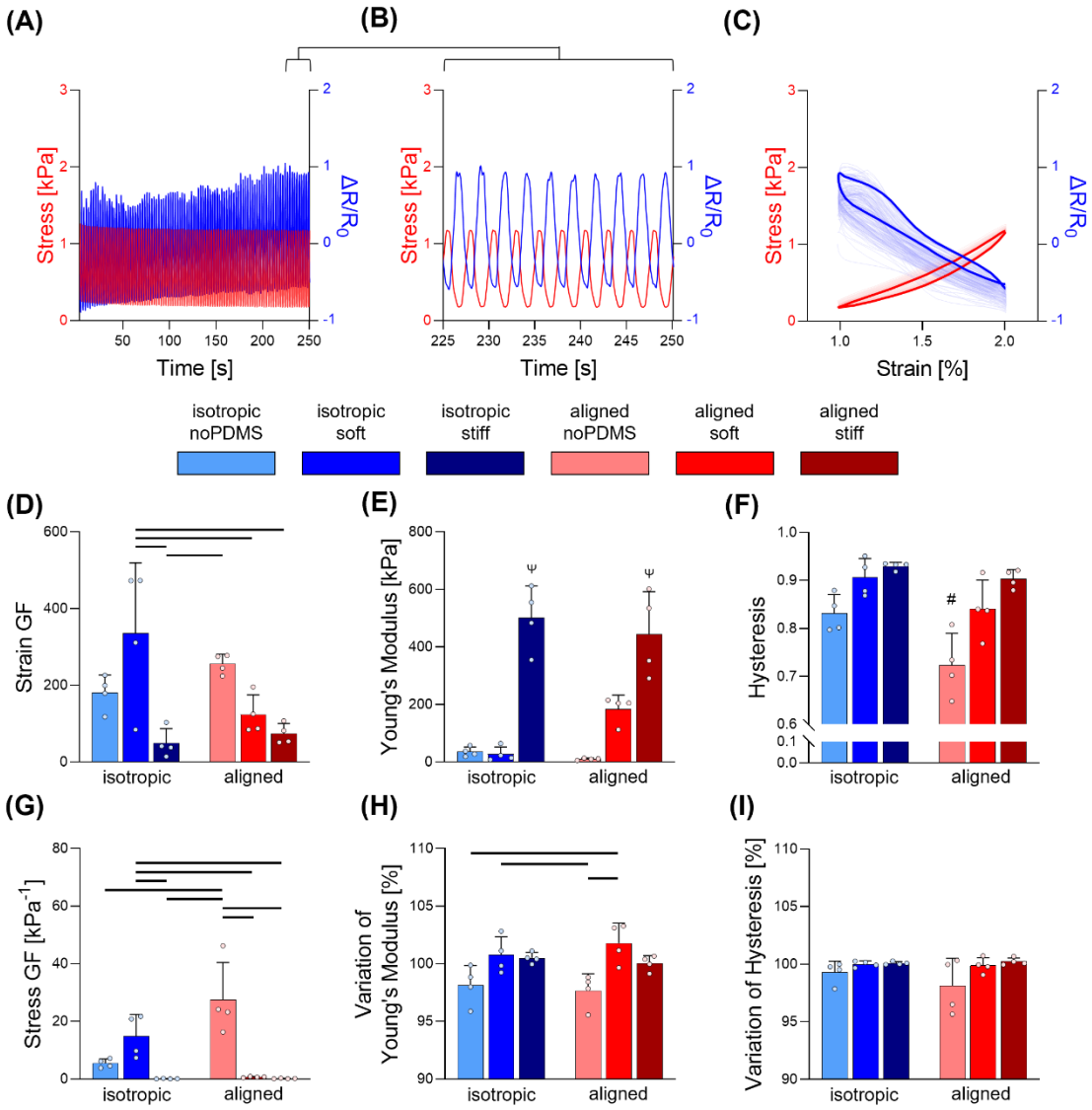


***Figure 4-5****. Analysis of the piezoresistive response of the biphasic EAS in the cyclic phase.* ***(A-C)*** *Representative curves of the stress and resistivity variation over time for the 100 cycles* ***(A)****, the last 10 cycles* ***(B)*** *and over strain* ***(C)****.* ***(D-I)*** *Quantification of different piezoresistivity parameters over the cyclic stimulation (n=4):* ***(D)*** *average Strain gauge factor of the last 10 cycles,* ***(E)*** *average Stress gauge factor of the last 10 cycles,* ***(F)*** *average Young's Modulus of the last 10 cycles,* ***(G)*** *average mechanical hysteresis of the last 10 cycles* ***(H)*** *variation of the average Young's Modulus between the cycles 21-30 and the last 10,* ***(I)*** *variation of the average Young's Modulus between the cycles 21-30 and the last 10. Bar graphs demonstrate the mean with error bars representing standard deviation. Data values are presented as associated points. Line represents statistical significance (p<0.05) between indicated groups, # represents statistical significance (p<0.05) between the indicated group and all other groups, ψ represents statistical significance (p<0.05) between the indicated group and all other groups excluded the one with same stiffness. Statistical analysis was performed using two-way ANOVA with Tukey's post-hoc test.*

standard bandage plaster (**Figure 4-6.A**). In this validation I focused on simple body movements such as finger and knee bending, swallowing and muscle tensing (**Figure 4-6.B-E**). Signals were detected with a sourcemeter and it was possible to observe clear repetitive patterns proper of each movement. With this approach, it would be possible to adopt any combination of microarchitecture and elastomer stiffness towards applications with known stress and strain range. Although two contrasting stiffnesses were investigated in this study, one could fine tune the mechanics of the matrix easily by varying the ratio between the two types of PDMS.

For the validation of this new family of biphasic EAS, I adopted PEDOT:PSS-GOPS scaffolds that were characterised by relatively high stiffness and low conductivity. Our group has previously demonstrated how both the mechanical and electrical properties of this

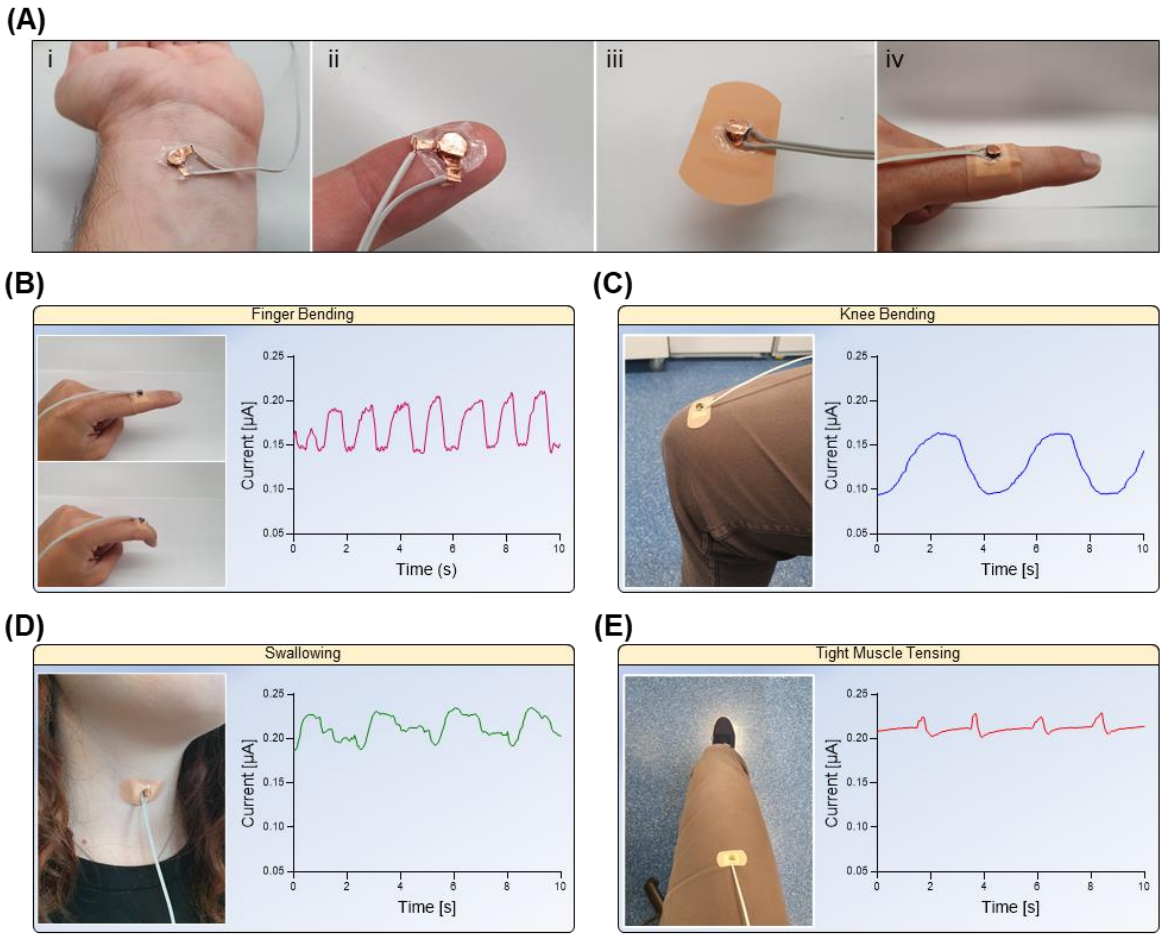


***Figure 4-6**. Fabrication of a piezoresistive sensor prototype. **(A)** Application of the sensor directly to the skin of the arm and to the tip of the finger (i/ii), or attached to a standard plaster and then applied to the skin (iii/iv). **(B-E)** Sensor Proof-of-Concept Signals: **(B)** finger bending, **(C)** knee bending, **(D)** swallowing and **(E)** thigh muscle tensing.*

material can be affected and ameliorated by crystallisation post-treatment with sulphuric acid [306] or how such properties can be influenced by the use of different crosslinker as poly(ethylene glycol)diglycidyl ether.[305] Such approaches could be used to modify this platform even further. The use of these materials as electroconductive scaffolds combined with a soft elastomer could lead to EAS characterised by wider high sensitivity strain range and possibly able to detect even lower stresses.

### *4.3. Conclusions*

In the development piezoresistive components for wearable sensors, conductive fillers such as graphene or silver nanowires are most frequently being used to achieve superior sensitivity, but they are associated with significant drawbacks such as high cost, toxicity and complex fabrication methods which limit their scalability and accessibility. PEDOT:PSS, on the other hand, is an intrinsically conductive polymer that can easily and safely be handled and processed in a laboratory and which exhibits piezoresistive properties. Also, as this compound is often provided as a dispersion in water, the morphology of the final constructs can be controlled by use of different freeze-drying parameters during fabrication.

Here I presented the fabrication of a range of PEDOT:PSS-based porous structures and their combination with a PDMS elastomer for the obtainment of EAS. When benchmarking our approach against previous reports on the use of conductive polymers as coatings upon a porous material or mixed as a secondary component in a slurry containing an elastomer, I instead fabricate three-dimensional PEDOT:PSS-GOPS scaffolds and afterwards infuse with elastomer to obtain biphasic EAS. Mechanical and piezoresistive properties of these EAS were characterised, providing detailed sets of results on their response in ramp and cyclic conditions, as well as on their performance as piezoresistive sensors.

It was demonstrated that an isotropic electroconductive scaffold provides better overall mechanics with an extended toe region, lower hysteresis and - when combined with an elastomeric matrix - their yield point was extended up to beyond 30% strain, demonstrating that these constructs can be used for a wide range of deformation without progressing into

plastic transition. Significantly, I demonstrate that the presence of a stiffer PDMS filling yields a reduction in the range of high sensitivity, however it also caused a profound increase in strain-dependent gauge factors with values up to almost 400 for the isotropic group, that few reports were able to reach. Conversely, the use of a softer matrix yielded lower sensitivity, but within an extended strain range. It can be concluded that I optimised a method for the cheap and safe fabrication of piezoresistive sensors with adaptable sensitivity range and high strain sensitivity. According to the final application of the piezoresistive sensor, namely the strain or stress range and the required sensitivity, a different combination of microarchitecture and elastomer stiffness can be used for achieving the best output.

# 5. PEDOT:PSS interfaces stabilised using a PEGylated crosslinker yield improved conductivity and biocompatibility

A significant amount of this *Chapter* has been published previously in:

**Solazzo, M**., Zhussupbekova A., Krukiewicz K., Fleisher K., Biggs M. J. P., Monaghan, M. G. PEDOT:PSS interfaces stabilised using a PEGylated crosslinker yield improved conductivity and biocompatibility. Journal of Materials Chemistry B. 7, 4811—4820 (2019).

## *5.1. Abstract*

The rapidly expanding fields of bioelectronics, and biological interfaces with electronic sensors and stimulators, is placing an increasing demand on candidate materials to serve as robust surfaces that are both biocompatible, stable and electroconductive. Amongst conductive polymers, poly(*3,4*-ethylenedioxythiophene):poly(styrene sulfonate) (PEDOT: PSS) is a promising material in biomedical research due to its appropriate stability and high conductivity, however its intrinsic solubility requires a crosslinking process that can limit its conductivity and biocompatibility. Poly(ethylene glycol) is known to be a suitably anti-immunogenic moiety and its derivatives have been widely used for biomedical applications. In this study I investigate the application of poly(ethylene glycol) diglycidyl ether (PEGDE) as an effective crosslinker and conductive filler for PEDOT:PSS. From our interpretation of XPS analysis I hypothesise that the crosslinking reaction is occurring via the epoxy ring of PEGDE interacting with the sulfonic groups of excess PSS chains, which reaches a saturation at 3 w/v% PEGDE concentration. PEGDE crosslinked films did not disperse in aqueous environments, had enhanced electrical conductivity and imparted a significant degree of hydrophilicity to PEDOT:PSS films. This hydrophilicity and the presence of biocompatible PEGDE led to good cell viability and a significantly increased degree of cell

spreading on PEDOT:PSS films. In comparison to widely reported chemical crosslinking via glycidoxy propyltrimethoxysilane (GOPS), this original crosslinking yields a highly hydrophilic 2D film substrate with increased electroconductive and biocompatibility properties, resulting in a next-generation formulation for bioengineering applications.

## *5.2. Introduction*

The interface between electronics and biological components is a rapidly expanding field with applications within the next generation of implants and sensor devices, adaptive drug delivery systems [341], and tissue engineered therapeutics. Such interfaces determine biocompatibility and the efficiency of the intended function. Since their initial discovery and landmark research towards the end of the last century [342-344], conjugated polymers (CPs) have gathered considerable attention due to several attractive features: tunability of physical properties, flexibility, stimuli responsiveness and processability [184]. Traditionally, CPs such as polyaniline (PANI) and polypyrrole (PPy) have been investigated and applied for several decades [212,345]. However, their long-term stability and availability to be dispersed in non-toxic carriers or solvents to permit facile manipulation and fabrication through relatively easy, cheap and reliable techniques (i.e. spin coating, casting etc.) is lacking. Poly(*3,4*-ethylenedioxythiophene) (PEDOT) on the other hand, a conjugated polymer; is readily dispersed in aqueous solutions and can be doped with polystyrene sulfonate (PEDOT:PSS), to formulate a conducting polymer for biological applications with good conductivity, chemical stability and processability [213]. PEDOT:PSS possesses both ionic and electronic conductive properties and has been the subject of extensive research in the fields of microelectronics [214], sensor technology [215], actuation [216] and has been explored extensively in biological scaffold development, neural implant [217] and optoelectronic applications [218].

Previous reports have demonstrated PEDOT:PSS as cytocompatible in vitro [346]; however, crosslinking of PEDOT:PSS is often essential in order to prevent delamination and redispersion of conducting PEDOT:PSS films placed in aqueous physiological

conditions for long-term applications. Efforts have explored methods such as UV light [347], poly (ethylene oxide) treatment [348] and in particular the use of silanes [349]; with notable attention focused towards glycidoxypropyltrimethoxysilane (GOPS) crosslinking of PEDOT:PSS 2D films [30] and 3D scaffolds [350]. Such GOPS crosslinking is based on a hypothesis that the epoxy ring group in GOPS reacts with sulfonic groups of PSS chains leading to a change in PEDOT:PSS film morphology while the oxidation level of PEDOT remains unaffected [30].

One disadvantage of GOPS crosslinking is that it requires high curing temperatures (~140 ˚C for ~1 hour) and imparts a compromising effect on PEDOT conductivity values [351,352]. This also hinders incorporation of natural biomolecules during the fabrication process which can degrade at high temperatures. As a result of this, GOPS is often used in combination with secondary doping agents such as ethylene glycol or DMSO to restore some degree of conductivity [353]. As such, improved conductivity imparted by the addition of ethylene glycol has been attributed to a phase segregation of excess PSS resulting in the formation of a three-dimensional conducting network [354].

Considering this, I hypothesise that an alternative crosslinker, that simultaneously combines the conductive filler properties of ethylene glycol and an epoxy ring structure to bind with sulfonic groups present in excess PSS, can achieve superior crosslinking to generate stable structures whilst also achieving increased conductivity of PEDOT:PSS (**Scheme 5-1**). Poly(ethylene glycol) diglycidyl ether (PEGDE) is a water soluble epoxy resin, considered a flexible chain polymer and has been adopted as a biocompatible crosslinker for freeze-dried silk sericin [355] and for low temperature processed silk fibroin films [356,357]. PEGDE molecules also have the potential to covalently bind with amino- and carboxyl groups of proteins as well as with hydroxyl groups via its epoxide terminations, and has been adopted as a crosslinker agent in redox hydrogels for biosensors [358].

In this work I have employed PEGDE as an alternative crosslinker of PEDOT:PSS to enhance its stability for long-term biological applications and to allow resultant thin films to be cured at ambient temperatures. Suspensions of crosslinked material were optimised and

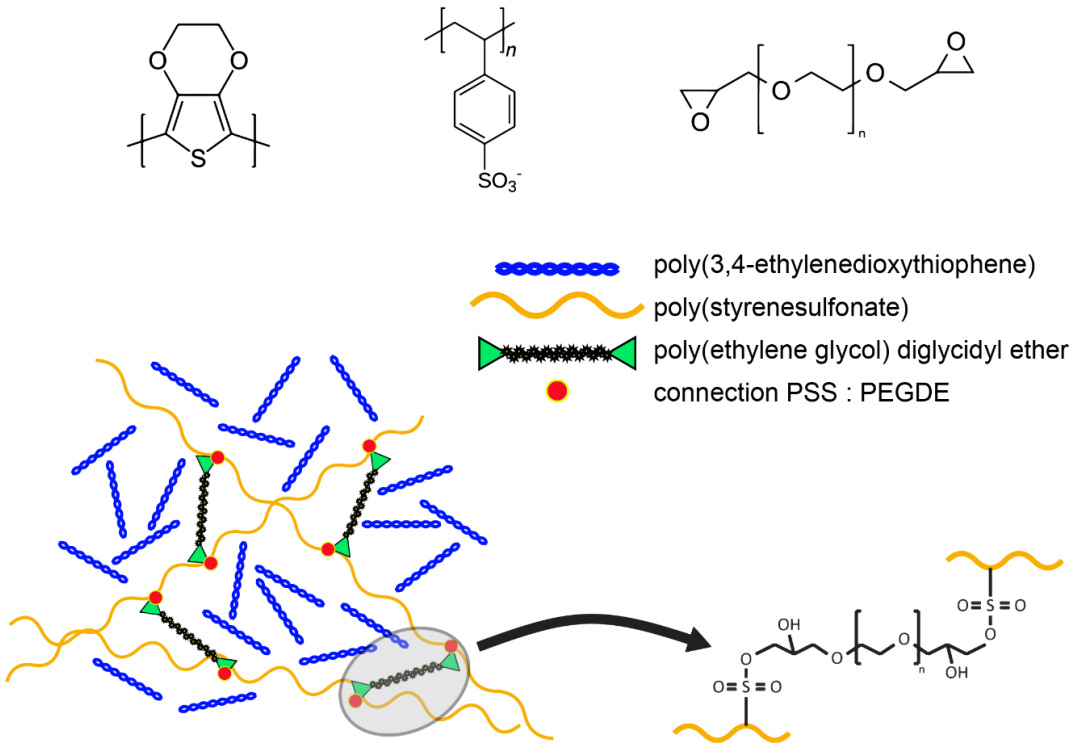


***Scheme 5-1.*** *At the top, from left to right: monomer of 3,4-ethylenedioxythiophene (EDOT), monomer of styrene sulfonate (SS) and poly (ethylene glycol) diglycidyl ether (PEGDE). At the bottom: hypothesised crosslinking reaction of PEGDE with PEDOT:PSS. The schematic demonstrates the proposed mechanism of epoxy rings at each end of the PEGDE reacting with $SO_3^-$ moiety of PSS chains.*

characterised using x-ray Photoelectron Spectroscopy (XPS) and Fourier Transform Infrared Spectroscopy (FT-IR) to verify the reaction of crosslinking; with GOPS as a control. On physical assessment of crosslinked films, they resist dissolution in aqueous environments, are highly hydrophilic, and possess superior conductivity when compared to that of GOPS crosslinked films. I also demonstrate an enhanced biocompatibility and increased cell spreading on PEGDE crosslinked PEDOT:PSS films.

## 5.3. Experimental section

### 5.3.1. Preparation of crosslinked films

PEDOT:PSS 1.3 wt.% dispersion in water (Sigma-Aldrich, Ireland) was mixed with PEGDE (Sigma-Aldrich, Ireland) at concentrations of 0, 1, 3, 5, 10 w/v%. GOPS was employed at a concentration of 3 v/v% as previously reported by others.[350] Indium tin oxide (ITO) coated glass slides (Sigma-Aldrich, Ireland) were prepared by sonication in consecutive washes of soap (Liquinox, Alconox, Inc, USA), tetrahydrofuran,

isopropanol:acetone 2:1 solution, isopropanol and distilled water. Slides were then dried in oven at 110 °C for 20 minutes and surface activated by oxygen plasma treatment (Diener Electronic, Plasma Surface Technology, PICO, Germany) at 200 W for 10 minutes. Afterwards, 150 µl of the filtered PEDOT:PSS blends were spin coated on the ITO surfaces at 1500 rpm for 30 seconds using a spin coater (WS-400BX-6nPP/LITE, Laurell, Technologies Corporation, Pennsylvania, USA), and dried to remove excess water. Films used for the physicochemical evaluation of crosslinking were left overnight at 37 °C; while substrates for the other tests were dried in oven at 120 °C for 1 hour, as a higher drying temperature resulted in quicker evaporation and more homogeneous films. Thicker 2D films were prepared by drop casting 1 ml of a mixture upon a metal substrate and evaporating the water content at room temperature overnight. PEDOT:PSS crosslinked controls (GOPS) were cured for an additional hour in oven at 140 °C based on established protocols [30].

### *5.3.2. Assessment of crosslinking: XPS, FT-IR, dissolution study*

XPS was performed in an Omicron MultiProbe XPS using a monochromised Al Kα source (XM 1000, 1486.7eV). The instruments base pressure was 5 x $10^{-11}$ mbar and the instrumental resolution was 0.6 eV. To minimise unintentional surface contaminations all samples were prepared, cut and mounted in a fume hood and transported to the instrument in an inert atmosphere ($N_2$). Air exposure was minimised to a brief exposure of 30 seconds – 1 minute during loading of the samples into the XPS. Spectra were analysed and fitted with CasaXPS (http://www.casaxps.com). Of particular interest is the fine structure of the sulphur (S) 2p XPS peak as it is able to distinguish S within the PSS and PEDOT subunits, and is sensitive to the chemical environment of the $SO^{3-}$ groups in the PSS [30,359]. To analyse the S2p multiple $S2p_{3/2}$, $S2p_{1/2}$ doublets were used with a fixed spin orbit split of 1.202 eV and a line shape described by a sum of a Gaussian and Lorentzian peak (SGL, 10% Gauss). Both splitting and shape had been previously determined on highly ordered, epitaxial $MoS_2$ layers measured in the same instrument [360]. To describe the asymmetric line shape of the PEDOT related sulphur component with a minimum number of additional fitting parameters,

an exponential asymmetric blend of the SGL shape was used. To quantitatively describe the peak changes for an increased cross-linker concentration all shape related fitting parameters were kept unchanged after optimisation for the plain PEDOT:PSS reference film (SGL ratio, Asymmetry parameter T for the PEDOT component), while amplitude, peak positions and broadening of all components where fitted for each sample.

To further assess the crosslinking effectiveness of the substrate, the chemical composition of 2D drop-casted films was investigated with FT-IR using a PerkinElmer® Spectrum 100™ (PerkinElmer, USA) machine measuring 32 frames per sample. Afterwards, spectra were analysed with PerkinElmer® Spectrum software (PerkinElmer, USA) and characteristic peaks were identified.

Finally, macroscopic assessment of PEDOT:PSS crosslinking was performed by immersing 2D drop-casted films into distilled water. Specimens were incubated in petri dishes containing distilled water and sealed using parafilm at room temperature. Dynamic conditioning (100 rpm on orbital shaker) was applied for 48 hours, and images were obtained immediately before immersion in water and 48 hours later.

### *5.3.3. Electroconductivity characterisation*

Electrochemical performance of PEDOT:PSS films was measured using a PARSTAT 2273 potentiostat in a three-electrode set-up, comprising a PEDOT-coated ITO glass slide as a working electrode, Ag/AgCl (3 M KCl) (EDAQ) as a reference electrode and a Ti/Pt rod (EDAQ) as an auxiliary electrode. Volumetric capacitance (Cvol) was assessed from the cyclic voltammetric (CV) curves collected in a physiologically relevant 1x PBS solution, within the potential range from −0.3 to 1.0 V (vs. Ag/AgCl) at 100 mV s−1 for 3 CV cycles. Cvol values were calculated as the electric charge integrated under a corresponding CV curve during one CV cycle, divided by the volume of the specimen. The volumetric charge injection capacities ($CIC_{vol}$) were quantified by the integration of chronoamperometric curves comprising a single biphasic potential pulse consisting of a 5 ms application of a reduction potential (−0.5 V *vs*. Ag/AgCl) followed by a 5 ms application of an oxidative

potential (0.5 V *vs.* Ag/AgCl). Electrochemical Impedance Spectroscopy (EIS) spectra were collected in a 1x PBS solution within a frequency range from 100 mHz to 100 kHz, with AC amplitude of 40 mV (*vs.* Ag/AgCl) and DC potential equal to 0 V (*vs.* Ag/AgCl). The results were presented on Bode plots and compared to those of a bare ITO electrode. EIS Spectrum Analyzer 1.0 software and the Powell algorithm were used to fit the experimental data to an equivalent circuit model. The simulations of the EIS data was performed with the use of an equivalent circuit model, comprising a combination of solution resistance ($R_1$), charge transfer resistance ($R_2$), two constant phase elements ($CPE_1$ and $CPE_2$) and Warburg diffusion element (W), In order to ensure the high goodness of fit, the relative deviation of the calculated spectrum from the measured data was restricted not to exceed 2%.

### *5.3.4. Surface characterisation*

Films were observed via brightfield microscope and their thicknesses were measured using a profilometer (Dektak 6M stylus profiler, Veeco, USA), providing also an estimation of roughness as arithmetical mean deviation Ra. Hydrophilicity measurements were performed with a FTA125 contact angle analyser (First Ten Angstroms, USA), by depositing a single droplet of distilled water onto the samples and measuring the angle between the surface and water droplet using the associated software. Tissue culture plastic Ibidi® petri dishes have been used as controls (Ibidi, Germany) (TCP).

### *5.3.5. Cytotoxicity*

Film substrates, at different crosslinker concentrations were prepared on ITO coated square glass slides with an approximate size of 10 mm per side and investigated for cytocompatibility. Following the pre-conditioning, cells were seeded with a density of 2,000 cells/cm$^2$ into the well containing film substrates with Ibidi® petri dishes as controls.

Following 48 hours incubation, the substrates were imaged using brightfield microscope, after which cell viability was assessed using a live/dead assay (n=4). Cell spreading was evaluated using cytofluorescent staining and mean cell area was computed as the area of

the picture positively stained for f-actin normalised by the number of cells.

## *5.4. Results and discussion*

### *5.4.1. PEGDE effectively crosslinks PEDOT:PSS at low temperature*

Chemical crosslinking of PEDOT:PSS has been mainly achieved via GOPS with high temperatures for annealing. Other works have alluded to the possibility of low temperature crosslinking via the use of divinylsulfone in blend but these also contain GOPS (albeit in minimal amounts) [225]. The use of a low temperature method paves the way to new fascinating prospective of hybrid compound combining synthetic conductive polymers with natural proteins as decellularised biological material.

To verify our hypothesis concerning the interaction between PEDOT:PSS and PEGDE, XPS was performed on pristine and PEGDE crosslinked PEDOT:PSS films deposited on ITO coated glass slides (**Figure 5-1**). The spectra of S2p core levels (**Figure 5-1.A**) revealed that no sulphur was removed in the reaction, with the ratio between sulphur in PEDOT and in PSS blocks remaining constant for all crosslinker concentrations. Pristine PEDOT:PSS is Na doped [361]; possessing two PSS related components, namely the plain $SO_3^-$ and the other the $SO_3$-X, where X can be Na or H atoms. The introduction of PEGDE does not influence the low binding energy band (163-167 eV) characteristic of C-S-C bonds within PEDOT chains. However, the high binding energy band (167-171 eV) proper of the $SO_3^-$ group in PSS chain was significantly affected by PEGDE, yielding a significant increase in reacted $SO_3$-X groups represented by an increase in the deconvolution area attributed to this bond (**Figure 5-1.C**) and a shift of the peak up to 0.4 eV to higher binding energy. These reactions saturate at low crosslinker content, and exponential fits of the data suggest that 96% of all possible bonds have occurred at 2 w/v%. The XPS on the Carbon (**Figure 5-1.B**) can be deconvoluted into two C components for all sample, and the higher binding energy component, indicated as the CC1 deconvolution, linearly increases (**Figure 5-1.D** and inset) with crosslinker concentration.

These findings strongly support an interaction between PEGDE and PSS, while PEGDE does not directly react with the PEDOT moieties. Specifically, I put forward that the crosslinking takes place between the epoxy ring groups of PEGDE molecules and the sulfonate groups of PSS; in a similar manner proposed for GOPS crosslinking of PEDOT:PSS by Hakånsson et al [30]. The shift to higher binding energy of the deconvolution C1s is index of a decrease in electron density that can be attributed to the bond between the delocalised electrons on PSS chain and the epoxy ring of PEGDE. Moreover, the increase in the typical binding energy of $SO_3$-X suggests a stronger interaction of the sulphur atoms of PSS with the PEGDE molecules than with the unaffected sulphur atoms of PEDOT molecules. Ultimately, the three relative areas of the deconvolutions of S2p core levels and (D) the relative contents of the two deconvolutions of C1s core levels confirm the reaction saturates at the concentration of 3 w/v% PEGDE.

FT-IR spectra (**Figure 5-1.E**) of pure PEDOT:PSS, pure PEGDE and PEDOT:PSS scaffold crosslinked with 3 w/v% PEGDE (respectively black, red and blue lines) have been obtained. The peaks α at 2867 $cm^{-1}$ and γ at 1094 $cm^{-1}$ respectively characteristic of -CH stretch [362] and ether bond [363] of PEGDE, and the band β between 600 and 1500 $cm^{-1}$ of PEDOT:PSS [364] are all present in the final structure, confirming the effective interaction of the two molecules. Further FTIR spectra, specifically the effect of increasing crosslinker content are reported in Supporting Information.1.

To investigate effective crosslinking at a macroscopic and physical level; drop-casted films were incubated for 48 hours in deionised water at room temperature under gentle rocking (**Figure 5-1.F**). Pristine PEDOT:PSS (first column) dispersed instantly with complete dissolution at 48 hours. PEGDE crosslinked samples (third column) did not disperse in aqueous conditions and exhibited similar stability to GOPS crosslinked samples (middle column). This result is of pivotal importance as it is evident confirmation of PEGDE efficiency as crosslinker with PEDOT:PSS to achieve a final compound able to stand dynamic condition at room temperature, and it entitled to further proceed with studies in

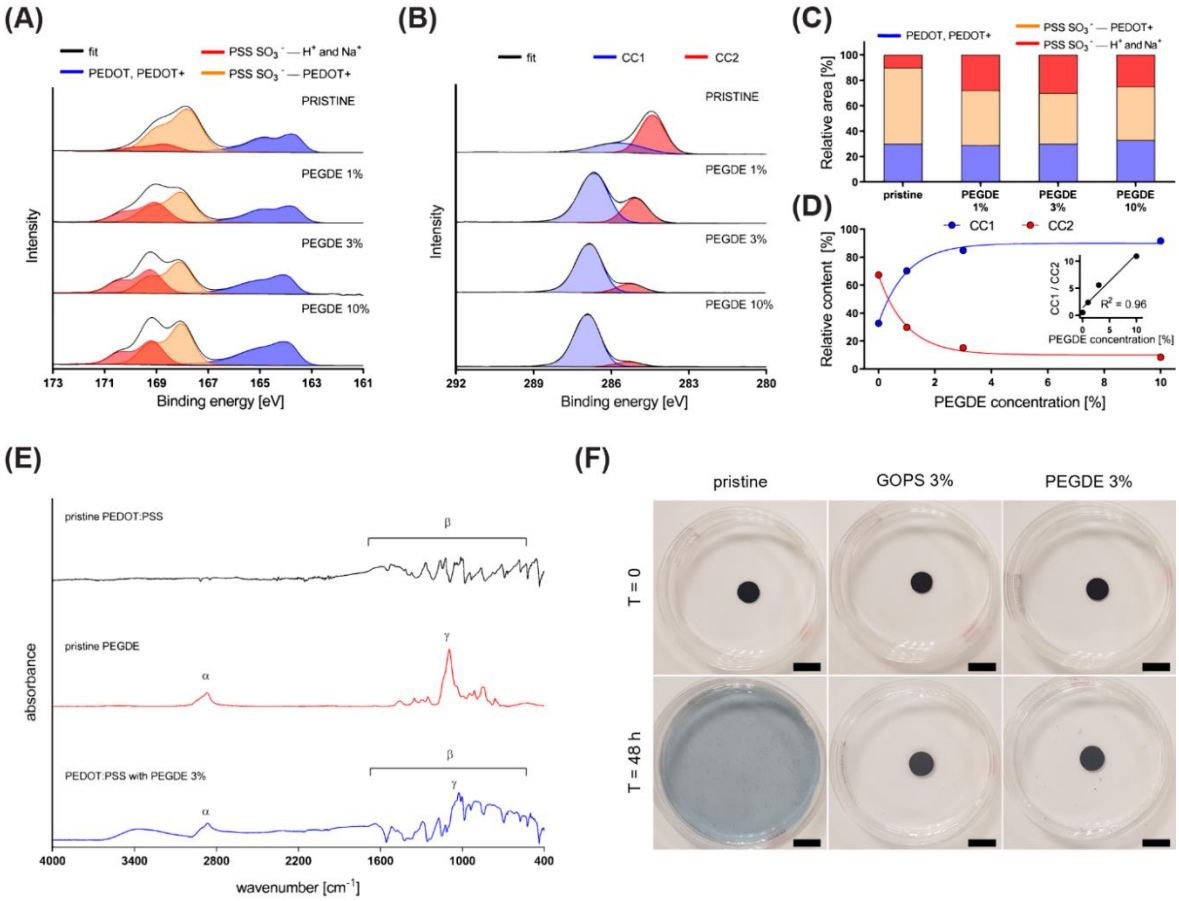


***Figure 5-1****. Establishment of PEDOT:PSS crosslinking using PEGDE.* ***(A-D)*** *XPS analysis on PEDOT:PSS samples with increasing PEGDE concentration. Spectra of* ***(A)*** *S2p and of* ***(B)*** *C1s core levels obtained on pristine and PEGDE crosslinked PEDOT:PSS films.* ***(C)*** *Relative areas of the three deconvolutions of S2p core levels and* ***(D)*** *the relative contents of the two deconvolutions of C1s core levels.* ***(E)*** *FT-IR spectra of pure PEDOT:PSS, PEGDE and PEDOT:PSS film crosslinked with PEGDE with characteristic peaks α, γ and band β.* ***(F)*** *Investigation of water dissolution of crosslinked and pristine PEDOT:PSS drop-casted films up to 48 hours. Scale bars: 10 mm.*

aqueous environment, such as cell culture.

### *5.4.2. Crosslinking of PEDOT:PSS with PEGDE increases film conductivity*

It has been proven that the addition of plasticisers can enhance the ionic mobility and therefore increases the conductivity of a matrix [365]. Treating of PEDOT:PSS films with ethylene glycol to enhance conductivity has been extensively reported [366,367]. Its mechanism of improving conductivity has been attributed by Mengistie et al. to be through the selective removal of PSS which leads to an increase in thermoelectric performance of PEDOT:PSS [368]. Lin et al. have explored this further and concluded that the addition of ethylene glycol to PEDOT:PSS leads to the increase of the density of charge carriers and an increase in the mobility of these carriers with an overall modification of electron-phonon coupling [369].

The evaluation of the electrochemical behaviour of all blends of PEDOT:PSS clearly showed the advantageous effects of using PEGDE as a crosslinking agent when compared with GOPS. As it can be seen in the EIS spectra (**Figure 5-2.A**), PEDOT:PSS crosslinked with PEGDE 3 w/v% exhibited the lowest impedance profile in a full range of investigated frequencies, outperforming other PEDOT:PSS formulations. The simulations of the EIS data with the use of an equivalent circuit model showed that the conductivity of PEDOT:PSS crosslinked with PEGDE 3 w/v% reached a value of 706 ± 32 S/cm, greatly outperforming the conductivity of pristine PEDOT:PSS which is typically only ~0.2 S/cm [219]. Furthermore, the low value of the impedance at 1 kHz (**Figure 5-2.D**), that was noted for both formulations of PEDOT:PSS crosslinked with PEGDE, indicated this chemistry as advantageous for neural stimulation/recording applications, since this frequency is biologically relevant and is used as the benchmark when analysing the efficacy of electrode systems [370].

All reported CV curves (**Figure 5-2.B**) possessed a rectangular shape, which is typical for PEDOT in aqueous medium [371] and indicates a capacitive behaviour of these materials. Consequently, the calculation of charge passing through the electrode modified with PEGDE crosslinked PEDOT:PSS demonstrates that the use of PEGDE as the stabilising

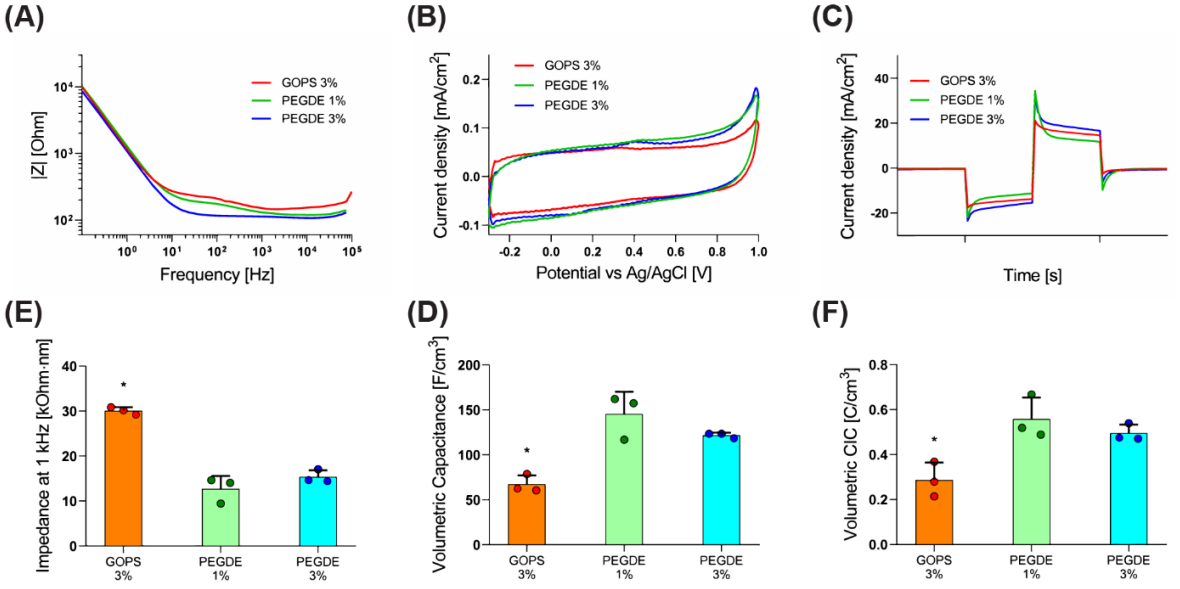


***Figure 5-2.*** *Electrochemical analysis of crosslinked PEDOT:PSS spin-coated on ITO coated glass slides.* ***(A)*** *Electrochemical Impedance Spectroscopy and* ***(D)*** *quantification of impedance at 1 kHz.* ***(B)*** *Cyclic Voltammetry and* ***(E)*** *quantification of Volumetric Capacitance ($C_{vol}$).* ***(C)*** *Three pulse chronoamperometric testing and* ***(F)*** *quantification of Volumetric Charge Injection Capacitance ($CIC_{vol}$). Data values are presented as associated points. * represents statistical significance ($p<0.05$) between indicated groups using one-way ANOVA with Tukey's post-hoc test.*

agent led to a significant enhancement in the volumetric capacitance of PEDOT:PSS. Since both the calculations and previous experiments report the capacitance per volume of PEDOT:PSS to be typically of 6–57 F/cm$^3$ [372], the value of 121 ± 2.9 F/cm$^3$ that was noted for PEDOT:PSS-PEGDE (3 w/v%) clearly shows the efficiency of the described approach to enhance the electrochemical behaviour of PEDOT:PSS. Although $2C_{vol}$ describes the maximum amount of charge that can be stored within a polymer matrix in a steady state conditions, the actual biomedical applications usually employ short electrical pulses which are far from the equilibrium state. Therefore, it is the volumetric charge injection capacity ($CIC_{vol}$) that indicates how much charge can be delivered in a single stimulation pulse. For instance, neural implants employ CIC values ranging from 2.3 µC/cm$^2$ to 2.3 mC/cm$^2$ [373]. With a $CIC_{vol}$ of approx. 500 mC/cm$^3$, PEDOT:PSS-PEGDE can serve as an advantageous neural coating material capable of reaching a range of desired CIC values by tailoring its thickness.

### *5.4.3. Crosslinking of PEDOT:PSS with PEGDE increases film hydrophilicity*

Spin coating yielded homogenous films (**Figure 5-3.A**) for all blends of PEDOT:PSS investigated, with the crosslinking formulations lending specific surface features. The typical configuration of PEDOT:PSS films consisting of rich PEDOT clusters in a lamellar backbone of PSS [374] was observable using brightfield microscope (**Figure 5-3.A ii-v**). A smooth coating with a low contrast between PEDOT rich and PSS rich sites was obtained with pristine PEDOT:PSS (**Figure 5-3.A ii**). Crosslinking of PEDOT:PSS conferred variable superficial features on resultant films with a high visual contrast present on GOPS 3 v/v% (**Figure 5-3.A iii**) and PEGDE 3 w/v% (**Figure 5-3.A v**) crosslinked specimens, and to a lesser extent on PEGDE 1 w/v% (**Figure 5-3.A iv**) crosslinked substrates.

Quantification via profilometry confirmed that the GOPS crosslinked films were significantly thicker than those created using pristine PEDOT:PSS with or without PEGDE crosslinking. No significant increase in thickness occurred when PEGDE was introduced when compared to pristine PEDOT:PSS (**Figure 5-3.B**). Substrate thickness is an important

characteristic of many materials utilised in biological applications as cells can sense the stiffness of underlying substrates at depths from 10 µm onwards [375]. However, the thicknesses obtained in our PEDOT:PSS films which were used for subsequent cell studies were all in the nanometre range (**Figure 5-3.B**). Profilometry also enabled the estimation of film roughness as an arithmetical mean deviation Ra (**Figure 5-3.C**), and I found a similar trend to that of substrate thickness whereby Ra values were significantly higher on GOPS crosslinked films when compared with pristine PEDOT:PSS films. PEGDE crosslinked specimens did tend to yield Ra values higher than pristine PEDOT:PSS and lower than GOPS crosslinked samples, but these differences were not statistically significant. With regard to its application in biological sensors and materials, the role of surface roughness is not univocally defined; as authors have reported that a high roughness has been shown to increase surface adsorption of vitronectin and fibronectin, to achieve higher cell cardiomyocytes growth [376], while others proved that increasing nanometer surface roughness enhanced the adhesion of vascular

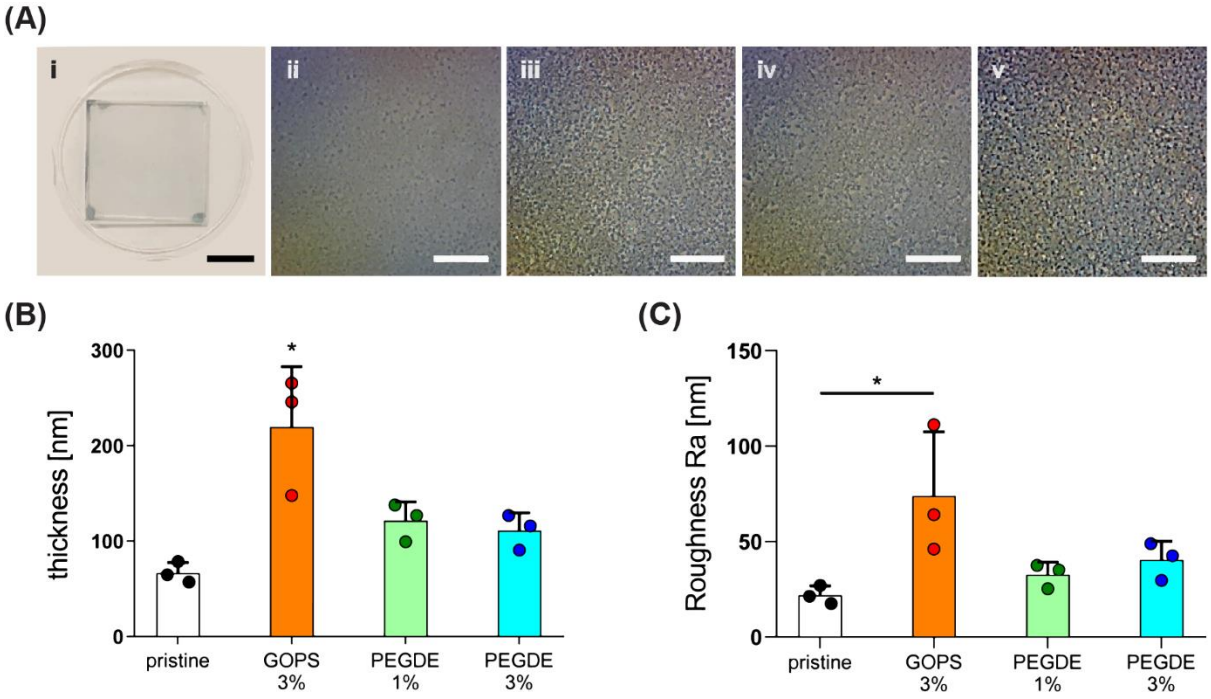


***Figure 5-3.*** *Profilometry characterisation of crosslinked PEDOT:PSS films.* ***(A)*** *i = picture of spin coated film on ITO, ii = pristine PEDOT:PSS, iii = GOPS 3 v/v% crosslinked PEDOT:PSS, iv = PEGDE 1 w/v% crosslinked PEDOT:PSS, v = PEGDE 3 w/v% crosslinked PEDOT:PSS.* ***(B)*** *Thickness quantification via profilometry.* ***(C)*** *Roughness quantification as arithmetical mean deviation Ra via profilometry. Scale bars: Ai = 1 cm, Aii-Av = 50 µm. Bar graphs demonstrate the mean of n=3 with error bars representing standard deviation. Data values are presented as associated points. * represents statistical significance (p<0.05) between indicated groups using one-way ANOVA with Tukey's post-hoc test.*

smooth muscle cell but decreased endothelial cell attachment [377].

The use of PEG has been widely studied and reported in its ability to behave appropriately with blood components [49], and it is used extensively to improve the biocompatibility of biomaterials for both in vivo and ex vivo applications [378]. This has been attributed to its resistance to protein adsorption which is important due to protein adsorption being a well-established first step in the response to foreign materials [379]. Given that the purpose of this study was to lend improved conductivity, stability and biocompatibility to PEDOT:PSS films using PEGDE; I also sought to determine the wettability of resultant films. Material hydrophilicity is known to have a reflection on cellular attachment and activity, and water contact angle investigation is a useful evaluation to predict cell interaction with the substrate [134,380]. **Figure 5-4** highlights that the use of PEGDE crosslinking (at both 1 w/v% and 3 w/v% concentrations) significantly reduced the water contact angle and therefore increases the wettability and hydrophilicity of PEDOT:PSS films.

### *5.4.4. PEDOT:PSS-PEGDE yields biocompatible films which increase cell spreading*

CH310 mouse embryonic fibroblasts exhibited good cell viability on all samples and controls tested (**Figure 5-5.A**) with no significant difference amongst substrates and with all the values above 85% (**Figure 5-5.B**). Upon investigating cell morphology, it became strikingly apparent that a greater degree of cell spreading (determined via quantification of

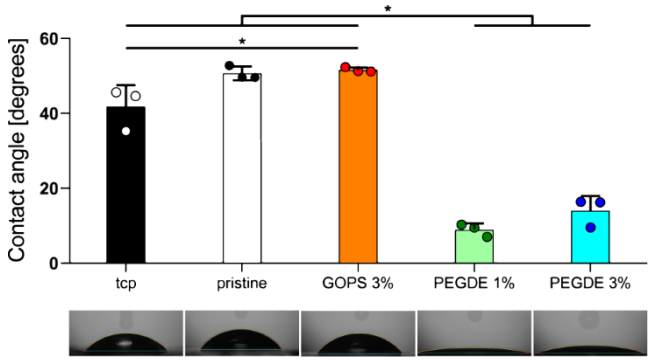


***Figure 5-4.*** *Hydrophilicity assessment via quantification of water contact angle measurement of spin coated films on ITO with tissue culture plastic Ibidi ® petri dish (TCP) included as control. Bar graphs demonstrate the mean of n=3 with error bars representing standard deviation. Data values are presented as associated points. * represents statistical significance (p<0.05) between indicated groups using one-way ANOVA with Tukey's post-hoc test.*

cell area) was occurring on PEDOT:PSS samples crosslinked using PEGDE (at both a 1 w/v% and 3 w/v% concentrations). Cell area was significantly increased on PEGDE 3 w/v% crosslinked PEDOT:PSS samples when compared to GOPS 3 v/v% crosslinked films and TCP as a control. Pristine PEDOT:PSS was not employed as a control in this study as it rapidly dissolved upon contact with cell culture media. Although cell area is higher on PEGDE 1 w/v% crosslinked PEDOT:PSS scaffolds when compared to GOPS and TCP, no statistically significant increase is detected. The results of cell area possess a significant negative correlative relationship between surface contact-angle and cell area, with a Pearson's correlation coefficient r = -0.85 and $R^2$ = 0.65 (**Figure 5-5.D**). The increased cell spreading cannot be exclusively linked to the contact angle values reported in this study as there is a certain range of hydrophilicity deemed optimal for cell adherence and spreading [53], outside of which is unfavourable for such cell behaviour. Indeed, the contact measurements reported in **Figure 5-4** are outside of such limits [381,382]. Although surface roughness could come into play to the effect of cell spreading and adhesion, the surface roughness and magnitudes of variation between the groups are rather modest compared to those investigated in previous reports [54]. This led to the conclusion that the combined presentation of material chemistries, and preparation steps of PEDOT:PSS films for cell culture studies are driving this cell-spreading observation.

Previously reported mechanisms of PEDOT:PSS stabilisation have been previously proposed, such as the solution-processed crystallisation reported by Kim et al. [31]. Similarly, crosslinking via PEGDE is a promising solution that may achieve thicker stable surfaces which could have great impact in the fields of electronics as charge storage systems or as more potent materials for bioelectronics. Moreover, PEGDE crosslinking of PEDOT:PSS does not require the use of toxic compounds or high temperature treatments, opening to the development of biohybrid constructs based on biological tissues. The beneficial

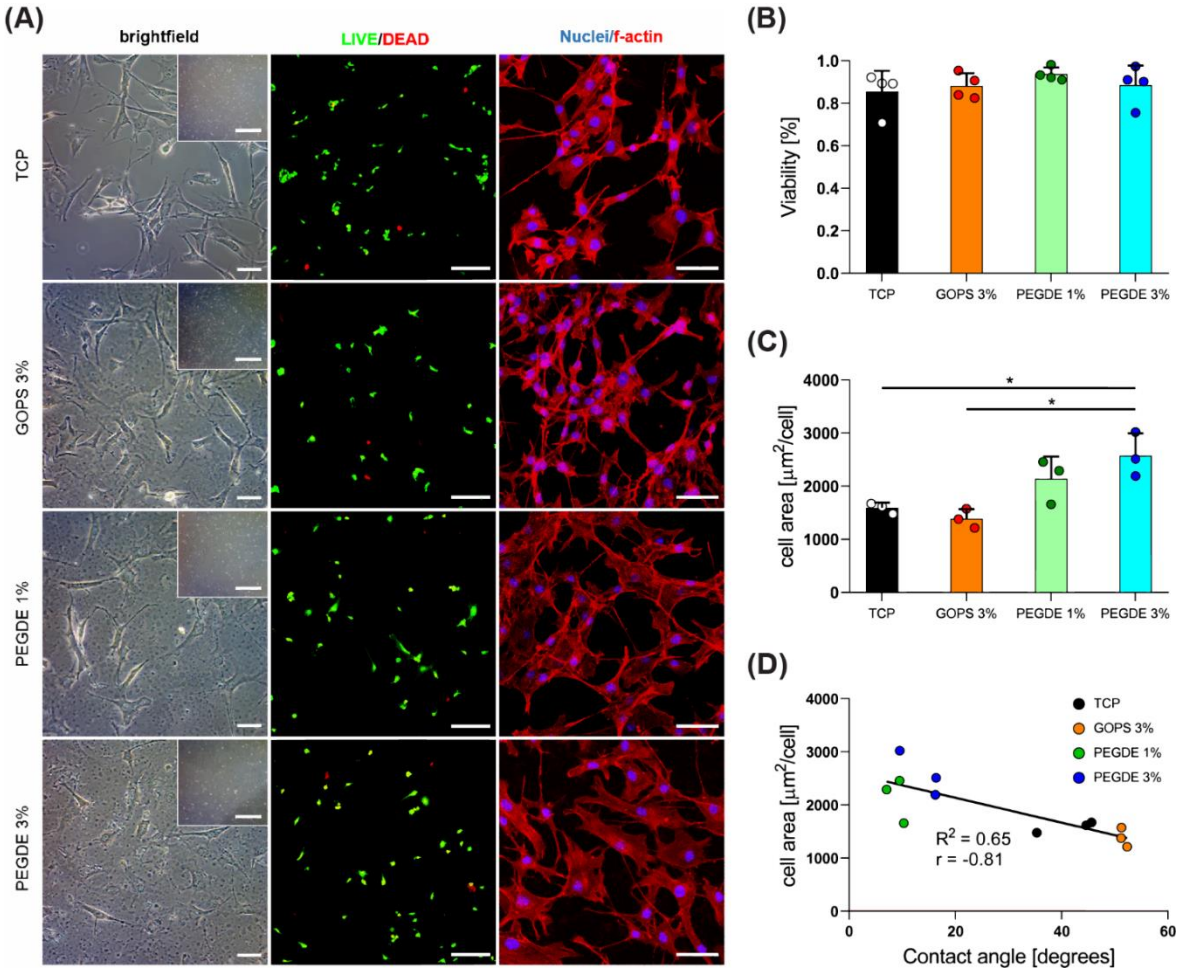


***Figure 5-5.*** *Cytocompatibility of crosslinked PEDOT:PSS films.* ***(A)*** *Micrographs of CH310 cells at 48 hours seeded on tissue culture plastic (TCP) and on PEDOT:PSS films crosslinked with GOPS 3 v/v%, PEGDE 1 w/v% and PEGDE 3 w/v%. First column and insets: brightfield microscope. Second and third columns showing confocal microscope fluorescent staining for live/dead and nuclei/f-actin respectively.* ***(B)*** *Quantification of viability (extracted from live/dead Staining) at 48 hours.* ***(C)*** *Quantification of cell surface area at 48 hours.* ***(D)*** *Pearsons correlation coefficient "r" and $R^2$ analysis between contact angle and cell surface. Scale bars: brightfield = 50 µm, brightfield inset 500 µm, live/dead = 200 µm, Nuclei/f-actin: 50 µm. Bar graphs demonstrate the mean of n=3 with error bars representing standard deviation. Data values are presented as associated points. * represents statistical significance (p<0.05) between indicated groups using one-way ANOVA with Tukey's post-hoc test.*

integration of PEG in the PEDOT:PSS structure is not limited to just its effect on stabilisation, indeed it may confer appropriate biological properties, such as protein rejection, formation of two-phase systems with other polymers, and lack of immunogenicity and antigenicity [383]. Furthermore, the presence of the epoxy groups specific of the PEGDE molecule has shown to induce the adhesion of specific peptides [384]. I have demonstrated enhanced cell spreading with no evidence of cytotoxicity at 48 hours as demonstrated by high cell viability, while longer term cytotoxic effects might not be seen at this early time point. This present study focused employed a short-term in vitro study to evaluate the acute

biocompatibility reaction and the material stability. Future work will embark on long-term studies together with the application of electrical stimulation [385] to access the potential of this new substrate to effectively deliver electrical stimulation and modulate tissue performances.

## *5.5. Conclusions*

A novel PEGylated crosslinker to accomplish stable PEDOT:PSS substrates, which are highly stable and exhibit superior electrical conductivity, has been achieved. From XPS analysis it was hypothesised that the crosslinking reaction is occurring via the epoxy ring of PEGDE interacting with the sulfonic groups of excel PSS chains, which reaches a saturation at 3 w/v% PEGDE concentration. PEGDE crosslinked films did not disperse in aqueous environments, had enhanced electrical conductivity and imparted a significant degree of hydrophilicity to PEDOT:PSS films. This hydrophilicity and the presence of biocompatible PEGDE led to good cell viability and a significantly increased degree of cell spreading on PEDOT:PSS films. This research has significant implications in the fields of biomaterials, sensor development and actuation whereby this molecule is serving both as a crosslinker and as a secondary dopant. The opportunity to process these materials at room temperature at relatively physiological conditions offers the potential to incorporate natural biomolecules and proteins within PEDOT:PSS films for advanced biomaterial scaffolds. Such stability can facilitate the long-term measurement of electrical signals, the production of more advanced biomaterials and scaffolds for tissue engineering using a relatively straight-forward fabrication process.

# 6. PEGDE crosslinks PEDOT:PSS porous scaffolds towards increased conductivity

A significant amount of this *Chapter* has been submitted at Synthetic Materials and is currently under revision:

**Solazzo, M**., Monaghan, M. G. Hydrophilic, conductive and flexible piezoresistive PEDOT:PSS 3D sensors with tunable microarchitecture and crosslinked using a PEGylated crosslinker.

## *6.1. Abstract*

Poly(*3,4*-ethylenedioxythiophene):poly(styrene sulfonate) (PEDOT:PSS) is an emerging biomaterial that – due to its stability and conductivity - has been adopted for diverse biomedical technologies, such as biosensors, coatings for electrodes, and substrates for tissue engineering. Currently, researchers are focusing on the processing of this biomaterial into three-dimensional (3D) scaffolds, either in the form of fibrous structures, porous sponge-like constructs or hydrogels. However, because of its instability in aqueous environment, challenges occur when applying manufacturing techniques to PEDOT:PSS. Moreover, the standardised use of covalent crosslinking via glycidoxypropyltrimethoxysilane (GOPS) negatively impacts the conductive properties of the material.

In this work, poly(ethylene glycol) diglycidyl ether (PEGDE) – which was previously demonstrated to stabilise PEDOT:PSS films (in *Chapter 3*) - has been used as crosslinker to generate 3D electroconductive porous biomaterial scaffolds via lyophilisation. Both isotropic and anisotropic porous scaffolds were obtained, and although macroscopically similar to GOPS-crosslinked samples (reported in *Chapter 4*), these constructs exhibited different chemical and physical features. PEGDE crosslinking of 3D PEDOT:PSS sponges enhanced material hydrophilicity, softness, and electrical conductivity, but also led to

weaker stability in aqueous environment and poor biocompatibility.

Investigations over the use of these constructs as piezoresistive sensors highlighted an unstable response in cyclic regime, ultimately opposing to their use as biosensors or as substrates for tissue engineering at the current state.

## *6.2. Introduction*

Achieving biomimicry with biomaterials and scaffolds is often a key determinant of successful tissue regeneration.[386-388] Typically, these platforms aim to replicate the physiological native environment, with attention paid to features such as stiffness and morphology, while exhibiting suitable chemistry, degradation rate and several other properties.[389] Electrical conductivity is one such feature that started to be implemented in recent decades and that can be obtained by the use of electroconductive materials, as discussed extensively in *Chapter 2*.

With most reports on electroconductive biomaterials focussing on the development of 2D substrates [28], hydrogels [259], and fibrous structures [205], there is still a need for the development of 3D constructs that can not only capture the native electrical conductivity, but that can also show adequate stiffness and tissue-inductive morphology. In particular, 3D porous PEDOT:PSS-GOPS scaffolds are easy to process and mechanically stable, but they present conductivity values in the order of $10^{-5}$ S/m [9] that do not capture that of the native myocardium, reported to have conductivity of about $10^{-1}$ S/m.[61] As the crosslinking is the main cause for this drop of electrical conductivity [30], one approach to address this limitation is to employ an alternative crosslinker: one which is less insulating yet able to stabilise the PEDOT:PSS chain.[390] In C*hapter 5*, it was shown that poly(ethylene glycol) diglycidyl ether (PEGDE) is a candidate crosslinker for PEDOT:PSS coatings, increasing their hydrophilicity and conductivity. PEGDE is water soluble-therefore easily mixed with water-based PEDOT:PSS dispersion; moreover, it has already been processed via lyophilisation with silk sericin [355], and it is capable of crosslinking other compounds, such as hyaluronic acid.[391,392]

Not limited to tissue engineering, 3D electroconductive porous constructs have also been employed as piezoresistive sensors [305-308], an application which can highly benefit both mechanically and electrically of the stretchability of a porous or sponge-like architecture.[314] As previously reported in C*hapter 4*, the electromechanical features of PEDOT:PSS make such material a suitable candidate to generate 3D piezoresistive sensor with tailored sensitivity.

In this work, utilising different moulds and freezing parameters, I obtained both aligned or isotropic 3D porous PEDOT:PSS-PEGDE scaffolds via lyophilisation. These scaffolds had increased softness and conductivity compared to GOPS-crosslinked counterparts. I then analysed the response of C3H10 mouse embryonic fibroblasts in direct contact with PEDOT:PSS-PEGDE scaffolds to evaluate material biocompatibility. Finally, to investigate the piezoresistivity of this new family of constructs, scaffolds were embedded into a polydimethylsiloxane (PDMS, Sylgard® 184) elastomeric matrix that enhanced the flexibility and the range of elastic deformation of the structures. This procedure enabled the fabrication of biphasic electroactive sponges (EAS), similar to those presented in C*hapter 4*. Scaffolds and biphasic EAS were tested for their piezoresistivity in quasi-static and cyclic conditions, showing sub-optimal performance compared to results previously achieved for PEDOT:PSS-GOPS, in particular in terms of consistency between replicates.

## *6.3. Experimental section*

Processes such as preparation of polymeric solutions, lyophilisation, study of morphology, mechanical test, measurement of electrical conductivity with 2-point probe and the analysis of biocompatibility were all performed as described in *Chapter 3*. Minor changes were applied to these protocols, namely the substitution of GOPS with PEGDE 3 w/v% during the preparation of the polymeric solutions, and the absence of thermal treatment after lyophilisation which is not necessary for PEGDE crosslinking.

For the initial proof of crosslinking: non-crosslinked, GOPS-crosslinked and PEGDE-crosslinked 3D scaffolds were submerged in distilled water at 37 °C and observed after 24

hours.

For degradation studies, GOPS- or PEGDE-crosslinked cylindrical samples 3 mm thick and with a diameter of 8 mm were soaked into PBS and incubated at 37 °C. Their wet weight was recorded after 1 hour (day 0) and at specific timepoints up to day 21. Residual wet weight was calculated as the ration between wet mass at the specific timepoint and the wet mass at day zero (n=5).

For testing injectability, a cylindrical dry scaffold 1 mm thick and 6 mm wide was manually rolled, then inserted into a 16G needle and finally ejected into a PBS bath.

## *6.4. Results and discussion*

### *6.4.1. 3D PEDOT:PSS-PEGDE scaffolds are hydrophilic and less stable*

3D PEDOT:PSS-PEGDE scaffolds were fabricated in both isotropic and aligned configurations, with morphological results comparable to GOPS-crosslinked scaffolds (**Figure 6-1.A**). Cell culture plastic multi-well plate enabled the formation of pores with symmetric and relatively homogenous geometries. Using a custom-made mould, anisotropy was obtained, resulting in microarchitectures characterised by lamellae preferentially oriented in one same direction (**Figure 6-1.B**).

3D scaffolds were stable when soaked in distilled water for 24 hours similar to GOPS-crosslinked scaffolds, while non-crosslinked PEDOT:PSS underwent complete dispersion (**Figure 6-1.C**). However, a longer term degradation study did show that PEDOT:PSS-PEGDE scaffolds lost over 30% of their wet mass by day 21, while no mass loss was detected for PEDOT:PSS-GOPS scaffolds (**Figure 6-1.D**). This finding, together with a significant increase in water uptake (**Figure 6-1.E**), led to the conclusion that PEGDE provide a more hydrophilic yet less efficient stabilising effect on 3D scaffolds compared to GOPS.

The increased hydrophilicity and reduced stiffness of this scaffold could allow for its injection through a needle (**Figure 6-1.F)**, considering a potential minimally invasive delivery

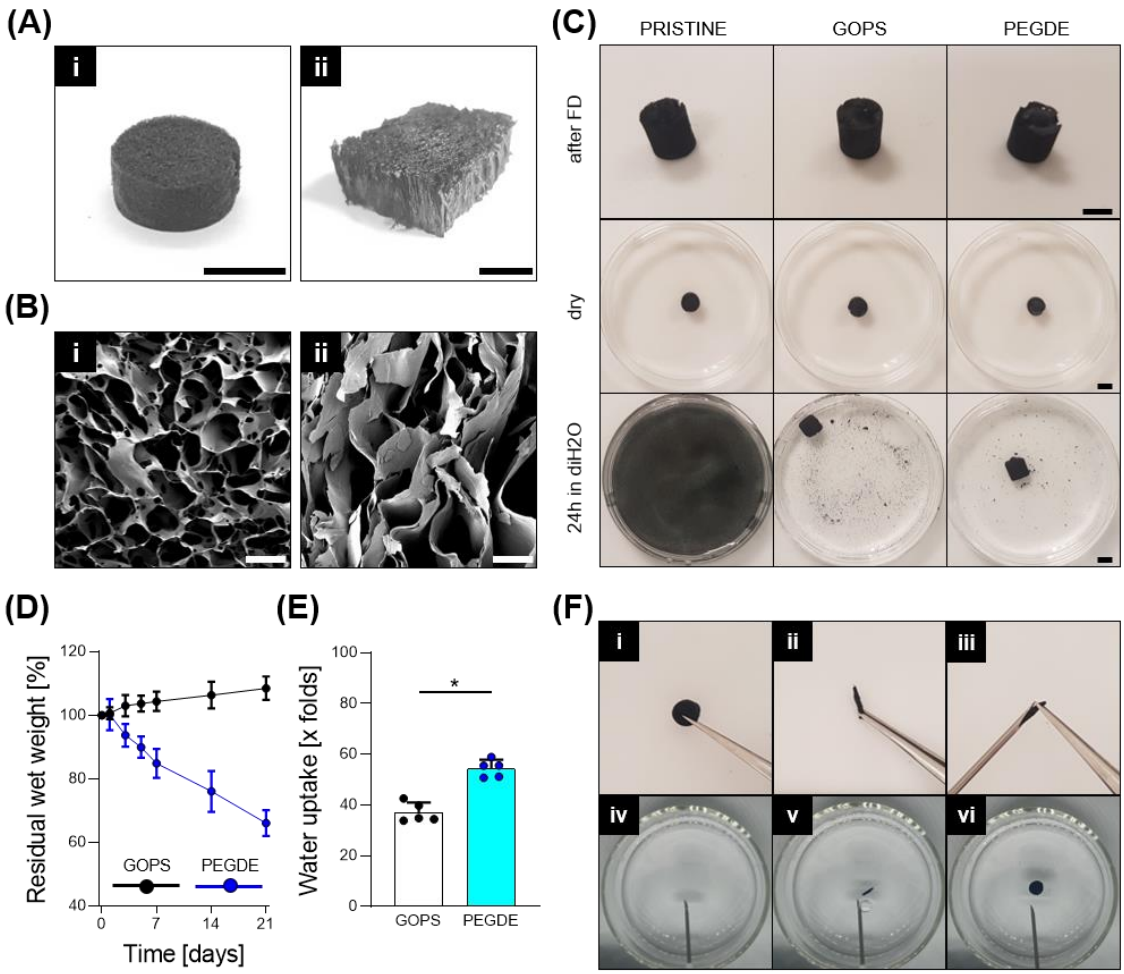


***Figure 6-1**. Fabrication of PEDOT:PSS-PEGDE scaffolds. **(A)** Pictures of (i) isotropic and (ii) aligned PEDOT:PSS-PEGDE scaffolds. **(B)** SEM micrographs of (i) isotropic and (ii) aligned scaffolds. **(C)** Proof of crosslinking with PEDOT:PSS scaffolds pristine non-crosslinked or crosslinked with GOPS or PEGDE. **(D)** Degradation study up to 21-days comparing GOPS- and PEGDE- crosslinked scaffolds. **(E)** Wettability study up comparing GOPS- and PEGDE- crosslinked scaffolds. **(F)** Proof of injectability of PEDOT:PSS-PEGDE scaffolds. Scale bars: A = 1 cm; B = 100 µm; C = 5 mm. Graphs demonstrate the mean with error bars representing standard deviation. Data values are presented as associated points. * represents statistical significance ($p<0.05$) between indicated groups using Student's unpaired t-test.*

strategy for future applications. The scaffold was successfully delivered via a 16-gauge needle and it instantaneously recovered its original shape when in contact with PBS.

### *6.4.2. Lyophilisation conditions affects morphology of isotropic PEDOT:PSS-PEGDE scaffolds*

Aiming to modify the microarchitecture of the porous isotropic scaffolds, three freezing temperatures were adopted, namely -20/-40/-80 °C. While these scaffolds exhibited macroscopic features similar to the GOPS-crosslinked scaffolds, quantitative analysis of the microarchitecture highlighted a decreasing trend- yet non-significant - in pore size for

groups manufactured with lower freezing temperatures (**Figure 6-2).** This is attributed to the faster nucleation rate of the ice crystals together with a slower heat transfer which was discussed in *Chapter 4*.[331] With an average pore size in the order of 150 - 170 µm, all three groups might be suitable for culture of diverse cell types, such as dermal fibroblasts, vascular smooth muscle cells, and bone resident cells.[56,393] In particular, the -40 °C and -80 °C groups are more indicated for cell adhesion, as a smaller pore size determines a higher adhesion surface.[332] The group processed at -80°C also had the most irregular porous structure, demonstrated by the highest pore diameter variance (0.53 ± 0.03), the lowest circularity (0.64 ± 0.02), and the highest eccentricity (0.76 ± 0.02). Taken together, these data confirmed that PEGDE crosslinks PEDOT:PSS and supports the formation of 3D structures similarly to GOPS. Indeed, both formulations enabled to recreate sponge-like

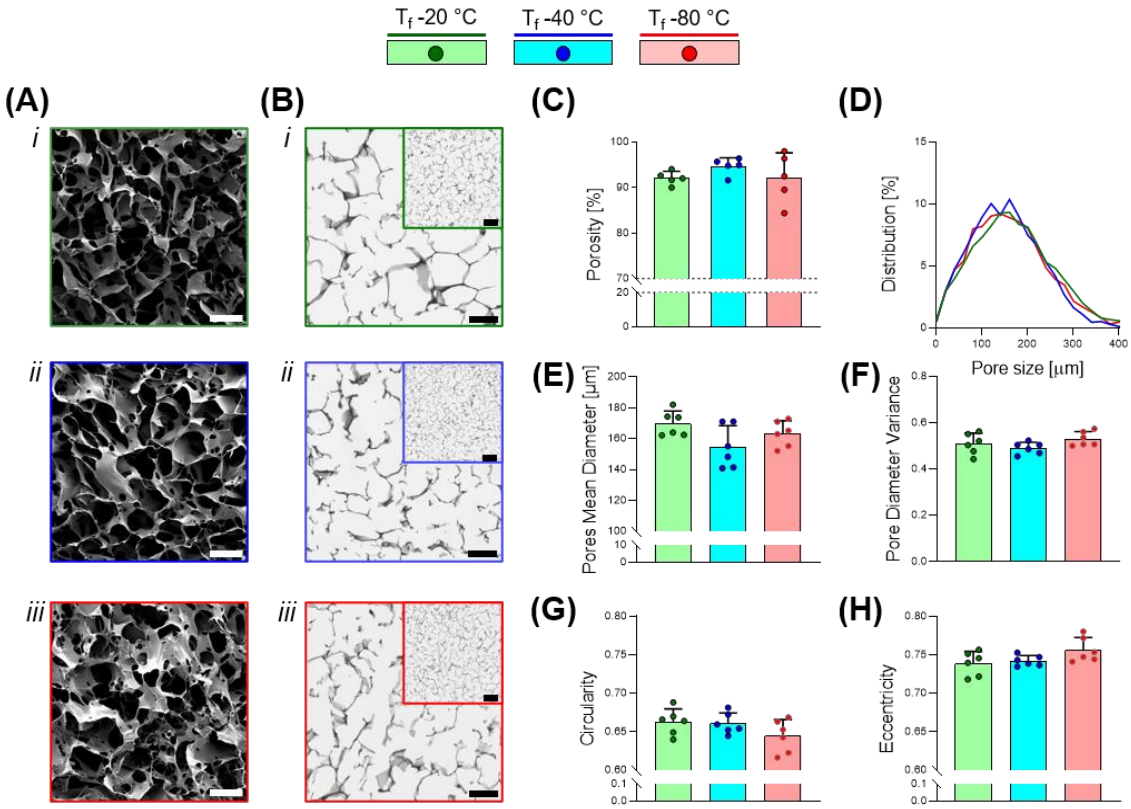


***Figure 6-2**. Morphological characterisation of isotropic PEDOT:PSS-PEGDE scaffolds processed at different Freezing Temperatures ($T_f$), namely -20 / -40 /-80 ºC. **(A)** SEM micrographs. **(B)** Sliced agarose embedded scaffolds. **(C-H)** Quantitative analysis of the effect of $T_f$ on the size and shape of isotropic samples (n=3 per direction): **(C)** distribution of pore size as percentage, **(D)** Pores Mean Diameter, **(E)** Pores Mean Variance, **(F)** Porosity, **(G)** Circularity and **(H)** Eccentricity.*
*Scale bars: A = 100 µm; B = 100 µm, insets = 200 µm. Bar graphs demonstrate the mean with error bars representing standard deviation. Data values are presented as associated points. Statistical analysis was performed using one-way ANOVA with Tukey's post-hoc test.*

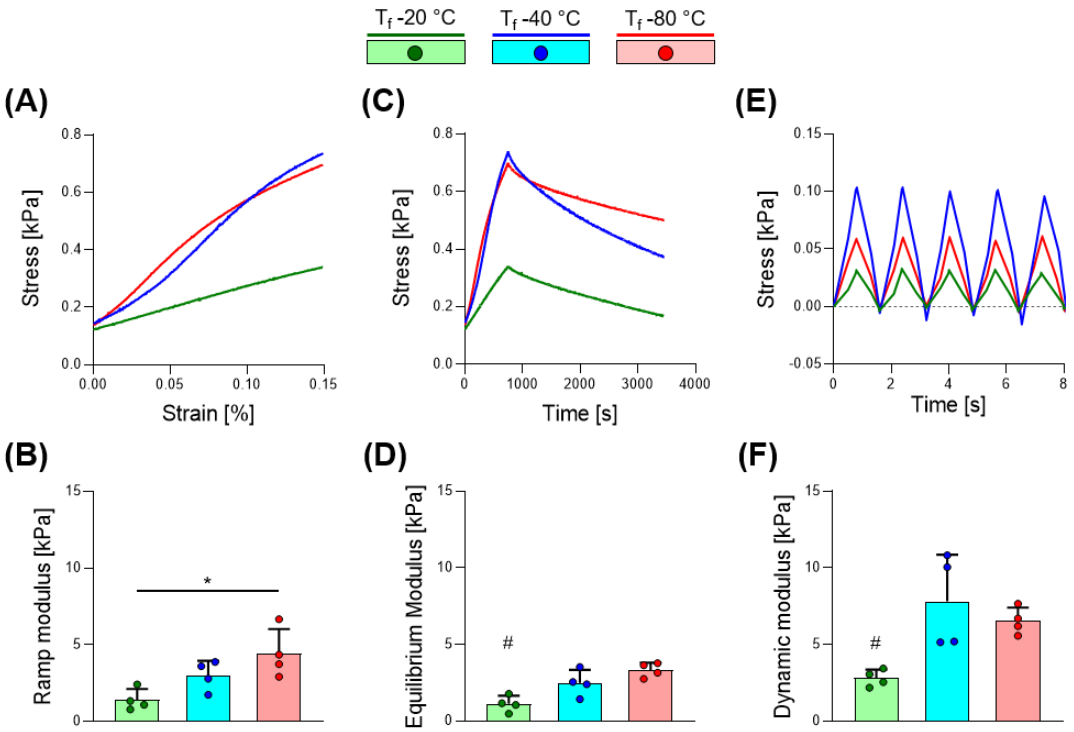


***Figure 6-3**. Stress relaxation followed by dynamic cyclic compression test for isotropic PEDOT:PSS-PEGDE scaffolds. **(A)** Stress-strain curves representing mean response during ramp phase. **(B)** Ramp Modulus. **(C)** Stress-time curves representing mean response during relaxation phase. **(D)** Equilibrium Modulus. **(E)** Stress-time curves representing a standard response during dynamic cyclic loading phase. **(F)** Dynamic Modulus. Bar graphs demonstrate the mean of n=4 replicates with error bars representing standard deviation. Data values are presented as associated points. * and # represent statistical significance (p<0.05) (* between indicated groups, # with all other groups) using one-way ANOVA with Tukey's post-hoc test.*

scaffolds with aligned geometry, and also produced isotropic structures with microarchitectures that could be changed by using different freezing temperature.

### *6.4.3. Smaller pore size increases scaffolds stiffness*

Mechanical tests were designed with a stress-relaxation phase followed by a dynamic sequence, where it was possible to quantify the stiffness of the samples in wet conditions in terms of ramp, equilibrium, and dynamic moduli (**Figure 6-3**). These three parameters were found to be inversely proportional to the freezing temperature used, suggesting that scaffolds with smaller pores were characterised by a stiffer mechanical response, in agreement with previous reports.[394]

In **Figure 6-4**, the same analysis for aligned scaffolds is reported, with emphasis on the material response when the load was applied either along the direction longitudinal to the lamellae transversally. These scaffolds were found to be on average up to eight-fold stiffer

along the longitudinal direction, thus demonstrating an anisotropic mechanical response. The longitudinal direction of the aligned samples was also stiffer than the isotropic group

All results are summarised in **Table 6-1**. Overall, PEDOT:PSS-PEGDE scaffolds proved to be over one order of magnitude softer than PEDOT:PSS-GOPS counterpart (described in more detail in C*hapter 7* for context). In particular, the dynamic moduli were in the range 1 to 10 kPa, that in the context of tissue engineering may be suitable for inducing differentiation of stem cells towards adipogenesis and myogenesis.[395]

### *6.4.4. Scaffolds generated at lower temperature are more conductive*

Dry PEDOT:PSS-PEGDE scaffolds with both isotropic and aligned microarchitecture were then investigated for their electrical conductivity with a 2-point probe test. Due to the larger pore size and the homogeneous inner architecture, samples processed at -20 ºC were significantly more conductive than to the -80 ºC group (**Figure 6-5**), in agreement with previous results.[396] On average, conductivity values were in the range of $10^{-3}$ S/m, two

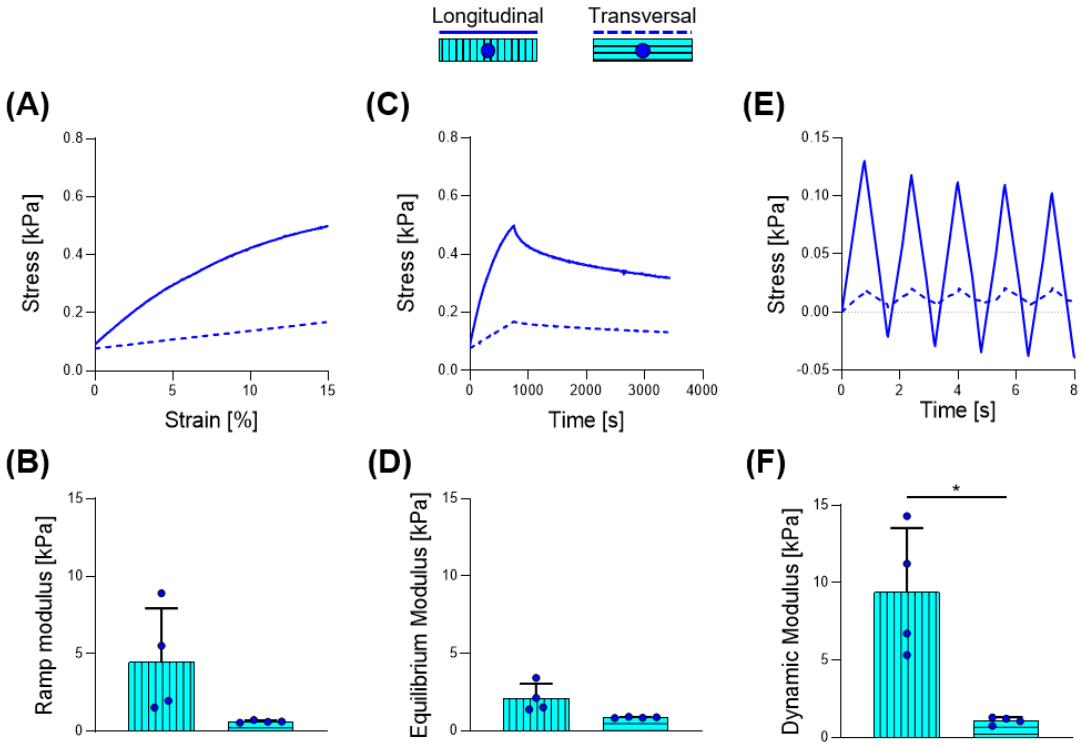


***Figure 6-4.*** *Stress relaxation followed by dynamic cyclic compression test for aligned PEDOT:PSS-PEGDE scaffolds.* ***(A)*** *Stress-strain curves representing mean response during ramp phase.* ***(B)*** *Ramp Modulus.* ***(C)*** *Stress-time curves representing mean response during relaxation phase.* ***(D)*** *Equilibrium Modulus.* ***(E)*** *Stress-time curves representing a standard response during dynamic cyclic loading phase.* ***(F)*** *Dynamic Modulus. Bar graphs demonstrate the mean of n=4 replicates with error bars representing standard deviation. Data values are presented as associated points. * represents statistical significance (p<0.05) between indicated groups using Student's unpaired t-test.*

orders of magnitude higher than 3D PEDOT:PSS-GOPS samples documented in C*hapters 4* and *7.* Aligned samples were found to be on average over 10-fold more conductive along the longitudinal direction rather than on the transversal one, in agreement with trends described for PEDOT:PSS-GOPS aligned scaffolds. The obtained anisotropy is of great importance to mimic those native body tissues which possess anisotropic conductivity, such as the skeletal muscle, the myocardium, the bone and nerves.[61]

PEGDE-crosslinking is confirmed to generate more electroconductive bonds, as seen previously with 2D PEGDE crosslinked films reported in *Chapter 5*. However, the enhancement found in 3D scaffolds is not sufficient to match the electrical conductivity reported for body tissues described in **Figure 2.1**. Exploring alternative strategies for 3D

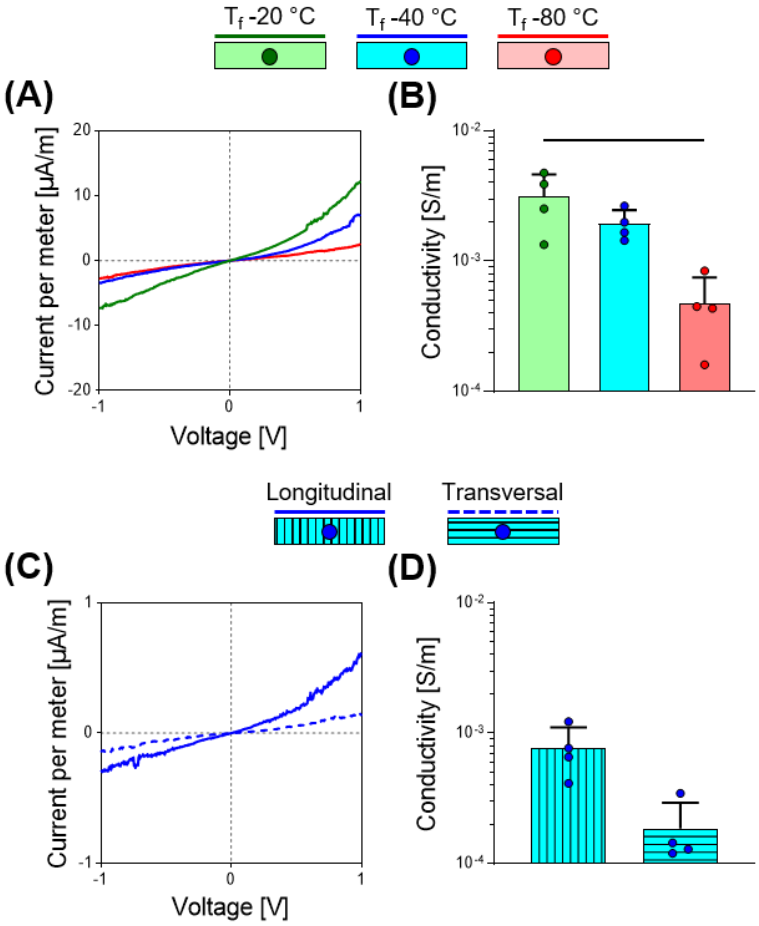


***Figure 6-5.*** *Electrical conductivity measurements via 2-point probe.* ***(A, C)*** *I-V curves of isotropic* ***(A)*** *and aligned* ***(C)*** *PEDOT:PSS-PEGDE scaffolds.* ***(B, D)*** *Conductivity quantification of isotropic* ***(B)*** *and aligned* ***(D)*** *PEDOT:PSS-PEGDE scaffolds from linear regression of I-V curves in the linear region 0.5 - 1 V (n=4). Bar graphs demonstrate the mean with error bars representing standard deviation. Data values are presented as associated points. * represents statistical significance (p<0.05) between indicated groups using one-way ANOVA with Tukey's post-hoc test (B) or Student's unpaired t-test (D).*

PEDOT:PSS-based constructs, other groups have shown that the addition of dodecylbenzenesulfonic acid (DBSA) at high concentration generates conductive self-healing hydrogels. Conductivity reached 10 S/m, remarkably higher than sponge-like scaffolds crosslinked with either GOPS or PEGDE. However, these hydrogels required constant hydration to be maintained functional and further information over their biocompatibility is required.[397]

Overall, considering their improved conductivity and their stability in both dry and hydrated states, 3D PEDOT:PSS-PEGDE scaffolds are a promising solution towards more functional conductive platforms. Inclusion of additives such as DBSA could further improve

***Table 6-1.*** *Summary of mechanical and electrical (n=4) properties of tested samples. Data are presented as mean ± standard deviation*

| Material | Geometry | Ramp Modulus [kPa] | Equilibrium Modulus [kPa] | Dynamic Modulus [kPa] | Conductivity [S/m] |
|---|---|---|---|---|---|
| Isotropic | Tf -20°C | 1.41 ± 0.71 | 1.12 ± 0.54 | 2.82 ± 0.55 | $3.13 \pm 1.50 \times 10^{-3}$ |
| | Tf -40°C | 3.01 ± 0.96 | 2.48 ± 0.86 | 7.81 ± 3.05 | $1.94 \pm 0.53 \times 10^{-3}$ |
| | Tf -80°C | 4.42 ± 1.61 | 3.33 ± 0.47 | 6.54 ± 0.88 | $0.47 \pm 0.28 \times 10^{-3}$ |
| Aligned | Longitudinal | 4.48 ± 3.45 | 2.11 ± 0.93 | 9.40 ± 4.13 | $0.76 \pm 0.34 \times 10^{-3}$ |
| | Transversal | 0.64 ± 0.08 | 0.87 ± 0.03 | 1.08 ± 0.24 | $0.18 \pm 0.11 \times 10^{-3}$ |

their conductivity. PEDOT:PSS-PEGDE isotropic scaffolds processed at -40 °C provided the best balance between morphological homogeneity, stiffness, and electrical conductivity. Thus, they were chosen for the next studies.

### *6.4.1. 3D PEDOT:PSS-PEGDE scaffolds have limited biocompatibility*

C3H10 cells were seeded onto either PEDOT:PSS-PEGDE or collagen scaffolds (as control) to compare the biocompatibility of the substrates. A live/dead assay showed few cells attached to the PEDOT:PSS-PEGDE scaffolds compared to the collagen group at day 1, and an even more profound difference was evident at day 7 (**Figure 6-6.A**). Quantification of DNA content demonstrated that while significant proliferation was present within the collagen group, an opposite trend was present with PEDOT:PSS-PEGDE scaffolds (**Figure 6-6.B**). The assessment of metabolism, measured with AlamarBlue™, led to similar observations (**Figure 6-6.C**). To avoid any doubt, these experiments were repeated several

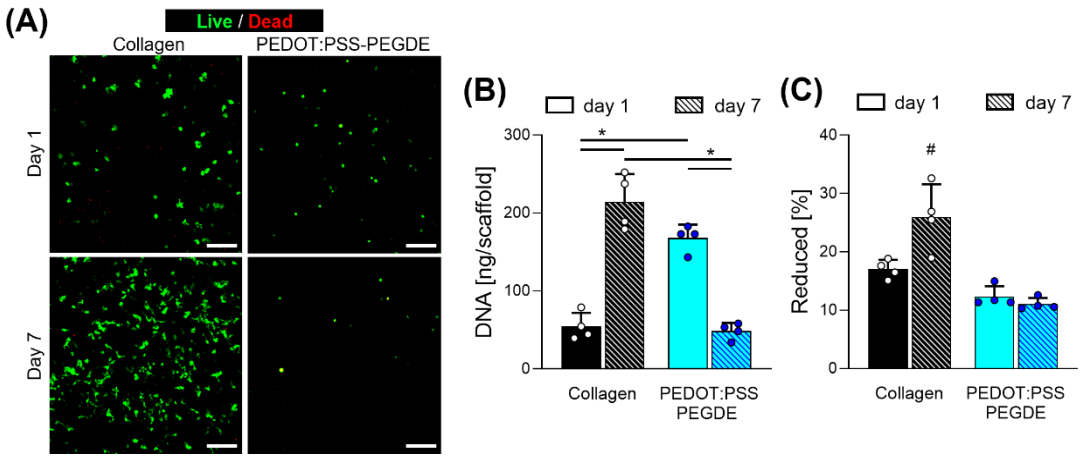


***Figure 6-6**. Cytocompatibility of C3H10 cells on scaffolds via direct contact. **(A)** Micrographs from confocal microscope fluorescent staining for live/dead of CH310 cells at days 1 and 7, seeded on scaffolds. **(B)** Quantification of DNA via Picogreen™ assay, expressed as ng per scaffold (n=4). **(C)** AlamarBlue™ assay performed on scaffolds (n=4). Scale bars: A = 200 µm. Bar graphs demonstrate the mean with error bars representing standard deviation. Data values are presented as associated points. * and # represent statistical significance (p<0.05) (* between indicated groups, # with all other groups) using two-way ANOVA with Tukey's post-hoc test.*

times leading to the same outcome and reducing any human error or external circumstance. It is hypothesised that the overall reduction of DNA overtime is caused by a combination of lack of proliferation and cell death, suggesting a potentially cytotoxic nature of the material. Other researchers have reported an excessive amount of PEGDE leading to ulceration in a subcutaneous study on a mouse model.[398] Moreover, as shown in **Figure 6-1**, PEGDE is a suboptimal crosslinker of PEDOT:PSS, inducing degradation over time. The subsequent release of PSS in the surrounding environment is speculated to further contribute to toxicity.[232] Together, these data proved that PEDOT:PSS-PEGDE is significantly less cytocompatible than the collagen sponge control.

### *6.4.2. PEDOT:PSS-PEGDE response as piezoresistive sensors*

The softness of PEDOT:PSS-PEGDE scaffolds did not interfere with their embedding into a PDMS Sylgard 184 elastomeric matrix. The electroconductive structure of the scaffold was preserved, generating biphasic electroactive sponges (EAS). Their piezoresistivity and that of PEDOT:PSS-PEGDE scaffolds alone were tested via a cyclic deformation sequence followed by a ramp phase, according to the protocols described in *Chapter 4*. No results on the tests performed in cyclic regime are presented in this section of the thesis as the data

related to PEDOT:PSS-PEGDE scaffolds alone consisted prevalently of noise and no parameters could be objectively quantified. The increased softness of these scaffolds came with an increased viscous component of the viscoelastic response and a slower mechanical recovery during the decompression phase. This was cause for an inconsistent contact between the upper plate of the testing machine and the sample, ultimately breaking the conduction and resulting in noise.

From the analysis of stress-strain curves, it was possible to quantify mechanical parameters as toe region, toe region elastic modulus, Young's modulus and yield strain (**Figure 6-7.A,B**). The response of isotropic and aligned scaffolds exhibited large variability between replicates, which could be observed by the individual curves. In the case of biphasic EAS, due to the high stiffness of PDMS, the elastomeric matrix was the principal load bearing component and the main responsible for the mechanical response. The consistency in the PDMS physical properties allowed for the fabrication of samples with almost identical behaviour within the same experimental group. Statistical analysis revealed that the introduction of PDMS infilling significantly impacted on the mechanical characteristics of the material, while the effect of microarchitectures was minor. Stiffness of both the toe and the elastic regions was increased by the presence of PDMS. Furthermore, the biphasic EAS were also characterised by an increase of the yield strain, that in the case of the isotropic group was beyond the studied range.

Electromechanical measurements provided by the ramp phase of the test showed unstable signals and the presence of artifacts causing wide variance between replicates. Scaffolds were impacted to a greater extent, but also biphasic EAS were affected, as it can be observed from **Figure 6-7.C**. Signals presented evident variability and instability, but from their analyses it was yet possible to determine the strain- and the stress-dependent gauge factor, together with the maximum strain and stress limits of the high gain region (**Figure 6-7D**). Biphasic EAS showed lower strain limit and stress-dependent gauge factor, together with higher stress-limit and strain-dependent gauge factor. Instead, no notable differences due to the microarchitecture of the internal PEDOT:PSS scaffolds were

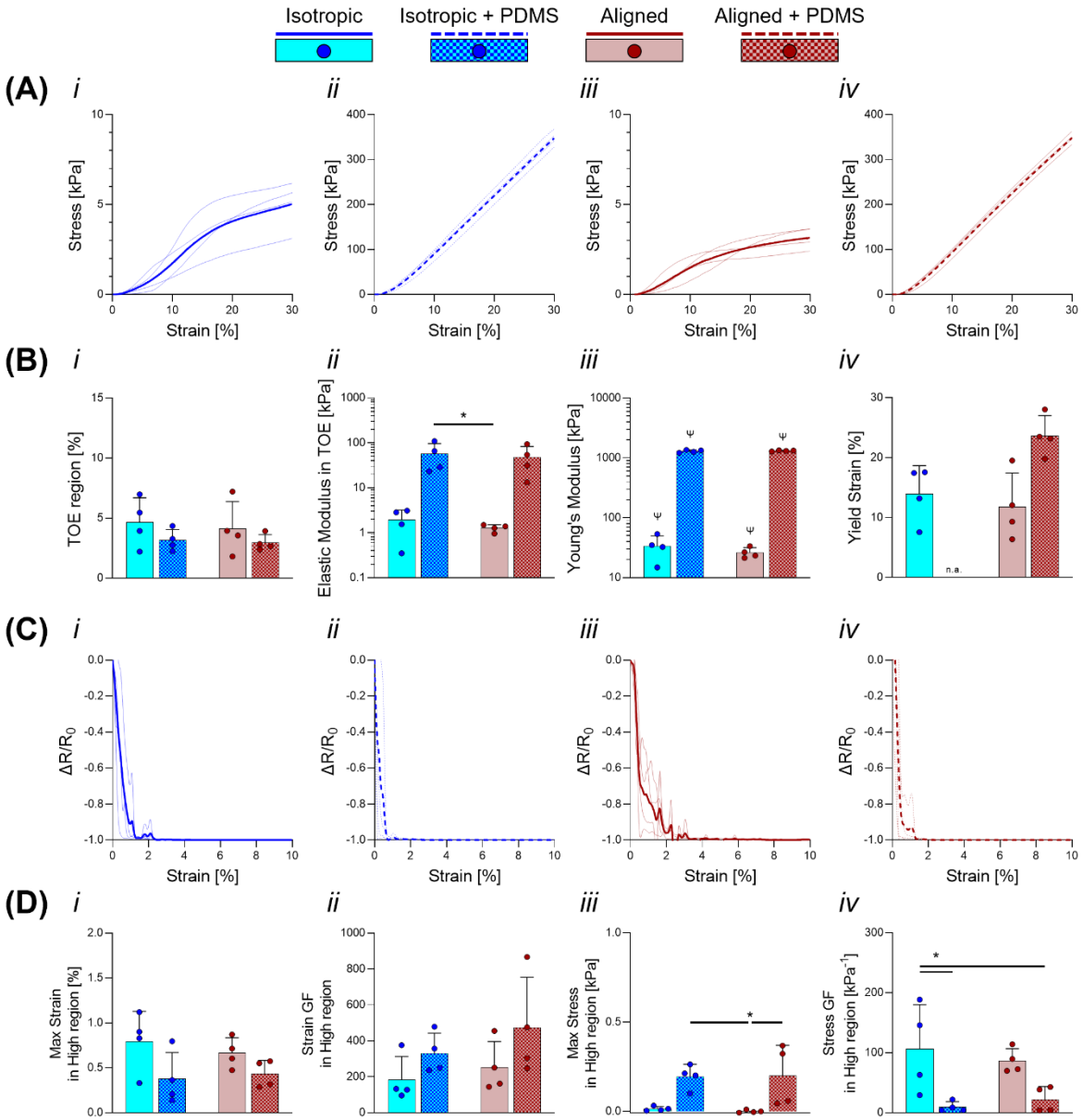


***Figure 6-7.*** *Analysis of the piezoresistive response in the ramp phase.* ***(A)*** *Individual replicates (thin lines) and mean (thick lines) stress-strain curves for scaffolds and EAS with isotropic and aligned morphology.* ***(B)*** *Quantification of different mechanical parameters (n=4): extension of the toe region , **e**lastic modulus of the toe region, Young's modulus and yield strain, where "n.a.„ indicates that the yield strain was not reached in the range of deformation applied in the test.* ***(C)*** *Mean curves of the variation of resistivity over strain for scaffolds and biphasic EAS with isotropic and aligned morphology.* ***(D)*** *Quantification of different piezoresistivity parameters for the High region* ***(D)*** *(n=4): maximum strain, strain gauge factor, maximum stress and stress gauge factor. Bar graphs demonstrate the mean with error bars representing standard deviation. Data values are presented as associated points. * represents statistical significance (p<0.05) between indicated groups, ψ represents statistical significance (p<0.05) between the indicated group and all other groups excluded the one with same stiffness. Statistical analysis was performed using two-way ANOVA with Tukey's post-hoc test.*

reported.

As discussed in C*hapter 4*, the use of elastomeric fillers to generate biphasic constructs is meant to overcome the typical limitations of CP-based sensors. The common strategy of

coating electroconductive materials onto pre-existing substrates is a facile solution to fabricate piezoresistive with high sensitivity. However, the resulting constructs are often characterised by poor long term stability due to recurring delamination.[295] Alternatively, the addition of electroconductive materials to an insulant material before the processing allows for more stable and performant devices.[312,324] For such constructs, the versatility and the modification of the architectures are mainly dependent on the insulant material, potentially hindering the generation of complex morphological features. Instead in the current work, the creation of biphasic EAS was a two-step fabrication protocol, whereby the processing of PEDOT:PSS-PEGDE was prior to the addition of any secondary material. In this way, the lyophilisation of the liquid blend of PEDOT:PSS-PEGDE enabled the generation of both isotropic and aligned electroconductive scaffolds.

**Table 6-2** summarises main mechanical and piezoresistive data obtained for PEDOT:PSS-

PEGDE in this current *Chapter* together with those of the PEDOT:PSS-GOPS investigated in *Chapter 4*, for a direct comparison of the two materials. The use of different microarchitectures and the presence of elastomeric matrices had similar effects for both materials. PEDOT:PSS-PEGDE sensors acted similarly or even better than their GOPS

***Table 6-2**. Summary of mechanical and piezoresistive parameters for PEDOT:PSS-GOPS and PEDOT:PSS-PEGDE scaffolds and biphasic EAS. Data are presented as mean ± standard deviation*

| Material and Geometry | Matrix | Mechanical parameters | | | | Piezoresistive parameters in High region | | | |
|---|---|---|---|---|---|---|---|---|---|
| | | Toe region [%] | Elastic modulus in toe [kPa] | Young's modulus [kPa] | Yield strain [%] | MAX Strain [%] | Strain GF | MAX Stress [kPa] | Stress GF [kPa$^{-1}$] |
| *PEDOT:PSS GOPS isotropic* | *noPDMS* | 3.4 ± 1 | 17.5 ± 7.1 | 105.3 ± 35.9 | 9.6 ± 3.1 | 0.71 ± 2.6 | 134 ± 45 | 0.15 ± 0.08 | 7.71 ± 3.86 |
| | *Stiff PDMS* | 3.5 ± 0.4 | 97 ± 36.6 | 1283.8 ± 51.5 | n.a. | 0.22 ± 0.06 | 387.8 ± 53.2 | 0.32 ± 0.24 | 6.53 ± 3.22 |
| *PEDOT:PSS GOPS aligned* | *noPDMS* | 4 ± 1.4 | 2.5 ± 1.5 | 36 ± 8.1 | 14.2 ± 6.1 | 1.06 ± 0.27 | 89.6 ± 27 | 0.03 ± 0.02 | 37.04 ± 16.38 |
| | *Stiff PDMS* | 3.1 ± 1 | 61.1 ± 33.9 | 1302.7 ± 98.7 | 23.8 ± 2 | 0.4 ± 0.03 | 257 ± 30.4 | 0.23 ± 0.13 | 6.33 ± 5.36 |
| *PEDOT:PSS PEGDE isotropic* | *noPDMS* | 4.6 ± 2.1 | 1.9 ± 1.3 | 34 ± 15.9 | 13.9 ± 4.7 | 0.8 ± 0.33 | 183.3 ± 129.8 | 0.014 ± 0.013 | 106.7 ± 73.4 |
| | *Stiff PDMS* | 3.2 ± 0.9 | 56.9 ± 39.9 | 1296.4 ± 64.2 | n.a. | 0.38 ± 0.29 | 330.8 ± 112.4 | 0.19 ± 0.07 | 9.9 ± 8.5 |
| *PEDOT:PSS PEGDE aligned* | *noPDMS* | 4.1 ± 2.2 | 1.3 ± 0.2 | 26.2 ± 5.4 | 11.8 ± 5.6 | 0.67 ± 0.17 | 253.5 ± 142.4 | 0.001 ± 0.008 | 86.6 ± 20.3 |
| | *Stiff PDMS* | 2.9 ± 0.7 | 48.2 ± 34.8 | 1318 ± 25 | 23.6 ± 3.4 | 0.43 ± 0.15 | 473.5 ± 280 | 0.2 ± 0.17 | 22.2 ± 21.3 |

counterpart. In terms of strain-dependent gauge factor, both PEDOT:PSS-PEGDE scaffolds and biphasic EAS outperformed most of the reported compressive sensors, which have shown to reach peaks between 20 and 300.[327,334] Different conclusions can be made about the extension of the high-sensitivity strain region, generally between 0.38% and 0.8% strain. These ranges enabled the sensor to be highly sensitive to small deformations and limited their operative regions, thus quickly reaching signal saturation. The stress-dependent gauge factor of the *isotropic noPDMS* group reached peaks as high as 106 $kPa^{-1}$ - the highest amongst all combinations of material and architecture that were evaluated in this thesis. Such a response is readily explained by the significantly softer structure of this family of scaffolds, from which it derives that a higher resistivity variance occurred in a reduced stress range.

## *6.5. Conclusions*

With the growing interest in the discovery of new electroconductive materials for application in the biomedical sciences, conjugated polymers - in particular PEDOT:PSS - offer a promising way towards the realisation of cheap and manufacturable products. Going beyond 2D coatings and thin films, researchers have been increasingly focussing on the fabrication of 3D structures.

Here PEGDE was used to crosslink PEDOT:PSS and enable the generation of 3D sponge-like scaffolds via lyophilisation. Both isotropic and anisotropic structured with tailored architectures were manufactured, showing dependence between their morphology and their mechanical and electrical features. Compared to the standard method of GOPS-crosslinking, these constructs exhibited an overall weaker stability in water environment and an enhanced electrical conductivity. In vitro analysis showed indications of cytotoxicity.

The embedding of the PEDOT:PSS-PEGDE scaffolds into PDMS enabled the fabrication of biphasic electroactive sponges (EAS). Investigation over their piezoresistivity response revealed high strain-dependent gauge factor, but also poor consistency between replicates. Overall, this data discourages the use of PEDOT:PSS-PEGDE scaffolds as biosensors and

as substrates for tissue engineering at the current state. Further studies might reveal new strategies to improve the sensor performances.

# 7. Structural crystallisation of crosslinked 3D PEDOT:PSS anisotropic porous biomaterials to generate highly conductive platforms for tissue engineering applications

A significant amount of this C*hapter* has been published previously in:

**Solazzo, M.,** Monaghan, M. G. Structural crystallization of crosslinked 3D PEDOT:PSS anisotropic porous biomaterials to generate highly conductive platforms for tissue engineering applications. Biomaterials Science, 9, 4317-4328 (2021).

## *7.1. Abstract*

An emerging class of materials finding applications in biomaterial science - conjugated polymers (CPs): are enabling the achievement of smarter electrode coatings, piezoresistive components within biosensors, and scaffolds for tissue engineering. Despite their advances in recent years, there exist still some challenges which have yet to be addressed, such as long-term stability in physiological conditions, adequate long-term conductivity and optimal biocompatibility. Additionally, another hurdle to the use of these materials is their adaptation towards three-dimensional (3D) scaffolds; a feature that is usually achieved by virtue of applying CPs as a functionalised coating on a bulk material. Poly(*3,4*-ethylenedioxythiophene):poly(styrene sulfonate) (PEDOT:PSS) is by far one of the most promising CPs in terms of its stability and conductivity, with the latter capable of being enhanced via a crystallisation treatment using sulphuric acid. In this work, I present a new generation of 3D electroconductive porous biomaterial scaffolds based on PEDOT:PSS crosslinked via glycidoxypropyltrimethoxysilane (GOPS) and subjected to a sulphuric acid crystallisation. The resultant isotropic and anisotropic crystallised porous scaffolds exhibited, on average, a 1000-fold increase in conductivity when compared with untreated scaffolds. Moreover, I also document precise control over pore microarchitecture, size and

anisotropy with high repeatability to achieve both isotropic and aligned scaffolds with mechanical and electrical anisotropy, while exhibiting adequate biocompatibility. These findings herald a new approach towards generating anisotropic porous biomaterial scaffolds with superior conductivity achieved through a safe and scalable post-treatment.

## *7.2. Introduction*

The use of biomaterials in medical implants, sensors, devices and tissue engineered constructs is continuously evolving with more advanced materials (synthetic and natural) and novel manufacturing approaches emerging to achieve new requirements and demands.[399]

One such emerging group of biomaterials is that of conjugated polymers (CPs).[304] These materials exist in many forms and can be fabricated into films [305], coatings [400], hydrogels [231] and scaffolds.[213,401] CP-based three-dimensional (3D) scaffolds can be challenging to fabricate as many CPs are thermoset materials, deeming them inappropriate for extrusion-based techniques, which primarily rely on polymer melting. One class of CPs of interest is polythiophenes which can exist in a dispersed form in non-polar solvents. Poly(*3,4*-ethylenedioxythiophene) (PEDOT) is one such polythiophene conjugated polymer and it is widely the most investigated one because of its availability in dispersed in aqueous solutions with polystyrene sulfonate (PSS) as primary counterion. Despite this formulation impeding somewhat the original conductivity of pure PEDOT, the resulting material is relatively easy to be processed while offering exhibiting chemical stability. [214,215] In addition to its use in electronic devices [9], it has emerged as a candidate in biomedical application ranging from fabrication of scaffolds for tissue engineering [9] to neural implants. [217]

The use of PEDOT:PSS in creating 3D scaffolds is limited by its inherent property of being dispersible in aqueous solutions; and for this reason, two main approaches have been adopted so far. First: the combination of the electroconductive compound within a bulk matrix, with one example whereby EDOT was polymerised in the presence of alginate to achieve porous PEDOT alginate scaffolds with conductivity in the order of S/m.[11] Second:

via chemically crosslinking of PEDOT:PSS slurries with crosslinking agents such as glycidoxypropyltrimethoxysilane (GOPS).[9,402] The latter approach poses drawbacks in that a rather brittle structure is attained which at the same time compromises the overall conductivity of the scaffold. For instance, PEDOT:PSS films crosslinked at a content of GOPS greater than 1 v/v% have a 500-fold reduction in conductivity.[30] Regardless, GOPS has demonstrated great potential in the fields of tissue engineering and biomaterials due to its adequate cytocompatibility and ease of processing. Towards achieving improved electrical conductivities of PEDOT:PSS, several post-treatments have been reported [224], with the highest values to date resulting from the treatment of spin-coated PEDOT:PSS with sulphuric acid; a process that has adopted the nomenclature 'crystallisation' due to the stacked interweaving nanostructure imparted on the material.[31] With this approach it was determined that the exposure of dried PEDOT:PSS with sulphuric acid removes PSS and generates nanofibrils of PEDOT from its characteristic grain-like morphology via a structural transition mechanism. Since this initial report, this crystallisation process has been applied in vitro [385] and used in the generation of 3D hydrogels.[403]

In this study, I sought to establish if, in scaffolds previously crosslinked and annealed using GOPS, the use of sulphuric acid could achieve such crystallisation and circumnavigate the drawback imparted upon conductivity by GOPS. Therefore, I hypothesise that sulphuric crystallisation can enhance conductivity of GOPS crosslinked PEDOT:PSS scaffolds, while retaining their stability and cytocompatibility.

As PEDOT:PSS is water dispersible; it is an ideal candidate for lyophilisation processing when crosslinked; through which one can have control over pore size, quantity and directionality. Indeed, directional lyophilisation of GOPS crosslinked PEDOT:PSS scaffolds has been previously reported; yet with modest conductivities.[6] Here I document a new generation of sulphuric crystallised GOPS-crosslinked PEDOT:PSS porous scaffolds with a significant increase in conductivity and elasticity, while at the same time maintaining biocompatibility. A detailed characterisation of scaffold anisotropy not limited to the morphology but also extending to its mechanical and electroconductive properties is also

presented.

## *7.3. Experimental section*

### *7.3.1. Fabrication of 3D GOPS crosslinked porous scaffolds*

To proceed with acidic crystallisation of the resultant porous constructs, I adopted a method previously reported [31] that briefly entailed soaking the construct in 100% sulphuric acid. All samples, both untreated and crystallised, were subjected to multiple washings using deionised water and shaped to optimised thickness with a vibratome (VT 1200S, Leica. Germany) Finally, a second lyophilisation process carried out to fully dry the materials.

For in vitro studies, collagen scaffolds were adopted as controls.

### *7.3.2. Scaffold morphology*

Micrographs from aligned scaffolds were then post processed with ImageJ plugin OrientationJ [404] so to derive the lamellae alignment and the degree of anisotropy.

### *7.3.3. X-ray Diffraction (XRD)*

XRD investigation was carried out on two-dimensional drop-casted samples with a Benchtop X-Ray Diffractometer (D2 Phaser 2$^{nd}$ generation. Bruker). The PEDOT:PSS-GOPS slurry was injected on PTFE substrates and let dry for 2 hours at 60 °C. Afterwards, crystallisation and a series of washings were performed as for the 3D structures, finally followed by a second drying phase.

### *7.3.4. Mechanical characterisation*

In addition to the stress-relaxation test described ion C*hapter 3*, a cyclic test with increasing strain to detect measure of the viscoelastic response of the constructs [405]. After the application of a preload of 0.005N, samples were compressed at 0.5 %/sec from 1% to 60% with variable steps of 1% strain per cycle between 1% and 5%, of 5% strain from 5% to 30%, and finally of 10% strain from 30% to 60%. The amount of hysteresis of each cycle

were computed with a custom made Matlab® script as a ratio between unloading/loading areas. The deformation at which an abrupt reduction of this ratio happened was identified as the elastic/plastic transition point. From the same dataset, it was also possible to derive the residual strain deformation at zero stress per every strain cycle.

### *7.3.5. Biocompatibility studies*

To assess any potential influence of the crystallisation process on material biocompatibility, indirect and direct cytotoxic tests were performed.

For the indirect contact assay, untreated and crystallised scaffolds were sterilised with multiple washings in 70 v/v% ethanol and exposed to UV light. Following rinsing with PBS, specimens were let to macerate in growth media with a ratio of 10 mg of dry material per ml of media. I obtained extraction media substituting the liquid in contact with the material at day 1, 3, 5, 7, in order to identify any potential effect of early days by-products release. Cells were seeded on standard tissue culture plate at a density of $10 \times 10^4$ cells per $cm^2$ in standard growth media. At 24 hours, standard media was replaced by extraction media that was left in contact with the cells for more 24 hours.

To evaluate cell condition, I performed a standard AlamarBlue™ metabolic assay, and I qualitatively observed cell morphology by cytofluorescent staining.

For the direct contact in vitro study, scaffolds with 6 mm diameter and 1 mm thickness were adopted. Following the pre-conditioning, a cell suspension of 20 µl growth media and 250k cells was injected on each scaffold, and after two hours more culture medium was added. Cells were fed every other day up to day 7.

Cell viability was evaluated at day 1 and 7 with live/dead assay. DNA was quantified with a Picogreen™ biochemical assay on papain digested specimens. As for the indirect contact test, both AlamarBlue™ assay and staining for nuclei/f-actin were performed.

## 7.4. Results and discussion

### 7.4.1. Crystallisation of 3D porous scaffolds increases their overall porosity and volume and can be fabricated into anisotropic porous scaffolds

High porosity, adequate pore size and fibre orientation are some of the topological requirements for tissue engineering scaffolds, together with suitable stiffness.[304] With the ultimate goal of obtaining control over these features, several advanced manufacturing techniques have been implemented ranging from salt leaching, thermal induced phase separation, electrospinning and the more recent advent of additive manufacturing via exploitation of fused deposition modelling [406] and even more recently, melt electrospinning writing.[407] In this context, based upon clear and defined concepts of physics and thermodynamics, lyophilisation (also known as ice-templating or freeze-drying) has been demonstrated as an appropriate technique to achieve a high level of porosity and anisotropy within scaffolds. PEDOT:PSS is commonly dispersed in water, making it extremely suitable for freeze-drying. In this study, 3D GOPS-crosslinked PEDOT:PSS scaffolds were fabricated using a freeze-drying technique similar to that reported by others [9,402] and were subjected to a sulphuric crystallisation treatment reported previously in two-dimensional coatings of PEDOT:PSS.[31] The fabrication of these scaffolds enabled the creation of broad range of sizes, shapes and anisotropy as shown in **Figure 7-1.A** and **S7.A**.

Sulphuric crystallisation yielded a 10% decrease in mass together with a volumetric expansion of approximately 100% (**Figure S7.B**), and an increase in porosity from 95.4 ± 2.1 % to 98.5 ± 0.5 % that was measured via ethanol intrusion (**Figure 7-1.B**). Scanning electron microscopy (SEM) validated a porous homogeneous structure for both untreated and crystallised PEDOT:PSS scaffolds, confirming that the sulphuric acid treatment did not lead to any major detrimental change in the porous microarchitecture (**Figure 7-1.C**). Morphological quantification of scaffold sections enabled an accurate understanding of pore

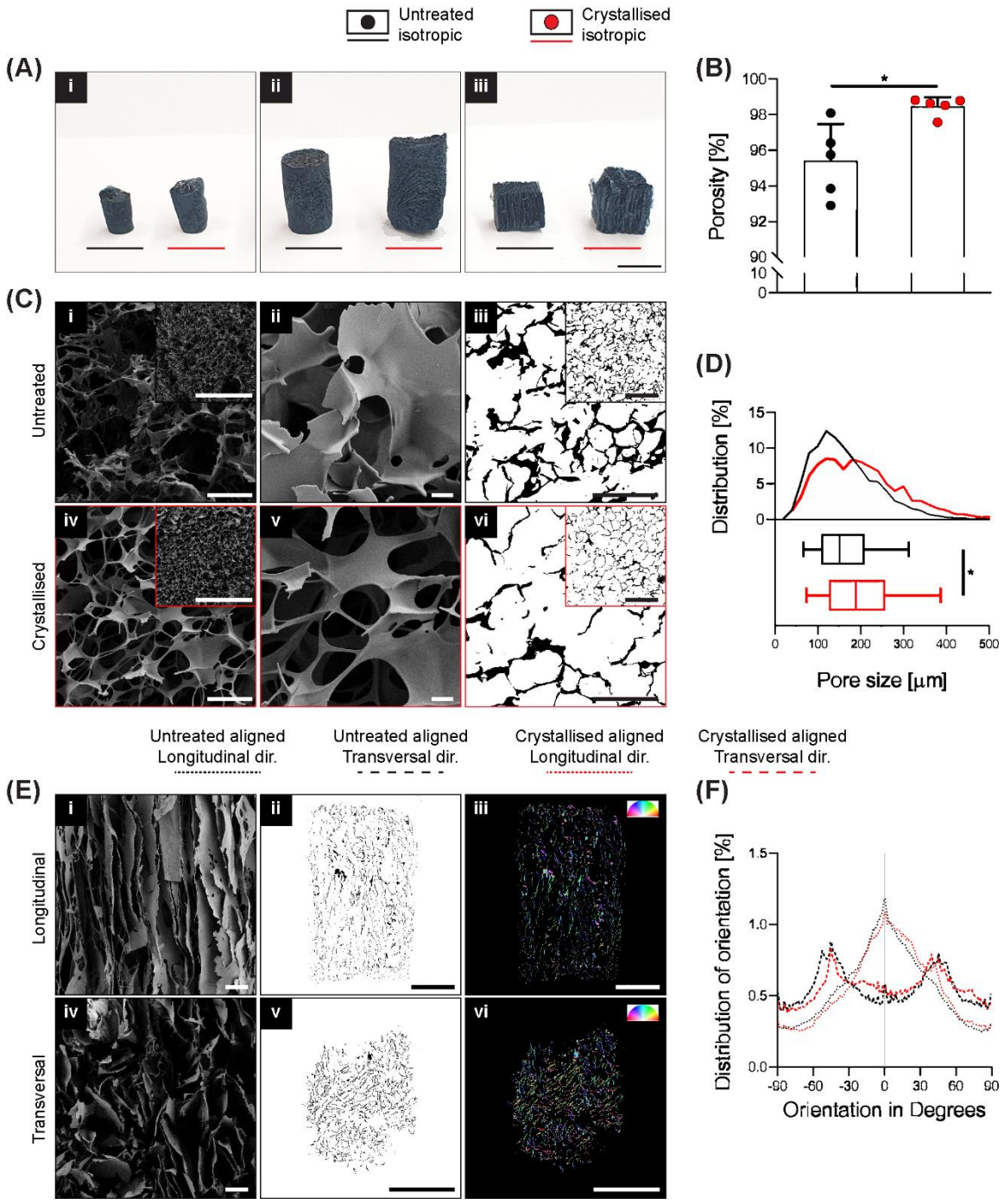


***Figure 7-1*** *Processing effects on PEDOT:PSS 3D scaffolds* ***(A)*** *Images of three pairs of freeze-dried scaffolds of different shapes demonstrating both untreated the crystallised examples. i: "isotropic small", ii: "isotropic big", iii: "aligned".* ***(B)*** *Porosity of isotropic scaffolds evaluated by ethanol intrusion method (n=5).* ***(C)*** *Evaluation of microarchitecture on isotropic scaffolds via SEM micrographs (C i/ii/iv/v) and sliced agarose embedded scaffolds (C iii/vi).* ***(D)*** *Pore size quantification from analysis of sliced agarose embedded scaffolds (n=3 per direction). Top: distribution of pore size as percentage; bottom: cumulative mean and standard deviation.* ***(E)*** *Evaluation of microarchitecture on aligned scaffolds via SEM micrographs (E i/iv) and sliced agarose embedded scaffolds (E ii/iii/v/vi).). E iii/vi: colour survey representation of fibre orientation via OrientationJ (ImageJ plugin).* ***(F)*** *Distribution of orientation, with 0° representing the fibre direction in the Longitudinal view (n=3 per direction). Scale bars: A = 1 cm; C i/ii/iv/v = 100 µm; C i/iv inset = 1 mm; C iii/vi = 200 µm; C iii/vi inset = 500 µm, E i/iv = 200 µm, E ii/iii/v/vi = 2 mm . Bar graphs demonstrate the mean with error bars representing standard deviation. Data values are presented as associated points. * represents statistical significance (p<0.05) between indicated groups using Student's unpaired t-test.*

size on isotropic scaffolds and detected a significant increase from 165 ± 78 µm to 202 ± 100 µm when scaffolds were crystallised using sulphuric acid (**Figure 7-1.C iii/vi** and **7-1. D**).

In several tissue engineering applications control over substrate topography and attainment of anisotropic constructs to mimic physiological substrates is an important consideration. Here, freezing the PEDOT:PSS solutions along a preferential axis of heat transfer by virtue of a custom-made mould enabled the fabrication of highly aligned scaffolds (**Figure 7-1.A iii**). This preferential axis of heat transfer and subsequent sublimation of ice crystals generated a highly anisotropic structure consisting of parallel two-dimensional lamellae with a dominant directionality along the axis of heat-transfer (i.e. freezing vertically) clearly demonstrated by SEM micrographs in both longitudinal and transversal directions in **Figure 7-1.E**.

In a similar manner, aligned samples were sectioned for imaging analysis to quantify pore orientation within the internal structure (**Figure 7-1.E ii/iii/v/vi**). This quantification is summarised in **Figure 7-1.F** and testifies a high degree of pore alignment along the plane longitudinal to the fibers (i.e. identified at 0° in the plot) that results in a Gaussian-like distribution of orientation with peak in proximity of the 0° direction, while a dispersed distribution with no prevalent directionality was found for the transversal plane. SEM at higher magnifications revealed the presence of cracks along on the surface of the material which were not present on the smooth surface of untreated porous scaffolds and that may represent crystal boundaries as previously reported [31,403] (**Figure 7-2.A i/iii**). These boundary features have been previously reported as characteristic of the process of PEDOT:PSS crystallisation, attributed to the removal of excess PSS and to the stacking of PEDOT into a more lamellar fashion.[31] **Figure 7-2.A ii/iv** show typical effects of the etching process by use of strong acids: a substantial thinning of the porous scaffold struts which is in agreement with the mass loss, the significant increase porosity and pore size caused by the process; ultimately suggesting a partial surface erosion of the porous scaffolds. From the same figures, it is possible to observe how the inner portion of the struts, despite being

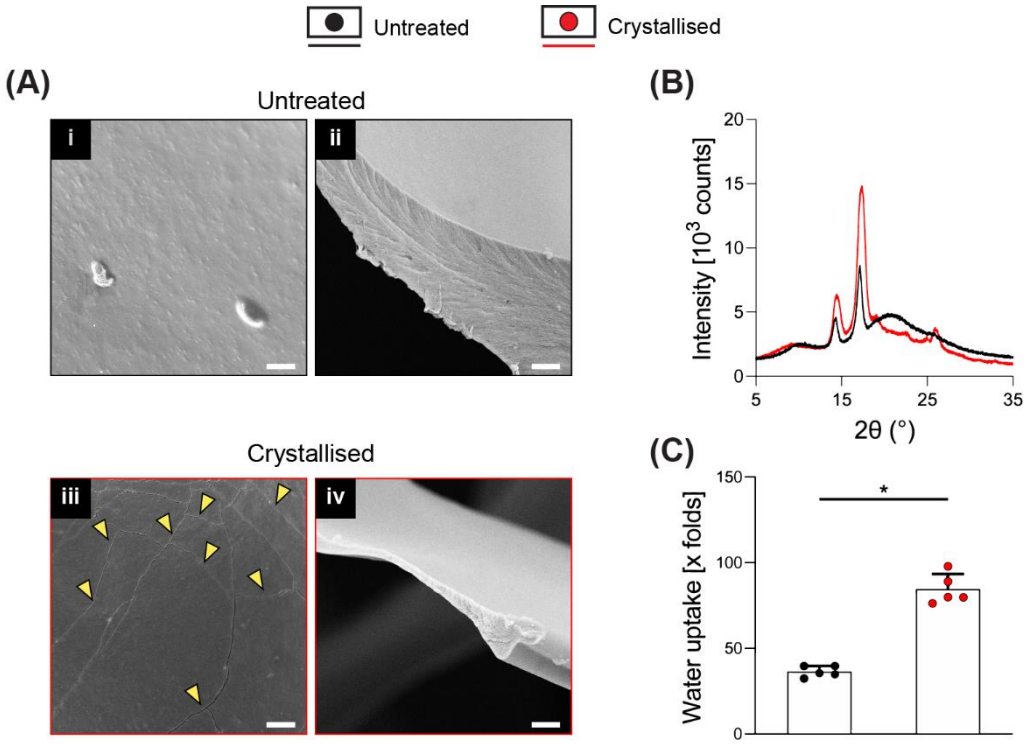


***Figure 7-2*** *Assessment of crystallisation treatment on material microstructure, chemistry and swelling properties.* ***(A)*** *Micrographs from high magnification SEM showing details of the surface (i/iii) and of the section (ii/iv) of the scaffolds. Yellow arrows pointing to cracks.* ***(B)*** *X-ray diffraction (XRD) patterns of drop casted thin sheets.* ***(C)*** *Swelling of dry scaffolds soaked in deionised water, measured as water uptake (n=5). Scale bars: A = 2 µm. Bar graphs demonstrate the mean with error bars representing standard deviation. Data values are presented as associated points. * represents statistical significance (p<0.05) between indicated groups using Student's unpaired t-test.*

reduced in thickness, did not present any other major conformational changes after crystallisation, maintaining the same marbled pattern; further evidencing that the crystallisation treatment mainly influences the outer part of the strut. Towards physicochemical verification of this treatment, XRD analysis was applied to drop casted samples (of GOPS-crosslinked PEDOT:PSS) that underwent the same crystallisation protocol of the 3D scaffolds (**Figure 7-2.B**). GOPS-crosslinked PEDOT:PSS samples subjected to crystallisation lacked the characteristic peak of PSS at 2θ = 20.5° [408] - an observation that has been reported to similar crystallisation treatments of PEDOT:PSS.[31] Crystallised scaffolds demonstrated a significant increase in water intake up to 85 times their dry weight (**Figure 7-2.C**), that is remarkably higher compared to recently reported 3D PEDOT-Alginate hydrogel [11] and which I postulate as being a direct effect of the significant increase in porosity, volume and pore size. The efficacy of GOPS crosslinking was not compromised by the crystallisation treatment. Indeed, scaffolds were able to maintain

exceptional durability in water environment, with no evidence of macroscopical deterioration after 3 months at room temperature.

One previous study reports sulphuric crystallisation on thin PEDOT:PSS coatings (with a thickness in the range of hundreds of nm) whereby PEDOT:PSS was used in its pristine form with no additional molecules or crosslinkers were used. In order to achieve 3D conformations, a crosslinker such as poly(ethylene glycol) diglycidyl ether or GOPS can be adopted, but with the later potentially lowering conductivity of PEDOT:PSS.[30] Whether the presence of a crosslinking agent may have hindered the efficacy of the sulphuric crystallisation was one point of query prior to beginning this study. However, crystallisation via sulphuric acid post-treatment in this study was successfully applied to 3D porous constructs while at the same time enabling concise control over scaffold micro-architecture.

### *7.4.2. Crystallised anisotropic scaffolds exhibit more elastic behaviour that behaves anisotropically*

We performed a detailed series of mechanical tests to gain an overview of the mechanical performance of scaffolds in hydrated conditions, a typical environment of most biomedical applications. Indeed, the liquid present in the surrounding environment plays an important role, influencing the overall response of biomaterial scaffolds.[409] This is particularly relevant for the constructs presented in this work, whereby a >95% porosity (**Figure 7-1.B**) and substantial water intake occurs (**Figure 7-2.C**) which may potentially impact temporal viscoelastic properties. Therefore, a series of phases in mechanical testing allows one to decouple the different components and determine the extent to which the porous morphology and water uptake influence the overall mechanical outcome.[292]

In **Figure 7-3** a combination of stress-relaxation and dynamic test are reported. Within the first phase of the test, samples were compressed up to 15% strain with a relatively slow strain rate in order to derive the stiffness of the construct for a standard unconfined compression. The Ramp Modulus was derived as the slope of the curve in the range 5-10% of deformation, where the stress-strain relationship is linear, ultimately obtaining a stiffness

value in the range of previous works on PEDOT:PSS.[402] The 15% strain was then maintained for 45 minutes, to accommodate relaxation of the scaffold structure. The Equilibrium Modulus was derived as the ratio between stress and strain at the end of relaxation, providing a measure of stiffness without any hydraulic fluid pressurisation. The last cyclic loading phase enabled determination of the scaffold's responses in physiological regimes, where the viscous component of the fluid has a significant impact. Notably, the

Dynamic Modulus reflects the permeability of the matrix and the ease at which the structure can exudate fluids when subjected to a deformation. This aspect is an index of how a construct can generate fluid load support; all important considerations to be taken into account for anatomic structures that rely on a fluid component, for example articular cartilage.[409] Results are summarised in **Table 7-1**, demonstrating how the morphological

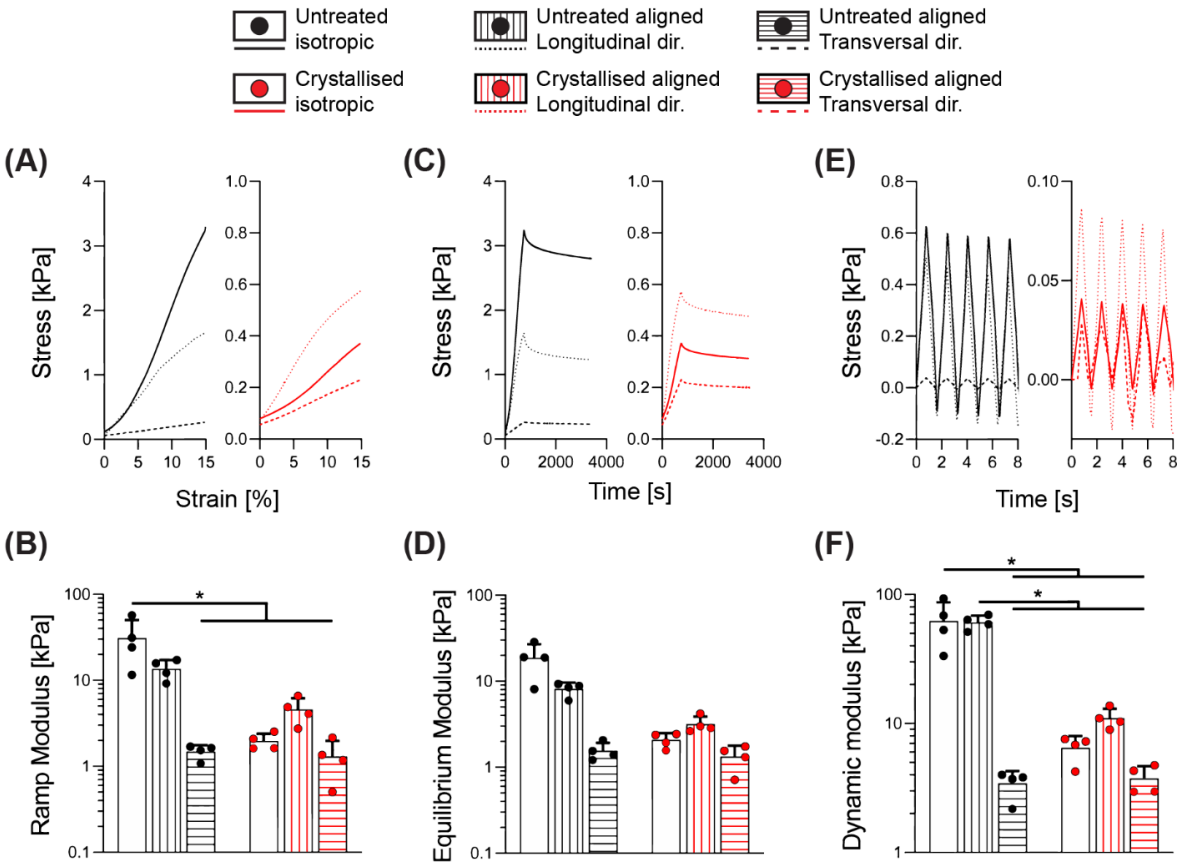


***Figure 7-3*** *Stress relaxation followed by dynamic cyclic compression test.* ***(A)*** *Stress-strain curves representing mean response during ramp phase.* ***(B)*** *Ramp Modulus.* ***(C)*** *Stress-time curves representing mean response during relaxation phase.* ***(D)*** *Equilibrium Modulus.* ***(E)*** *Stress-time curves representing a standard response during dynamic cyclic loading phase.* ***(F)*** *Dynamic Modulus. Bar graphs demonstrate the mean of n=4 replicates with error bars representing standard deviation. Data values are presented as associated points. * and # represent statistical significance (p<0.05) (* between indicated groups, # with all other groups) using two-way ANOVA with Tukey's post-hoc test.*

***Table 7-1**. Summary of mechanical (n=4) and electrical (n=5) properties of tested samples. Data are presented as mean ± standard deviation*

| Material | Geometry | Ramp Modulus [kPa] | Equilibrium Modulus [kPa] | Dynamic Modulus [kPa] | Conductivity [S/m] |
|---|---|---|---|---|---|
| Untreated | Isotropic | 31.02 ± 19.23 | 18.66 ± 8.39 | 62.16 ± 25.26 | $7.01 \pm 5.01 \times 10^{-5}$ |
| | Longitudinal | 13.61 ± 3.62 | 8.14 ± 1.49 | 60.82 ± 7.73 | $2.33 \pm 2.05 \times 10^{-5}$ |
| | Transversal | 1.49 ± 0.28 | 1.55 ± 0.37 | 3.43 ± 0.85 | $3.69 \pm 3.51 \times 10^{-6}$ |
| Crystallised | Isotropic | 1.96 ± 0.43 | 2.08 ± 0.41 | 6.47 ± 1.52 | $3.45 \pm 2.83 \times 10^{-2}$ |
| | Longitudinal | 4.58 ± 1.61 | 3.18 ± 0.71 | 11 ± 2.01 | $1.18 \pm 0.53 \times 10^{-1}$ |
| | Transversal | 1.30 ± 0.68 | 1.33 ± 0.45 | 3.75 ± 0.92 | $1.39 \pm 1.42 \times 10^{-2}$ |

anisotropy has a significant effect on the elasticity of the aligned scaffolds for all three types of moduli investigated (Ramp, Equilibrium, Dynamic), with a longitudinal/transversal ratios of 9.16, 5.24, 17.74 for the untreated groups while diminished ratios of 3, 54, 2.39, 2.94 respectively were derived for the crystallised samples. Crystallisation of the scaffolds yielded a significant decrease in stiffness for the isotropic and the aligned scaffolds in the longitudinal direction, while no major effect was found in the transversal direction. This observation can be rationalised by the topographical alterations elicited by crystallisation; an increase in pore size and porosity accompanied by the thinning of the struts. As demonstrated in **Figure S8**, significant trends in peak stress to equilibrium stress ratio were observed between the different geometries, with a reduction in this ratio with isotropic crystallised scaffolds and in transversal direction for both untreated and crystallised aligned structures. These findings suggest that the sulphuric acid treatment and the direction of loading both contribute to a diminished ability to maintain fluid load support.

Correlating the mechanical resilience of the structures with the dissipative energy of each deformation cycle, I performed a hysteresis analysis with cyclic loading constantly increasing the strain up to 60% (**Figure 7-4**). The decrease of the ratio between unloading area (recovered energy) over loading area (applied energy) is characteristic of the transition between elastic to plastic deformation [405]. This transition occurred within the range of 30-40% for both the isotropic and the aligned scaffolds when evaluated transversally, while an initial decrease was visible already at 15% strain for the longitudinally compressed aligned

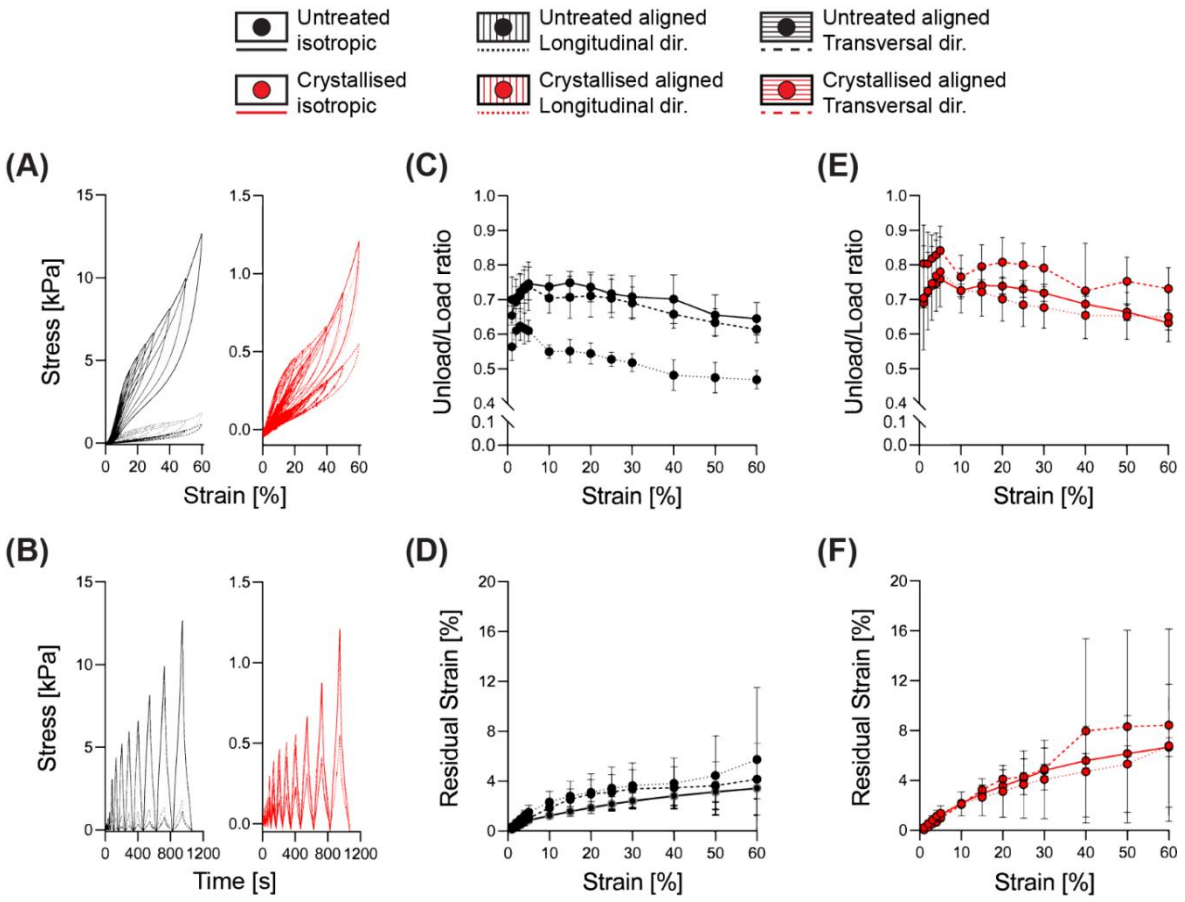


***Figure 7-4*** *Elasto-plastic response as analysis of hysteresis for isotropic and aligned scaffolds.* ***(A, B)*** *Stress-strain and stress-time curves representing a standard response within cycles.* ***(C, E)*** *Unload/Load ratio response at different strain amplitude.* ***(D,F)*** *Residual strain quantified as unrecovered deformation at zero force for each cycle. Data points demonstrate the mean of n=4 replicates with error bars representing standard deviation.*

structures. This event is mainly based on the morphology of the aligned samples, as a compression parallel to the lamellae will first lead to a compacting between them, before beginning to deform permanently, and similarly for the isotropic structures where the pseudo-spherical shape of the pores allows for a higher range of elastic deformation. Instead, a compression perpendicular to the lamellae would directly operate on the struts, causing deformation starting from lower strain levels.

### *7.4.3. Crystallisation of porous scaffolds yields over a thousand-fold increase in conductivity that can be tuned anisotropically*

While it is often taken for granted that CPs are inherently easy to process in comparison to standard metals - this is an over-simplification by nature of their classification as polymers. Achieving a construct based on CPs as the bulk and only material component

has been mostly limited to two-dimensional films or thin sheets, or to 3D structures compromised by relatively low conductivity values. Most works report the fabrication of electrically conductive hydrogels or porous structures; however, all rely on the combination of the CP with a supporting matrix.[11,410]

Here I discovered that the sulphuric crystallisation yielded a profound increase in conductivity, of approximately 500-fold for the isotropic scaffolds; while the aligned scaffolds went even further with a conductivity increase in the order of 4000- and 5000-fold for the transversal and the longitudinal directions, respectively (**Figure 7-5.C** and **Table 7-1**). Furthermore, I also found a substantial difference in conductivity that was significantly influenced by the diverse geometries of the samples. The longitudinal direction, being constituted by parallel lamellae acted as a highway for the electrical conduction, leading to a conductivity of 6.3 and 8.4 folds higher when compared to the transversal direction, respectively for both the untreated and the treated groups (**Figure 7-5.C**).

When comparing electrical conductivity results from reported from various studies; it is appropriate that the technique being adopted is considered, with 4-point probe being used for 2D substrates [305], 2-point probe for 3D constructs [9] and electrochemical impedance spectroscopy (EIS) as a valid method for both configurations.[305,403] One example of a highly

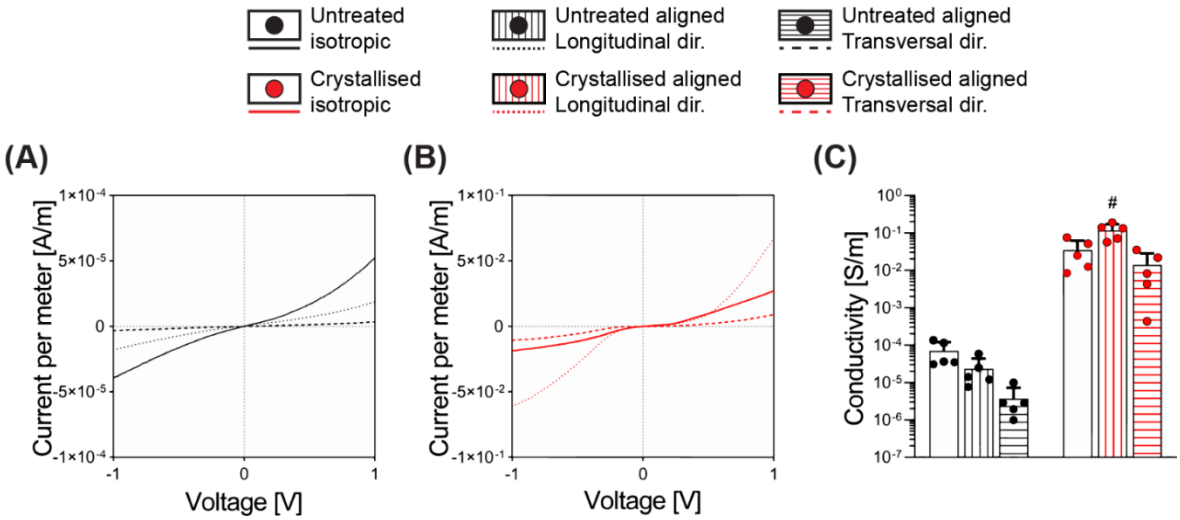


***Figure 7-5*** *Electrical conductivity measurements via 2-point probe.* ***(A-B)*** *I-V curves of untreated (A) and crystallised (B) PEDOT:PSS scaffolds.* ***(C)*** *Conductivity quantification from linear regression of I-V curves in the linear region 0.5 - 1 V (n=5). Bar graphs demonstrate the mean with error bars representing standard deviation. Data values are presented as associated points. # represent statistical significance (p<0.05) with all other groups) using two-way ANOVA with Tukey's post-hoc test.*

conductive material achieved via a solvent approach entailed the fabrication of thick 2D hydrogels and anisotropic drying without the addition of secondary molecules. Here the authors reported values in the range of 20 S/cm in PBS, with such conductivity acquired from 2D constructs using a 4-point probe setup, therefore not directly comparable to the scaffolds I report in this study.[411]

In this work, I adopted a 2-point probe measurement in order to successfully delineate a relationship between scaffold pore directionality and conductivity. Another matter that one must consider is that the values I report here for all electrical characterisation have been measured on samples that have been washed multiple times and freeze-dried again, a process that purifies the material from unreacted products, but that reduces conductivity. GOPS-crosslinked PEDOT:PSS porous constructs have been reported with electrical conductivities in the order of $1.5 \pm 0.5 \times 10^{-3}$ S/m when freshly prepared which can deteriorate by one order of magnitude after 4 days in culture media.[9] This mediocre conductivity can be somewhat overcome through the addition of secondary dopants (such as dodecylbenzenesulfonic acid, DBSA) which can boost the conductivity for the initial days of culture.

A stand-alone example of PEDOT:PSS porous 3D structure with no presence of supporting compound relied on the gelation process achieved by sulphuric acid, however the 12-hours long post treatment potentially caused disadvantages in terms of biocompatibility that have not been assessed yet. Moreover, despite providing promising conductivity values up to 880 S/m (as measured by EIS), the gelation process adopted did not permit for control over the microarchitecture.

To the best of our knowledge, this work is the first successful attempt to merge the precise optimisation of the morphology via ice-templating technique together with crystallisation treatment on a PEDOT:PSS chemically crosslinked scaffold that had not been combined with a supporting material.

### *7.4.4. Crystallised PEDOT:PSS porous scaffolds are cytocompatible and serve as a 3D scaffold for 3D cell culture*

An initial concern of using the sulphuric crystallisation approach was the risk of residual acid remaining on the scaffold. Phenol red-containing media was adopted for all studies in this work, and no change in the media colour was ever observed, an initial indication of the absence of acidic residue. Therefore, I proceeded with more thorough evaluations of cytotoxicity, via an indirect test and direct seeding of cells onto these scaffolds.

The release of toxic by-products into media was assessed by applying an extraction media (whereby scaffolds were placed in an extraction medium for 24 hours) onto C3H10 cells seeded on standard tissue culture plates. Cellular metabolism was evaluated using the AlamarBlue™ assay (**Figure S9.A**) and results were normalised to the metabolism of cells grown in standard media that was conditioned in the same environment of the extraction media. This assay detected no statistically significant difference between the untreated and crystallised groups at the same timepoint. A qualitative observation of cell morphology via a nuclei (DAPI)/f-actin (phalloidin) fluorescent staining revealed no substantial difference in either cell adherence or spreading, suggesting that the crystallisation process did not have any residual toxic drawbacks on cell physiology.

Considering the promising results of this indirect evaluation of cytocompatibility, I proceeded with direct seeding of C3H10 cells onto these scaffolds with the scaffold dimensions being standardised to disks of 6 mm in diameter and 1 mm in thickness. 1-ethyl-3-(-3-dimethylaminopropyl) carbodiimide hydrochloride (EDC) crosslinked collagen porous scaffolds have been widely tested with positive outcomes in tissue engineering [412], hence they were adopted as reference control in this work. Assessment of cell response was compared between day 1 and 7 after seeding, via live/dead fluorescent staining (**Figure 7-6.A and S10**) that demonstrated a high viability at both timepoints, with the scaffolds exhibiting an adequate cell attachment at early timepoints and showing high proliferation for the untreated group at day 7. Despite the total number of live cells resulted significantly lower for the crystallised group at day 7 compared to the untreated one (**Figure 7-6.B**), an

opposite trend was found once these values were normalised by the total number of cells and presented as viability % (**Figure S11**). This fact supports the claim that the diminished live cell density may be an effect of the reduced space offered by the struts, leaving cells further from each other and less capable of bridging the pores. This hypothesis was confirmed by fluorescent staining (**Figure 7-6.C**) where cells showed to be adherent to the substrates in all groups and timepoints tested, excluding a detrimental effect due to the material chemistry. The combined increase in both porosity and mean pore size caused a reduced surface area available to the cells for attachment that can also explain their reduced proliferation compared to the untreated group and ultimately a lower value in DNA quantity (**Figure 7-6.D**) and reduction % in AlamarBlue™ assay(**Figure S12**). These findings support the claim of adequate biocompatibility of the crystallised GOPS-crosslinked PEDOT:PSS scaffolds, both with indirect test and with direct contact, paving the way for their use in application of tissue regeneration, biosensors for in vivo studies or monitoring interfaces for in vitro platform

## *7.5. Conclusions*

Several groups are currently working towards solutions to deliver highly conductive and tuneable 3D constructs for tissue engineering and biomaterial applications. The platform I have described here has a significant advantage over similar materials reported to date and has significant potential within and outside the field or biomaterials and tissue engineering. Since its initial report and those following it; GOPS crosslinking of PEDOT:PSS has been associated with a compromise of conductivity properties. I have overcome this through a simple, safe and scalable sulphuric acid crystallisation step which does not impact the stability of 3D porous scaffolds. The porous scaffolds reported in this study (both treated and crystallised) were capable of being fashioned into anisotropic porous configurations which in turn enabled a morphological anisotropy (via pore orientation) which in itself imparted a mechanical and electrical anisotropy to the material. This could have significant impact in situations whereby topographical alignment of cellular growth and cell orientation

are warranted. Indeed, this improved conductivity; and isotropic/anisotropic porous configuration could enable enhanced interaction between tissue and electrode sensing/stimulation systems whereby a more compliant match of electrode conductivity properties with increased surface areas could enhance device performance and overall patient healthcare.

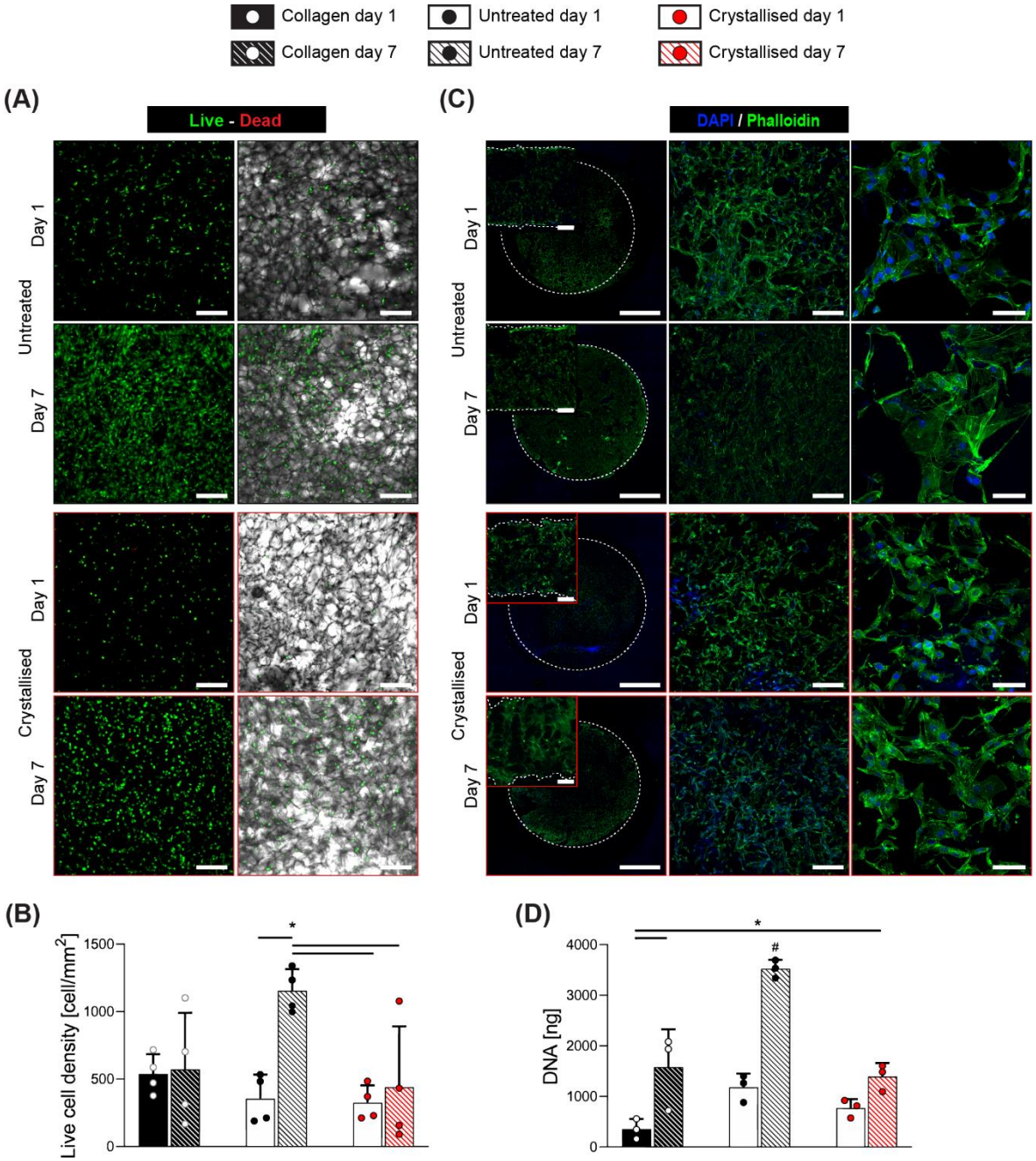


***Figure 7-6.*** *Cytocompatibility of C3H10 cells on scaffolds via direct contact.* ***(A)*** *Micrographs from confocal microscope fluorescent staining for live/dead of CH310 cells at days 1 and 7, seeded on scaffolds. Left: live/dead channels. Right: live/dead/brightfield channels.* ***(B)*** *Quantification of viability (extracted from live/dead Staining) at days 1 and 7, quantified as live cells density (n=4).* ***(C)*** *Micrographs from confocal microscope fluorescent staining for nuclei/f-actin (DAPI and Phalloidin respectively), seeded on scaffolds. Pictures refer to top surface of the samples. Insets refer to the section view of the sample showing cells migrating through all the thickness of the scaffolds. Dotted lines identify samples' borders.* ***(D)*** *Quantification of DNA via Picogreen™ assay, expressed as ng per scaffold (n=3). Scale bars: A = 200 µm; C left = 2 mm; C left insets = 200 µm; C middle = 200 µm; C right = 50 µm. Bar graphs demonstrate the mean with error bars representing standard deviation. Data values are presented as associated points. * and # represent statistical significance (p<0.05) (* between indicated groups, # with all other groups) using two-way ANOVA with Tukey's post-hoc test.*

# 8. An in vitro cardiac model based on 3D PEDOT scaffolds: development and validation of a pacing bioreactor and a flexible holder system to enable contraction performance tracking

## *8.1. Abstract*

Engineered heart tissues (EHTs) are a modern approach for the development of functional in vitro cardiac models, with great translational potential to the pharmaceutical industry and - in the not so immediate future - to heal the infarcted myocardium. While in recent decades researchers have explored the use of different cell types and bio-physical cues to ameliorate their EHTs, the application of novel biomaterials has been negligible, with most approaches relying on scaffold-free strategies. However, the rapid improvement of electroconductive scaffolds may lead to a change in this trend, with constant evidence supporting the benefit of electrically active materials and their influence on the maturation of cardiac cells and tissues.

In this work, I adopt a previously reported porous poly(*3,4*-ethylene dioxythiophene): polystyrene sulfonate (PEDOT:PSS) scaffold for the validation of **R3S** - **R**ig for **S**timulation of **S**ponge-like **S**caffolds. This system has been designed for pacing and simultaneously live tracking of EHTs. It was proven that the synergistic presence of topographical and electrical cues - derived by externally pacing C3H10 cells on an aligned porous scaffold - was responsible for metabolic increase and enhanced cell alignment. Although primary cardiomyocytes (CMs) were successfully seeded onto the scaffolds, their beating was non-homogeneous and further optimisation is required to achieve EHT with adequate functionality. With its improved morphology, cardio-inductive stiffness, and biomimetic electroconductivity, the presented setup is a promising system for scaffold-based EHTs.

## *8.2. Introduction*

Myocardial infarction (MI) leads to the death of cardiomyocytes (CM) in the heart muscle which - for the most part - cannot be replaced.[40,41] Every sixth man and seventh woman will die from a heart attack or related complications, and to date there is no clinical solution to regenerate the myocardium.[413] Pharmacological research has proposed diverse treatments that can prevent the occurrence or limit the damage caused by MI; however, the response to a drug is a multifactorial process highly dependent on the individual patient and therefore success is widely variable.[414,415] Therefore, there is a need for functional in vitro platforms able to replicate complex physiological and pathological mechanisms, that can be used as surrogates of the patient's myocardium. This would facilitate and accelerate the discovery and testing of new medicines, as well as the screening of the most effective treatment for each specific patient.[23]

Engineered heart tissues (EHT) are cardiac in vitro models created to provide a solution to such challenges, as well as an ambitious attempt to recreate myocardium for future transplantation.[416] These platforms aim to replicate the 3D environment of the myocardium with the morphological and metabolic features that impact its contractile function.[18] Over the past 25 years,[20] diverse configurations have been proposed, containing varying cell types, materials, and morphology. The most modern systems are constituted by multiple types of hiPSC-derived cells embedded in fibrin [417] or collagen [18] gels, and mostly shaped as tubules [417], rings [418] or patches.[17] EHTs are often combined with bioreactors capable of delivering diverse cues (e.g. shear rate, mechanical constrain, electrical stimulation), that have proven to support the maturation of cells and tissues towards more adult-like phenotypes and functionality.[241] In particular, electrical pacing can synchronise cells beating with an effect similar to the action potential generated in the sinoatrial node, and it can also be used to tune the beating frequency of the EHT itself.[419]

EHTs have mostly been processed via a scaffold-free approach using biologically-derived materials, such as fibrin or collagen gels, which enable the spontaneous process of

self-assembly typical of cells in a media suspension, and has been applied to the generation of EHTs since 1997.[20] An alternative strategy is seeding isolated cells onto a pre-existing porous scaffold, to provide a substrate with known geometry and stiffness.[420] Due to its reproducibility and simplicity of fabrication, many researchers have focussed on the scaffold-free method, leading to huge momentum and continuous progression in the functionality and size of the constructs, most recently with the generation of a human-size EHT.[17] Probably the most important reason for the disuse of the scaffold-based strategy has been the adoption of materials and constructs characterised by inadequate functionality, such as collagen sponges [21] or PLA fibrous scaffolds.[420] These platforms did not exploit the possible assets given by scaffolds with optimised morphology, stiffness, and electrical conductivity. Thus, they did not provide convincing alternatives to the evident technical advantages of the scaffold-free approach.

The progress in synthesising and processing electroconductive biomaterials, especially conjugated polymers (CPs), may impact this trend and rationalise scaffold use for EHTs. These materials have already proven their potential to assist the regeneration of the heart wall after MI,[24-26] and it is hypothesised that such electroconductive platforms can provide enhanced electrophysiological features rather than biologically derived materials, thus improving biomimicry.[6] However, despite their broad use as 2D substrates of heart models,[134] their inclusion in EHT has yet to be optimised. In addition, the use of porous scaffolds with predefined microarchitecture could directly influence cell response, in particular their spatial orientation. In the case of a highly anisotropic tissue such as the myocardium, this guides the alignment of CMs along the direction of contraction and their fusion into myofibres.[421,422] Material stiffness is another physical property known to play a significant role, and it has been reported that substrate stiffness in the range 10-15 kPa is the most suited for promoting the differentiation of stem cells into myocytes.[395]

In this work, electroconductive scaffolds based on crystallised PEDOT:PSS-GOPS were adopted as substrates for in vitro models. An in-house bioreactor able to deliver electrical pacing to monolayer culture as well as to 3D constructs was developed. Furthermore, I

conceptualised and manufactured **R3S** (**R**ig for the **S**timulation of **S**ponge-like **S**caffolds) an in vitro platform designed to maintain scaffolds suspended in media in the same location, while enabling free-contraction of the cell and simultaneously providing optical accessibility for both standard and inverted microscopy. This setup was validated with a C3H10 cell line, showing that scaffold morphology and electrical pacing play a synergistic role on the proliferation and metabolism of cells. Moreover, cells preferentially aligned along the direction of the electric field even in the absence of an aligned substrate. Finally, primary neonatal rat CM were isolated, seeded on 3D scaffolds, and maintained in culture up to 14 days. However, no global contraction of the scaffolds was observed, with separated clusters of cells showing inhomogeneous beating.

## *8.3. Experimental section*

### *8.3.1. Fabrication of pacing bioreactor*

To improve electrical maturation and coupling of cells, electrical stimulation was delivered via a custom-made bioreactor. I conceptualised and manufactured the system with the use of inexpensive rapid prototyping, gathering inspiration from existing models.[241,416] A schematic representation of the setup is shown in **Figures 8-1.A,B**. A set of twelve 22 mm long cylindrical carbon electrodes were cut from a 3 mm large carbon rod (Goodfellow Cambridge Ltd, UK) and a 1 mm large hole was drilled at one end, through which a platinum-iridium wire (Advent Research Materials Ltd, UK) was secured. A mould, consisting of a top and a bottom component (**Figure S12**), was 3D printed to allocate twelve electrodes and once the two components were sealed together, PDMS Sylgard™ 184 was introduced in the mould. After polymerisation, the mould was opened, and the electrodes could be collected (**Figure S13**). The silicon closures at both extremities of each carbon bar allowed permanent securing of the platinum-iridium wire and avoidance of any liquid infiltration, while also providing an anchorage system to the *lid adapter.* This 3D-printed part interfaced between the electrodes and the plate lid (**Figure 8-1.Bi** and **S14**); it holds 6 pairs

of carbon rod electrodes kept at 15 mm distance between each other and ultimately able to pace a 6-well plate. This component was designed to have slots for six screws to secure it to a 6-well plate lid, with openings in the area in between the electrodes for optical accessibility with both upright and inverted microscopes. A 5 mm large space between the interface and the lid was accounted for in the wiring. Electrodes are connected with copper wire to have a configuration in parallel as represented in **Figure S15**. The source ground and positive wires connected externally to a bread board where a waveform generator (RSDG2000X, Radionics) and an oscilloscope (RSDS 1052 DL +, Radionics) were also connected.

### *8.3.2. R3S: Rig for the Stimulation of Sponge-like Scaffolds*

For the stimulation and optical monitoring of 3D porous scaffolds, a specific rig that could maintain scaffolds in a stable position was developed. In addition, for the application of such a system to cardiac tissue engineering, this rig should not impede the typical contraction of the scaffolds generated by beating cardiomyocytes. The system presented in **figures 8-1.Bii** is constituted by a main body and four elastomeric bars. The main body (**Figure S16**) was designed to accommodate two 3D scaffolds that were to be kept parallel with the electric field generated by the bioreactor, that could be observed from optically accessible chambers placed underneath. On the side and at the extremities of each of these chambers, a pillar with a sharp tip anchors the elastomeric bars. These elastomeric bars were designed in dumbbell-shape and were placed in pairs at each extremity of the scaffold in a sandwich-like fashion. The fabrication was performed with a multi-component custom-made mould and the achieved bars had a square cross section with 1 mm long sides (**Figure S17**). PDMS constituted by a 1:5 ratio of Sylgard 184 and Sylgard 527 was used, to provide a material that could be strong enough to keep the scaffolds in place, but also flexible enough to be deflected by beating scaffolds.

To allow for the correct assembly of the rig and for consistency between replicates, while also confining the cell seeding volume, specific seeding chambers were designed. These

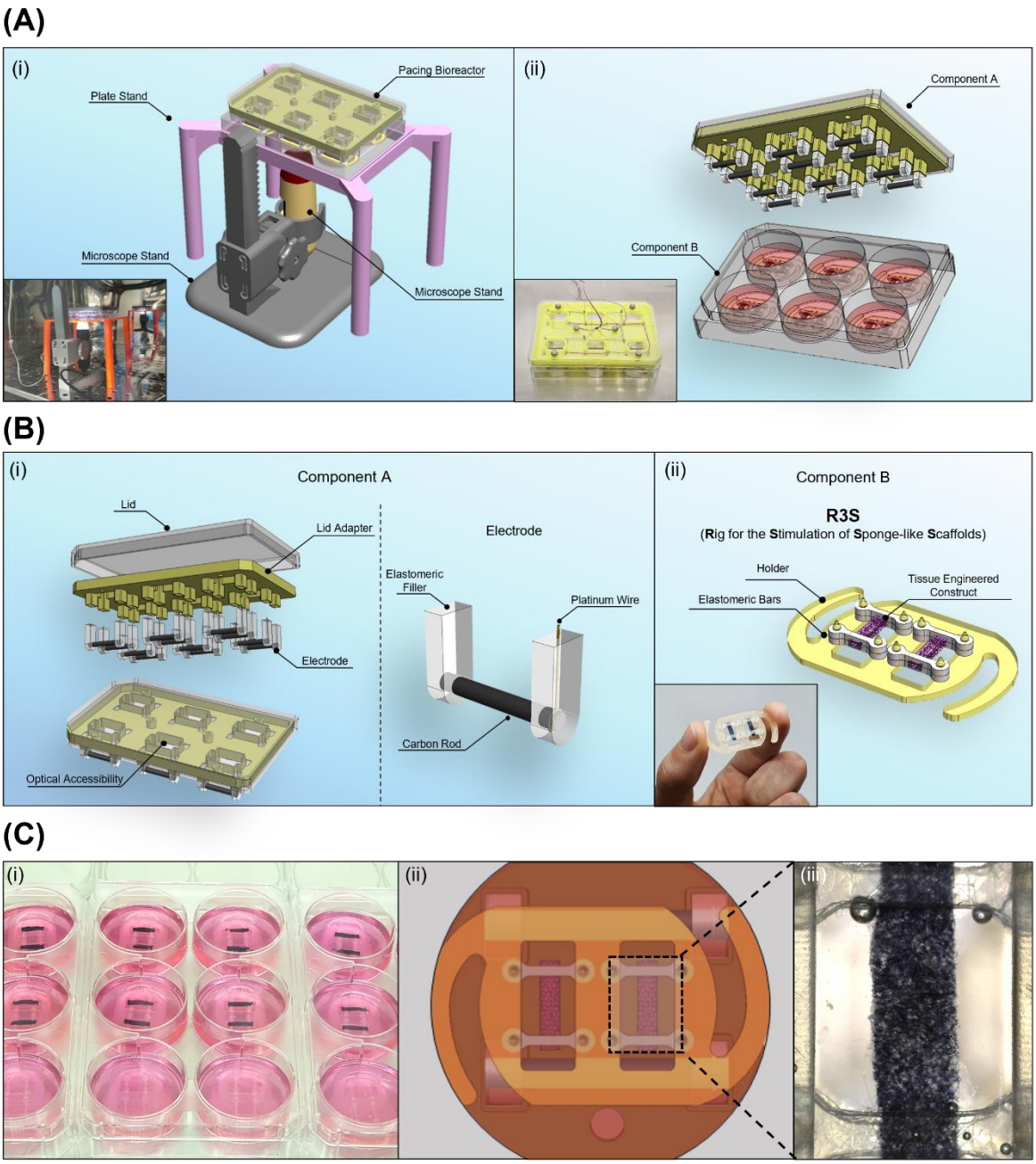


***Figure 8-1**. Overview of the setup for electrical pacing and scaffold holding rig. **(Ai)** Schematic of the custom-made setup for the observation and monitoring of scaffolds. Inset depicts a picture of the operating setup. **(Aii)** Schematic of the custom-made cell culture pacing setup composed of a top and a bottom section, Components A and B respectively. Inset depicts a picture of the prototype. **(Bi)** Assembled and exploded view of component A the electrical pacing bioreactor with details of the electrode. **(Bii)** Schematic and picture (inset) of Component B: H3S (Holder for the Stimulation of Sponge-like Scaffolds). **(C)** Assembled cell culture setup, showing **(Ci)** a picture of a set of plates with R3S, **(Cii)** a schematic of the view from the bottom of the plate with focus on a single well and finally **(Ciii)** a picture obtained with the microscope camera focusing on a single scaffold.*

were obtained from the addition of sterile 2 w/v% agarose solution into a 3D printed mould specifically designed to fit rectangular sponge-like scaffolds with dimensions of 2 x 1 x 9 mm and four elastomeric bars per scaffold (**Figure S18**). The agarose solution solidified in

a few minutes, then making it possible to remove the seeding chamber and proceed with the in vitro experiment.

### *8.3.3. Tensile test of elastomeric bars*

Uniaxial tensile tests were performed on elastomeric bars to evaluate their stiffness and ultimately use the extent of their deflection to determine the force generated by the EHTs. First, a cyclic sequence with increasing strain from 5% to 30% by 5% increments was performed to assess the absence of hysteresis in dynamic conditions. Then, a ramp until failure followed to verify the rupture limit (**Figure 8-2**). Bars had a mean elastic modulus of 54.3 ± 15.7 kPa and no evidence of hysteresis was observed in the tested range.

### *8.3.4. Seeding protocol and validation of pacing bioreactor with C3H10*

Collagen and crystallised PEDOT:PSS-GOPS scaffolds were prepared as in *Chapter 7*. Briefly, after lyophilisation and subsequent thermal annealing, PEDOT:PSS-GOPS samples - with both isotropic and aligned architecture - were submerged into a bath of 100% sulphuric acid for 15 minutes, then subjected to multiple washings using deionised water, and finally sectioned at 1 mm thickness with a vibratome (VT 1200S, Leica. Germany). Regular rectangular strips 9 mm long and 2 mm wide were manually cut using razor blade, followed by sterilisation and preconditioning were performed as described in *Chapter 3*.

For validation of the pacing bioreactor and of R3S, C3H10 were seeded as illustrated in **Figure S19**. Specifically, two elastomeric bars were set in each compartment of the seeding

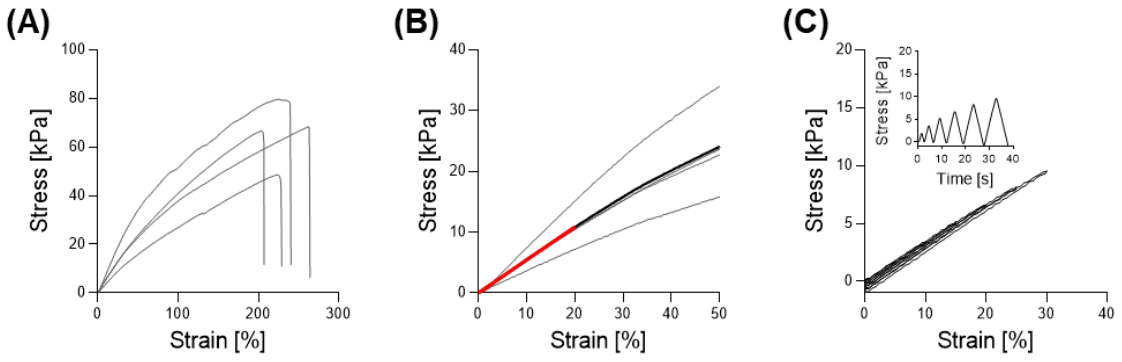


***Figure 8-2**. Mechanical characterisation of PDMS bars via uniaxial tensile test. **(A)** Tension until rupture. **(B)** Tension in the range 0-50% strain with mean linear interpolation in red. **(C)** Stress-strain and stress-time curves representing a standard response within cycles from 5% to 30% strain.*

chamber. Scaffolds were added, and any excess liquid removed. The cell suspension was mixed in equal amount with Matrigel™ to reach a final seeding volume of 20 µl and 250k cells that was pipetted onto the dry scaffold. After an incubation of 30 minutes at 37 °C, to allow the transition from liquid to gel of the media/Matrigel, two more elastomeric bars were placed on top of the scaffold in a sandwich-like fashion. At this stage, the main body of R3S was pressed into the seeding chamber, piercing the agarose and locking in position the elastomeric bars and the scaffolds. The setup could be flipped and moved to a 6-well plate which was prefilled with culture media. After one more hour of incubation, the agarose seeding chamber was removed.

Starting from day 3, cells were paced with a biphasic pulsatile regime in the order of ±2.5 V, 2 ms pulse, 2 Hz. A daily 1 hour long conditional session was carried out until day 7. Cell performance was evaluated at days 3 and 7 in terms of viability via live/dead assay, proliferation via Picogreen™ DNA quantification, metabolism via AlamarBlue™, and morphology via DAPI/Phalloidin fluorescent staining.

### *8.3.5. Isolation and handling of neonatal rat cardiomyocytes*

Primary CM were isolated from neonatal rat hearts (nrCM) using a protocol adapted from the Pierce Primary Cardiomyocyte Isolation Kit from Thermo Scientific (88281, Thermo Fisher Scientific). Cells were seeded immediately after isolation either on Matrigel-coated 6-well plates or on sponge-like scaffolds, for 2D or 3D studies respectively. For 2D studies, the recommended seeding density of $2.5 \times 10^5$ cells/cm$^2$ was adopted. For 3D studies, the same seeding protocol described for C3H10 cells was used, but seeding density was adjusted to $1 \times 10^6$ cells per scaffold.

### *8.3.6. Monitoring cardiac cells contraction and morphology*

Cell and construct beating status was recorded every day from day 3 until the endpoint. For monolayer evaluations (without scaffolds and/or bioreactor culture), 20 second long videos were recorded with a 10x objective on an Olympus IX83 epifluorescent microscope (Olympus, Germany, For scaffolds mounted on R3S, a Dino-Lite AM4113T USB

Microscope was used.

Immunofluorescent staining for cardiac markers was performed with an internal protocol at day 14. Briefly, the cell membrane was lysed in 1 v/v% Triton X-100 (T8787, Sigma-Aldrich), then samples were blocked with a PBS-based solution consisting of 4 w/v% BSA (A2153-50G) for stabilisation, 0.05 v/v% Triton X-100 to enhance permeabilisation, 0.05 v/v% Tween20 (P1379, Sigma-Aldrich)) to reduce surface tension. Cardiac troponin T (cTnT, ab8295 Abcam), connexin 43 (Cx43, ab11370 Abcam) and sarcomeric α-actinin (α-act, EA53 Thermofisher) were used as primary antibodies and diluted 1:300 (cTnT and Cx43) or 1:100 (α-act) in antibody dilution buffer containing PBS with 1 w/v% BSA, 0.05 v/v% Triton X-100, 0.05 v/v% Tween20. Secondary antibodies were diluted 1 in 250 in antibody dilution buffer. The secondary antibodies used for this study were Alexa Fluor® 594 for Cx-43 (ab150076, Abcam) and Alexa Fluor® 488 for cTnT and α-act (ab150113, Abcam). Rhodamine Phalloidin (00027, VWR) at concentration of 5 u/ml was incubated together with the secondary antibody for α-act. DAPI solution was made from a 1000X stock concentrate (32670, Sigma-Aldrich). All washings were performed with PBS and 0.05 v/v% Tween20.

## *8.4. Results and discussion*

### *8.4.1. Electrical pacing preserves viability, enhances performance and promotes alignment of C3H10 cell line*

In this study, I implemented a setup for holding and pacing 3D sponge-like scaffolds, together with a custom-made bioreactor to provide electrical pacing. To enable the assembly of the R3S system and to promote the adhesion of CMs to the scaffolds, the seeding protocol used in C*hapters 6* and *7* was modified. The seeding chambers were fabricated with agarose instead of PDMS, while cells were delivered in a Matrigel mix which could undergo a rapid sol/gel transition. The use of R3S also involved also a compression operated by the elastomeric bars on the scaffolds, as well as permanent suspension of the

scaffolds in a floating, stable position at constant distance from the bottom of the plate. All these factors might hinder cell delivery to the scaffolds and subsequent seeding density. At day 1, DNA content between groups seeded with C3H10 via standard protocol or via R3S was comparable, and no difference was evident amongst different scaffold types, confirming that the aforementioned changes did not negatively impact the seeding yield (**Figure S20**).

Samples seeded with C3H10 in R3S were then studied up to day 7, applying electrical pacing with an in-house bioreactor and their performance compared to day 3. Electrical cues have potential to ameliorate cell performance and to influence their differentiation fate, however, the application of an improper electrical signal can drive uneven electric field distribution, excess of ions with generation of by-products, all eventually leading to detrimental effect on cell viability.[423] Pacing patterns, pulse duration, peak intensity, pulse frequency, and duration of the pacing session are all key players in the effective delivery of pacing.[424] In particular, the adoption of a biphasic pulse instead of monophasic has shown to reduce the risk of by-products production by limiting the formation of nonreversible-Faradaic reactions.[241]

As demonstrated by live/dead imaging and its quantification, cells were viable at both day 3 and 7, with no difference between groups of different material, with or without electrical pacing (**Figure 8-3**). From the mosaic micrographs, the cells are clearly distributed homogeneously across the scaffolds, with the exception of the terminal regions, corresponding to the sites of anchoring to the elastomeric bars. Here, the elastomeric bars held the scaffolds without breaking them, and by day 7 a permanent deformation of the material occurred together with less cell presence.

DNA quantification highlighted cell proliferation for all groups, with trends of increased proliferation for paced groups compared to controls (**Figure 8-4.A**). Similar results were obtained for the analysis of cell metabolism; in particular, cells on paced aligned scaffolds demonstrated significant increases in metabolism compared to all collagen and isotropic groups, suggesting a benefit on cell performance by the synergistic effect of an anisotropic morphology and the external pacing (**Figure 8-4.B**).

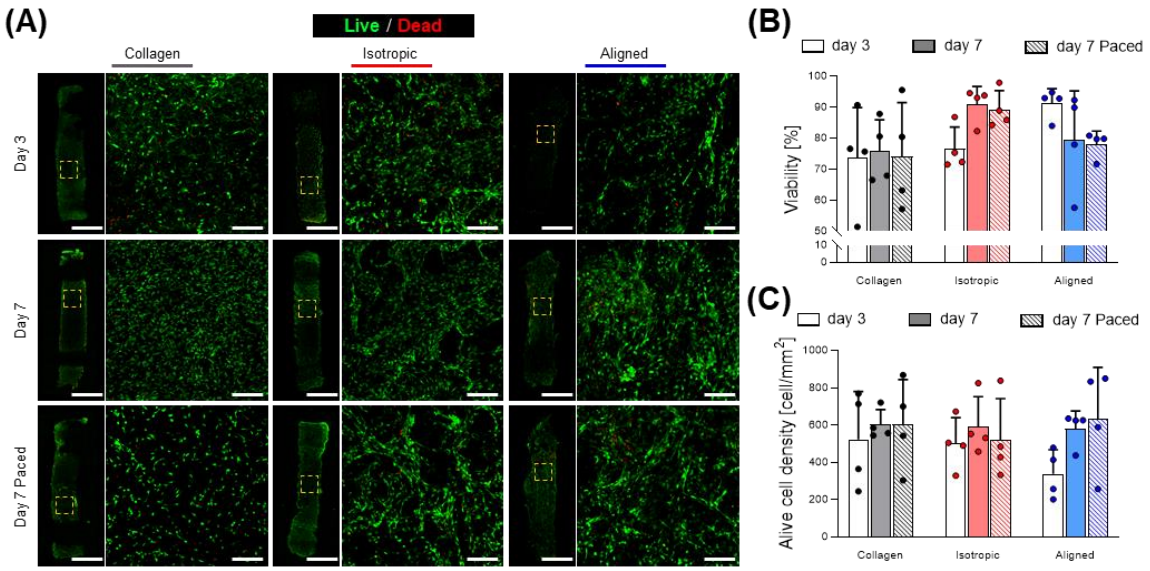


***Figure 8-3**. Effects of pacing C3H10 cells in scaffolds on viability. **(A)** Micrographs from confocal microscope fluorescent staining for live/dead of CH310 cells at days 3, 7 with and without pacing. **(B, C)** Quantification of viability (extracted from live/dead staining) at days 3, 7 with and without pacing quantified as viability and alive cell density (n=4). Scale bars: A = 200 µm; A insets = 200 µm. Bar graphs demonstrate the mean with error bars representing standard deviation. Data values are presented as associated points. Statistical significance was performed using two-way ANOVA with Tukey's post-hoc test.*

In terms of cell morphology, no major qualitative difference was observed; when focussing on cell orientation as it related to nuclei orientation, it could be observed that cells aligned along the lamellae of the aligned samples already from day 3 and they maintained such directionality up to day 7. As expected, cells on collagen or isotropic substrates did not have any preferential alignment at either day 3 or at day 7 without pacing, however this behaviour was due to a preferential alignment along the electric field of those samples that were subject to electrical pacing. While more studies are necessary to further validate and finalise the present results, here it is confirmed that orientation of C3H10 cell line can be influenced by either scaffold alignment or external pacing, similar to other cell types such as neural stem cells PC-12 [425] and H9C2 rat cardiomyoblast.[426]

The choice of a biphasic pulsatile stimulation and 1-hour long training sessions have been implemented with a conservative approach to preserve cell wellbeing and prevent excessive production of potentially harmful redox oxygen species. The findings presented here are proof that such choices successfully maintained cells viability and provides sufficient signalling cues to obtain a positive effect on their activity.

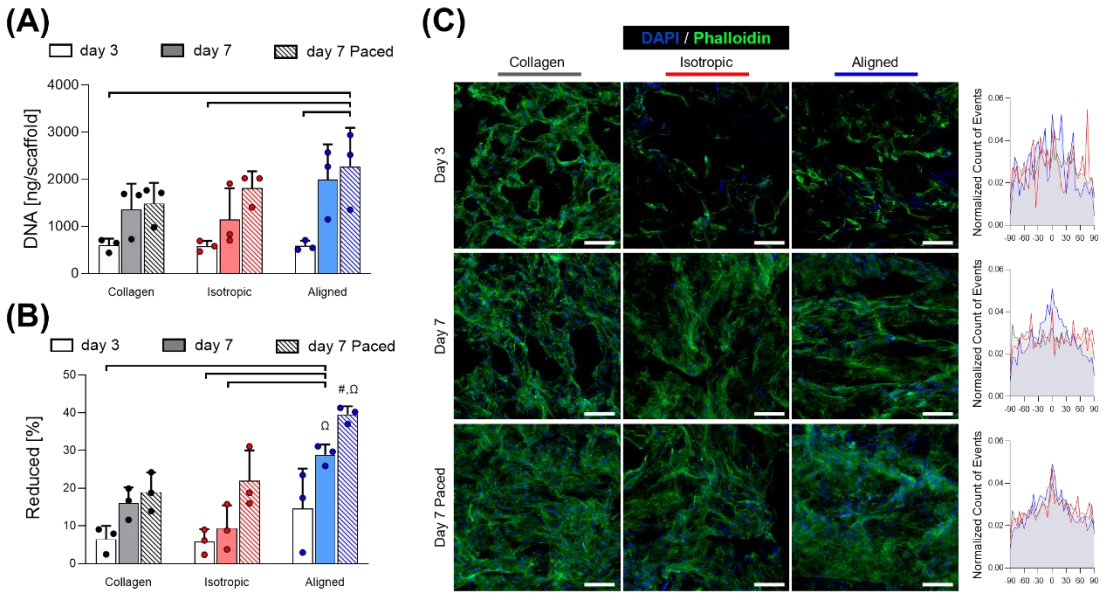


***Figure 8-4.*** *Effects of pacing C3H10 cells in scaffolds on cell proliferation, metabolism,and alignment.* ***(A)*** *Quantification of DNA via Picogreen™ assay, expressed as ng per scaffold (n=3).* ***(B)*** *AlamarBlue™ assay performed on scaffolds (n=3).* ***(C)*** *Micrographs from confocal microscope fluorescent staining for nuclei/f-actin (DAPI and Phalloidin respectively) and distribution of nuclei alignment. Scale bars: C = 100 µm. Bar graphs demonstrate the mean with error bars representing standard deviation. Data values are presented as associated points. * and # represent statistical significance (p<0.05) (* between indicated groups, # with all other groups), while Ω is shared by groups that are not statistically significant using two-way ANOVA with Tukey's post-hoc test.*

### *8.4.2. Preliminary study on neonatal rat cardiomyocytes*

Having demonstrated R3S and the bioreactor to be reliable assets for the generation of in vitro paced models, the subsequent study in this research involved the isolation of primary nrCM and their use on 3D scaffolds towards the generation of EHT. Cells were successfully isolated and seeded on both 2D and 3D constructs, and spontaneous beating of CM either individually or in clusters was observed after 1 day. **Figure 8-5** shows that cells plated on cell culture plastic expressed cardiac markers such as cTnT, Cx43 and α-actinin at day 7. A certain degree of variability in CM maturation stage and myofibrillogenesis was observed, proven by staining for cTnT and α-actinin. The first marker is colocalised on myofilaments [427] and it showed how such structures were fully aligned along the directions of principal contraction for some cells, while they were more randomly orientated for others. α-actinin is an indicator of the Z line of the sarcomere; and, for some cells, it resembled the characteristic repetitive parallel configuration of contractile myocytes, while for other cells,

although expressed, it did not highlight a specific morphological disposition. In addition, a substantial number of cells did not express either of these two markers, as shown by the presence of cells stained only by DAPI or f-actin. However, this was in line with the manufacturer of the isolation kit that predicts a purity of CM population as high as 80% by day 7. The expression of Cx43 was limited and showed little presence of gap junctions, an example of which is reported in **Figure 8-5.A.iv**. This can potentially be caused by the presence of a low number of cells due to an inadequate seeding density.

Monitoring the 3D scaffolds revealed partial beating of separated clusters of cells but no global contraction of the scaffolds. Considering the low proliferation rate of CM, an insufficient seeding density might be cause for the absence of homogenous contraction, with cells not able to connect to each other as they did in the monolayer culture. Immunostaining of **Figure S21** proved that only a limited number of cells were present on the scaffolds by day 14, some expressing α-actinin and others only f-actin, confirming the presence of multiple cell populations together with CM.

It is worth mentioning that this imaging analysis resulted in poor resolution, as collagen

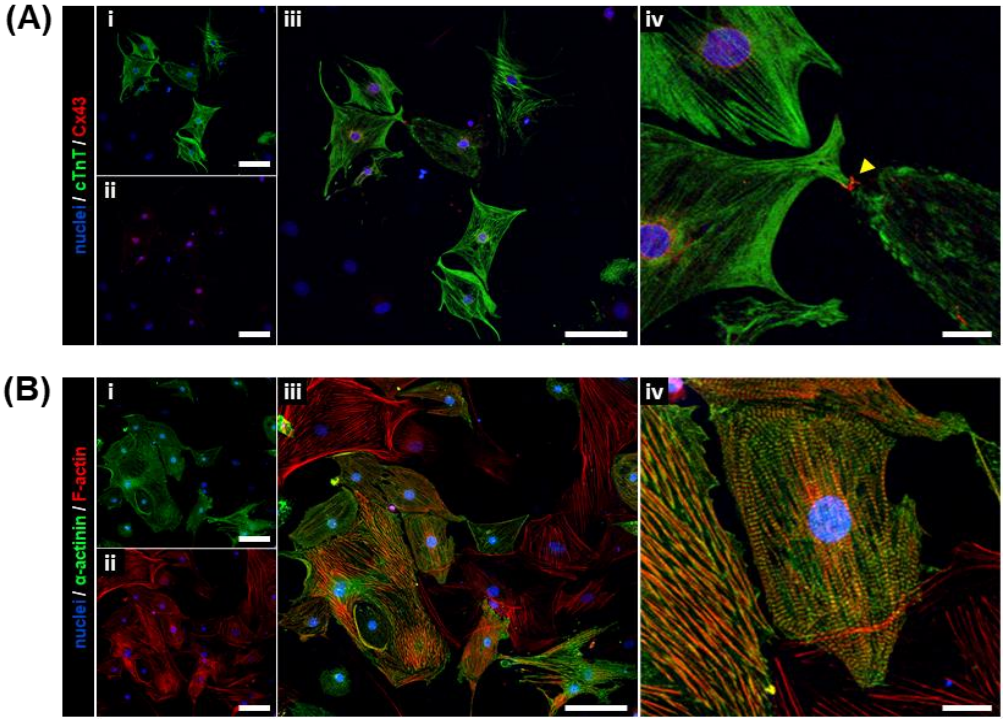


***Figure 8-5**. Immuno-fluorescent staining on nrCM on cell culture plastic at day 7. Micrographs from confocal microscope fluorescent staining for **(A)** nuclei / cTnT / Cx43 with yellow arrow pointing to gap junctions highlighted by Cx43 and **(B)** nuclei / sarcomeric α-actinin / f-actin. Scale bars: Ai-iii, Bi-iii = 100 µm; Aiv, Biv = 20 µm.*

and PEDOT:PSS scaffolds generated autofluorescence leading to technical challenges in the identification of the antibody markers. For future studies, it is recommended to perform immunostaining on microtome sliced samples.

## *8.5. Conclusions*

Reported in this work was the fabrication and validation of a R3S - Rig for Stimulation of Sponge-like Scaffolds - which can allow for real time monitoring of the contraction of EHT. Using rapid prototyping for the manufacturing process, both the pacing bioreactor and R3S were shown to be inexpensive and scalable devices.

Application of external pacing to C3H10 cells had no detrimental effect on cell viability, while a synergistic increase in metabolism and cell orientation was found with the combination of aligned scaffolds and pacing. CMs seeded on scaffolds showed spontaneous beating in separate clusters, but no global contraction was observed, with excessive rigidity of the elastomeric bars and a too low cell density as the probable causes. Once such limitations are overcome, it is believed that the setup presented will be a promising solution for the development of scaffold-based EHT with controlled morphology, stiffness, and electrically biomimetic properties.

# 9. Discussion

## *9.1. Summary*

The main objective of this doctoral thesis was to process 3D porous scaffolds with the electroconductive polymer PEDOT:PSS and use them as piezoresistive sensors and platforms for tissue engineering. One great advantage of PEDOT:PSS is its capacity to be dispersed in water, making it possible to be easily mixed with other compounds and processed with straightforward techniques such as lyophilisation. However, to then be employed in an aqueous environment, the PEDOT:PSS chains also need to be stabilised with crosslinking. The most known and used form of covalent crosslinking is via GOPS, which comes at the expense of reducing conductivity of the final material.

In a nutshell, in this work I focussed on two aspects of PEDOT:PSS and its processing chain: chemistry and morphology. Changing the composition of the material on one side, and the microarchitecture of the manufactured constructs on the other, I investigated how these aspects could affect mechanical, electrical, piezoresistive and biological responses.

Finally, the scaffolds with the most suitable physical features were incorporated in an in vitro model for the creation of an EHT.

### *9.1.1. PEDOT:PSS sponge-like scaffolds are promising platforms for piezoresistive sensors*

In *Chapter 4*, PEDOT:PSS-GOPS scaffolds were fabricated via lyophilisation and their piezoresistivity was studied. This investigation required a customised setup on a Zwick uniaxial test device. Signals from the mechanical apparatus and from an external sourcemeter were merged during post processing using original Matlab® scripts. In this way, mechanical and piezoresistive parameters such as strain- and stress-dependent gauge factors, as well as gain region extensions, were obtained in both ramp and cyclic regimes.

In order to improve the otherwise relatively weak mechanical properties, elastomeric matrices of different stiffnesses were embedded into electroconductive scaffolds obtaining biphasic EAS. A total of six combinations of microarchitecture and stiffness were achieved and compared for their performance as piezoresistive sensors. It was demonstrated that isotropic architecture provides better overall mechanics than its aligned counterpart. Specifically, the presence of a stiffer PDMS matrix led to a reduction in the range of high sensitivity and a profound increase in strain-dependent gauge factor, reaching values close to 400. Finally, a sensor device prototype was used for monitoring simple body movements, demonstrating that the biphasic EAS are a promising choice for elastic and highly responsive sensors.

It can be concluded that I developed a cheap and safe fabrication method of piezoresistive sensors with both adaptable sensitivity ranges and sensationally high strain sensitivities.

### *9.1.2. PEGDE enhances hydrophilicity and conductivity of PEDOT:PSS for coatings*

As GOPS-crosslinked scaffolds do not reach the target native myocardium conductivity range, it was necessary to explore alternative materials. Here, PEDOT:PSS was functionalised using a PEGDE crosslinker to stabilise it in water and to maintain its electroconductive properties. PEGDE was hypothesised to crosslink with PEDOT:PSS via the epoxy ring of PEGDE interacting with the sulfonic groups of excess PSS chains, which reaches a saturation at 3 w/v% PEGDE. The material was fabricated into 2D films which were characterised both chemically and physically via profilometry, XPS, FT-IR, contact angle measurements, four-point probe testing and EIS. Biocompatibility was assessed in terms of viability and spreading of a C3H10 cell line in a 48-hour study. Overall, PEGDE facilitated a more hydrophilic and electrically conductive polymer, with this molecule serving both as a crosslinker and a secondary dopant.

### *9.1.3. PEGDE enables the fabrication of 3D sponge-like scaffolds but with reduced stability and biocompatibility compared to GOPS*

I proceeded with scaling up the constructs from 2D coatings to 3D scaffolds, applying the same lyophilisation method used for PEDOT:PSS-GOPS piezoresistive sensors. Sponge-like scaffolds were processed with either isotropic or aligned microarchitecture, with isotropic ones also being processed at different freezing temperatures. Features of the resultant scaffolds were investigated with a focus on how a change in morphology could be responsible for different mechanical and electrical properties. I found that a smaller pore size was responsible for stiffer but less conductive scaffolds. I then embedded the scaffolds within a PDMS elastomeric matrix fabricating biphasic EAS and I characterised their piezoresistivity, as previously done for PEDOT:PSS-GOPS. Despite an improved average response in the ramp phase compared to GOPS-crosslinked samples, this set of piezoresistive sensors was characterised by a high variability between replicates that makes them a less precise tool for reproducible signals. When investigating whether these scaffolds had adequate biocompatibility for the development of an in vitro model, it was observed that by day 7 a reduction in viability, proliferation and metabolism occurred. Taken together, although PEGDE-crosslinking allowed for the fabrication of 3D sponge-like scaffolds with enhanced hydrophilicity and conductivity, currently such constructs are neither an appealing option for the development of piezoresistive sensors nor as tissue engineered platforms.

### *9.1.4. Crystallisation post-treatment of GOPS-crosslinked PEDOT:PSS sponge-like scaffolds boosts conductivity while preserving sufficient biocompatibility*

With PEDOT:PSS-PEGDE not satisfying biocompatibility requirements, it was necessary to reconsider the choice of the material for scaffold manufacturing. Crystallisation via sulphuric acid is a post-treatment option previously adopted for boosting the conductivity of PEDOT:PSS coatings and is assumed to cleave out excess insulant PSS molecules and

convert PEDOT grain-like clusters into a crystalline lattice.[31] However, reports of use of this treatment in either 3D constructs or on PEDOT:PSS-GOPS blends are largely limited. It was therefore decided to investigate whether crystallisation was applicable to 3D scaffolds and if it could lead to an increase in electrical conductivity within the native tissue range. Once the treatment was optimised and crystallisation was verified by SEM and XRD analysis, samples from control and crystallised groups - both isotropic and anisotropic - were characterised for their morphological, mechanical and electrical properties. Crystallisation caused significant swelling of the scaffolds, which was reflected in an increase in pore size and porosity. Another effect was an over 10-fold reduction in stiffness bringing it closer to the 10 - 15 kPa range that is considered to be the most auspicious for induction of myogenesis. [395] More importantly, conductivity was enhanced on average by 1000-fold, reaching peaks of $10^{-1}$ S/m - near the target value for a biomimetic myocardium.[73,74]

In vitro studies with direct contact on C3H10 cell line reported reduction in overall cellular performances of crystallised scaffolds compared to untreated ones; however, the response was not different compared to the collagen control. Moreover, indirect in vitro tests showed no influence on cellular responses caused by the crystallisation of PEDOT:PSS-GOPS. It was concluded that the crystallisation treatment was an effective and straightforward strategy for fabricating highly electroconductive scaffolds with aligned morphology and suitable stiffness for development of an in vitro cardiac model.

### *9.1.5. PEDOT:PSS scaffolds as EHT: development of a rig and a bioreactor for monitoring heart-like beating.*

The final study of this PhD thesis incorporated 3D crystallised PEDOT:PSS-GOPS electroconductive scaffolds into a bioreactor for the development of an EHT. Working with porous sponge-like scaffolds, several practical challenges arose. First, specific protocols for both the setup assembly and the cell seeding had to be established for limiting human error and preserving sterility and reproducibility throughout the procedure. Next, there was

a need to keep the scaffolds floating in media, in a stable location, while not blocking the beating of cardiomyocytes. Such a setup had to guarantee optical accessibility and allow the user to track scaffold contraction and provide live information about the functionality of the EHT. All these requirements were satisfied by the conceptualisation and manufacturing of R3S - Rig for the Stimulation of Sponge-like Scaffolds. Next, I developed an electrical pacing bioreactor. This device was designed to apply electrical stimulation to both 2D and 3D cultures in a standard 6-well plate. A wave generator was chosen as the source of stimulation as it was able to deliver a fully customisable signal.

By seeding C3H10 cell line on isotropic and aligned crystallised PEDOT:PSS-GOPS scaffolds and on a collagen control, it was possible to validate the performance of both the R3S and the bioreactor. After 7 days, cells were viable on all constructs. Proliferation, metabolism and cell alignment were improved using aligned samples and by the electrical pacing. Finally, in a conclusive study, rodent primary CMs were isolated and seeded onto the crystallised PEDOT:PSS-GOPS scaffolds and monitored up to 14 days. Although cells were spontaneously beating in individual clusters on the scaffolds, it was not possible to observe any global contraction of the material. An excess stiffness of the elastomeric PDMS bars holding the scaffolds or a too low a cell density may be the motivations for the absence of movement. With further optimisation of R3S and of the seeding sequence, this limitation will be overcome.

## *9.2. Limitation and future works*

### *9.2.1. Piezoresistive sensors*

Although the piezoresistive sensor developed in C*hapter 4* showed promising piezoresistive responses in both ramp and cyclic regimes, the sensor prototype requires more improvements to provide consistency and replicability. To further corroborate its efficacy, the sensor could be included in a motion-control system for detection of both the distribution and direction of load.[330,334] In addition, it would be possible to use this sensor for

determining range of motion for specific actions after adequate calibration, such as knee bending during walking which would allow for discerning a healthy or pathological patient.[295]

Indeed, one feature that is commonly characterised for piezoresistive sensors is their dependence on the stimulation frequency, where a range between 0.1 Hz up to 100 Hz or more are applied.[327] In this thesis, the use of a Zwick uniaxial testing machine limited the range of strain rate that could be applied to the sensor as well the number of cycles performed, which was maintained at the maximum recommended frequency of 0.5 Hz and 100 cycles during the cyclic phase. Although useful insights on the cyclic behaviour of the sensor have already been provided with such a method, for a more complete and extended investigation over the frequency domain the use of a vibration exciter is suggested.

### *9.2.2. PEGDE-crosslinking*

Studies on the biocompatibility of PEDOT:PSS-PEGDE showed that for 2D coating high viability was preserved with cells appearing even more spread than on the PEDOT:PSS-GOPS, while for 3D samples PEGDE-crosslinking led to significant reduction in cell performance suggesting a toxic interaction. At first these results can appear contradictory; however, diverse explanations justify such conflicting responses. First, 2D coatings had a thickness on the order of 100 nm while 3D scaffolds are structures on the mm scale with strut thickness around of 1-10 µm. Therefore, more material is present in the culture environment and with it more absolute content of PEGDE, potentially contributing to reduced biocompatibility. Second, the in vitro study on 3D scaffolds lasted 7 days, while 2D coatings were kept in culture only up to 48 hours due to their relatively lower stability than the GOPS counterpart. It is possible that the reduced duration of the experiment did not allow for the observation of detrimental effects on cell behaviour in 2D coatings.

With results achieved to date, 3D PEDOT:PSS-PEGDE did not match expectations as a sensor or tissue engineered platforms. Working with collaborators, I am currently investigating whether their enhanced electrical properties might be suitable for the development of super capacitors and batteries.[428] The description of this is outside the

current scope of this PhD thesis.

### *9.2.3. EHT*

Though successful designing and manufacturing of R3S and of a bioreactor for electrical stimulation was accomplished, more work must be done on the optimisation of the setup for achieving a functional EHT. Herein a list of modifications, upgrades and analyses that are suggested to ameliorate the current system.

To date, the main limitation of this system is that no macroscopic contraction was observed when primary rat cardiomyocytes were seeded on the scaffolds. This might be caused by an excess rigidity of the elastomeric bars of R3S, as cardiomyocytes were indeed able to beat in clusters but not as a unique tissue. Changing the design of the bars is not preferrable, as this might result in a complete redesigning of R3S. One approach to potentially solve this issue is to reduce the size of the elastomeric bars, because a lower cross section would imply a reduced rigidity of the bar that could deflect when scaffold contraction occurs. A reduction in overall stiffness can also be achieved by changing the composition of the PDMS blend. This can be done either by increasing the concentration of Sylgard 527 compared to the Sylgard 184 from the current 5:1, up to 10:1 or also 1:0 [326], or by reducing the concentration of crosslinker agent in the preparation of Sylgard 184 from the standard 1:10 to 1:20.[429]

While the experiments in *Chapter 8* used the C3H10 cell line and primary neonatal rat cardiomyocytes, most modern EHT systems are based on the use of hiPS-CM.[17,19] Other researchers have recently established protocols for the obtainment of such cell populations, with final goal being the inclusion of hiPS-CM in the EHT platform presented in this thesis. Preliminary experiments showed that ZsGreen-primed hiPS-CM could adhere onto the crystallised PEDOT:PSS-GOPS scaffolds, but further investigations have not been completed at present.

Another aspect that will be investigated is the stimulation with signals of different patterns, intensities and frequencies. As discussed in C*hapters 2* and *8*, several types of electrical stimulations have been applied to cells throughout the years. To date, the development of the most advanced and physiologically relevant hiPS-CM EHT have been realised with the support of an intensity training pattern that consisted of an increase in frequency starting from 2 Hz on day 7 and reaching 6 Hz by day 21 [19]. It is planned that for future studies implementing hiPS-CM, such patterns will be adopted with an aim to replicate the promising results showed in the literature. By varying the signal source, non-physiological intensity and frequency pacing regimes could be explored for the recreation of in vitro pathological models, such as the hypertrophic heart.[240,430]

The use of specific drugs which are known to have an impact on heart functionality is a common method to validate the degree of functionality of EHT. In future experiments, reagents such as caffeine and the cardiotoxic drug doxorubicin will be used to replicate physiological responses in terms of change in beating frequency, intensity or synchronisation.

It is speculated that a system comprising all or most of the cell populations present in the native myocardium would be a more physiologically relevant model.[431] Many groups have been working on the addition and combination of different cell types to their cardiac models, with particular interest to fibroblasts [432], endothelial cells [417] and macrophages.[433] Following the achievement of a functionally beating EHT populated with hiPS-CM, further studies will be performed to include the aforementioned cell types and to investigate how their presence might affect the EHT performance and maturation.

One more common use of EHT is to simulate a pathological model of infarcted heart and apply it to study the reaction of different cell populations to the changed biological

environment. A similar model could be created in a relatively easy manner by inducing cryoinjury on a healthy EHT, as it is the case for in vivo model of myocardium infarction.[434] Such a system might aid in determining how specific drugs could alter their own efficacy depending on external (e.g. paracrine effect of adjacent healthy constructs, media supplements, pH, oxygen level or temperature) or internal factors (e.g. cell population constituting the EHT, size and severity of the injury).

Finally, once a reliable EHT model is established, more insights over the biology of specific cell interactions and responses could be provided by high resolution non-invasive microscopy techniques. Multiphoton microscopy combined with fluorescent life-time imaging (FLIM) can allow for the live tracking of the metabolic activity of cells without the use of any staining or reagent.[435] The use of this technique alone - or in combination with electrical pacing - might be applied to all scenarios before listed, contributing to the explanation of how cell contraction is correlated to the upregulation or downregulation of specific metabolic mechanisms.[436]

## *9.3. Conclusions*

Conductive polymers, and especially PEDOT:PSS, are a topic of growing interest in many engineering fields. In this thesis, I presented the processing and use of PEDOT:PSS, with the ultimate goal of fabricating a 3D porous scaffold for in vitro cardiac model.

- I focused on the lyophilisation process to manufacture isotropic or aligned microarchitectures, and I investigated how mechanical and electrical properties would be affected by a change in morphology. This resulted in the establishment of a cheap and efficient method for the fabrication of piezoresistive sensors in the form of biphasic EAS, characterised by high sensitivity and adjustable range of application.
- I explored strategies to improve the conductivity of 3D porous PEDOT:PSS scaffolds, to obtain more biomimetic and cardio-inductive platforms for tissue engineering.
    - It was discovered that PEGDE can crosslink PEDOT:PSS and generate constructs with higher hydrophilicity and conductivity than those obtained with standard GOPS-crosslinking.
    - A crystallisation post-treatment with sulphuric acid was proved to be applicable to GOPS-crosslinked 3D scaffolds, leading to a 1000-fold increase in conductivity that makes them an asset for cardiac tissue engineering.
- Crystallised PEDOT:PSS-GOPS scaffolds were assembled on R3S - Rig for the Stimulation of Sponge-like Scaffolds - and electrically paced with a custom-made bioreactor. This system proved to support adhesion and maturation of C3H10 cell line and primary rat cardiac cells.

# References


1. Sharma M., et al. Chapter 17 - Biomedical Engineering: The Recent Trends. In: Barh D, Azevedo V, eds. *Omics Technologies and Bio-Engineering*. Academic Press. 323-336. 2018.
2. Duerig T., et al. An overview of nitinol medical applications. *Materials Science and Engineering: A.* 273-275. 149-160. 1999.
3. Hassler M. 3 - Other commonly used biomedical coatings: pyrolytic carbon coatings. In: Driver M, ed. *Coatings for Biomedical Applications*. Woodhead Publishing. 75-105. 2012.
4. Wang Y., et al. Sensors based on conductive polymers and their composites: a review. *Polymer International.* 69. 1. 7-17. 2019.
5. Park M., et al. Fast and Stable Ionic Electroactive Polymer Actuators with PEDOT:PSS/(Graphene(-)Ag-Nanowires) Nanocomposite Electrodes. *Sensors (Basel).* 18. 9. 3126. 2018.
6. Balint R., et al. Conductive polymers: towards a smart biomaterial for tissue engineering. *Acta Biomaterialia.* 10. 6. 2341-2353. 2014.
7. Guimard N.K., et al. Conducting polymers in biomedical engineering. *Progress in Polymer Science.* 32. 8-9. 876-921. 2007.
8. Auersperg J., et al. Effects of residual stresses on cracking and delamination risks of an avionics MEMS pressure sensor. *Microelectronics Reliability.* 64. 665-668. 2016.
9. Guex A.G., et al. Highly porous scaffolds of PEDOT:PSS for bone tissue engineering. *Acta Biomaterialia.* 62. 91-101. 2017.
10. Wang Y., et al. Percolation threshold and electrical conductivity of graphene-based nanocomposites with filler agglomeration and interfacial tunneling. *Journal of Applied Physics.* 118. 6. 065101. 2015.
11. Yang B., et al. A conductive PEDOT/alginate porous scaffold as a platform to modulate the biological behaviors of brown adipose-derived stem cells. *Biomaterials Science.* 8. 11. 3173-3185. 2020.
12. Wan A.M., et al. 3D Conducting Polymer Platforms for Electrical Control of Protein Conformation and Cellular Functions. *Journal of Material Chemisry B.* 3. 25. 5040-5048. 2015.
13. Zhang X., et al. Aligned/unaligned conducting polymer cryogels with three-dimensional macroporous architectures from ice-segregation-induced self-assembly of PEDOT-PSS. *Langmuir.* 27. 5. 1915-1923. 2011.
14. Gaziano T.A. Cardiovascular disease in the developing world and its cost-effective management. *Circulation.* 112. 23. 3547-3553. 2005.
15. Thygesen K., et al. Third universal definition of myocardial infarction. *Circulation.* 126. 16. 2020-2035. 2012.
16. Kirk J.A., et al. Electromechanical dyssynchrony and resynchronization of the failing heart. *Circulation Research.* 113. 6. 765-776. 2013.
17. Querdel E., et al. Human Engineered Heart Tissue Patches Remuscularize the Injured Heart in a Dose-Dependent Manner. *Circulation.* 143. 20. 1991-2006. 2021.
18. Zhao Y., et al. A Platform for Generation of Chamber-Specific Cardiac Tissues and Disease Modeling. *Cell.* 176. 4. 913-927 e918. 2019.
19. Ronaldson-Bouchard K., et al. Advanced maturation of human cardiac tissue grown from pluripotent stem cells. *Nature.* 556. 7700. 239-243. 2018.
20. Eschenhagen T., et al. Three-dimensional reconstitution of embryonic cardiomyocytes in a collagen matrix: a new heart muscle model system. *FASEB journal : official publication of the Federation of American Societies for Experimental Biology.* 11. 8. 683-694. 1997.
21. Radisic M., et al. High-density seeding of myocyte cells for cardiac tissue engineering. *Biotechnology and Bioengineering.* 82. 4. 403-414. 2003.
22. Nunes S.S., et al. Biowire: a platform for maturation of human pluripotent stem cell-derived cardiomyocytes. *Nature Methods.* 10. 8. 781-787. 2013.

23. de Korte T., et al. Unlocking Personalized Biomedicine and Drug Discovery with Human Induced Pluripotent Stem Cell-Derived Cardiomyocytes: Fit for Purpose or Forever Elusive? *Annual Review of Pharmacoloy and Toxicology.* 60. 529-551. 2020.
24. Zhou J., et al. Engineering the heart: evaluation of conductive nanomaterials for improving implant integration and cardiac function. *Scientific Reports.* 4. 3733. 2014.
25. Chen S., et al. A conductive cell-delivery construct as a bioengineered patch that can improve electrical propagation and synchronize cardiomyocyte contraction for heart repair. *Journal of Control Release.* 320. 73-82. 2020.
26. Wang L., et al. Mussel-Inspired Conductive Cryogel as Cardiac Tissue Patch to Repair Myocardial Infarction by Migration of Conductive Nanoparticles. *Advanced Functional Materials.* 26. 24. 4293-4305. 2016.
27. Wang Y., et al. Intracellular calcium ions and morphological changes of cardiac myoblasts response to an intelligent biodegradable conducting copolymer. *Material Science and Engineering C.* 90. 168-179. 2018.
28. Spearman B.S., et al. Conductive interpenetrating networks of polypyrrole and polycaprolactone encourage electrophysiological development of cardiac cells. *Acta Biomaterialia.* 28. 109-120. 2015.
29. Martins A.M., et al. Electrically conductive chitosan/carbon scaffolds for cardiac tissue engineering. *Biomacromolecules.* 15. 2. 635-643. 2014.
30. Håkansson A., et al. Effect of (3-glycidyloxypropyl)trimethoxysilane (GOPS) on the electrical properties of PEDOT:PSS films. *Journal of Polymer Science Part B: Polymer Physics.* 55. 10. 814-820. 2017.
31. Kim N., et al. Highly conductive PEDOT:PSS nanofibrils induced by solution-processed crystallization. *Advanced Materials.* 26. 14. 2268-2272, 2109. 2014.
32. Anderson R.H., et al. The anatomy of the cardiac conduction system. *Clinical Anatomy.* 22. 1. 99-113. 2009.
33. Abraham W.T., et al. Cardiac resynchronization in chronic heart failure. *The New England journal of medicine.* 346. 24. 1845-1853. 2002.
34. Wang J.C., et al. Coronary artery spatial distribution of acute myocardial infarction occlusions. *Circulation.* 110. 3. 278-284. 2004.
35. Dowe D.A., et al. *Imaging coronary arteries.* Springer; 2013.
36. Iaizzo P.A. Handbook of Cardiac Anatomy, Physiology, and Devices. Humana Press; 2009.
37. Williams M.J., et al. Assessment of the mechanical properties of coronary arteries using intravascular ultrasound: an in vivo study. *International journal of cardiac imaging.* 15. 4. 287-294. 1999.
38. Grossman W., et al. Wall stress and patterns of hypertrophy in the human left ventricle. *Journal of Clinical Investigation.* 56. 1. 56-64. 1975.
39. Shipsey S.J., et al. Effects of hypertrophy on regional action potential characteristics in the rat left ventricle: a cellular basis for T-wave inversion? *Circulation.* 96. 6. 2061-2068. 1997.
40. Bergmann O., et al. Evidence for cardiomyocyte renewal in humans. *Science.* 324. 5923. 98-102. 2009.
41. Bangalore S., et al. Renin angiotensin system inhibitors for patients with stable coronary artery disease without heart failure: systematic review and meta-analysis of randomized trials. *British Medical Journal.* 356. j4. 2017.
42. Freemantle N., et al. beta Blockade after myocardial infarction: systematic review and meta regression analysis. *British Medical Journal.* 318. 7200. 1730-1737. 1999.
43. Hashizume R., et al. Biodegradable elastic patch plasty ameliorates left ventricular adverse remodeling after ischemia-reperfusion injury: a preclinical study of a porous polyurethane material in a porcine model. *Journal of Thoracic and Cardiovascular Surgery.* 146. 2. 391-399 e391. 2013.
44. Liu Y.W., et al. Human embryonic stem cell-derived cardiomyocytes restore function in infarcted hearts of non-human primates. *Nature Biotechnology.* 36. 7. 597-605. 2018.
45. Holladay C.A., et al. Recovery of cardiac function mediated by MSC and interleukin-10 plasmid functionalised scaffold. *Biomaterials.* 33. 5. 1303-1314. 2012.

46. Monaghan M.G., et al. Interference: an alteRNAtive therapy following acute myocardial infarction. *Trends in pharmacological sciences.* 33. 12. 635-645. 2012.
47. Monaghan M.G., et al. Exogenous miR-29B Delivery Through a Hyaluronan-Based Injectable System Yields Functional Maintenance of the Infarcted Myocardium. *Tissue Engineering Part A.* 24. 1-2. 57-67. 2018.
48. Hinderer S., et al. Generation and Assessment of Functional Biomaterial Scaffolds for Applications in Cardiovascular Tissue Engineering and Regenerative Medicine. *Advanced Healthcare Materials.* 4. 16. 2326-2341. 2015.
49. Dash B.C., et al. The influence of size and charge of chitosan/polyglutamic acid hollow spheres on cellular internalization, viability and blood compatibility. *Biomaterials.* 31. 32. 8188-8197. 2010.
50. Bartalena G., et al. Biomaterial surface modifications can dominate cell–substrate mechanics: the impact of PDMS plasma treatment on a quantitative assay of cell stiffness. *Soft Matter.* 8. 3. 673-681. 2012.
51. Wang W., et al. An injectable conductive hydrogel encapsulating plasmid DNA-eNOs and ADSCs for treating myocardial infarction. *Biomaterials.* 160. 69-81. 2018.
52. He S., et al. Preservation of conductive propagation after surgical repair of cardiac defects with a bio-engineered conductive patch. *Journal of Heart and Lung Transplantation.* 37. 7. 912-924. 2018.
53. Shiba Y., et al. Allogeneic transplantation of iPS cell-derived cardiomyocytes regenerates primate hearts. *Nature.* 538. 7625. 388-391. 2016.
54. Whyte W., et al. Sustained release of targeted cardiac therapy with a replenishable implanted epicardial reservoir. *Nature Biomed Engineering.* 2. 6. 416-428. 2018.
55. Paul A., et al. Injectable graphene oxide/hydrogel-based angiogenic gene delivery system for vasculogenesis and cardiac repair. *ACS Nano.* 8. 8. 8050-8062. 2014.
56. Zeltinger J., et al. Effect of pore size and void fraction on cellular adhesion, proliferation, and matrix deposition. *Tissue engineering.* 7. 5. 557-572. 2001.
57. Ko U.H., et al. Promotion of Myogenic Maturation by Timely Application of Electric Field Along the Topographical Alignment. *Tissue Eng Part A.* 24. 9-10. 752-760. 2018.
58. Stella J.A., et al. On the biomechanical function of scaffolds for engineering load-bearing soft tissues. *Acta Biomaterialia.* 6. 7. 2365-2381. 2010.
59. Dahl S.L., et al. Mechanical properties and compositions of tissue engineered and native arteries. *Annals of Biomedical Engineering.* 35. 3. 348-355. 2007.
60. Shin S.R., et al. Carbon-nanotube-embedded hydrogel sheets for engineering cardiac constructs and bioactuators. *ACS Nano.* 7. 3. 2369-2380. 2013.
61. Gabriel C., et al. Electrical conductivity of tissue at frequencies below 1 MHz. *Physics in Medicine and Biology.* 54. 16. 4863-4878. 2009.
62. Langer G.A. *The myocardium.* Academic Press; 1997.
63. Holzapfel G.A., et al. *Biomechanics of soft tissue in cardiovascular systems.* Vol 441: Springer; 2014.
64. Souders C.A., et al. Cardiac fibroblast: the renaissance cell. *Circulation Research.* 105. 12. 1164-1176. 2009.
65. Anderson R.H., et al. *Paediatric cardiology.* Vol 2: Churchill Livingstone; 2010.
66. Kaushik G., et al. From stem cells to cardiomyocytes: the role of forces in cardiac maturation, aging, and disease. *Progress in Molecular Biology and Translational Science.* 126. 219-242. 2014.
67. Richardson W.J., et al. Physiological Implications of Myocardial Scar Structure. *Comprehensive Physiology.* 5. 4. 1877-1909. 2015.
68. Scanlon V.C., et al. *Essentials of anatomy and physiology.* 5th ed. Philadelphia: F. A. Davis Company; 2007.
69. Anderson R.H., et al. The anatomy of the cardiac conduction system. *Clinical Anatomy.* 22. 1. 99-113. 2009.
70. Opie L.H. *Heart physiology: from cell to circulation.* Lippincott Williams & Wilkins; 2004.
71. Tortora G.J., et al. *Principles of Anatomy and Physiology.* Hoboken, NJ: John Wiley & Sons

Inc.; 2014.

72. Gabriel S., et al. The dielectric properties of biological tissues: II. Measurements in the frequency range 10 Hz to 20 GHz. *Physics in Medicine and Biology.* 41. 11. 2251-2269. 1996.
73. Roberts D.E., et al. Effect of tissue anisotropy on extracellular potential fields in canine myocardium in situ. *Circulation Research.* 50. 3. 342-351. 1982.
74. Tsai J.Z., et al. In-vivo measurement of swine myocardial resistivity. *IEEE Transactions on Biomedical Engineering.* 49. 5. 472-483. 2002.
75. Brette F., et al. T-tubule function in mammalian cardiac myocytes. *Circulation Research.* 92. 11. 1182-1192. 2003.
76. Doenst T., et al. Cardiac metabolism in heart failure: implications beyond ATP production. *Circulation Research.* 113. 6. 709-724. 2013.
77. Toyoshima H., et al. Effect of ventricular hypertrophy on conduction velocity of activation front in the ventricular myocardium. *The American journal of cardiology.* 49. 8. 1938-1945. 1982.
78. Cheng J.M., et al. Percutaneous left ventricular assist devices vs. intra-aortic balloon pump counterpulsation for treatment of cardiogenic shock: a meta-analysis of controlled trials. *European Heart Journal.* 30. 17. 2102-2108. 2009.
79. Manyalich M., et al. The need and opportunity for donation after circulatory death worldwide. *Current Opinion in Organ Transplantation.* 23. 1. 136-141. 2018.
80. Orlic D., et al. Bone marrow cells regenerate infarcted myocardium. *Nature.* 410. 6829. 701-705. 2001.
81. Dawn B., et al. Cardiac stem cells delivered intravascularly traverse the vessel barrier, regenerate infarcted myocardium, and improve cardiac function. *Proceedings of the National Academy of Sciences of the United States of America.* 102. 10. 3766-3771. 2005.
82. Orlic D., et al. Mobilized bone marrow cells repair the infarcted heart, improving function and survival. *Proceedings of the National Academy of Sciences of the United States of America.* 98. 18. 10344-10349. 2001.
83. Beltrami A.P., et al. Adult cardiac stem cells are multipotent and support myocardial regeneration. *Cell.* 114. 6. 763-776. 2003.
84. Hodgkinson C.P., et al. Emerging Concepts in Paracrine Mechanisms in Regenerative Cardiovascular Medicine and Biology. *Circulation Research.* 118. 1. 95-107. 2016.
85. Romagnuolo R., et al. Programming cells for cardiac repair. *Current Opinion in Biotechnology.* 47. 43-50. 2017.
86. Ieda M., et al. Direct reprogramming of fibroblasts into functional cardiomyocytes by defined factors. *Cell.* 142. 3. 375-386. 2010.
87. Zhao Y., et al. High-efficiency reprogramming of fibroblasts into cardiomyocytes requires suppression of pro-fibrotic signalling. *Nature Communications.* 6. 8243. 2015.
88. Monaghan M.G., et al. Cardiomyocyte generation from somatic sources - Current status and future directions. *Current Opinion in Biotechnology.* 40. 49-55. 2016.
89. Chen V.C., et al. Development of a scalable suspension culture for cardiac differentiation from human pluripotent stem cells. *Stem Cell Research.* 15. 2. 365-375. 2015.
90. Song K., et al. Heart repair by reprogramming non-myocytes with cardiac transcription factors. *Nature.* 485. 7400. 599-604. 2012.
91. Pittenger M.F., et al. Multilineage potential of adult human mesenchymal stem cells. *Science.* 284. 5411. 143-147. 1999.
92. Galipeau J., et al. Mesenchymal Stromal Cells: Clinical Challenges and Therapeutic Opportunities. *Cell Stem Cell.* 22. 6. 824-833. 2018.
93. Li Q., et al. Gata4, Tbx5 and Baf60c induce differentiation of adipose tissue-derived mesenchymal stem cells into beating cardiomyocytes. *The International Journal of Biochemistry & Cell Biology Biol.* 66. 30-36. 2015.
94. Metzele R., et al. Human adipose tissue-derived stem cells exhibit proliferation potential and spontaneous rhythmic contraction after fusion with neonatal rat cardiomyocytes. *FASEB journal: official publication of the Federation of American Societies for Experimental Biology.*

25. 3. 830-839. 2011.

95. Xu C., et al. Characterization and enrichment of cardiomyocytes derived from human embryonic stem cells. *Circulation Research.* 91. 6. 501-508. 2002.

96. Chong J.J., et al. Human embryonic-stem-cell-derived cardiomyocytes regenerate non-human primate hearts. *Nature.* 510. 7504. 273-277. 2014.

97. Shen N., et al. Steps toward Maturation of Embryonic Stem Cell-Derived Cardiomyocytes by Defined Physical Signals. *Stem Cell Reports.* 9. 1. 122-135. 2017.

98. Takahashi K., et al. Induction of pluripotent stem cells from mouse embryonic and adult fibroblast cultures by defined factors. *Cell.* 126. 4. 663-676. 2006.

99. Burridge P.W., et al. Production of de novo cardiomyocytes: human pluripotent stem cell differentiation and direct reprogramming. *Cell Stem Cell.* 10. 1. 16-28. 2012.

100. Lu T.Y., et al. Repopulation of decellularized mouse heart with human induced pluripotent stem cell-derived cardiovascular progenitor cells. *Nature Communications.* 4. 2307. 2013.

101. Liu B., et al. Cardiac recovery via extended cell-free delivery of extracellular vesicles secreted by cardiomyocytes derived from induced pluripotent stem cells. *Nature Biomedical Engineering.* 2. 5. 293-303. 2018.

102. Ribeiro J., et al. Evaluation of PVA biodegradable electric conductive membranes for nerve regeneration in axonotmesis injuries: the rat sciatic nerve animal model. *Journal of Biomedical Materials Research Part A.* 105. 5. 1267-1280. 2017.

103. Rahaman M., et al. A New Insight in Determining the Percolation Threshold of Electrical Conductivity for Extrinsically Conducting Polymer Composites through Different Sigmoidal Models. *Polymers (Basel).* 9. 10. 527. 2017.

104. Rueda-Gensini L., et al. Graphene Oxide-Embedded Extracellular Matrix-Derived Hydrogel as a Multiresponsive Platform for 3D Bioprinting Applications. *International Journal of Bioprinting.* 7. 3. 353. 2021.

105. Iijima S. Helical microtubules of graphitic carbon. *Nature.* 354. 6348. 56-58. 1991.

106. Harrison B.S., et al. Carbon nanotube applications for tissue engineering. *Biomaterials.* 28. 2. 344-353. 2007.

107. Amezcua R., et al. Nanomaterials for Cardiac Myocyte Tissue Engineering. *Nanomaterials (Basel).* 6. 7. 133. 2016.

108. Yu M.F., et al. Tensile loading of ropes of single wall carbon nanotubes and their mechanical properties. *Physical Review Letters.* 84. 24. 5552-5555. 2000.

109. Demczyk B.G., et al. Direct mechanical measurement of the tensile strength and elastic modulus of multiwalled carbon nanotubes. *Materials Science and Engineering: A.* 334. 1-2. 173-178. 2002.

110. Orlita M., et al. Approaching the dirac point in high-mobility multilayer epitaxial graphene. *Physical Review Letters.* 101. 26. 267601. 2008.

111. Nardecchia S., et al. Three dimensional macroporous architectures and aerogels built of carbon nanotubes and/or graphene: synthesis and applications. *Chemical Society Reviews.* 42. 2. 794-830. 2013.

112. Veetil J.V., et al. Tailored carbon nanotubes for tissue engineering applications. *Biotechnology Progress.* 25. 3. 709-721. 2009.

113. Huang Y.J., et al. Carbon nanotube rope with electrical stimulation promotes the differentiation and maturity of neural stem cells. *Small.* 8. 18. 2869-2877. 2012.

114. Cellot G., et al. Carbon nanotubes might improve neuronal performance by favouring electrical shortcuts. *Nature Nanotechnology.* 4. 2. 126-133. 2009.

115. Cancian G., et al. Carbon nanotubes play an important role in the spatial arrangement of calcium deposits in hydrogels for bone regeneration. *Journal of Materials Science: Materials in Medicine.* 27. 8. 126. 2016.

116. Afroze J.D., et al. An efficient method to prepare magnetic hydroxyapatite-functionalized multi-walled carbon nanotubes nanocomposite for bone defects. *Materials Science and Engineering: C.* 86. 95-102. 2018.

117. Sitharaman B., et al. In vivo biocompatibility of ultra-short single-walled carbon nanotube/biodegradable polymer nanocomposites for bone tissue engineering. *Bone.* 43. 2.

362-370. 2008.

118. Ghaziof S., et al. Preparation, Characterization, Mechanical Properties and Electrical Conductivity Assessment of Novel Polycaprolactone/Multi-Wall Carbon Nanotubes Nanocomposites for Myocardial Tissue Engineering. *Acta Physica Polonica A.* 131. 3. 428-431. 2017.
119. Yildirim E.D., et al. Fabrication, characterization, and biocompatibility of single-walled carbon nanotube-reinforced alginate composite scaffolds manufactured using freeform fabrication technique. *Journal of Biomedical Materials Research - Part B.* 87. 2. 406-414. 2008.
120. Huang B., et al. Fabrication and characterisation of 3D printed MWCNT composite porous scaffolds for bone regeneration. *Materials Science and Engineering: C.* 98. 266-278. 2019.
121. Mooney E., et al. The electrical stimulation of carbon nanotubes to provide a cardiomimetic cue to MSCs. *Biomaterials.* 33. 26. 6132-6139. 2012.
122. Meng J., et al. Immune responses of BALB/c mice to subcutaneously injected multi-walled carbon nanotubes. *Nanotoxicology.* 5. 4. 583-591. 2011.
123. Novoselov K.S., et al. Electric field effect in atomically thin carbon films. *Science.* 306. 5696. 666-669. 2004.
124. Berger C., et al. Electronic confinement and coherence in patterned epitaxial graphene. *Science.* 312. 5777. 1191-1196. 2006.
125. Lee C., et al. Measurement of the elastic properties and intrinsic strength of monolayer graphene. *Science.* 321. 5887. 385-388. 2008.
126. Marcano D.C., et al. Improved synthesis of graphene oxide. *ACS Nano.* 4. 8. 4806-4814. 2010.
127. Hernandez Y., et al. High-yield production of graphene by liquid-phase exfoliation of graphite. *Nature Nanotechnology.* 3. 9. 563-568. 2008.
128. Eda G., et al. Large-area ultrathin films of reduced graphene oxide as a transparent and flexible electronic material. *Nature Nanotechnology.* 3. 5. 270-274. 2008.
129. Rodriguez-Perez L., et al. The chemistry of pristine graphene. *Chemical Communications journal.* 49. 36. 3721-3735. 2013.
130. Shen H., et al. Biomedical applications of graphene. *Theranostics.* 2. 3. 283-294. 2012.
131. Liu Z., et al. PEGylated nanographene oxide for delivery of water-insoluble cancer drugs. *Journal of the American Chemical Society.* 130. 33. 10876-10877. 2008.
132. Wang W., et al. Enhancing the Hydrophilicity and Cell Attachment of 3D Printed PCL/Graphene Scaffolds for Bone Tissue Engineering. *Materials (Basel).* 9. 12. 992. 2016.
133. Li N., et al. The promotion of neurite sprouting and outgrowth of mouse hippocampal cells in culture by graphene substrates. *Biomaterials.* 32. 35. 9374-9382. 2011.
134. Ryan A.J., et al. Electroconductive Biohybrid Collagen/Pristine Graphene Composite Biomaterials with Enhanced Biological Activity. *Advanced Materials.* 30. 15. e1706442. 2018.
135. Norahan M.H., et al. Electroactive graphene oxide-incorporated collagen assisting vascularization for cardiac tissue engineering. *Journal of Biomedical Materials Research Part A.* 107. 1. 204-219. 2019.
136. Kang S., et al. Covalent conjugation of mechanically stiff graphene oxide flakes to three-dimensional collagen scaffolds for osteogenic differentiation of human mesenchymal stem cells. *Carbon.* 83. 162-172. 2015.
137. Alam A., et al. Novel polyacrylamide hydrogels by highly conductive, water-processable graphene. *Composites Part A: Applied Science and Manufacturing.* 93. 1-9. 2017.
138. Jo H., et al. Electrically conductive graphene/polyacrylamide hydrogels produced by mild chemical reduction for enhanced myoblast growth and differentiation. *Acta Biomaterialia.* 48. 100-109. 2017.
139. Shin S.R., et al. Reduced Graphene Oxide-GelMA Hybrid Hydrogels as Scaffolds for Cardiac Tissue Engineering. *Small.* 12. 27. 3677-3689. 2016.
140. Jing X., et al. Mussel-inspired electroactive chitosan/graphene oxide composite hydrogel with rapid self-healing and recovery behavior for tissue engineering. *Carbon.* 125. 557-570. 2017.
141. Shi X., et al. Regulating Cellular Behavior on Few-Layer Reduced Graphene Oxide Films

with Well-Controlled Reduction States. *Advanced Functional Materials.* 22. 4. 751-759. 2012.

142. Parish R.V. Gold in Medicine - Chrysotherapy. *Interdisciplinary Science Reviews.* 17. 3. 221-228. 2013.

143. Salomoni R., et al. Antibacterial effect of silver nanoparticles in Pseudomonas aeruginosa. *Nanotechnology, Science and Applications.* 10. 115-121. 2017.

144. Brett D.W. A discussion of silver as an antimicrobial agent: alleviating the confusion. *Ostomy/wound management.* 52. 1. 34-41. 2006.

145. Radomska A., et al. The Nanopharmacology and Nanotoxicology of Nanomaterials: New Opportunities and Challenges. *Advances in clinical and experimental medicine : official organ Wroclaw Medical University.* 25. 1. 151-162. 2016.

146. Arbain R., et al. Preparation of iron oxide nanoparticles by mechanical milling. *Minerals Engineering.* 24. 1. 1-9. 2011.

147. Ibanez M., et al. Core-shell nanoparticles as building blocks for the bottom-up production of functional nanocomposites: PbTe-PbS thermoelectric properties. *ACS Nano.* 7. 3. 2573-2586. 2013.

148. Mallick K., et al. Fabrication of a metal nanoparticles and polymer nanofibers composite material by an in situ chemical synthetic route. *Langmuir.* 21. 17. 7964-7967. 2005.

149. Akbarzadeh A., et al. Magnetic nanoparticles: preparation, physical properties, and applications in biomedicine. *Nanoscale Res Lett.* 7. 1. 144. 2012.

150. Xu Z.P., et al. Inorganic nanoparticles as carriers for efficient cellular delivery. *Chemical Engineering Science.* 61. 3. 1027-1040. 2006.

151. Shanmugasundaram T., et al. Biocompatible silver, gold and silver/gold alloy nanoparticles for enhanced cancer therapy: in vitro and in vivo perspectives. *Nanoscale.* 9. 43. 16773-16790. 2017.

152. Chithrani B.D., et al. Determining the size and shape dependence of gold nanoparticle uptake into mammalian cells. *Nano LettERS.* 6. 4. 662-668. 2006.

153. Tan H.L., et al. Application of Metal Nanoparticle(-)Hydrogel Composites in Tissue Regeneration. *Bioengineering (Basel).* 6. 1. 17. 2019.

154. Hasan A., et al. Nanoparticles in tissue engineering: applications, challenges and prospects. *International Journal of Nanomedicine.* 13. 5637-5655. 2018.

155. Alarcon E.I., et al. Safety and efficacy of composite collagen-silver nanoparticle hydrogels as tissue engineering scaffolds. *Nanoscale.* 7. 44. 18789-18798. 2015.

156. Gonzalez-Sanchez M.I., et al. Silver nanoparticle based antibacterial methacrylate hydrogels potential for bone graft applications. *Materials Science and Engineering: C.* 50. 332-340. 2015.

157. Ribeiro M., et al. Antibacterial silk fibroin/nanohydroxyapatite hydrogels with silver and gold nanoparticles for bone regeneration. *Nanomedicine.* 13. 1. 231-239. 2017.

158. Liu H., et al. Less harmful acidic degradation of poly(lacticco-glycolic acid) bone tissue engineering scaffolds through titania nanoparticle addition. *International Journal of Nanomedicine.* 1. 4. 541-545. 2006.

159. Esmaeili E., et al. Magnetoelectric nanocomposite scaffold for high yield differentiation of mesenchymal stem cells to neural-like cells. *Journal of Cellular Physiology.* 234. 8. 13617-13628. 2019.

160. Grant S.A., et al. Gold Nanoparticle-Collagen Gels for Soft Tissue Augmentation. *Tissue Engineering Part A.* 24. 13-14. 1091-1098. 2018.

161. Behzadi S., et al. Cellular uptake of nanoparticles: journey inside the cell. *Chemical Society Reviews.* 46. 14. 4218-4244. 2017.

162. Lim D., et al. Multi stimuli-responsive hydrogel microfibers containing magnetite nanoparticles prepared using microcapillary devices. *Soft Matter.* 11. 8. 1606-1613. 2015.

163. Zulkifli F.H., et al. A facile synthesis method of hydroxyethyl cellulose-silver nanoparticle scaffolds for skin tissue engineering applications. *Materials Science and Engineering: C.* 79. 151-160. 2017.

164. Fadeel B., et al. Advanced tools for the safety assessment of nanomaterials. *Nature Nanotechnology.* 13. 7. 537-543. 2018.

165. Gliga A.R., et al. Size-dependent cytotoxicity of silver nanoparticles in human lung cells: the role of cellular uptake, agglomeration and Ag release. *Particle and Fibre Toxicology.* 11. 1. 11. 2014.

166. Naguib M., et al. Two-dimensional transition metal carbides. *ACS Nano.* 6. 2. 1322-1331. 2012.

167. Naguib M., et al. Two-dimensional nanocrystals produced by exfoliation of Ti3 AlC2. *Advanced Materials.* 23. 37. 4248-4253. 2011.

168. Anasori B., et al. 2D metal carbides and nitrides (MXenes) for energy storage. *Nature Reviews Materials.* 2. 16098. 2017.

169. Naguib M., et al. 25th anniversary article: MXenes: a new family of two-dimensional materials. *Advanced Materials.* 26. 7. 992-1005. 2014.

170. Liu G., et al. Surface Modified Ti3C2 MXene Nanosheets for Tumor Targeting Photothermal/Photodynamic/Chemo Synergistic Therapy. *ACS Applied Materials and Interfaces.* 9. 46. 40077-40086. 2017.

171. Xue Q., et al. Photoluminescent Ti3 C2 MXene Quantum Dots for Multicolor Cellular Imaging. *Advanced Materials.* 29. 15. 1604847. 2017.

172. Wang F., et al. An Organ-Like Titanium Carbide Material (MXene) with Multilayer Structure Encapsulating Hemoglobin for a Mediator-Free Biosensor. *Journal of The Electrochemical Society.* 162. 1. B16-B21. 2014.

173. Xu B., et al. Ultrathin MXene-Micropattern-Based Field-Effect Transistor for Probing Neural Activity. *Advanced Materials.* 28. 17. 3333-3339. 2016.

174. Rasool K., et al. Antibacterial Activity of Ti(3)C(2)Tx MXene. *ACS Nano.* 10. 3. 3674-3684. 2016.

175. Zhang C.J., et al. Transparent, Flexible, and Conductive 2D Titanium Carbide (MXene) Films with High Volumetric Capacitance. *Advanced Materials.* 29. 36. 1702678. 2017.

176. Lin H., et al. Two-Dimensional Ultrathin MXene Ceramic Nanosheets for Photothermal Conversion. *Nano Lett.* 17. 1. 384-391. 2017.

177. Xuan J., et al. Organic-Base-Driven Intercalation and Delamination for the Production of Functionalized Titanium Carbide Nanosheets with Superior Photothermal Therapeutic Performance. *Angewandte Chemie (International ed in English).* 55. 47. 14569-14574. 2016.

178. Lin H., et al. Theranostic 2D Tantalum Carbide (MXene). *Advanced Materials.* 30. 4. 1703284. 2018.

179. Lin H., et al. A Two-Dimensional Biodegradable Niobium Carbide (MXene) for Photothermal Tumor Eradication in NIR-I and NIR-II Biowindows. *Journal of the American Chemical Society.* 139. 45. 16235-16247. 2017.

180. Han X., et al. 2D Ultrathin MXene-Based Drug-Delivery Nanoplatform for Synergistic Photothermal Ablation and Chemotherapy of Cancer. *Advanced Healthcare Materials.* 7. 9. e1701394. 2018.

181. Zhang X., et al. Single-layered graphitic-C(3)N(4) quantum dots for two-photon fluorescence imaging of cellular nucleus. *Advanced Materials.* 26. 26. 4438-4443. 2014.

182. Chiang C.K., et al. Electrical Conductivity in Doped Polyacetylene. *Physical Review Letters.* 39. 17. 1098-1101. 1977.

183. Heeger A.J. Semiconducting and Metallic Polymers: The Fourth Generation of Polymeric Materials. *The Journal of Physical Chemistry B.* 105. 36. 8475-8491. 2001.

184. Nezakati T., et al. Conductive Polymers: Opportunities and Challenges in Biomedical Applications. *Chemical Reviews.* 118. 14. 6766-6843. 2018.

185. Letheby H. XXIX.—On the production of a blue substance by the electrolysis of sulphate of aniline. *Journal of the Chemical Society.* 15. 0. 161-163. 1862.

186. Jozefowicz M., et al. Conductivité Electronique et Propriétés Chimiques de Polyanilines Oligomères. *Journal of Polymer Science Part C: Polymer Symposia.* 16. 5. 2943-2954. 1967.

187. Cao Y., et al. Counter-ion induced processibility of conducting polyaniline and of conducting polyblends of polyaniline in bulk polymers. *Synthetic Metals.* 48. 1. 91-97. 1992.

188. Macdiarmid A.G., et al. Polyaniline: a new concept in conducting polymers. *Synthetic Metals.* 18. 1-3. 285-290. 1987.

189. de Albuquerque J.E., et al. Study of the interconversion of polyaniline oxidation states by optical absorption spectroscopy. *Synthetic Metals.* 146. 1. 1-10. 2004.

190. Zarrintaj P., et al. Bio - Conductive Scaffold Based on Agarose - Polyaniline for Tissue Engineering. *Journal of Skin and Stem Cell.* In Press. In Press. e67394. 2017.

191. Qazi T.H., et al. Development and characterization of novel electrically conductive PANI-PGS composites for cardiac tissue engineering applications. *Acta Biomaterialia.* 10. 6. 2434-2445. 2014.

192. Wu Y., et al. Fabrication of conductive gelatin methacrylate-polyaniline hydrogels. *Acta Biomaterialia.* 33. 122-130. 2016.

193. Thrivikraman G., et al. Intermittent electrical stimuli for guidance of human mesenchymal stem cell lineage commitment towards neural-like cells on electroconductive substrates. *Biomaterials.* 35. 24. 6219-6235. 2014.

194. Guo X.-L., et al. Preparation and characterization of conductive poly-dl-lactic-acid/tetra-aniline conduit for peripheral nerve regeneration. *Journal of Bioactive and Compatible Polymers.* 34. 2. 190-208. 2018.

195. Zhao X., et al. Antibacterial anti-oxidant electroactive injectable hydrogel as self-healing wound dressing with hemostasis and adhesiveness for cutaneous wound healing. *Biomaterials.* 122. 34-47. 2017.

196. Zhang Q.S., et al. Synthesis of a novel biodegradable and electroactive polyphosphazene for biomedical application. *Biomedical Materials.* 4. 3. 035008. 2009.

197. Zarrintaj P., et al. Oligoaniline-based conductive biomaterials for tissue engineering. *Acta Biomaterialia.* 72. 16-34. 2018.

198. McNeill R., et al. Electronic Conduction in Polymers. I. The Chemical Structure of Polypyrrole. *Australian Journal of Chemistry.* 16. 6. 1056. 1963.

199. Dall'Olio A., et al. Electron paramagnetic resonance and conductiviy of electrocatalytic oxypyrrole (pyrrole polymer) black. *Comptes rendus de l'Académie des Sciences.* 267. C. 433. 1968.

200. Mathys G.I., et al. Spectroscopic study of thermo-oxidative degradation of polypyrrole powder by FT-IR. *Synthetic Metals.* 89. 2. 103-109. 1997.

201. Kang H.C., et al. Enhanced electrical conductivity of polypyrrole prepared by chemical oxidative polymerization: effect of the preparation technique and polymer additive. *Polymer.* 41. 18. 6931-6934. 2000.

202. Kai D., et al. Polypyrrole-contained electrospun conductive nanofibrous membranes for cardiac tissue engineering. *Journal of Biomedical Materials Research Part A.* 99. 3. 376-385. 2011.

203. Huang Z.-B., et al. Conducting polypyrrole in tissue engineering applications. *Frontiers of Materials Science.* 8. 1. 39-45. 2014.

204. Wong J.Y., et al. Electrically conducting polymers can noninvasively control the shape and growth of mammalian cells. *Proceedings of the National Academy of Sciences of the United States of America.* 91. 8. 3201-3204. 1994.

205. Tsui J.H., et al. Conductive Silk-Polypyrrole Composite Scaffolds with Bioinspired Nanotopographic Cues for Cardiac Tissue Engineering. *Journal of Materials Chemistry B.* 6. 44. 7185-7196. 2018.

206. Shrestha S., et al. Electrodeless coating polypyrrole on chitosan grafted polyurethane with functionalized multiwall carbon nanotubes electrospun scaffold for nerve tissue engineering. *Carbon.* 136. 430-443. 2018.

207. Gelmi A., et al. Direct Mechanical Stimulation of Stem Cells: A Beating Electromechanically Active Scaffold for Cardiac Tissue Engineering. *Advanced Healthcare Materials.* 5. 12. 1471-1480. 2016.

208. Lee J.Y., et al. Polypyrrole-coated electrospun PLGA nanofibers for neural tissue applications. *Biomaterials.* 30. 26. 4325-4335. 2009.

209. Massoumi B., et al. Electrically conductive nanofibrous scaffold composed of poly(ethylene glycol)-modified polypyrrole and poly(epsilon-caprolactone) for tissue engineering applications. *Materials Science and Engineering: C.* 98. 300-310. 2019.

210. Sajesh K.M., et al. Biocompatible conducting chitosan/polypyrrole-alginate composite

scaffold for bone tissue engineering. *International Journal of Biological Macromolecules.* 62. 465-471. 2013.

211. Vishnoi T., et al. Conducting cryogel scaffold as a potential biomaterial for cell stimulation and proliferation. *Journal of Materials Science: Materials in Medicine.* 24. 2. 447-459. 2013.
212. Elschner A., et al. *PEDOT: principles and applications of an intrinsically conductive polymer.* CRC Press; 2010.
213. Groenendaal L., et al. Poly(3,4-ethylenedioxythiophene) and Its Derivatives: Past, Present, and Future. *Advanced Materials.* 12. 7. 481-494. 2000.
214. Zhang P., et al. Direct Writing and Characterization of Three-Dimensional Conducting Polymer PEDOT Arrays. *ACS Applied Materials and Interfaces.* 10. 14. 11888-11895. 2018.
215. Gualandi I., et al. A simple all-PEDOT:PSS electrochemical transistor for ascorbic acid sensing. *Journal of Materials Chemistry B.* 3. 33. 6753-6762. 2015.
216. Wang F., et al. A soft biomolecule actuator based on a highly functionalized bacterial cellulose nano-fiber network with carboxylic acid groups. *Soft Matter.* 12. 1. 246-254. 2016.
217. Khodagholy D., et al. In vivo recordings of brain activity using organic transistors. *Nature Communications.* 4. 1575. 2013.
218. Levermore P.A., et al. High efficiency organic light-emitting diodes with PEDOT-based conducting polymer anodes. *Journal of Materials Chemistry.* 18. 37. 4414-4420. 2008.
219. Yu Z., et al. PEDOT:PSS Films with Metallic Conductivity through a Treatment with Common Organic Solutions of Organic Salts and Their Application as a Transparent Electrode of Polymer Solar Cells. *ACS Applied Materials and Interfaces.* 8. 18. 11629-11638. 2016.
220. Marzocchi M., et al. Physical and Electrochemical Properties of PEDOT:PSS as a Tool for Controlling Cell Growth. *ACS Applied Materials and Interfaces.* 7. 32. 17993-18003. 2015.
221. Amorini F., et al. Electrically Controlled "Sponge Effect" of PEDOT:PSS Governs Membrane Potential and Cellular Growth. *ACS Applied Materials and Interfaces.* 9. 8. 6679-6689. 2017.
222. Pires F., et al. Neural stem cell differentiation by electrical stimulation using a cross-linked PEDOT substrate: Expanding the use of biocompatible conjugated conductive polymers for neural tissue engineering. *Biochimica et Biophysica Acta.* 1850. 6. 1158-1168. 2015.
223. Wang S., et al. Hyaluronic acid doped-poly(3,4-ethylenedioxythiophene)/chitosan/gelatin (PEDOT-HA/Cs/Gel) porous conductive scaffold for nerve regeneration. *Materials Science and Engineering: C.* 71. 308-316. 2017.
224. Fan Z., et al. Significantly Enhanced Thermoelectric Properties of PEDOT:PSS Films through Sequential Post-Treatments with Common Acids and Bases. *Advanced Energy Materials.* 7. 8. 1602116. 2017.
225. Mantione D., et al. Low-Temperature Cross-Linking of PEDOT:PSS Films Using Divinylsulfone. *ACS Applied Materials and Interfaces.* 9. 21. 18254-18262. 2017.
226. Chen C., et al. Electrically-responsive core-shell hybrid microfibers for controlled drug release and cell culture. *Acta Biomaterialia.* 55. 434-442. 2017.
227. Xu C., et al. Biodegradable and electroconductive poly(3,4-ethylenedioxythiophene)/ carboxymethyl chitosan hydrogels for neural tissue engineering. *Materials Science and Engineering: C.* 84. 32-43. 2018.
228. Bessaire B., et al. Synthesis of Continuous Conductive PEDOT:PSS Nanofibers by Electrospinning: A Conformal Coating for Optoelectronics. *ACS Applied Materials and Interfaces.* 9. 1. 950-957. 2017.
229. Mawad D., et al. Electroconductive Hydrogel Based on Functional Poly(Ethylenedioxy Thiophene). *Chemistry of Materials.* 28. 17. 6080-6088. 2016.
230. Heo D.N., et al. Development of 3D printable conductive hydrogel with crystallized PEDOT:PSS for neural tissue engineering. *Materials Science and Engineering: C.* 99. 582-590. 2019.
231. Del Agua I., et al. Conducting Polymer Scaffolds Based on Poly(3,4-ethylenedioxythiophene) and Xanthan Gum for Live-Cell Monitoring. *ACS Omega.* 3. 7. 7424-7431. 2018.
232. Spencer A.R., et al. Electroconductive Gelatin Methacryloyl-PEDOT:PSS Composite Hydrogels: Design, Synthesis, and Properties. *ACS Biomaterials Science & Engineering.* 4. 5. 1558-1567. 2018.

233. Johansen A.K., et al. Postnatal Cardiac Gene Editing Using CRISPR/Cas9 With AAV9-Mediated Delivery of Short Guide RNAs Results in Mosaic Gene Disruption. *Circulation Research.* 121. 10. 1168-1181. 2017.

234. Savoji H., et al. Cardiovascular disease models: A game changing paradigm in drug discovery and screening. *Biomaterials.* 198. 3-26. 2019.

235. Jackman C., et al. Long-term contractile activity and thyroid hormone supplementation produce engineered rat myocardium with adult-like structure and function. *Acta Biomaterialia.* 78. 98-110. 2018.

236. Bursac N., et al. Cardiac muscle tissue engineering: toward an in vitro model for electrophysiological studies. *American Journal of Physiology.* 277. 2. H433-444. 1999.

237. Li R.K., et al. Construction of a bioengineered cardiac graft. *The Journal of Thoracic and Cardiovascular Surgery.* 119. 2. 368-375. 2000.

238. Radisic M., et al. Functional assembly of engineered myocardium by electrical stimulation of cardiac myocytes cultured on scaffolds. *Proceedings of the National Academy of Sciences of the United States of America.* 101. 52. 18129-18134. 2004.

239. Boudou T., et al. A microfabricated platform to measure and manipulate the mechanics of engineered cardiac microtissues. *Tissue Engineering Part A.* 18. 9-10. 910-919. 2012.

240. Hirt M.N., et al. Functional improvement and maturation of rat and human engineered heart tissue by chronic electrical stimulation. *Journal of Molecular and Cellular Cardiology.* 74. 151-161. 2014.

241. Tandon N., et al. Electrical stimulation systems for cardiac tissue engineering. *Nature Protocols.* 4. 2. 155-173. 2009.

242. Visone R., et al. Enhancing all-in-one bioreactors by combining interstitial perfusion, electrical stimulation, on-line monitoring and testing within a single chamber for cardiac constructs. *Scientific Reports.* 8. 1. 16944. 2018.

243. You J.O., et al. Nanoengineering the heart: conductive scaffolds enhance connexin 43 expression. *Nano Letters.* 11. 9. 3643-3648. 2011.

244. Baei P., et al. Electrically conductive gold nanoparticle-chitosan thermosensitive hydrogels for cardiac tissue engineering. *Materials Science and Engineering: C.* 63. 131-141. 2016.

245. Smith A.S.T., et al. Micro- and nano-patterned conductive graphene-PEG hybrid scaffolds for cardiac tissue engineering. *Chemical Communications.* 53. 53. 7412-7415. 2017.

246. Mooney E., et al. Carbon nanotubes and mesenchymal stem cells: biocompatibility, proliferation and differentiation. *Nano Letters.* 8. 8. 2137-2143. 2008.

247. Ahadian S., et al. Moldable elastomeric polyester-carbon nanotube scaffolds for cardiac tissue engineering. *Acta Biomaterialia.* 52. 81-91. 2017.

248. Liu Y., et al. Tuning the conductivity and inner structure of electrospun fibers to promote cardiomyocyte elongation and synchronous beating. *Materials Science and Engineering: C.* 69. 865-874. 2016.

249. Hsiao C.W., et al. Electrical coupling of isolated cardiomyocyte clusters grown on aligned conductive nanofibrous meshes for their synchronized beating. *Biomaterials.* 34. 4. 1063-1072. 2013.

250. Kai D., et al. Biocompatibility evaluation of electrically conductive nanofibrous scaffolds for cardiac tissue engineering. *Journal of Materials Chemistry B.* 1. 17. 2305-2314. 2013.

251. Wu Y., et al. Interwoven Aligned Conductive Nanofiber Yarn/Hydrogel Composite Scaffolds for Engineered 3D Cardiac Anisotropy. *ACS Nano.* 11. 6. 5646-5659. 2017.

252. Baheiraei N., et al. Preparation of a porous conductive scaffold from aniline pentamer-modified polyurethane/PCL blend for cardiac tissue engineering. *Journal of Biomedical Materials Research Part A.* 103. 10. 3179-3187. 2015.

253. Chan Y.C., et al. Electrical stimulation promotes maturation of cardiomyocytes derived from human embryonic stem cells. *Journal of Cardiovascular Translational Research.* 6. 6. 989-999. 2013.

254. Hernandez D., et al. Electrical Stimulation Promotes Cardiac Differentiation of Human Induced Pluripotent Stem Cells. *Stem Cells Int.* 2016. 1718041. 2016.

255. Tulloch N.L., et al. Growth of engineered human myocardium with mechanical loading and vascular coculture. *Circulation Research.* 109. 1. 47-59. 2011.

256. Mannhardt I., et al. Human Engineered Heart Tissue: Analysis of Contractile Force. *Stem Cell Reports.* 7. 1. 29-42. 2016.

257. Ruan J.L., et al. Mechanical Stress Conditioning and Electrical Stimulation Promote Contractility and Force Maturation of Induced Pluripotent Stem Cell-Derived Human Cardiac Tissue. *Circulation.* 134. 20. 1557-1567. 2016.

258. Mohammadi Amirabad L., et al. Enhanced Cardiac Differentiation of Human Cardiovascular Disease Patient-Specific Induced Pluripotent Stem Cells by Applying Unidirectional Electrical Pulses Using Aligned Electroactive Nanofibrous Scaffolds. *ACS Applied Materials and Interfaces.* 9. 8. 6849-6864. 2017.

259. Roshanbinfar K., et al. Electroconductive Biohybrid Hydrogel for Enhanced Maturation and Beating Properties of Engineered Cardiac Tissues. *Advanced Functional Materials.* 28. 42. 1803951. 2018.

260. Ma R., et al. Electrical Stimulation Enhances Cardiac Differentiation of Human Induced Pluripotent Stem Cells for Myocardial Infarction Therapy. *Antioxidants & Redox Signaling.* 28. 5. 371-384. 2018.

261. Fujimoto K.L., et al. In vivo evaluation of a porous, elastic, biodegradable patch for reconstructive cardiac procedures. *The Annals of Thoracic Surgery.* 83. 2. 648-654. 2007.

262. D'Amore A., et al. Bi-layered polyurethane - Extracellular matrix cardiac patch improves ischemic ventricular wall remodeling in a rat model. *Biomaterials.* 107. 1-14. 2016.

263. Borriello A., et al. Optimizing PANi doped electroactive substrates as patches for the regeneration of cardiac muscle. *Journal of Materials Science: Materials in Medicine.* 22. 4. 1053-1062. 2011.

264. Dvir T., et al. Nanowired three-dimensional cardiac patches. *Nature Nanotechnology.* 6. 11. 720-725. 2011.

265. Wickham A.M., et al. Polycaprolactone-thiophene-conjugated carbon nanotube meshes as scaffolds for cardiac progenitor cells. *Journal of Biomedical Materials Research Part B.* 102. 7. 1553-1561. 2014.

266. Izadifar M., et al. UV-Assisted 3D Bioprinting of Nanoreinforced Hybrid Cardiac Patch for Myocardial Tissue Engineering. *Tissue Engineering Part C Methods.* 24. 2. 74-88. 2018.

267. Hoang A.-P., et al. Porous and sutureless bioelectronic patch with retained electronic properties under cyclic stretching. *Applied Materials Today.* 15. 315-322. 2019.

268. Mawad D., et al. A conducting polymer with enhanced electronic stability applied in cardiac models. *Science Advances.* 2. 11. e1601007. 2016.

269. Kapnisi M., et al. Auxetic Cardiac Patches with Tunable Mechanical and Conductive Properties toward Treating Myocardial Infarction. *Advanced Functional Materials.* 28. 21. 1800618. 2018.

270. Saravanan S., et al. Graphene Oxide-Gold Nanosheets Containing Chitosan Scaffold Improves Ventricular Contractility and Function After Implantation into Infarcted Heart. *Scientific Reports.* 8. 1. 15069. 2018.

271. Song X., et al. In situ pPy-modification of chitosan porous membrane from mussel shell as a cardiac patch to repair myocardial infarction. *Applied Materials Today.* 15. 87-99. 2019.

272. Liang S., et al. Paintable and Rapidly Bondable Conductive Hydrogels as Therapeutic Cardiac Patches. *Advanced Materials.* 30. 23. e1704235. 2018.

273. Hosoyama K., et al. Nanoengineered Electroconductive Collagen-Based Cardiac Patch for Infarcted Myocardium Repair. *ACS Applied Materials and Interfaces.* 10. 51. 44668-44677. 2018.

274. Qu J., et al. Injectable antibacterial conductive hydrogels with dual response to an electric field and pH for localized "smart" drug release. *Acta Biomaterialia.* 72. 55-69. 2018.

275. Mihic A., et al. A Conductive Polymer Hydrogel Supports Cell Electrical Signaling and Improves Cardiac Function After Implantation into Myocardial Infarct. *Circulation.* 132. 8. 772-784. 2015.

276. Cui Z., et al. Polypyrrole-chitosan conductive biomaterial synchronizes cardiomyocyte contraction and improves myocardial electrical impulse propagation. *Theranostics.* 8. 10. 2752-2764. 2018.

277. Bao R., et al. A pi-pi conjugation-containing soft and conductive injectable polymer hydrogel

highly efficiently rebuilds cardiac function after myocardial infarction. *Biomaterials.* 122. 63-71. 2017.

278. Cui H., et al. In vitro study of electroactive tetraaniline-containing thermosensitive hydrogels for cardiac tissue engineering. *Biomacromolecules.* 15. 4. 1115-1123. 2014.
279. Hori M., et al. Oxidative stress and left ventricular remodelling after myocardial infarction. *Cardiovascular research.* 81. 3. 457-464. 2009.
280. Cui H., et al. In situ electroactive and antioxidant supramolecular hydrogel based on cyclodextrin/copolymer inclusion for tissue engineering repair. *Macromolecular Bioscience.* 14. 3. 440-450. 2014.
281. Guo B., et al. Biodegradable and electrically conducting polymers for biomedical applications. *Progress in Polymer Science.* 38. 9. 1263-1286. 2013.
282. Mytych J., et al. Nanoparticle technology as a double-edged sword: cytotoxic, genotoxic and epigenetic effects on living cells. *Journal of Biomaterials and Nanobiotechnology.* 4. 01. 53. 2013.
283. Ali-Boucetta H., et al. Pharmacology of carbon nanotubes: toxicokinetics, excretion and tissue accumulation. *Advanced Drug Delivery Reviews.* 65. 15. 2111-2119. 2013.
284. Ou L., et al. Toxicity of graphene-family nanoparticles: a general review of the origins and mechanisms. *Particle and Fibre Toxicology.* 13. 1. 57. 2016.
285. Syama S., et al. Comprehensive Application of Graphene: Emphasis on Biomedical Concerns. *Nano-Micro Letters.* 11. 1. 6. 2019.
286. Asplund M., et al. Toxicity evaluation of PEDOT/biomolecular composites intended for neural communication electrodes. *Biomedical Materials.* 4. 4. 045009. 2009.
287. Yslas E.I., et al. Polyaniline nanofibers: Acute toxicity and teratogenic effect on Rhinella arenarum embryos. *Chemosphere.* 87. 11. 1374-1380. 2012.
288. Bobo D., et al. Nanoparticle-Based Medicines: A Review of FDA-Approved Materials and Clinical Trials to Date. *Pharmaceutical Research.* 33. 10. 2373-2387. 2016.
289. Molino P.J., et al. Influence of Biodopants on PEDOT Biomaterial Polymers: Using QCM-D to Characterize Polymer Interactions with Proteins and Living Cells. *Advanced Materials Interfaces.* 1. 3. 1300122. 2014.
290. Yang C. Enhanced physicochemical properties of collagen by using EDC/NHS-crosslinking. *Bulletin of Materials Science.* 35. 5. 913-918. 2012.
291. Haugh M.G., et al. Novel freeze-drying methods to produce a range of collagen-glycosaminoglycan scaffolds with tailored mean pore sizes. *Tissue Engineering Part C Methods.* 16. 5. 887-894. 2010.
292. Schipani R., et al. Reinforcing interpenetrating network hydrogels with 3D printed polymer networks to engineer cartilage mimetic composites. *Biofabrication.* 12. 3. 035011. 2020.
293. Patel S., et al. A review of wearable sensors and systems with application in rehabilitation. *Journal of NeuroEngineering and Rehabilitation.* 9. 1. 21. 2012.
294. Joshi M., et al. Wearable sensors to improve detection of patient deterioration. *Expert review of medical devices.* 16. 2. 145-154. 2019.
295. Yang J.C., et al. Microstructured Porous Pyramid-Based Ultrahigh Sensitive Pressure Sensor Insensitive to Strain and Temperature. *ACS Applied Materials and Interfaces.* 11. 21. 19472-19480. 2019.
296. Zhao G., et al. Transparent and stretchable triboelectric nanogenerator for self-powered tactile sensing. *Nano Energy.* 59. 302-310. 2019.
297. Sax F.L., et al. Medical patients at high risk for catastrophic deterioration. *Critical care medicine.* 15. 5. 510-515. 1987.
298. Bode B.W., et al. Continuous glucose monitoring used to adjust diabetes therapy improves glycosylated hemoglobin: a pilot study. *Diabetes research and clinical practice.* 46. 3. 183-190. 1999.
299. Amjadi M., et al. Stretchable, Skin-Mountable, and Wearable Strain Sensors and Their Potential Applications: A Review. *Advanced Functional Materials.* 26. 11. 1678-1698. 2016.
300. Zhang J.X.J., et al. Chapter 6 - Mechanical transducers: Cantilevers, acoustic wave sensors, and thermal sensors. In: Zhang JXJ, Hoshino K, eds. *Molecular Sensors and Nanodevices*

*(Second Edition)*. Academic Press. 311-412. 2019.

301. Kuang J., et al. Synergistic effects from graphene and carbon nanotubes endow ordered hierarchical structure foams with a combination of compressibility, super-elasticity and stability and potential application as pressure sensors. *Nanoscale.* 7. 20. 9252-9260. 2015.
302. Heikenfeld J., et al. Wearable sensors: modalities, challenges, and prospects. *Lab on a Chip.* 18. 2. 217-248. 2018.
303. Xu F., et al. Recent Developments for Flexible Pressure Sensors: A Review. *Micromachines (Basel).* 9. 11. 2018.
304. Solazzo M., et al. The rationale and emergence of electroconductive biomaterial scaffolds in cardiac tissue engineering. *APL Bioengineering.* 3. 4. 041501. 2019.
305. Solazzo M., et al. PEDOT:PSS interfaces stabilised using a PEGylated crosslinker yield improved conductivity and biocompatibility. *Journal of Materials Chemistry B.* 7. 31. 4811-4820. 2019.
306. Solazzo M., et al. Structural crystallisation of crosslinked 3D PEDOT:PSS anisotropic porous biomaterials to generate highly conductive platforms for tissue engineering applications. *Biomaterials Science.* 9. 12. 4317-4328. 2021.
307. de Camp N.V., et al. Light-cured polymer electrodes for non-invasive EEG recordings. *Scientific Reports.* 8. 1. 14041. 2018.
308. Ding Y., et al. Flexible and Compressible PEDOT:PSS@Melamine Conductive Sponge Prepared via One-Step Dip Coating as Piezoresistive Pressure Sensor for Human Motion Detection. *ACS Applied Materials and Interfaces.* 10. 18. 16077-16086. 2018.
309. Zhou J., et al. Conductive Polymer Protonated Nanocellulose Aerogels for Tunable and Linearly Responsive Strain Sensors. *ACS Applied Materials and Interfaces.* 10. 33. 27902-27910. 2018.
310. Ko Y., et al. Fabrication of Highly Conductive Porous Cellulose/PEDOT:PSS Nanocomposite Paper via Post-Treatment. *Nanomaterials (Basel).* 9. 4. 2019.
311. Verpoorten E., et al. Design and Optimization of Piezoresistive PEO/PEDOT:PSS Electrospun Nanofibers for Wearable Flex Sensors. *Nanomaterials (Basel).* 10. 11. 2166. 2020.
312. Zahed M.A., et al. Highly flexible and conductive poly (3, 4-ethylene dioxythiophene)-poly (styrene sulfonate) anchored 3-dimensional porous graphene network-based electrochemical biosensor for glucose and pH detection in human perspiration. *Biosensors and Bioelectronics.* 160. 112220. 2020.
313. Kayser L.V., et al. Stretchable Conductive Polymers and Composites Based on PEDOT and PEDOT:PSS. *Advanced Materials.* 31. 10. e1806133. 2019.
314. Vries D. Characterization of polymeric foams. 2009.
315. Song Y., et al. Highly Compressible Integrated Supercapacitor-Piezoresistance-Sensor System with CNT-PDMS Sponge for Health Monitoring. *Small.* 13. 39. 2017.
316. Chen G., et al. Strain- and Strain-Rate-Invariant Conductance in a Stretchable and Compressible 3D Conducting Polymer Foam. *Matter.* 1. 1. 205-218. 2019.
317. Al-Handarish Y., et al. Facile Fabrication of 3D Porous Sponges Coated with Synergistic Carbon Black/Multiwalled Carbon Nanotubes for Tactile Sensing Applications. *Nanomaterials (Basel).* 10. 10. 2020.
318. Lv B., et al. A Highly Sensitive Piezoresistive Pressure Sensor Based on Graphene Oxide/Polypyrrole@Polyurethane Sponge. *Sensors (Basel).* 20. 4. 2020.
319. Abe Y., et al. Oligo- and polysiloxanes. *Progress in Polymer Science.* 29. 3. 149-182. 2004.
320. Lötters J.C., et al. The mechanical properties of the rubber elastic polymer polydimethylsiloxane for sensor applications. *Journal of Micromechanics and Microengineering.* 7. 3. 145-147. 1997.
321. Wang Y., et al. Wearable and Highly Sensitive Graphene Strain Sensors for Human Motion Monitoring. *Advanced Functional Materials.* 24. 29. 4666-4670. 2014.
322. Rinaldi A., et al. A Flexible and Highly Sensitive Pressure Sensor Based on a PDMS Foam Coated with Graphene Nanoplatelets. *Sensors (Basel).* 16. 12. 2016.
323. Pan J., et al. A Highly Sensitive Resistive Pressure Sensor Based on a Carbon Nanotube-

Liquid Crystal-PDMS Composite. *Nanomaterials (Basel).* 8. 6. 2018.

324. Wu X., et al. Large-Area Compliant, Low-Cost, and Versatile Pressure-Sensing Platform Based on Microcrack-Designed Carbon Black@Polyurethane Sponge for Human-Machine Interfacing. *Advanced Functional Materials.* 26. 34. 6246-6256. 2016.
325. Al-Halhouli A., et al. Fabrication and Evaluation of a Novel Non-Invasive Stretchable and Wearable Respiratory Rate Sensor Based on Silver Nanoparticles Using Inkjet Printing Technology. *Polymers (Basel).* 11. 9. 2019.
326. Palchesko R.N., et al. Development of polydimethylsiloxane substrates with tunable elastic modulus to study cell mechanobiology in muscle and nerve. *PLoS One.* 7. 12. e51499. 2012.
327. Li J., et al. Ultrasensitive, flexible, and low-cost nanoporous piezoresistive composites for tactile pressure sensing. *Nanoscale.* 11. 6. 2779-2786. 2019.
328. Huang W., et al. Flexible and Lightweight Pressure Sensor Based on Carbon Nanotube/Thermoplastic Polyurethane-Aligned Conductive Foam with Superior Compressibility and Stability. *ACS Applied Materials and Interfaces.* 9. 48. 42266-42277. 2017.
329. Zhao T., et al. Highly Sensitive Flexible Piezoresistive Pressure Sensor Developed Using Biomimetically Textured Porous Materials. *ACS Applied Materials and Interfaces.* 11. 32. 29466-29473. 2019.
330. Zhai Y., et al. Flexible and wearable carbon black/thermoplastic polyurethane foam with a pinnate-veined aligned porous structure for multifunctional piezoresistive sensors. *Chemical Engineering Journal.* 382. 122985. 2020.
331. Kühn G. W. Kurz, D. J. Fisher, Fundamentals of Solidification. Trans Tech Publications, Switzerland-Germany-UK-USA, 1986 (Erstauflage 1984), 242 Seiten, zahlreiche Abbildungen und Tabellen, Sachwortindex, SFr 54.00, ISBN 0-87849-523-3. *Crystal Research and Technology.* 21. 9. 1176-1176. 1986.
332. O'Brien F.J., et al. The effect of pore size on cell adhesion in collagen-GAG scaffolds. *Biomaterials.* 26. 4. 433-441. 2005.
333. O'Brien F.J., et al. Influence of freezing rate on pore structure in freeze-dried collagen-GAG scaffolds. *Biomaterials.* 25. 6. 1077-1086. 2004.
334. Zhang S., et al. Ultrasensitive and Highly Compressible Piezoresistive Sensor Based on Polyurethane Sponge Coated with a Cracked Cellulose Nanofibril/Silver Nanowire Layer. *ACS Applied Materials and Interfaces.* 11. 11. 10922-10932. 2019.
335. Boland C.S., et al. Sensitive electromechanical sensors using viscoelastic graphene-polymer nanocomposites. *Science.* 354. 6317. 1257-1260. 2016.
336. Choong C.L., et al. Highly stretchable resistive pressure sensors using a conductive elastomeric composite on a micropyramid array. *Advanced Materials.* 26. 21. 3451-3458. 2014.
337. Christensen R.M. Chapter I - Viscoelastic Stress Strain Constitutive Relations. In: Christensen RM, ed. *Theory of Viscoelasticity (Second Edition)*. Academic Press. 1-34. 1982.
338. Tang Z., et al. 3D Printing of Highly Sensitive and Large-Measurement-Range Flexible Pressure Sensors with a Positive Piezoresistive Effect. *ACS Applied Materials and Interfaces.* 12. 25. 28669-28680. 2020.
339. Thaysen J., et al. Atomic force microscopy probe with piezoresistive read-out and a highly symmetrical Wheatstone bridge arrangement. *Sensors and Actuators A: Physical.* 83. 1-3. 47-53. 2000.
340. Loui A., et al. An analytic model of thermal drift in piezoresistive microcantilever sensors. *Journal of Applied Physics.* 107. 5. 054508. 2010.
341. Proctor C.M., et al. Electrophoretic drug delivery for seizure control. *Science Advances.* 4. 8. eaau1291. 2018.
342. Heeger A.J. Semiconducting and Metallic Polymers: The Fourth Generation of Polymeric Materials (Nobel Lecture) Copyright(c) The Nobel Foundation 2001. We thank the Nobel Foundation, Stockholm, for permission to print this lecture. *Angewandte Chemie (International ed in English).* 40. 14. 2591-2611. 2001.
343. Diaz A.F., et al. Electroactive polyaniline films. *Journal of Electroanalytical Chemistry and*

*Interfacial Electrochemistry.* 111. 1. 111-114. 1980.

344. Burroughes J.H., et al. Light-emitting diodes based on conjugated polymers. *Nature.* 347. 6293. 539-541. 1990.

345. Shirakawa H., et al. Synthesis of electrically conducting organic polymers: halogen derivatives of polyacetylene, (CH). *Journal of the Chemical Society, Chemical Communications.* 16. 578-580. 1977.

346. Stritesky S., et al. Printing inks of electroactive polymer PEDOT:PSS: The study of biocompatibility, stability, and electrical properties. *Journal of Biomedical Materials Research Part A.* 106. 4. 1121-1128. 2018.

347. Cao L., et al. Synthesis and performance of cross-linked PEDOT:MOI-P(SS-HEA) transparent conductive films by UV irradiation. *RSC Advances.* 6. 35. 29592-29597. 2016.

348. Huang T.-M., et al. Chemical cross-linking of conducting poly(3,4-ethylenedioxythiophene):poly(styrenesulfonate) (PEDOT:PSS) using poly(ethylene oxide) (PEO). *Polymer.* 54. 23. 6455-6462. 2013.

349. Kim S., et al. Multi-purpose overcoating layers based on PVA/silane hybrid composites for highly transparent, flexible, and durable AgNW/PEDOT:PSS films. *RSC Advances.* 6. 23. 19280-19287. 2016.

350. Guex A.G., et al. Highly porous scaffolds of PEDOT:PSS for bone tissue engineering. *Acta Biomaterialia.* 62. 91-101. 2017.

351. Zhang S., et al. Solvent-induced changes in PEDOT:PSS films for organic electrochemical transistors. *APL Materials.* 3. 1. 014911. 2015.

352. Stavrinidou E., et al. Direct Measurement of Ion Mobility in a Conducting Polymer. *Advanced Materials.* 25. 32. 4488-4493. 2013.

353. Nevrela J., et al. Secondary doping in poly(3,4-ethylenedioxythiophene):Poly(4-styrenesulfonate) thin films. *Journal of Polymer Science Part B: Polymer Physics.* 53. 16. 1139-1146. 2015.

354. Crispin X., et al. The Origin of the High Conductivity of Poly(3,4-ethylenedioxythiophene)−Poly(styrenesulfonate) (PEDOT−PSS) Plastic Electrodes. *Chemistry of Materials.* 18. 18. 4354-4360. 2006.

355. Tao W., et al. Preparation and Structure of Porous Silk Sericin Materials. *Macromolecular Materials and Engineering.* 290. 3. 188-194. 2005.

356. Motta A., et al. Stabilization of Bombyx mori silk fibroin/sericin films by crosslinking with PEG-DE 600 and genipin. *Journal of Bioactive and Compatible Polymers.* 26. 2. 130-143. 2011.

357. Wei Y., et al. Preparation and characterization of PEGDE crosslinked silk fibroin film. *Journal of Wuhan University of Technology - Materials Science Edition.* 29. 5. 1083-1089. 2014.

358. Heller A., et al. Electrochemical glucose sensors and their applications in diabetes management. *Chemical Reviews.* 108. 7. 2482-2505. 2008.

359. de Kok M.M., et al. Modification of PEDOT:PSS as hole injection layer in polymer LEDs. *Physica status solidi (a).* 201. 6. 1342-1359. 2004.

360. Gomes F.O.V., et al. Influence of temperature on morphological and optical properties of MoS 2 layers as grown based on solution processed precursor. *Thin Solid Films.* 645. 38-44. 2018.

361. Greczynski G., et al. Photoelectron spectroscopy of thin films of PEDOT–PSS conjugated polymer blend: a mini-review and some new results. *Journal of Electron Spectroscopy and Related Phenomena.* 121. 1-3. 1-17. 2001.

362. Zheng S., et al. PEG-nanolized ultrasmall selenium nanoparticles overcome drug resistance in hepatocellular carcinoma HepG2 cells through induction of mitochondria dysfunction. *International Journal of Nanomedicine.* 7. 3939-3949. 2012.

363. Li H., et al. Electron beam curing of poly(ethylene glycol) diglycidyl ether-functionalized MWNTs/epoxy composites. *Journal of Composite Materials.* 50. 12. 1595-1602. 2016.

364. Zhao Q., et al. The structure and properties of PEDOT synthesized by template-free solution method. *Nanoscale Research Letters.* 9. 1. 557. 2014.

365. Supri A.G., et al. Effect of type of conductive fillers and poly (ethylene glycol) diglycidyl ether on the electrical conductivity and morphology properties of poly (vinyl chloride)/poly (ethylene oxide) conductive films. *Polymer Bulletin.* 73. 10. 2831-2841. 2016.

366. Thomas J.P., et al. High-efficiency hybrid solar cells by nanostructural modification in PEDOT:PSS with co-solvent addition. *Journal of Materials Chemistry A.* 2. 7. 2383-2389. 2014.

367. Huang J., et al. Investigation of the Effects of Doping and Post-Deposition Treatments on the Conductivity, Morphology, and Work Function of Poly(3,4-ethylenedioxythiophene)/Poly(styrene sulfonate) Films. *Advanced Functional Materials.* 15. 2. 290-296. 2005.

368. Mengistie D.A., et al. Enhanced Thermoelectric Performance of PEDOT:PSS Flexible Bulky Papers by Treatment with Secondary Dopants. *ACS Applied Materials and Interfaces.* 7. 1. 94-100. 2015.

369. Lin Y.-J., et al. Effect of incorporation of ethylene glycol into PEDOT:PSS on electron phonon coupling and conductivity. *Journal of Applied Physics.* 117. 21. 215501. 2015.

370. Krukiewicz K., et al. Fractal form PEDOT/Au assemblies as thin-film neural interface materials. *Biomedical Materials.* 13. 5. 054102. 2018.

371. Krukiewicz K., et al. Evaluation of drug loading capacity and release characteristics of PEDOT/naproxen system: Effect of doping ions. *Electrochimica Acta.* 289. 218-227. 2018.

372. Proctor C.M., et al. Understanding volumetric capacitance in conducting polymers. *Journal of Polymer Science Part B: Polymer Physics.* 54. 15. 1433-1436. 2016.

373. Cogan S.F. Neural stimulation and recording electrodes. *Annual Review of Biomedical Engineering.* 10. 1. 275-309. 2008.

374. Nardes A.M., et al. Microscopic Understanding of the Anisotropic Conductivity of PEDOT:PSS Thin Films. *Advanced Materials.* 19. 9. 1196-1200. 2007.

375. Buxboim A., et al. How deeply cells feel: methods for thin gels. *Journal of physics Condensed matter: an Institute of Physics journal.* 22. 19. 194116. 2010.

376. Stout D.A., et al. Mechanisms of greater cardiomyocyte functions on conductive nanoengineered composites for cardiovascular application. *International journal of nanomedicine.* 7. 5653-5669. 2012.

377. Miller D.C., et al. Endothelial and vascular smooth muscle cell function on poly(lactic-co-glycolic acid) with nano-structured surface features. *Biomaterials.* 25. 1. 53-61. 2004.

378. Elbert D.L., et al. Surface Treatments of Polymers for Biocompatibility. *Annual Review of Materials Science.* 26. 1. 365-394. 1996.

379. Sheth S.R., et al. Measurements of attractive forces between proteins and end-grafted poly(ethylene glycol) chains. *Proceedings of the National Academy of Sciences of the United States of America.* 94. 16. 8399-8404. 1997.

380. Pappa A.M., et al. Oxygen-plasma-modified biomimetic nanofibrous scaffolds for enhanced compatibility of cardiovascular implants. *Beilstein Journal of Nanotechnology.* 6. 254-262. 2015.

381. Ruardy T.G., et al. Adhesion and spreading of human skin fibroblasts on physicochemically characterized gradient surfaces. *Journal of Biomedical Materials Research.* 29. 11. 1415-1423. 1995.

382. Dowling D.P., et al. Effect of surface wettability and topography on the adhesion of osteosarcoma cells on plasma-modified polystyrene. *Journal of Biomaterials Applications.* 26. 3. 327-347. 2011.

383. Harris J.M. *Poly (ethylene glycol) chemistry: biotechnical and biomedical applications.* Springer Science & Business Media; 2013.

384. Vasylieva N., et al. Covalent enzyme immobilization by poly(ethylene glycol) diglycidyl ether (PEGDE) for microelectrode biosensor preparation. *Biosensors and Bioelectronics.* 26. 10. 3993-4000. 2011.

385. Kim S.-M., et al. High-performance, polymer-based direct cellular interfaces for electrical stimulation and recording. *NPG Asia Materials.* 10. 4. 255-265. 2018.

386. Langer R., et al. Tissue engineering. *Science.* 260. 5110. 920-926. 1993.

387. Hubbell J.A. Biomaterials in tissue engineering. *Biotechnology (N Y).* 13. 6. 565-576. 1995.

388. Peppas N.A., et al. New challenges in biomaterials. *Science.* 263. 5154. 1715-1720. 1994.

389. O'Brien F.J. Biomaterials & scaffolds for tissue engineering. *Materials Today.* 14. 3. 88-95.

2011.

390. del Agua I., et al. DVS-Crosslinked PEDOT:PSS Free-Standing and Textile Electrodes toward Wearable Health Monitoring. *Advanced Materials Technologies.* 3. 10. 1700322. 2018.

391. Zerbinati N., et al. Toward Physicochemical and Rheological Characterization of Different Injectable Hyaluronic Acid Dermal Fillers Cross-Linked with Polyethylene Glycol Diglycidyl Ether. *Polymers (Basel).* 13. 6. 2021.

392. Monticelli D., et al. Chemical Characterization of Hydrogels Crosslinked with Polyethylene Glycol for Soft Tissue Augmentation. *Open Access Macedonian Journal of Medical Sciences.* 7. 7. 1077-1081. 2019.

393. Zhang Q., et al. Fabrication of three-dimensional poly(epsilon-caprolactone) scaffolds with hierarchical pore structures for tissue engineering. *Materials Science and Engineering: C.* 33. 4. 2094-2103. 2013.

394. Yu H., et al. Effect of porosity and pore size on microstructures and mechanical properties of poly-epsilon-caprolactone- hydroxyapatite composites. *Journal of Biomedical Materials Research Part B.* 86. 2. 541-547. 2008.

395. Engler A.J., et al. Matrix elasticity directs stem cell lineage specification. *Cell.* 126. 4. 677-689. 2006.

396. Ke Z., et al. Measurement of Electrical Conductivity of Porous Titanium and Ti6Al4V Prepared by the Powder Metallurgy Method. *Chinese Physics Letters.* 24. 1. 187-190. 2007.

397. Zhang S., et al. Room-Temperature-Formed PEDOT:PSS Hydrogels Enable Injectable, Soft, and Healable Organic Bioelectronics. *Advanced Materials.* 32. 1. e1904752. 2020.

398. Kim D.H., et al. Toxicity Assessment of a Single Dose of Poly(ethylene glycol) Diglycidyl Ether (PEGDE) Administered Subcutaneously in Mice. *Toxics.* 9. 12. 2021.

399. Olvera D., et al. Electroactive material-based biosensors for detection and drug delivery. *Advanced Drug Delivery Reviews.* 170. 396-424. 2021.

400. Olvera D., et al. Electroconductive Melt Electrowritten Patches Matching the Mechanical Anisotropy of Human Myocardium. *Advanced Functional Materials.* 30. 44. 1909880. 2020.

401. Gueye M.N., et al. Progress in understanding structure and transport properties of PEDOT-based materials: A critical review. *Progress in Materials Science.* 108. 100616. 2020.

402. Inal S., et al. Conducting Polymer Scaffolds for Hosting and Monitoring 3D Cell Culture. *Advanced Biosystems.* 1. 6. 1700052. 2017.

403. Yao B., et al. Ultrahigh-Conductivity Polymer Hydrogels with Arbitrary Structures. *Advanced Materials.* 29. 28. 2017.

404. Puspoki Z., et al. Transforms and Operators for Directional Bioimage Analysis: A Survey. *Advances in anatomy, embryology, and cell biology.* 219. 69-93. 2016.

405. Saidy N.T., et al. Biologically Inspired Scaffolds for Heart Valve Tissue Engineering via Melt Electrowriting. *Small.* 15. 24. e1900873. 2019.

406. Jammalamadaka U., et al. Recent Advances in Biomaterials for 3D Printing and Tissue Engineering. *Journal of Functional Biomaterials.* 9. 1. 2018.

407. Dalton P.D. Melt electrowriting with additive manufacturing principles. *Current Opinion in Biomedical Engineering.* 2. 49-57. 2017.

408. Zhang N., et al. Synthesis of silver nanoparticle-coated poly(styrene-co-sulfonic acid) hybrid materials and their application in surface-enhanced Raman scattering (SERS) tags. *RSC Advances.* 3. 33. 13740. 2013.

409. Gannon A.R., et al. The role of the superficial region in determining the dynamic properties of articular cartilage. *Osteoarthritis Cartilage.* 20. 11. 1417-1425. 2012.

410. Xu Y., et al. Reversibly Assembled Electroconductive Hydrogel via a Host-Guest Interaction for 3D Cell Culture. *ACS Applied Materials and Interfaces.* 11. 8. 7715-7724. 2019.

411. Lu B., et al. Pure PEDOT:PSS hydrogels. *Nature Communications.* 10. 1. 1043. 2019.

412. Hafemann B., et al. Cross-linking by 1-ethyl-3- (3-dimethylaminopropyl)-carbodiimide (EDC) of a collagen/elastin membrane meant to be used as a dermal substitute: effects on physical, biochemical and biological features in vitro. *Journal of Materials Science: Materials in Medicine.* 12. 5. 437-446. 2001.

413. Benjamin E.J., et al. Heart Disease and Stroke Statistics-2017 Update: A Report From the American Heart Association. *Circulation.* 135. 10. e146-e603. 2017.

414. Correale M., et al. New Targets in Heart Failure Drug Therapy. *Frontiers in Cardiovascular Medicine.* 8. 665797. 2021.

415. Dominguez-Rodriguez A., et al. Cardioprotection and pharmacological therapies in acute myocardial infarction: Challenges in the current era. *World Journal of Cardiology.* 6. 3. 100-106. 2014.

416. Hansen A., et al. Development of a drug screening platform based on engineered heart tissue. *Circulation Research.* 107. 1. 35-44. 2010.

417. Weinberger F., et al. Cardiac repair in guinea pigs with human engineered heart tissue from induced pluripotent stem cells. *Science Translational Medicine.* 8. 363. 363ra148. 2016.

418. Li J., et al. Circulating re-entrant waves promote maturation of hiPSC-derived cardiomyocytes in self-organized tissue ring. *Commun Biol.* 3. 1. 122. 2020.

419. Balint R., et al. Electrical stimulation: a novel tool for tissue engineering. *Tissue engineering Part B, Reviews.* 19. 1. 48-57. 2013.

420. Freed L.E., et al. Microgravity tissue engineering. *In Vitro Cellular & Developmental Biology – Animal.* 33. 5. 381-385. 1997.

421. Bray M.A., et al. Sarcomere alignment is regulated by myocyte shape. *Cell Motility and the Cytoskeleton.* 65. 8. 641-651. 2008.

422. Wilson A.J., et al. Cardiomyocyte growth and sarcomerogenesis at the intercalated disc. *Cellular and Molecular Life Sciences.* 71. 1. 165-181. 2014.

423. Nuccitelli R., et al. Nanosecond pulsed electric field stimulation of reactive oxygen species in human pancreatic cancer cells is Ca(2+)-dependent. *Biochemical and Biophysical Research Communications.* 435. 4. 580-585. 2013.

424. Lou L., et al. Integrated Perspective of Scaffold Designing and Multiscale Mechanics in Cardiac Bioengineering. *Advanced NanoBiomed Research.* 1. 12. 2100075. 2021.

425. Chen C., et al. Patterned iridium oxide film as neural electrode interface: Biocompatibility and improved neurite outgrowth with electrical stimulation. *Materials Science and Engineering: C.* 103. 109865. 2019.

426. Ganji Y., et al. Cardiomyocyte behavior on biodegradable polyurethane/gold nanocomposite scaffolds under electrical stimulation. *Materials Science and Engineering: C.* 59. 10-18. 2016.

427. Marques M.A., et al. Cardiac Troponin and Tropomyosin: Structural and Cellular Perspectives to Unveil the Hypertrophic Cardiomyopathy Phenotype. *Frontiers in Physiology.* 7. 429. 2016.

428. Moon I.K., et al. Three-dimensional porous stretchable supercapacitor with wavy structured PEDOT:PSS/graphene electrode. *Chemical Engineering Journal.* 392. 123794. 2020.

429. Mestre R., et al. Force Modulation and Adaptability of 3D-Bioprinted Biological Actuators Based on Skeletal Muscle Tissue. *Advanced Materials Technologies.* 1800631. 2018.

430. Hirt M.N., et al. Deciphering the microRNA signature of pathological cardiac hypertrophy by engineered heart tissue- and sequencing-technology. *Journal of Molecular and Cellular Cardiology.* 81. 1-9. 2015.

431. Stein J.M., et al. Engineered models of the human heart: Directions and challenges. *Stem Cell Reports.* 16. 9. 2049-2057. 2021.

432. Cyganek L., et al. Deep phenotyping of human induced pluripotent stem cell-derived atrial and ventricular cardiomyocytes. *JCI Insight.* 3. 12. 2018.

433. Yang L., et al. An Immuno-Cardiac Model for Macrophage-Mediated Inflammation in COVID-19 Hearts. *Circulation Research.* 129. 1. 33-46. 2021.

434. Richards D.J., et al. Human cardiac organoids for the modelling of myocardial infarction and drug cardiotoxicity. *Nature Biomedical Engineering.* 4. 4. 446-462. 2020.

435. Perottoni S., et al. Intracellular label-free detection of mesenchymal stem cell metabolism within a perivascular niche-on-a-chip. *Lab on a Chip.* 21. 7. 1395-1408. 2021.

436. Ulmer B.M., et al. Contractile Work Contributes to Maturation of Energy Metabolism in hiPSC-Derived Cardiomyocytes. *Stem Cell Reports.* 10. 3. 834-847. 2018.

# Appendix 1: Supplementary Information for *Chapter 3*

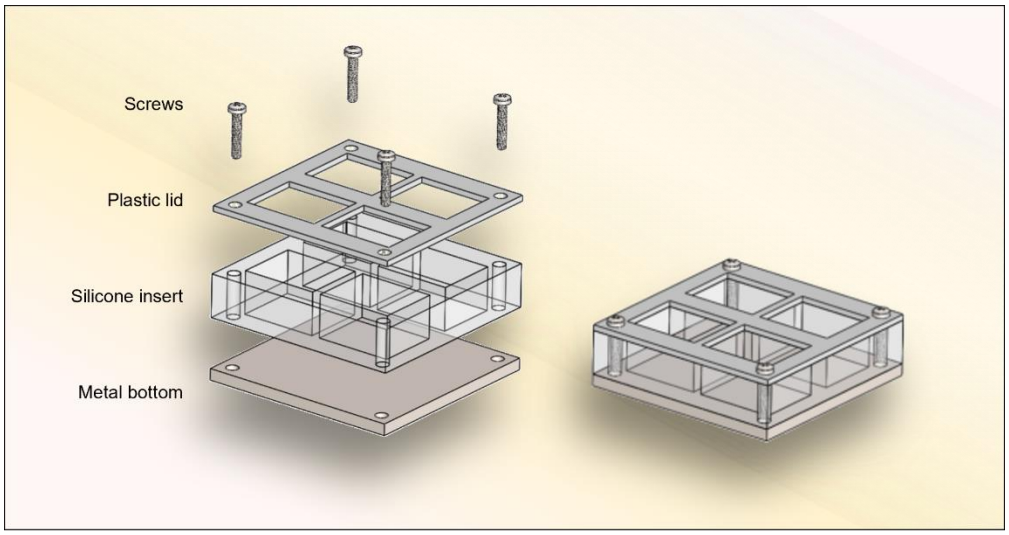


***Supporting Information 1****. Schematic showing the custom-made mould that was used for the manufacturing of aligned PEDOT:PSS-GOPS scaffolds.*

# Appendix 2: Supplementary Information for *Chapter 4*

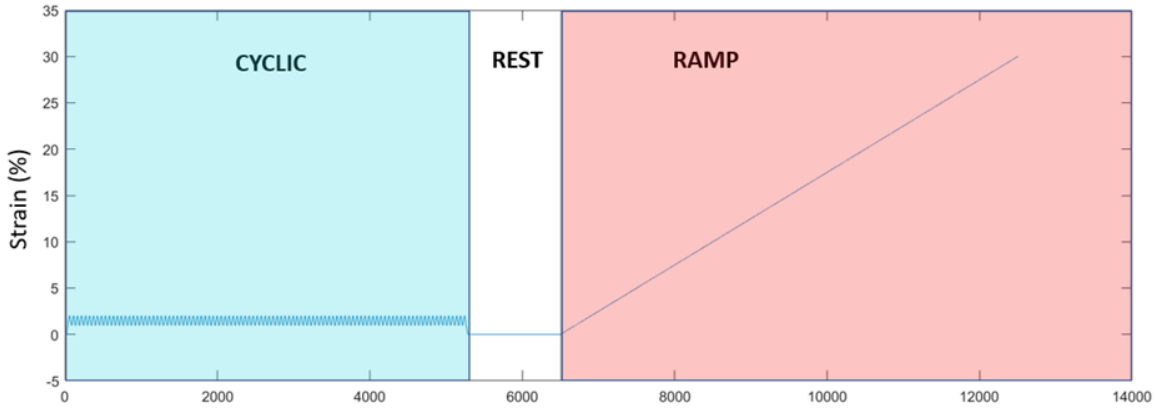


***Supporting Information 2**. Sequence of testing. Dynamic Cyclic Testing: 100 cycles, 1-2% strain, 1%/s. Rest – at preload, 60 seconds. Ramp Testing – 1 cycle, 0-30% strain, 0.1%/s.*

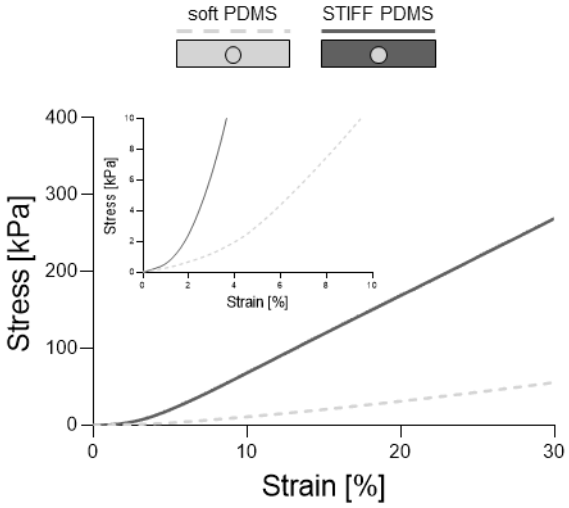


***Supporting Information 3.** Mean stress-strain curves for soft and stiff elastomers.*

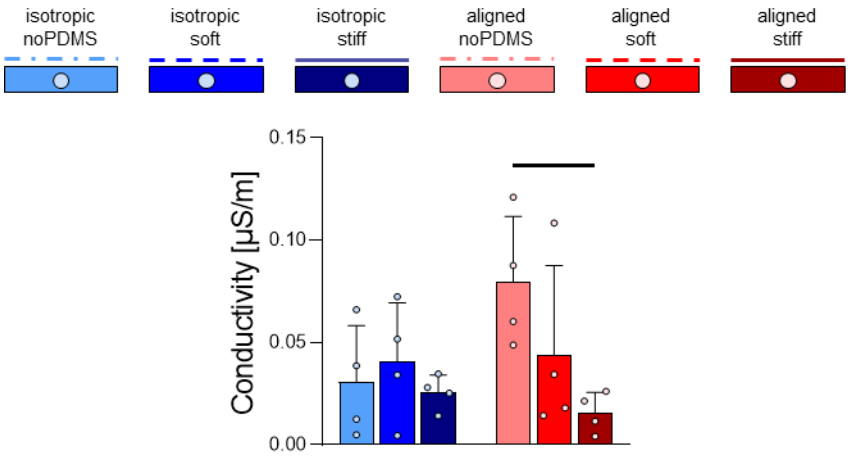


***Supporting Information 4***. *Quantification of conductivity at 0% strain. Bar graphs demonstrate the mean with error bars representing standard deviation. Data values are presented as associated points. Line represents statistical significance ($p<0.05$) between indicated groups using two-way ANOVA with Tukey's post-hoc test.*

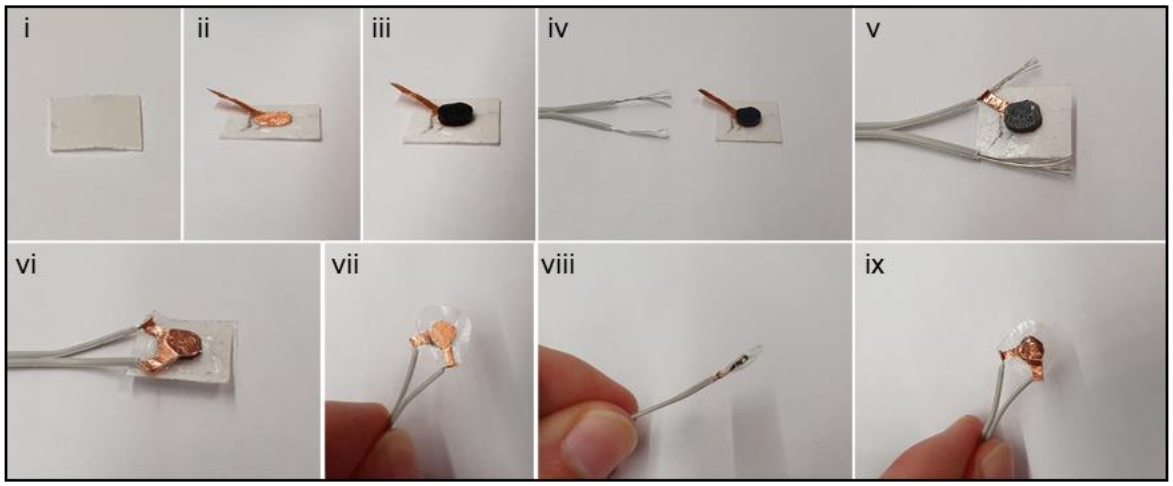


***Supporting Information 5.*** *Assembly sequence of the piezoresistive sensor prototype. (i-ii) Adhesive copper tape is sticked to a flexible double-side tape. (iii-v) A 1mm thick EAS is positioned on the copper tape and a wire is connected to the copper tape. (vi) A second copper tape is positioned at the top of the EAS and connected to a second wire. (vii-ix) Single side tape is applied on top of the system.*

# Appendix 3: Supplementary Information for *Chapter 5*

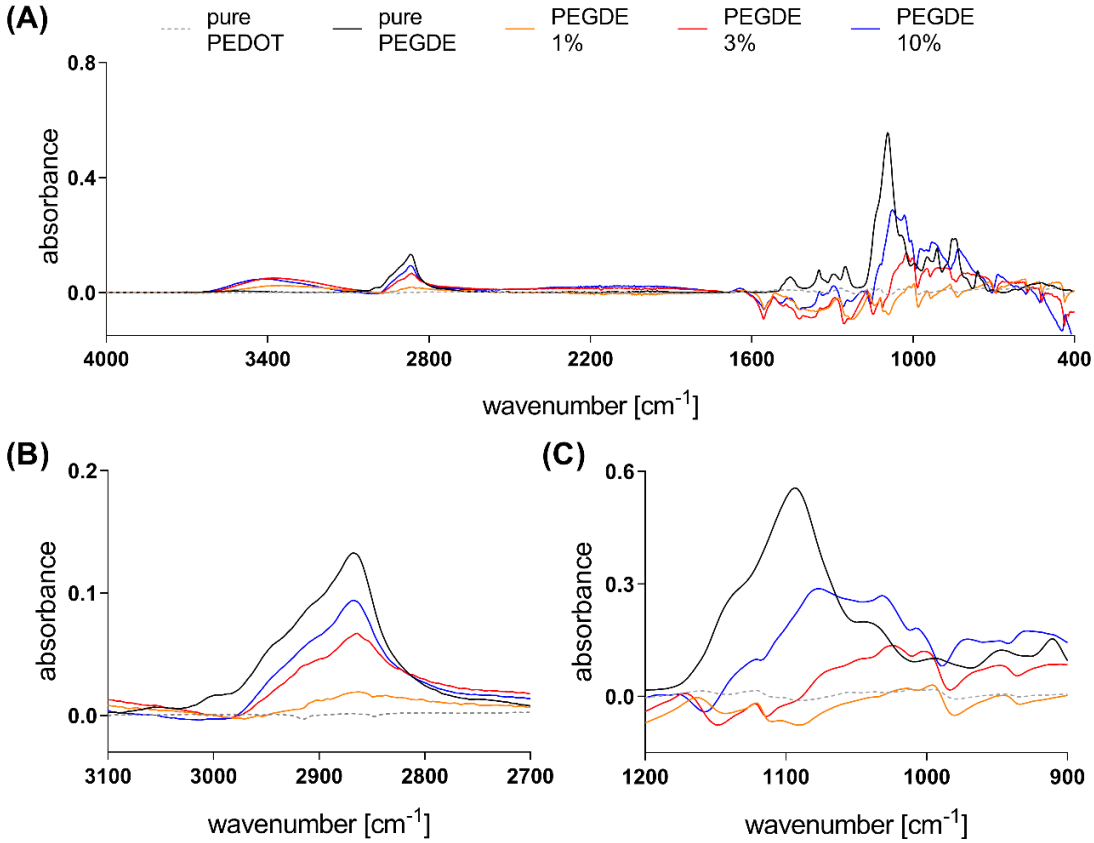


***Supporting Information 6**. FT-IR spectra of pure PEDOT:PSS, pure PEGDE and PEDOT:PSS film crosslinked with PEGDE at 1, 3 and 10 w/v%. (A) Whole spectra. (B) Detail spectra between 2700 and 3100 $cm^{-1}$. (C) Detail spectra between 900 and 1200 $cm^{-1}$.*

# Appendix 4: Supplementary Information for *Chapter 7*

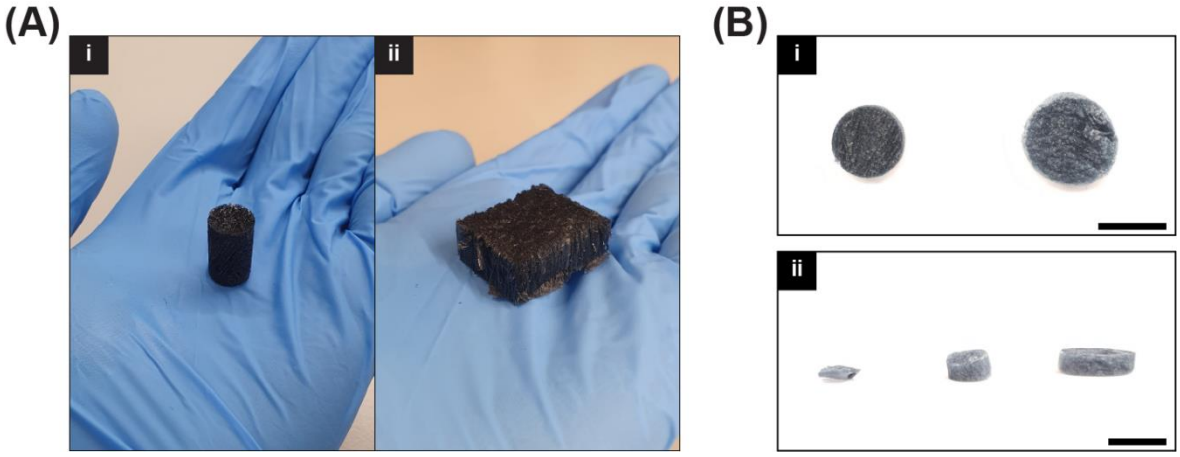


***Supporting Information 7**. **(A)** Overview of scaffolds with an isotropic cylindrical conformation (left) and an aligned rectangular one (right). **(B i)** Evidence of volumetric expansion following sulphuric acid crystallisation with an untreated sample (left) compared to a crystallised one (right). **(B ii)** Scalability of the combined freeze-drying and crystallisation process, represented by a range of specimens: 8 mm diameter and 500 µm thickness (left), 8 mm diameter and 3 mm thickness (middle), 14 mm diameter and 3 mm thickness (right). Scale bars: B = 1 cm.*

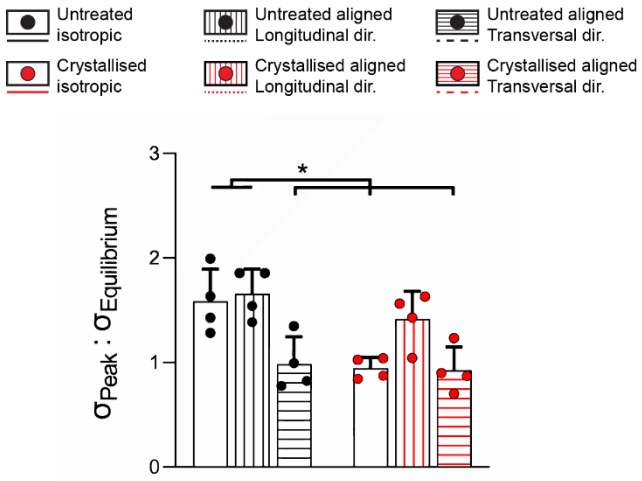


***Supporting Information 8**. Peak stress to Equilibrium stress ratio (n=4). Bar graphs demonstrate the mean with error bars representing standard deviation. Data values are presented as associated points. * represents statistical significance ($p<0.05$) between indicated groups using two-way ANOVA with Tukey's post-hoc test.*

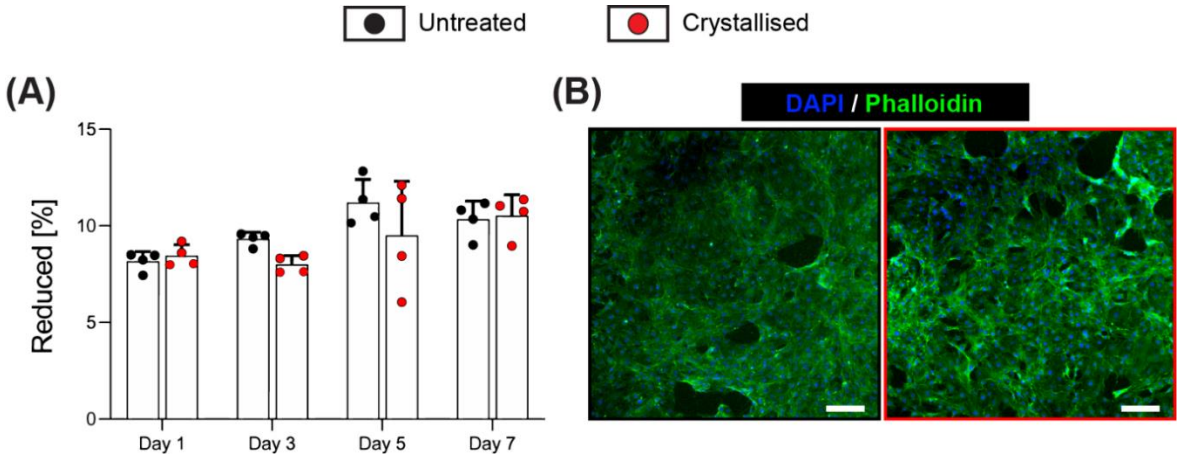


***Supporting Information 9.*** *Cytocompatibility of scaffolds on C3H10 cells via indirect contact. After the first 24 hours, growth media was replaced with extraction media for more 24 hours.* ***(A)*** *AlamarBlue™ assay performed with extraction media. Intensity being normalised to samples that were in contact with standard growth media only (n=4).* ***(B)*** *Fluorescent staining for nuclei/f-actin (DAPI and Phalloidin respectively) of day 7 groups. Scale bars: B = 100 µm. Bar graphs demonstrate the mean with error bars representing standard deviation. Data values are presented as associated points.*

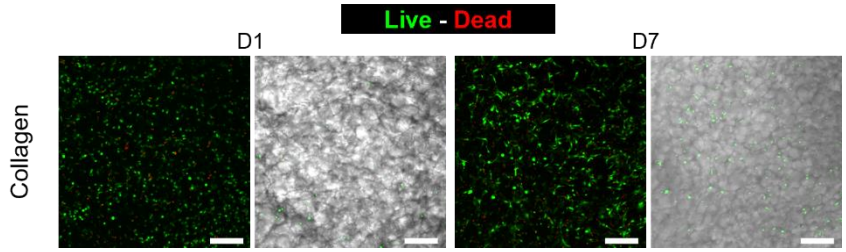


***Supporting Information 10.*** *Cytocompatibility of C3H10 cells on collagen scaffolds via direct contact. Micrographs from confocal microscope fluorescent staining for live/dead of CH310 cells at days 1 and 7. Left: live/dead channels. Right: live/dead/brightfield channels. Scale bars 200 µm.*

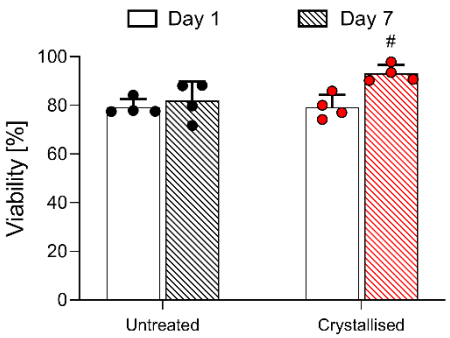


***Supporting Information 11**. Quantification of viability (extracted from live/dead Staining) at days 1 and 7, quantified as alive cells density (n=4). Bar graphs demonstrate the mean with error bars representing standard deviation. Data values are presented as associated points. # represent statistical significance (p<0.05) with all other groups using two-way ANOVA with Tukey's post-hoc test.*

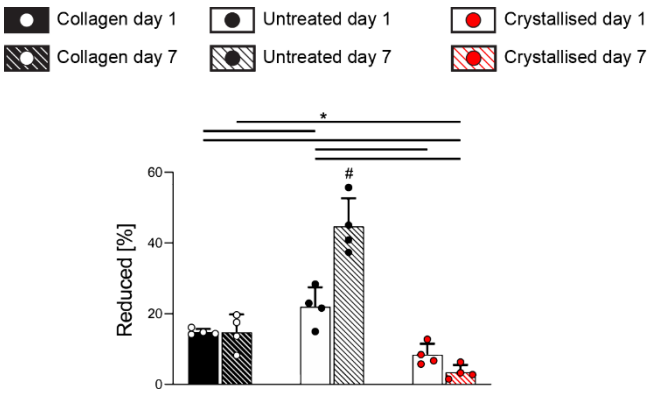


***Supporting Information 12**. AlamarBlue™ assay performed on scaffolds (n=4). Bar graphs demonstrate the mean with error bars representing standard deviation. Data values are presented as associated points. * represent statistical significance (p<0.05) with all other groups using two-way ANOVA with Tukey's post-hoc test.*

# Appendix 5: Supplementary Information for *Chapter 8*

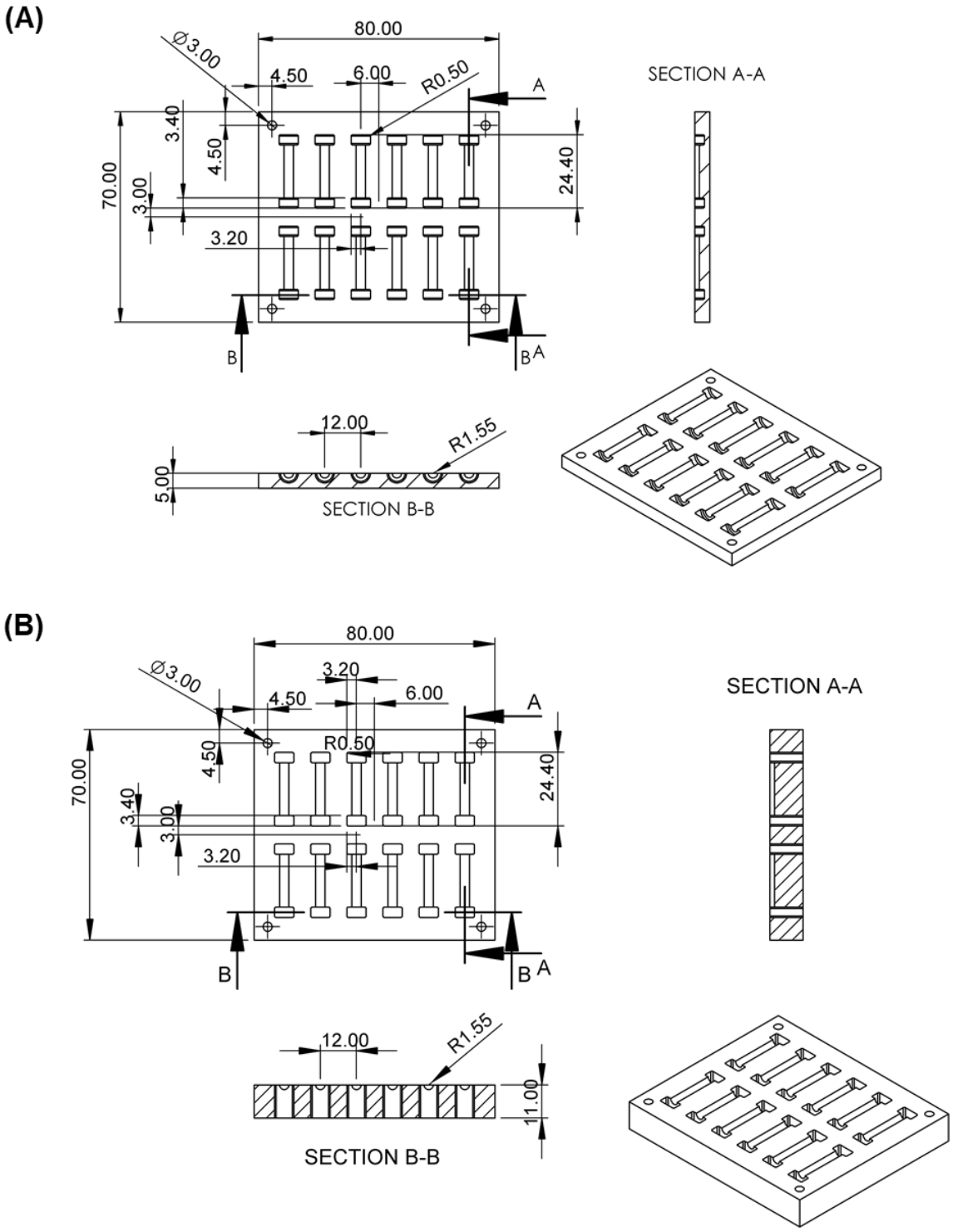


***Supporting Information 13.*** *Drawings of the Bottom* ***(A)*** *and Top* ***(B)*** *components of the mould for the embedding of PMDS on carbon bars for the development of electrodes. Dimensions are expressed in mm.*

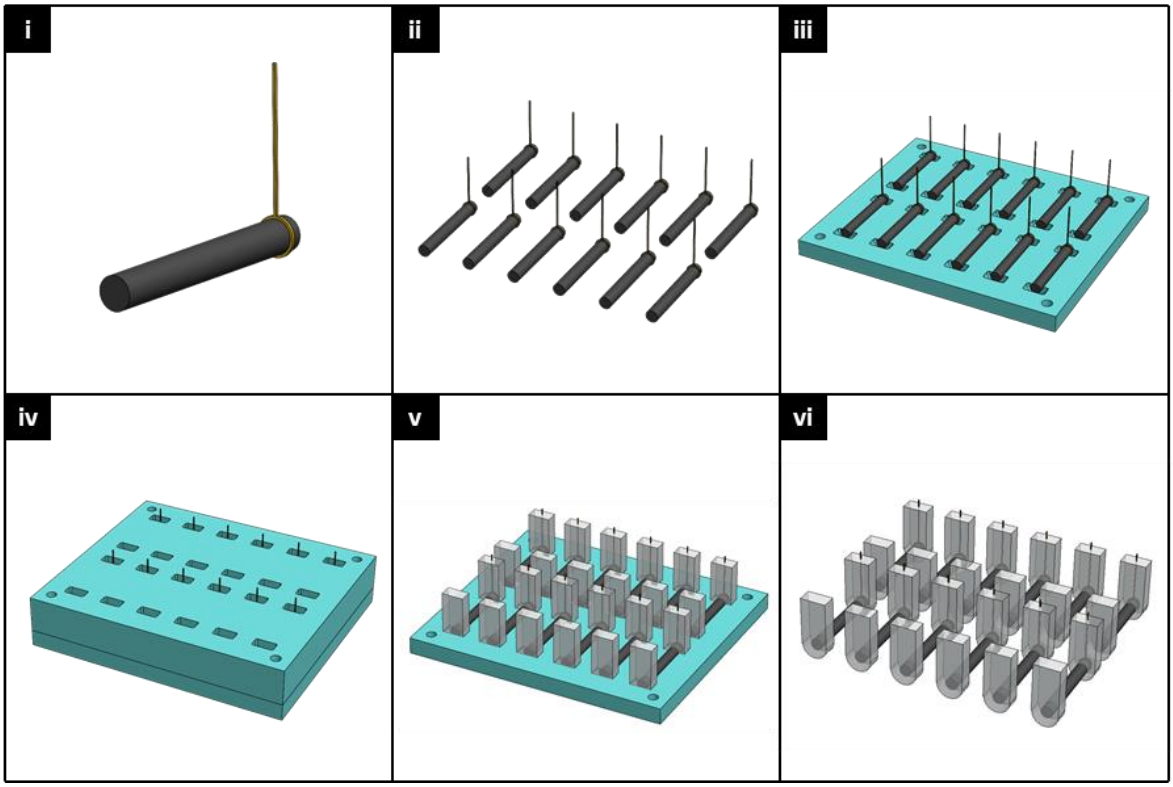


***Supporting Information 14.*** *Fabrication sequence of the electrodes.* ***(i)*** *A platinum-iridium wire is tightened to one extremity of a carbon bar.* ***(ii)*** *Step i is repeated until achievement of 12 elements.* ***(iii)*** *Bars are inserted into the bottom component of the mould.* ***(iv)*** *The top component of the mould is secured and pristine PDMS is poured into each hole.* ***(v)*** *polymerisation is completed, and the top component of the mould can be removed.* ***(vi)*** *Once the bottom component is removed, 12 carbon electrodes are achieved.*

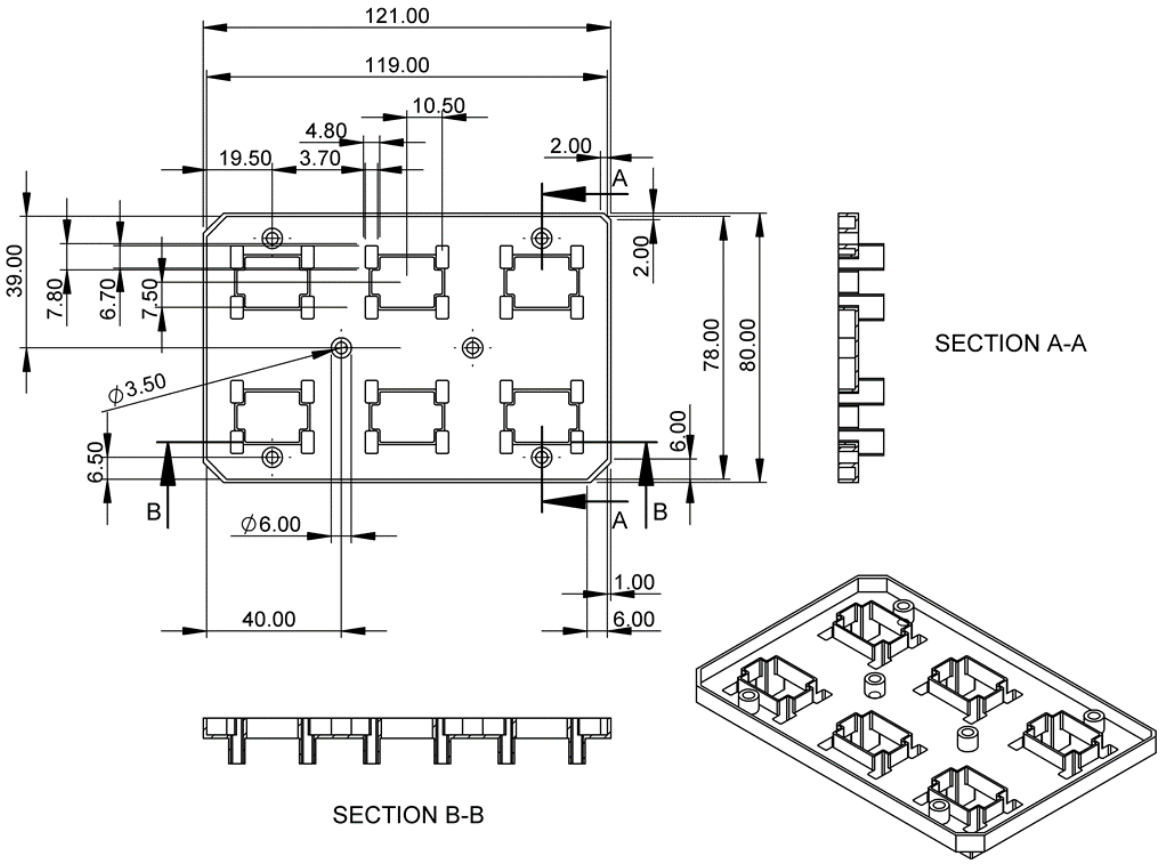


***Supporting Information 15**. Drawing of the lid adapter of the bioreactor. Dimensions are expressed in mm.*

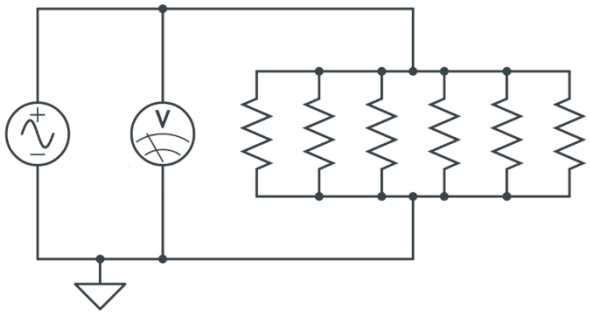

***Supporting Information 16**. Electrical circuit schematic of the Pacing Bioreactor*

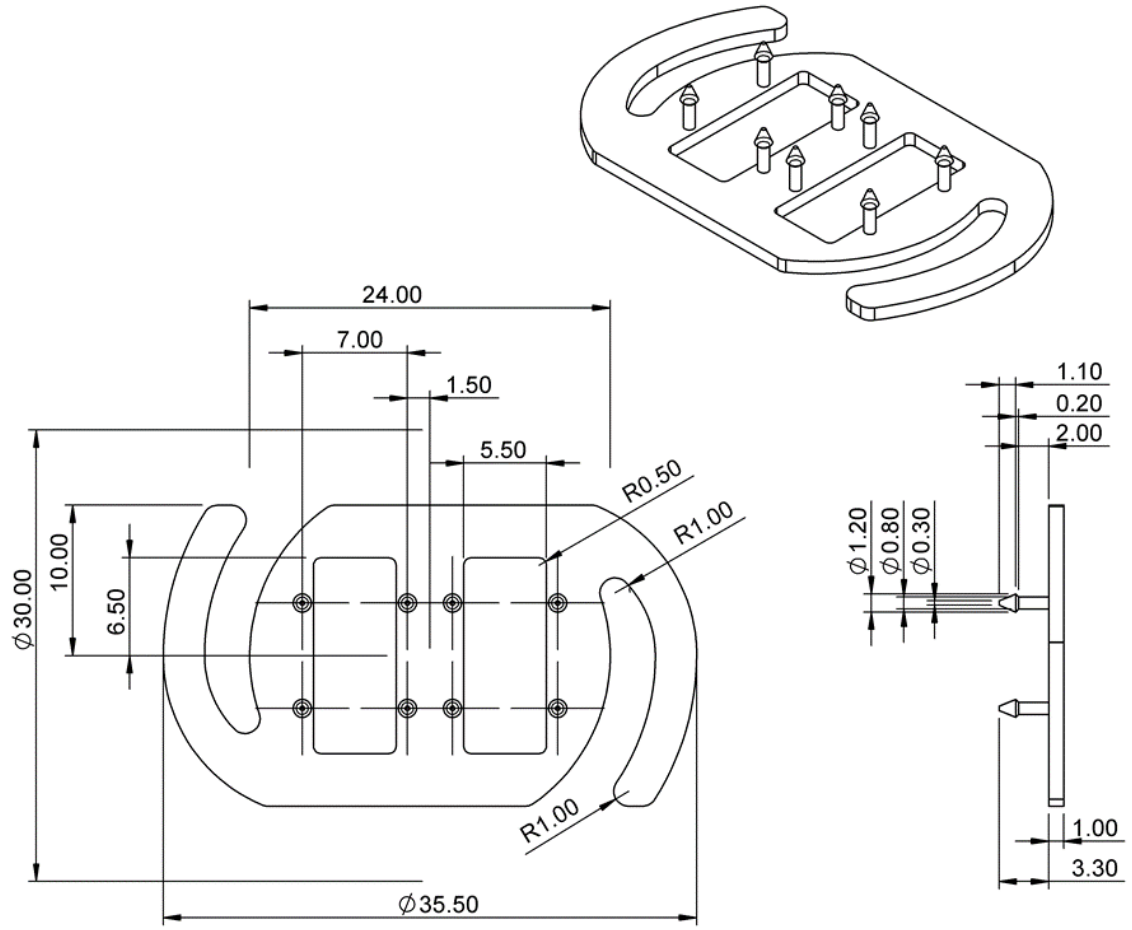


***Supporting Information 17**. Drawing of R3S - Rig for the Stimulation of Sponge-like Scaffolds. Dimensions are expressed in mm.*

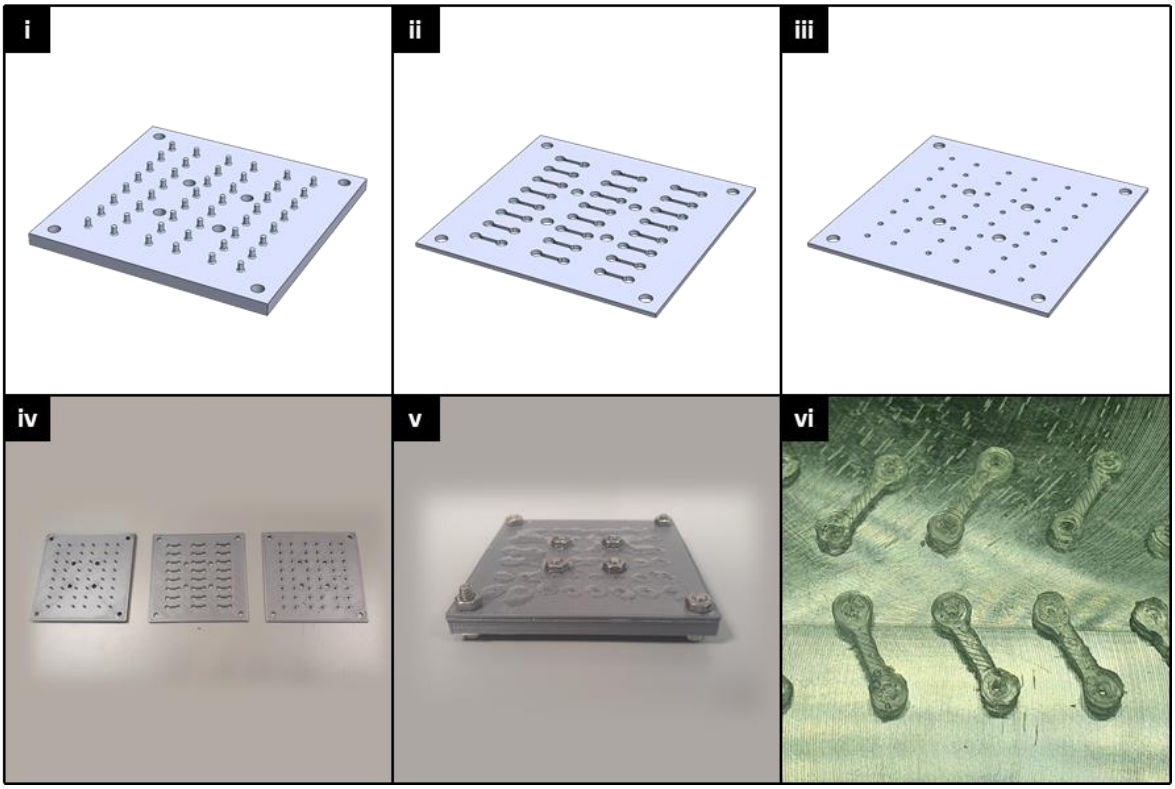


***Supporting Information 18.*** *Manufacturing of PDMS elastomeric bars.* ***(i-iii)*** *Illustrations of bottom, middle and top components of the mould.* ***(iv)*** *3D printed components of the mould.* ***(v)*** *Assembled Mould that has been filled with pristine PDMS.* ***(vi)*** *A set of manufactured PDMS elastomeric bars.*

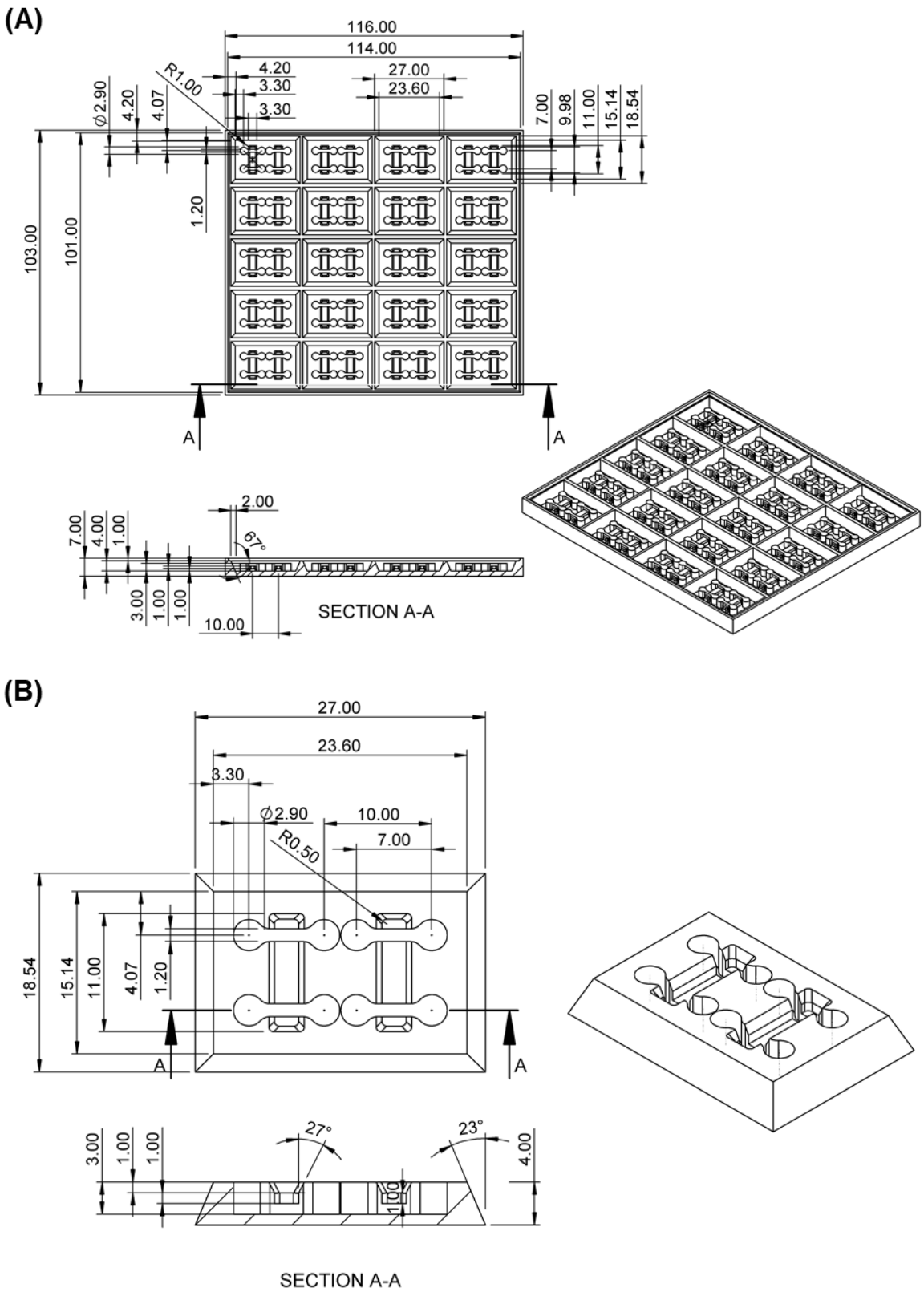


***Supporting Information 19.*** *Drawings of* ***(A)*** *Mould for Seeding chambers and of* ***(B)*** *a single seeding chamber. Dimensions are expressed in mm.*

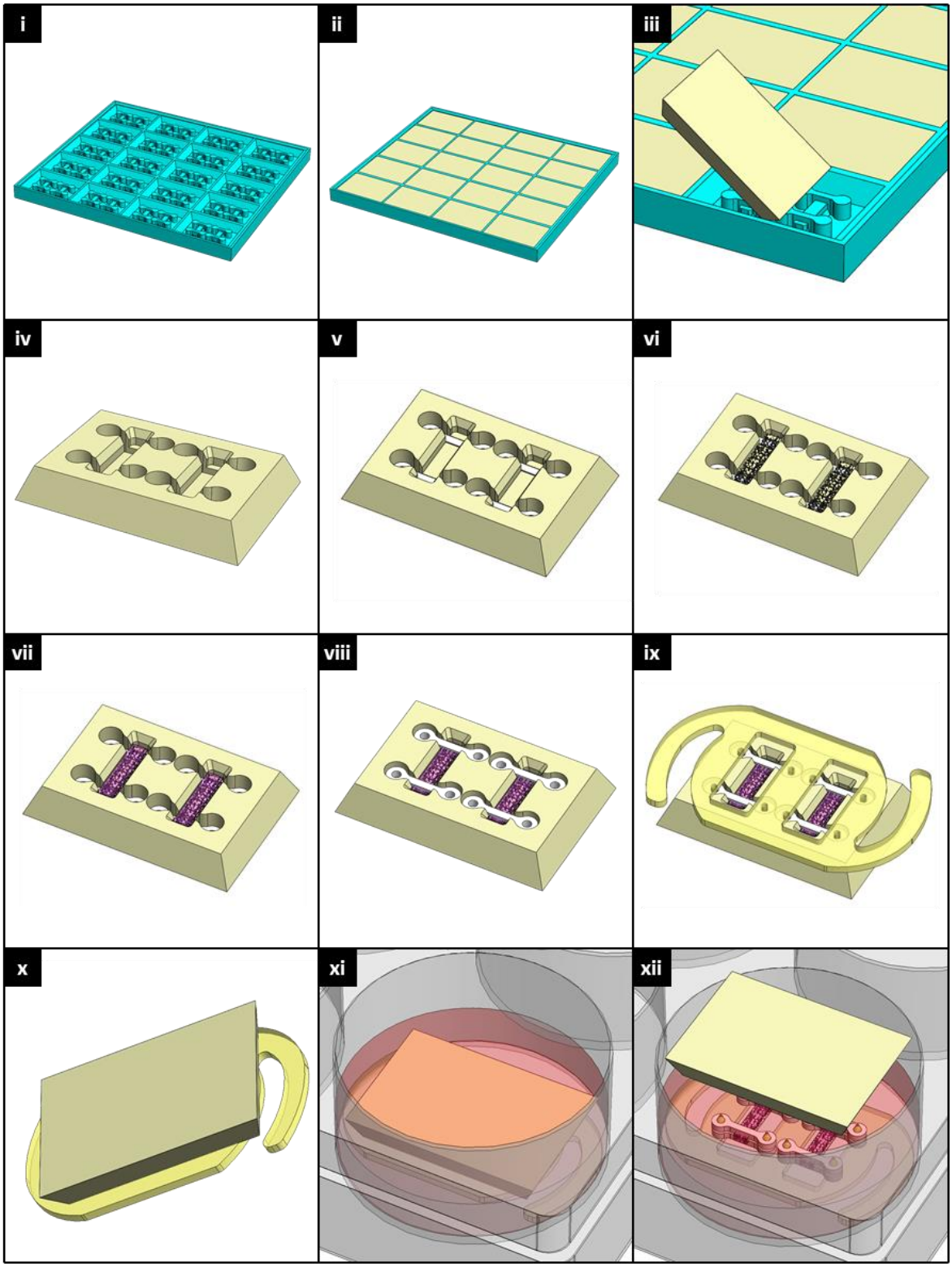


***Supporting Information 20***. *(i-iv) Sequence of preparation of seeding chambers (v-xii) Sequence of assembly of R3S.*

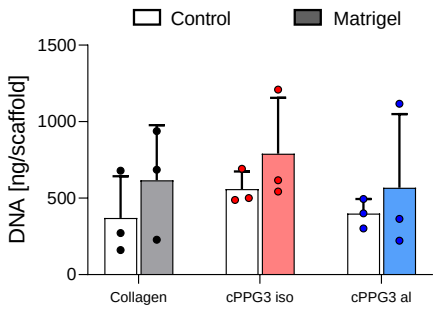


***Supporting Information 21**. Effects of seeding technique of C3H10 cells on scaffolds on cell proliferation. Quantification of DNA via Picogreen™ assay, expressed as ng per scaffold (n=3). Bar graphs demonstrate the mean with error bars representing standard deviation. Data values are presented as associated points. Statistically analysis was performed using two-way ANOVA with Tukey's post-hoc test*

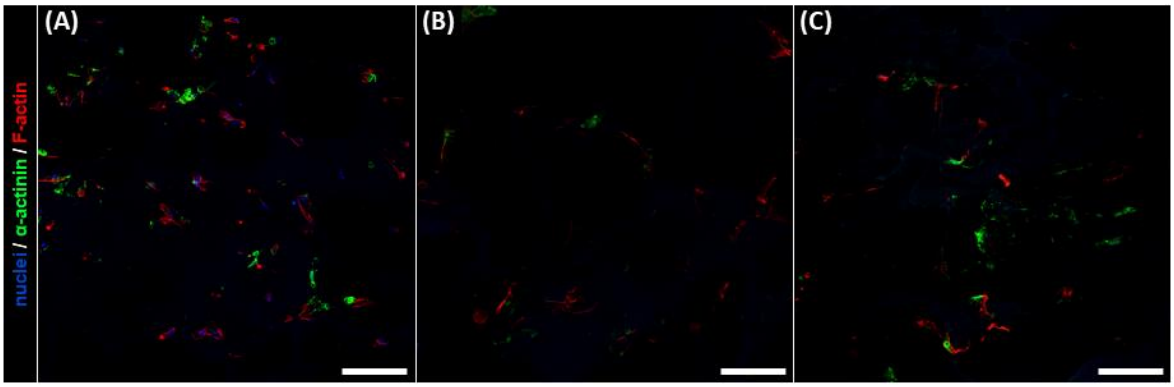


***Supporting Information 22**.. Immuno-fluorescent staining of nrCM on 3D scaffolds at d14 nrCM 7. Micrographs from confocal microscope fluorescent staining for nuclei / sarcomeric α-actinin / f-actin. **(A)** Collagen, **(B)** isotropic crystallised PEDOT:PSS-GOPS, **(C)** aligned crystallised PEDOT:PSS--GOPS. Scale bars: Ai-iii, Bi-iii = 100 µm; Aiv, Biv = 20 µm*